

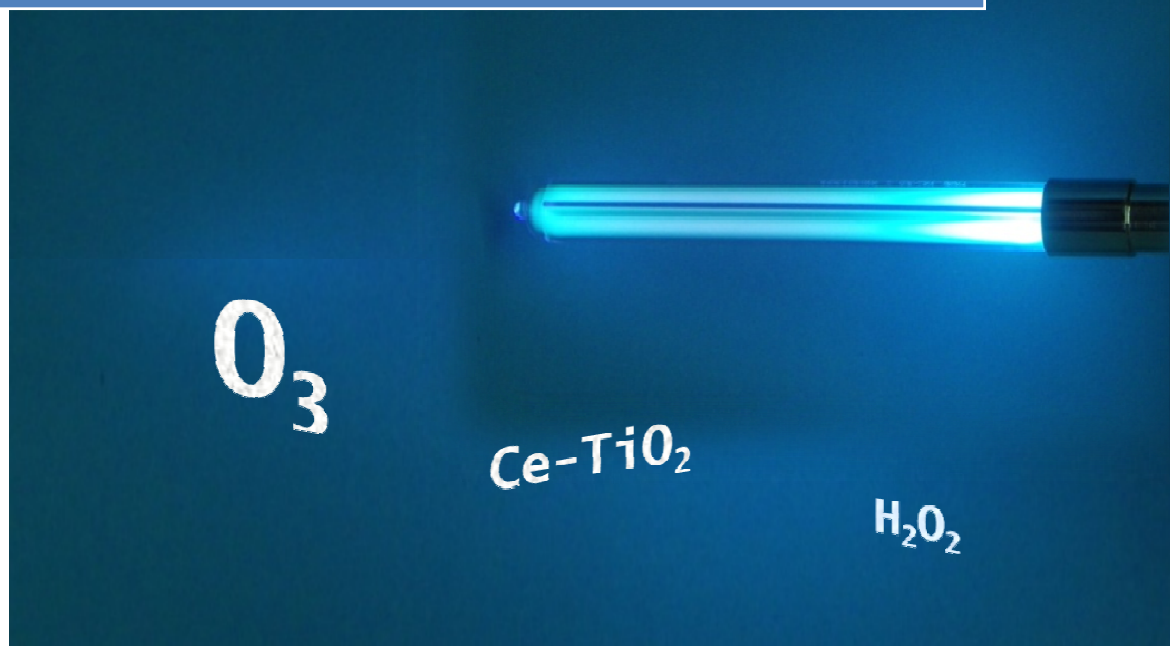


Universidad
de Alcalá

DEPARTAMENTO DE QUÍMICA
ANALÍTICA, QUÍMICA FÍSICA
E INGENIERÍA QUÍMICA

Ph.D. Thesis

Ozonation and irradiation treatments for the removal of emerging water pollutants



Javier Santiago Morales

2013

**ROBERTO ROSAL GARCÍA, Catedrático de Ingeniería Química del
Departamento de Química Analítica, Química Física e Ingeniería Química
de la Universidad de Alcalá,**

CERTIFICA:

Que el trabajo descrito en la presente memoria, titulado “Ozonation and irradiation treatments for the removal of emerging water pollutants”, ha sido realizado por D. Javier Santiago Morales bajo mi dirección en el Área de Ingeniería Química del Departamento de Química Analítica, Química Física e Ingeniería Química de la Universidad de Alcalá, excepto parte del trabajo experimental recogido en el Capítulo 3 que ha sido llevado a cabo en el Departamento de Ingeniería Química de la Universidad de Barcelona. Asimismo, autorizo su presentación para que sea defendido como Tesis Doctoral.

Y para que conste y surta los efectos oportunos, firma el presente en Alcalá de Henares a 27 de junio de 2013

Roberto Rosal García

ALBERTO ESCARPA MIGUEL, Profesor Titular de Química Analítica y Director del Departamento de Química Analítica, Química Física e Ingeniería Química de la Universidad de Alcalá,

CERTIFICA:

Que el trabajo descrito en la presente memoria, titulado “Ozonation and irradiation treatments for the removal of emerging water pollutants”, ha sido realizado en este departamento por D. Javier Santiago Morales bajo la dirección Dr. Roberto Rosal García, Catedrático de dicho departamento. Asimismo, autorizo su presentación para que sea defendido como Tesis Doctoral.

Y para que conste y surta los efectos oportunos, firma el presente en Alcalá de Henares a 27 de junio de 2013

Alberto Escarpa Miguel



Escuela de Posgrado de la Universidad de Alcalá

Programa de Doctorado en
Hidrología y Gestión de los Recursos Hídricos

PhD. Thesis

Ozonation and irradiation treatments for the removal of emerging water pollutants

Memoria presentada para optar al título de Doctor por la Universidad de Alcalá por:

Javier Santiago Morales

Alcalá de Henares (Madrid), 2013

Dirigida por:

Dr. Roberto Rosal García

Departamento de Química Analítica, Química Física e Ingeniería Química
Facultad de Biología, Ciencias Ambientales y Química
Universidad de Alcalá

La presente memoria ha sido realizada cumpliendo los requisitos para optar a la mención «Doctor Internacional».

Funding

This thesis was supported by the Spanish Government (Projects CSD2006-00044, CTM2005-03080/TECNO, CTM2008-04239/TECNO, CTM 2011-27657) and the Dirección General de Universidades e Investigación de la Comunidad de Madrid, Research Network 0505/AMB-0395. Javier Santiago Morales was supported by a FPU grant from Spanish Ministry of Education.

Agradecimientos

Quiero dar las gracias, en primer lugar, a mi director de tesis, Roberto Rosal, por darme la oportunidad de realizar este trabajo científico bajo su dirección. Me gustaría destacar que su experiencia, su entusiasmo, su facilidad para encontrar soluciones simples a problemas complejos, la posibilidad de que te respondiese a un correo electrónico casi al instante, el estar abierto a considerar cualquiera de mis propuestas y otras tantas cosas han hecho que este camino científico sea más fácil. Gracias por todo lo que me has enseñado.

Gracias también al grupo de Amadeo Rodríguez Fernández-Alba (a María José, Sonia, Marynka, Loli, Ana Agüera, María del Mar) por su trabajo bien hecho y por su inestimable colaboración en los trabajos que integran esta tesis. Asimismo, muchas gracias a toda la gente del IMDEA-Agua y del departamento de Biología de la Universidad Autónoma de Madrid.

Por supuesto, no quiero dejar pasar la oportunidad de agradecer la acogida recibida en el departamento de Ingeniería Química de la Universidad de Barcelona, en el grupo de Paul Christensen de la Universidad de Newcastle (Reino Unido), y en el “Laboratoire des Interactions Ecotoxicologie Biodiversité Ecosystèmes” (LIEBE) de Universidad de Lorraine (Francia). Gracias por vuestra ayuda y amistad.

Quiero acordarme también de mis profesores, desde la Educación Infantil hasta la Universidad, pues sois partícipes de que haya llegado hasta aquí.

Un pilar fundamental para la consecución de esta tesis han sido mis compañeros del departamento Química Analítica e Ingeniería Química. Gracias por crear el buen ambiente necesario para estimular a que me levantara cada mañana y que la hora y cuarto que tardaba en llegar se quedara en casi nada. Muchas gracias a todos los profesores (Karina, Antonio, Pedro, Guadalupe...) y a mis compañeros de "pipeteo" (Mar, Sole, Ainara, Alejandro, Zulema, Marta, Sonia, Leti, Jennifer, José "lalala", las 3 Cristinas, Clara, Patty, Raúl, Toni...) sin olvidarme de Toñi y el buen humor de Ana; gracias por vuestra ayuda y vuestras enseñanzas, conversaciones y risas tanto dentro como fuera del laboratorio.

No quiero olvidarme de todos mis amigos por estar ahí en cualquier circunstancia, incluso cuando me quedaba dormido en un bar un viernes tras una larga jornada en el labo, y compartir conmigo estos años de doctorado. Gracias a mis amigos del grupo "de la que se avecina", al grupo de los "pollos", a los de orquesta Camerata Musicalis, a los del máster de Hidrología, a los agrónomos y al resto que no se encuentran en estos grupos.

Por último quiero hacer una dedicatoria a mi familia, en especial a mis padres, Francisco y Mercedes, y a mi hermana Elena, por haberme apoyado cuando decidí embarcarme en esta aventura científica y haber estado siempre ahí. Gracias de todo corazón.

A mis padres y a mi hermana

Contents

Contents

Summary / Resumen	21
Chapter 1 Introduction	29
1.1. Background	31
1.1.1. Wastewater treatment and water reclamation scenarios	31
1.1.2. Removal treatments: Advanced oxidation processes	37
1.1.3. Transformation products and ecotoxicity	46
1.2. Objectives and outline of this thesis	49
1.3. References	52
Chapter 2 Oxidation by-products and ecotoxicity assessment during the photodegradation of fenofibric acid in aqueous solution with UV and UV/H₂O₂	59
2.1. Abstract	61
2.2. Introduction	62
2.3. Materials and methods	63
2.3.1. Reagents	63
2.3.2. Analytical methods	63
2.3.3. Toxicity test and data analysis	65
2.3.4. Experimental setup and procedure	66
2.4. Results and discussion	67
2.4.1. UV photolysis	67
2.4.2. Kinetics of UV/H ₂ O ₂ process	69
2.4.3. Identification of reaction intermediates and reaction pathway	72
2.4.4. Toxicity of partially oxidized mixtures	84
2.5. Conclusions	86

2.6. References	87
Chapter 3 Transformation products and reaction kinetics in simulated solar light photocatalytic degradation of propranolol using Ce-doped TiO₂	91
3.1. Abstract	93
3.2. Introduction	94
3.3. Materials and methods	97
3.3.1. Materials	97
3.3.2. Catalyst preparation and characterization	97
3.3.3. Analytical methods	101
3.3.4. Toxicity tests	103
3.3.5. Experimental setup and procedure	104
3.4. Results and discussion	105
3.4.1. Kinetics	105
3.4.2. Identification of reaction intermediates and reaction pathway	115
3.4.3. Toxicity of partially oxidized mixtures	129
3.5. Conclusions	132
3.6. Nomenclature	136
3.7. References	134
Chapter 4 Oxidative and photochemical processes for the removal of galaxolide and tonalide from wastewater	139
4.1. Abstract	141
4.2. Introduction	142
4.3. Methodology	146
4.3.1. Materials	146
4.3.2. Experimental setup and procedure	148
4.3.3. Analyses	151
4.3.4. Toxicity assessment	153
4.4. Results and discussion	154

4.4.1. Efficiency of hydroxyl radical formation during ozonation and irradiation processes	154
4.4.2. Removal of galaxolide and tonalide	158
4.4.3. Toxicity of raw and treated samples	163
4.5. Conclusions	167
4.6. References	168
Chapter 5 Energy efficiency for the removal of non-polar pollutants during ultraviolet irradiation, visible light photocatalysis and ozonation of a wastewater effluent	173
5.1. Abstract	175
5.2. Introduction	176
5.3. Methodology	179
5.3.1. Materials	179
5.3.2. Experimental setup and procedure	181
5.3.3. Analyses	182
5.4. Results and discussion	184
5.4.1. Removal of micropollutants	184
5.4.2. Energy efficiency	197
5.5. Conclusions	203
5.6. References	204
Chapter 6 Fate and toxicity of amine-terminated PAMAM dendrimers under ozonation and irradiation	213
6.1. Abstract	215
6.2. Introduction	216
6.3. Methodology	218
6.3.1. Materials	218
6.3.2. Experimental setup and procedure	218
6.3.3. Analyses	219
6.3.4. Toxicity determinations	220
6.4. Results	223
6.5. Discussion	232

	6.6. Conclusions	244
	6.7. References	245
Chapter 7	Conclusions and future challenges	249
	7.1. Conclusions	251
	7.2. Future challenges	252
Annex I	Figure index	257
Annex II	Table index	263
Annex III	Curriculum Vitae	267
Annex IV	Publication list	269

Summary/Resumen

Summary

Water pollution is a worldwide concern. The European Union has regulated the discharge of priority substances of anthropogenic origin to aquatic ecosystems. However, many compounds such as drugs, personal care or house cleaning products, which have been detected in water thanks to the recent improvement of analytical techniques, are not yet regulated. They are referred to as emerging micropollutants and include potentially bioaccumulative, persistent and toxic substances, some of which have been associated with endocrine disruption or antibiotic resistance. These contaminants enter the aquatic ecosystems mainly through conventional wastewater treatment plants, where most of them are not efficiently removed. Advanced oxidation technologies have been proposed for their removal based on the high oxidizing power of the hydroxyl radical. However, the oxidation of such pollutants may result in the accumulation of transformation products (TP) that can be even more toxic than their parent compounds.

The aim of the thesis work was the evaluation of several ozonation and irradiation based treatments for the removal of emerging pollutants. The degradation and transformation products of several polar, semipolar and non-polar compounds have been investigated. The research included a kinetic study of pollutant depletion, the identification of oxidation TP and the energetic and ecotoxicological assessment of the removal processes in order to identify efficient technologies. To this aim, the identification and the structure elucidation of TP was performed using gas or liquid chromatography coupled to mass spectrometry (SBSE-GC x GC-TOF-MS, LC-ESI-QTOF-MS/MS). The production of hydroxyl radicals was also

measured and related to the energy efficiency of the processes. The ecotoxicity assessment of treated mixtures was conducted using six different organisms belonging to three different trophic levels and three kingdoms. The bioassays used were the inhibition of the constitutive luminescence of the marine bacterium *Vibrio fischeri* (decomposer), the immobilization of the microcrustacean *Daphnia magna* (primary consumer), the multigenerational growth inhibition of the green alga *Pseudokirchneriella subcapitata*, and the seed germination phytotoxicity of *Licopersicon esculentum*, *Lactuca sativa* and *Lolium perenne*, all the latter primary producers.

The results showed that photodegradation treatments led to a lower hydroxyl radical production in comparison with ozonation processes. The combination of ozone with hydrogen peroxide or ultraviolet radiation increased the formation of hydroxyl radicals up to several orders of magnitude. The use of ozone in photo-assisted treatments provides a dual source of hydroxyl radicals allowing synergistic effects concerning hydroxyl radical generation. The studied pollutants were effectively removed by most treatments but in general ozonation was more effective than irradiation processes. Among the latter, the photocatalysis using cerium-doped TiO₂ was the process requiring the least amount of energy to remove the same amount of micropollutants. Neither ozonation nor irradiation treatments led to a complete mineralization of the organic compounds with the consequent accumulation of oxidation TP, most of which proceeded from the addition of hydroxyl groups or from ring-opening reactions of aromatic compounds. Concerning toxicity, it generally decreased during the ozonation but got enhanced during irradiation processes. However, a certain toxicity increase was observed in most treatments for a certain dosage of oxidant or irradiation. Prolonged treatments did not provide substantial advantages in terms of toxicity decrease, but processes using combined sources of hydroxyl radicals allowed the removal of more TP and could reach higher toxicity reductions.

Resumen

La contaminación del agua es un importante motivo de preocupación en todo el mundo. La Unión Europea ha regulado la descarga de sustancias prioritarias de origen antropogénico a los ecosistemas acuáticos. Sin embargo, muchos compuestos tales como fármacos, productos de higiene personal o de limpieza, que han sido detectados en el agua gracias a la reciente mejora de las técnicas analíticas, no están regulados todavía. Éstos son conocidos como microcontaminantes emergentes e incluyen sustancias potencialmente bioacumulativas, persistentes y tóxicas, algunas de las cuales han sido relacionadas con fenómenos de disrupción endocrina o resistencia a antibióticos. Estos contaminantes alcanzan los ecosistemas acuáticos a través de las descargas de efluentes de las plantas convencionales de tratamiento de aguas residuales, en las que muchos de ellos no se eliminan eficazmente. Para remediar esto, se ha propuesto utilizar tecnologías de oxidación avanzada, que se basan en el elevado poder oxidante del radical hidroxilo. Sin embargo, la oxidación de compuestos orgánicos dar lugar a la formación de productos de transformación que pueden ser incluso más tóxicos que los compuestos de partida.

En este trabajo se han evaluado varios tratamientos basados en el uso de ozono y radiación visible o ultravioleta con el objetivo de eliminar contaminantes emergentes. Se ha investigado la formación de productos de degradación y transformación de varios compuestos polares, semipolares y no polares. La investigación incluye el estudio cinético de la eliminación de los contaminantes, la identificación de productos de oxidación, y la evaluación energética y ecotoxicológica de los procesos

mencionados con el fin de identificar las tecnologías más eficientes. La identificación y elucidación de las estructuras se realizó mediante cromatografía de gases o líquida acopladas a espectrometría de masas (SBSE-GCxGC-TOF-MS, LC-ESI-QTOF-MS/MS). La generación de radicales hidroxilo se midió y se relacionó con el aporte de energía de cada proceso. La evaluación de la ecotoxicidad de las mezclas tratadas se llevó a cabo utilizando seis organismos pertenecientes a tres reinos y a diferentes niveles tróficos. Los bioensayos utilizados fueron la inhibición de la luminiscencia de la bacteria marina *Vibrio fischeri* (heterótrofo), la inmovilización del microcrustáceo *Daphnia magna* (consumidor primario), la inhibición del crecimiento del alga verde *Pseudokirchneriella subcapitata*, y la fitotoxicidad medida mediante la germinación de las semillas de *Licopersicon esculentum*, *Lactuca sativa* y *Lolium perenne*, todos ellos productores primarios.

Los resultados mostraron que los tratamientos de fotodegradación generaron menos radicales hidroxilos que los que utilizaban ozono. La combinación de ozono con peróxido de hidrógeno o radiación ultravioleta incrementó la producción de estos radicales varios órdenes de magnitud. El uso de ozono en tratamientos fotoasistidos proporcionó una doble fuente de radicales hidroxilos dando lugar a sinergias en la formación de estos radicales. Los contaminantes estudiados se eliminaron efectivamente en la mayoría de los tratamientos; pero en general la ozonización fue más efectiva que los procesos de irradiación. Entre estos últimos, la fotocatalisis empleando un catalizador de TiO₂ dopado con cerio resultó ser el proceso que menos energía necesitó para eliminar la misma cantidad de microcontaminantes. Ni la ozonización ni los tratamientos de irradiación consiguieron mineralizar por completo los compuestos orgánicos, con la consiguiente acumulación de subproductos de oxidación., la mayoría de ellos resultantes de la adición de grupos hidroxilo o bien de reacciones de apertura de anillo en compuestos aromáticos. En cuanto a la toxicidad, en general, ésta disminuyó durante los tratamientos con ozono mientras que

se incrementó durante los procesos de irradiación. Sin embargo, se observaron aumentos de toxicidad en la mayoría de tratamientos a ciertas dosis de oxidante o radiación. La prolongación de los tratamientos no ofreció ventajas substanciales en relación a la disminución de la toxicidad, si bien los procesos basados en el empleo combinado de distintas fuentes de radicales permitieron eliminar mayor cantidad de productos de transformación y alcanzar mayores reducciones de toxicidad.

Chapter 1

Introduction

Introduction

1.1 Background

1.1.1. Wastewater treatment and water reclamation scenarios

The pollution of water bodies is continuously increasing in a world characterized by a global water demand which has risen more than twice as much as growth in population during the last century (UN-WATER, 2013). It is expected that the world population will grow by 2.3 billion up to 9.1 billion between 2010 and 2050 in parallel with an increment of 70% for food needs and 50% for energy demand. Agriculture is the largest water consumer currently accounting for 69% of water withdrawals, and its management is one of the main policies for many governments and a key point for food security (AQUASTAT, 2013). Moreover, in the next decades a significant part of the world's population, particularly in Asia, will be moving from a starch-based diet to a meat-rich one. This will increase by a factor of four the amount of water required for food production in terms of water footprint. Sustainable water management is essential to protect human health and natural resources. For that reason, Millennium Development Goals highlighted the importance of providing safe and sufficient water obtained by sustainable methods to overcome the large number of people currently without access to microbiologically safe water (Millennium Project, 2005).

The worldwide society's growing pressure on freshwater resources is leading to higher water stress especially in overpopulated areas in Asia and Latin America (UNESCO, 2013). In the near future, intense water

scarcity is expected to occur around megacities, which will be absorbing most of the world's population increase. The other determining factor is the shortage of precipitations in arid and semiarid regions where water resources are limited and droughts are expected to increase as a consequence of climate changes. Without changes in water management policies, local scarcity will probably extend from regional to global contexts. Additionally, the water-energy nexus has been recently indicated as one of the main challenges to economic and social growth because of the double-sided interdependency of both resources. Water is needed for several energy production processes, such as raw materials extraction, powering turbines, cooling in thermal generation and crop cultivation. Energy is used for water transportation, pumping, treatment, irrigation and desalination, among others.

Several strategies are being implemented to fight against water scarcity such as improving water efficiency of crops, reducing water losses, increasing societal awareness or reclaiming wastewater (Barceló et al., 2011). Over 80% of the total amount of wastewater produced worldwide is discharged untreated to water bodies (Corcoran et al., 2010). Wastewater represents a readily available water source that could be used to reduce freshwater withdrawals, while contributing to lowering the environmental impact of wastewater discharges to aquatic ecosystems. Wastewater, however, contains a number of anthropogenic pollutants that eventual reach aquatic ecosystems. Water bodies are the final recipients of water usage and human pressure takes place not only through the water discharged from this usage but also as a consequence of water withdrawals. Their vulnerability comes from ecosystem fragmentation (e.g. reservoirs), ecosystem conversion (e.g. drainage) and degradation due to limited water renewal and poor water quality. A sustainable management of water as a global resource should ensure its availability not only for human use but for the preservation of wildlife and ecosystems.

Among all the anthropogenic pollutants discharged to the environment, persistent organic pollutants (POPs) stand out due to their ability to travel long distances from emission sources. In its address, the Stockholm Convention promoted by the United Nations Environmental Programme (UNEP) aims to reduce POPs worldwide by listing substances related to its persistence, bioaccumulation, potential for long-range environmental transport and toxicity. Currently it covers a series of pesticides, industrial chemicals and unintentionally produced substances (like polychlorinated dibenzo-p-dioxins and polychlorinated dibenzofurans) included in three annexes: elimination, restriction and reduction of unintentional production.

The European Union has proposed to reach a good chemical status of water bodies as a part of the implementation of the Water Framework Directive (WFD) (2000/60/EC of the European Parliament and Council). The objective of this regulatory framework is to set out protection for drinking water resources, for bathing water and for aquatic ecology, especially in cases of unique and valuable habitats. Chemical protection has been defined to achieve a series of quality standards established for individual chemical compounds and in compliance with this Directive and other legal texts (Decision 2455/2001/EC, Directive 2008/105/EC) a list of 48 priority substances endangering aquatic ecosystems, of which 21 are considered as priority hazardous substances, has been established (Proposal COM 2011, 876 final, 31.1.2012). This inventory is the result of the wide variety of anthropogenic organic pollutants detected in surface waters during the last decades. It includes biocides, chemicals, pesticides, polybrominated diphenyl ethers, polyaromatic hydrocarbons and metals. However, household cleaning, pharmaceutical, and personal care products, among others, are not yet included in monitoring programs of the European Union in spite of their occurrence having usually been reported in water bodies. These contaminants compose a new class of micropollutants frequently named as emerging micro-pollutants (Kümmerer, 2011).

Emerging micro-pollutants are not yet regulated but are showing up as an environmental concern. In particular, several groups of substances have been revealed as relevant: brominated flame retardants (other than PBDEs), organophosphate flame retardants and plasticizers, organometallics, nanomaterials (nanoparticles), drugs and their metabolites, perfluorinated compounds, hormones and other endocrine disrupting compounds, disinfection by-products, surfactants and their metabolites, algal and cyanobacterial toxins, polar pesticides and their transformation products, pharmaceuticals and personal care products (Petrovic et al., 2010). Except for toxins generated by algae and cyanobacteria in eutrophicated aquatic ecosystems, the rest of substances result directly from human activities (i.e. industry, urban businesses) and product consumption. Pharmaceuticals or their metabolites are normally excreted and personal care products enter sewage by bathing, washing and showering. Although emerging compounds can enter the aquatic environment through direct discharge, leakage of septic tanks, landfill leakage or water run-off, the effluents of wastewater treatment plants (WWTP) are the main pathway for them to enter the environment (Caliman and Gavrilescu, 2009). The reason for this is that conventional activated sludge processes are not particularly efficient in removing most of them. Roughly, the removal of pollutants in WWTP correlates well with their hydrophobicity measured in terms of logarithm of apparent octanol-water partition coefficient (Rosal et al., 2010).

The occurrence of emerging pollutants in WWTP effluents has been reported in concentrations ranged from ng/L to $\mu\text{g/L}$ (Rosal et al., 2010). Deblonde et al. (2011) reported that the most abundant ones ($>1.0 \mu\text{g/L}$) found in WWTP effluents were an antibiotic (tetracycline), an antiepileptic (codeine), an analgesic (ibuprofen), three diuretics (hydrochlorothiazide, amidotrizoic acid, iotalamic acid), three contrast media (iopromide, iomeprol, iohexol), a synthetic musk (galaxolide), a stimulant (caffeine) and two phthalates (di-(2-ethylhexyl) phthalate and

diisobutyl phthalate). Among these, the maximum reported concentrations were 14.2 µg/L for di-(2-ethylhexyl) phthalate, 12.6 µg/L for ibuprofen and 12.0 µg/L for caffeine (Deblonde et al., 2011). These figures are closely related with consumption: di-(2-ethylhexyl) phthalate is widely used in plastics composing up to 40% of PVC; the consumption of ibuprofen (self-medicated by 40.4% people in Spain) has been estimated at 100-200 tons year⁻¹ based on dispensed packages in 2009 (Ortiz de García et al., 2013); caffeine was consumed in Spain at a rate of 2985 tons year⁻¹ (179 mg per person and day) in 2009, based on the Food Balance Sheet (FAOSTAT, 2013) and estimated caffeine content (Fredholm et al., 1999).

The scientific community expressed concern about the fate and toxicity of these micropollutants. Many studies reported that some of these chemicals might be potentially bioaccumulative, persistent and toxic (Bolong et al., 2009; Esplugas et al., 2007; Grassi et al., 2013; Miège et al., 2012; Petrovic et al., 2004; Subedi et al., 2012). Subedi et al. (2012) found 2 pharmaceutical metabolites (diphenhydramine and desmethylertraline) and 2 synthetic musks (galaxolide, HHCB, and tonalide, ATHN) in fish tissue samples with higher concentrations in the proximity of WWTP discharge points. Miège et al. (2012) also detected hydrophobic emerging compounds in fishes, some of them at concentrations above the Environmental Quality Standards (EQS). The higher the lipophilicity, the higher the bioaccumulation and bioconcentration rates on lipid tissues and this is particularly true for species at top trophic levels, which could become an important exposure pathway for humans. Other emerging compounds can generate endocrine disruption by disturbing reproduction, stimulating hormones or causing feminization in fish, among others. It is also interesting to indicate that the presence of antibiotics in the water could compromise the effectiveness of antibiotic treatment because of bacteria resistance mechanisms (Bolong et al., 2009). WWTP generated sludge used as a fertilizer supposes the entrance pathway to soil of emerging contaminants either absorbed on the lipid fraction of the sludge

or adsorbed through electrostatic interaction between compounds and the surface of microorganisms. These compounds might alter soil flora and also enter the food chain after uptake by plants. This was reported by Kumar et al. (2005) and Michelini et al. (2012) for the antibiotics chlortetracycline and sulfadiazine, respectively. Environmental factors such as exposure time, removal and biotransformation mechanisms or photochemical degradation in surface waters affect micropollutant fate and toxicity. The generation of metabolites or transformation products has been shown to lead to products being even more toxic than the parent compounds (Esplugas et al., 2007; Santos et al., 2010).

The toxicity of emerging micropollutants measured in terms of ecotoxicological endpoints EC50 or LC50, usually range from $\mu\text{g/L}$ to mg/L according to the sensitivity of the test organism (Escher et al., 2011). EC50 is the half maximal effective concentration of a substance which leads to a response halfway between the maximum and minimum. LC50 (Half lethal concentration) is the concentration that results in 50% mortality of organisms exposed to a toxic compound. For instance, the pharmaceutical compound sulfamethoxazole led EC50 of $146 \mu\text{g/L}$ for algae *Pseudokirchneriella subcapitata* (Ferrari et al., 2004), 24h EC50 of 25.2 mg/L for *Daphnia magna* and LC50 of $>1000 \text{ mg/L}$ for *Danio rerio* (Isidori et al., 2005). In this case, the green alga is the most sensitive organism.

In order to perform environmental risk assessment (ERA), the US Food and Drug Administration (FDA) and European Commission (EC) designed systems based on the comparison between predicted environmental concentrations (PEC) and predicted no effect concentration for the worst case (PNEC), the latter of which can be estimated through standard bioassays (EC, 2003; FDA, 1998). The general indicator named risk quotient (RQ) is calculated as PEC/PNEC ratio and predicts ecotoxicological risk when $\text{RQ} > 1$ (EMEA, 2006; EC, 2003). According to this methodology, Ferrari et al. (2004) investigated the aquatic risk of six antibiotics in France

and Germany and reported $RQ > 1$, based on chronic toxicity, for propranolol, sulfamethoxazole and clofibric acid. Hernando et al. (2006) analyzed risk quotients for WWTP effluent, surface water and sediments for micropollutants at concentrations over 10 ng/L according to ERA procedure (EMEA, 2006) and concluded that most of them could cause a high ecological risk in WWTP effluents. This study did not consider the combined toxic effect of pharmaceutical mixtures that could have led to other potential toxicities. Based on MEC (maximum environmental concentration) and PNEC, Von der Oche et al. (2011) used two new indicators, the frequency of exceedance, which is the frequency of MEC/PNEC above one, and the Extent of Exceedance of PNEC, which is the ratio between the 95th percentile of all MEC figures and the lowest PNEC. They studied the environmental risk of 500 organic compounds in four European river basins and found that 15% of them supposed widespread potential hazard, of which 18 were priority substances. It is interesting to point out that 74% of the 44 compounds with MEC/PNEC ratio above ten corresponded to pesticides.

1.2. Removal treatments: Advanced oxidation processes

Due to the fact that conventional wastewater treatment methods are not capable of completely removing emerging substances, a technology improvement becomes necessary. The processes proposed to meet the challenge are coagulation-precipitation, adsorption, membrane-based and chemical, the latter being predominantly oxidative processes (Esplugas et al., 2007; Westerhoff et al., 2005). In terms of removal efficiencies, Westerhoff et al. (2005) reported that coagulation by aluminum or ferric sulphate achieved average removals of $6\% \pm 8\%$ and $26\% \pm 24\%$ for polar and nonpolar compounds, respectively. For powdered activated carbon, the average removal was about $76 \pm 13\%$ for hydrophobic compounds and $63 \pm 20\%$ for hydrophilic substances.

Regarding membrane technology, nanofiltration (600 Da molecular weight cut-off) and ultrafiltration (8 kDa MWCO) led to rejection efficiencies of about 30-90% and < 30%, respectively, for most micropollutants investigated (Yoon et al., 2007). These separation processes were initially determined by the adsorption of hydrophobic compounds, whereas steady-state operation became limited by pore retention. Reverse osmosis fed with WWTP effluents have also been used with similar results, also depending on the physical properties of compounds (Boleda et al., 2010). However, the latter is the most energy-intensive treatment, whose impact in terms of CO₂ emissions would be environmentally unfavourable (Muñoz et al., 2009).

Among oxidation processes, chlorine oxidation obtained removal efficiencies which range from no degradation until complete removal falling between 25-75% for most substances (Westerhoff et al., 2005). Ozonation usually displays higher removal efficiency than chlorine oxidation for most of ED/PPCP due to the fact that, in addition to molecular ozone, it generates hydroxyl radicals, which is a powerful non-selective oxidant species (Westerhoff et al., 2005). The standard potential of hydroxyl radical is 2.80 V, which makes it the strongest oxidant species apart from fluoride (Legrini et al., 1993). The presence of hydroxyl radicals (OH[•]) is the signature of a family of oxidation treatments referred to as Advanced Oxidation Processes (AOP), which at least in the case of ozone-driven processes is a readily available technology easy to implement in existent WWTP to degrade emerging pollutants. Hydroxyl radicals can be generated either by homogeneous or heterogeneous processes based on the combination of chemical agents (ozone, hydrogen peroxide) and energy sources (ultraviolet or visible light radiation, ultrasounds or hydrodynamic cavitation, electric current or γ -irradiation). Table 1.1 summarizes the main combinations proposed in the literature (Rodriguez et al., 2006; Pera-Titus et al., 2004; Mendez-Arriaga et al., 2009).

Table 1.1. Classification of advanced oxidation processes.

Homogeneous processes	
➤	No external energy supply
○	Alkaline ozonation (O_3/OH^-)*
○	Ozonation assisted with hydrogen peroxide (O_3/H_2O_2 , $O_3/H_2O_2/OH^-$)*
○	Ferrate ion ($K_2FeO_4, Fe(VI)$)
➤	External energy supply
○	Ultraviolet Irradiation (UV): VUV*, O_3/UV^* , H_2O_2/UV^* , $O_3/H_2O_2/UV^*$, Photo-Fenton (H_2O_2/Fe^{2+})
○	Ultrasounds (US): O_3/US , H_2O_2/US , $H_2O_2/Fe^{2+}/US$, $H_2O_2/Fe^{2+}/US/UV$
○	Electrochemistry (e^-): Anodic oxidation, electro-Fenton, Photoelectrocatalysis
Heterogeneous processes	
○	Catalytic ozonation (O_3/cat)*
○	Photocatalytic ozonation ($O_3/TiO_2/UV$)*
○	Photocatalysis with or without H_2O_2 (TiO_2/UV^* , $TiO_2/UV/H_2O_2$)
○	Visible light photocatalysis with or without H_2O_2 (cat/Xe^* , $cat/Xe/H_2O_2$)
○	Visible light sonophotocatalysis ($cat/Xe/US$)

*Treatments used in this work.

Hydroxyl radicals can react with organic compounds through hydrogen abstraction, electrophilic addition or electro-transfer reaction mechanisms. Another important reaction occurring at high hydroxyl radical concentration takes place between two hydroxyl radicals to yield hydrogen peroxide (Legrini et al., 1993). The rate constant for the reaction of hydroxyl radical with most organic compounds in aqueous solution ranges from $10^6 M^{-1}s^{-1}$ to $10^{10} M^{-1}s^{-1}$ (Buxton et al., 1988; Huber et al., 2003; von Gunten, 2003; Litter, 2005). Concerning emerging pollutants, most of them have a reaction rate constant with the hydroxyl radical near $10^9 M^{-1}s^{-1}$ (Wols and Hofman-Caris, 2012). The actual removal efficiency of target

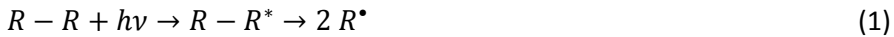
substances strongly depends on the presence of competing species which react with hydroxyl radicals. These chemicals, generally known as scavengers, include carbonate, bicarbonate, phosphate, natural dissolved organic matter or chemicals used in excess such as hydrogen peroxide (Ikehata et al., 2006; Beltran et al., 2010; Buffle et al., 2006). In that line, Rosendfeldt et al. (2006) reported different hydroxyl radical production efficiency according to freshwater characteristics and reaction pH. The effect of pH is important for ozonation kinetics because it affects ozone decomposition and chemical speciation (metal speciation, acid – base equilibrium), which in turn can favour or not the presence of reactive species such as carbonate and bicarbonate (Buffle et al., 2006). Moreover, according to the particular features of AOP, they may require special pH conditions. This is the case of ozonation, which proceeds faster under alkaline conditions or Fenton reactions whose optimum has been established around pH 2.8 (Buffle et al., 2006; Andreozzi et al., 1999). During reactions, pH must be controlled because the formation of acid species during oxidation process tends to lower the pH (Andreozzi et al., 1999).

The performance of AOP is also affected by light absorption, mass transfer limitations and OH^\cdot promoted species. Irradiation-based treatments are highly conditioned by the presence of substances competing for light absorption and obviously by the presence of a photocatalyst. Mass-transfer limitations affect all heterogeneous processes such as treatments involving ozone produced in gas-phase. Finally, some chemicals of freshwater and wastewater such as dissolved organic matter and nitrate can promote hydroxyl radical acting as a photosensitizer for the former or by photolysis for the latter (Andreozzi et al., 1999, Richard and Canonica, 2005; Friedmann et al., 2010; Lam et al., 2003).

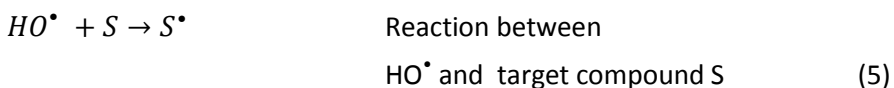
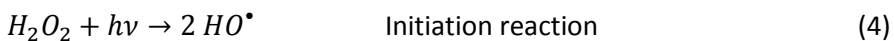
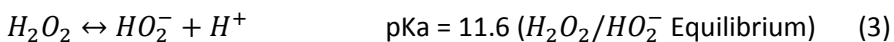
Among AOP, ozone and irradiation based treatments have been used in this thesis. The fundamentals of these processes are briefly ex-

plained below.

Photolysis allows homolytic or heterolytic molecule cleavage thanks to the radiation energy received which lead to excited states. Additional reactions can take place when oxygen is available (Litter, 2005). In any case, the emission spectrum from the radiation source must overlap the absorption spectrum of target compounds. This process can be assisted by photosensitizers, such as oxygen and fulvic acids, which absorb radiation achieving an excited state and are able to subsequently transfer energy excess to other molecules (Legrini et al., 1993; Litter, 2005).



UV/H₂O₂ is an advanced oxidation technology initiated by the photolysis of hydrogen peroxide into hydroxyl radicals. The rate of H₂O₂ photolysis increases in alkaline media because the conjugate anion of hydrogen peroxide has a higher extinction coefficient than H₂O₂ and allows higher HO[•] formation. However, an alkaline pH favours the increase of carbonate concentration, which is a well-known HO[•] scavenger. Moreover, two hydroxyl radicals might recombine into hydrogen peroxide and if H₂O₂ is in excess it can behave like a radical scavenger (Daneshvar et al., 2004; Legrini et al., 1993; Litter, 2005; Vogna et al., 2004).



Photocatalysis consists of photoexcitation of a semiconductor with a radiation of higher energy than its band-gap. Once excited, an electron is transferred from the valence band to the conduction band, generating a

positively charged hole in the former and an electron in the latter (Fig. 1.1). The hole may directly react oxidizing a target compound or may produce with water a hydroxyl radical which would then be a secondary oxidant. Meanwhile, the electron in the conduction band should react with other species, usually dissolved oxygen, via a reductive process in order to avoid electron-hole pair recombination. This is the limiting step that gives rise to the relatively low quantum yield of this type of process. Regarding its application, metal oxides, in particular TiO_2 , are the most widely investigated substances as photocatalysts. In the best case, they can be excited with solar light because of the absorption of radiation at wavelengths above 300 nm. This makes photocatalysis an environmentally friendly technology (Friedmann et al., 2010; Litter, 2005; Pera-Titus et al., 2004).

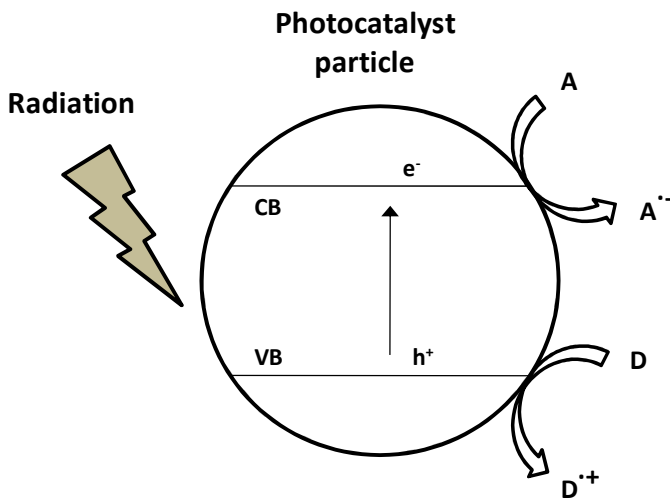
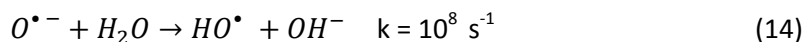
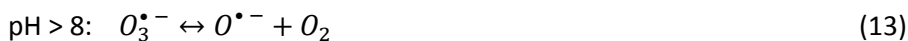
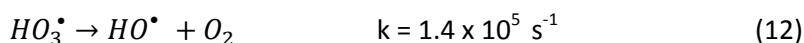
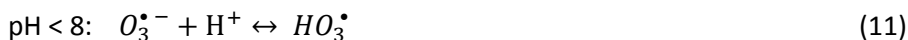


Figure 1.1. Overall mechanism of semiconductor photocatalysis. CB = conduction band; VB = valence band; A = electron acceptor; D = electron donor.

Ozonation is a widely used process whose main applications are oxidation and disinfection. Ozone is unstable in water and can decompose

into OH[•] radicals, a feature which is strongly-dependent on pH in aqueous solution. Hydroxide ions initiate ozone decomposition according to the following reactions as proposed by Stahelin-Hoigné-Bühler and Tomiyasu-Fukutomi-Gordon (Beltrán, 2003):



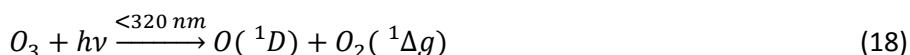
Ozone reacts in molecular form with natural organic matter, particularly with substances containing double bonds, amines, activated aromatic systems and sulfides, or indirectly, through OH[•] with the majority of organic and inorganic compounds in a reaction which is essentially diffusion-controlled (von Gunten, 2003). The oxidation of a target compound could involve both species, ozone and OH[•] radical, the former being a selective oxidant while the latter is unspecific as explained above.

Ozonation combined with hydrogen peroxide (O₃/H₂O₂) is another way to produce OH[•] radicals from ozone. Ozone can react directly with hydrogen peroxide at a very low rate or through its conjugate base (HO₂⁻) at a higher rate (Legrini et al., 1993). The reaction starts with the generation of hydroxyl radicals:



To avoid the excess of hydrogen peroxide, also a scavenger of hydroxyl radicals, an overall H₂O₂/O₃ molar ratio is suggested to be kept lower than 0.5 (Beltrán, 2003).

Ozone photolysis (O₃/UV) is a process which exploits the synergistic effects of various individual reactions, namely direct ozone attack, direct photolysis of target molecules and the production of hydroxyl radicals. The photolysis of dissolved ozone ($\epsilon_{254 \text{ nm water}} = 3300 \text{ M}^{-1} \text{ cm}^{-1}$) firstly yields oxygen atom O (¹D) and molecular oxygen (quantum yield = 0.9). Then singlet O (¹D), which is an excited species, reacts with H₂O to yield H₂O₂. Afterwards, the photolysis of hydrogen peroxide and its reaction with ozone initiate a series of reactions leading to hydroxyl radicals according to the reaction pathways shown in Eq. (16) and (17) for O₃/H₂O₂, and Eq. (4) for UV/H₂O₂ (Legrini et al., 1993; Reisz et al., 2003).



Solar light has also been used to improve ozonation in a process called Heliozon (**O₃/Xe**). This process uses radiation between 300-320 nm which is able to initiate O₃ photolysis (Sánchez et al., 2003).

Catalytic ozonation (O₃/cat). Ozonation can also use a catalyst to enhance the production of hydroxyl radicals with respect to non-catalytic ozonation. It can be conducted using a catalyst dispersed within the liquid phase suspended in a slurry or in a fixed bed. Metal oxide catalysts have been shown to increase hydroxyl radical-to- ozone ratio as demonstrated by Rosal et al. (2011). Moreover, when organics are not significantly adsorbed on the catalyst surface, the reaction should take place between non-adsorbed organics and oxidized surface site or between species in the bulk, the oxidant being in this case surface-generated hydroxyl radicals. Heterogeneous ozonation has the advantage of good separation. The main catalysts proposed for ozonation are transition metal oxides (e.g. MnO₂, TiO₂, Al₂O₃), granular or powdered activated carbon and certain mesoporous materials (e.g. MCM- or SBA-based) (Rodriguez et al., 2006).

In order to compare the efficiency of hydroxyl radical formation, which can vary with process conditions (e.g. pH, chemical doses, type of lamp) and the characteristics of water matrix (e.g. DOM, carbonate, nitrate), Elovitz and von Gunten (1999) defined the parameter R_{ct} as a ratio between integral ct -exposures to hydroxyl radicals and ozone:

$$R_{ct} = \frac{\int_0^t c_{HO} dt}{\int_0^t c_{O_3} dt} \quad (20)$$

Later, Rosenfeldt et al. (2006) introduced $R_{OH,UV}$ concept with the same aim of assessing hydroxyl radical production but adapted to irradiation based treatments:

$$R_{OH,UV} = \frac{\int_0^t c_{HO} dt}{E'_o t} \quad (21)$$

where E'_o is the average UV fluence rate per unit volume ($mW L^{-1}$) and $R_{OH,UV}$ is the hydroxyl radical exposure per UV fluence expressed in ($M L mW^{-1}$). Both parameters, R_{ct} and $R_{OH,UV}$ are useful to assess the potential hydroxyl radical generation in any water matrix and then energetic costs associated with it. A deeper insight on the environmental efficiency of AOP can be performed by using Life Cycle Analysis (LCA) tools. The reason is that these processes require a relatively high amount of energy supplied either as electricity or in the form of chemicals. Muñoz et al. (2006) used LCA to compare two solar driven treatments, photocatalysis and photo-Fenton, and found that the latter involved lower environmental impact for scale-up implementation. LCA also allows the inclusion of environmental impacts related to ecotoxicity and human toxicity. It has been noted that tertiary treatments of wastewater effluents can almost completely reduce the overall toxicity due to their discharge and constitute the best option in terms of global impact in comparison with direct water reuse or no reuse at all scenarios (Munoz et al., 2009).

1.3. Transformation products and ecotoxicity

The use of AOP to remove emerging compounds does not always lead to lower toxicity because of the fact, which has been widely reported, that transformation products (TP) can be even more toxic than the parent ones (Rosal et al., 2009; Schulze et al., 2010; Paul et al., 2010; Gómez et al., 2008; Postigo et al., 2011). Rosal et al. (2009) found a significant toxicity enhancement to *V. fischeri* and *D. magna* closely related to the presence of ring-opening TP during the ozonation of clofibric acid. In the same address, Paul et al. (2010) assessed the antibacterial activity during the photolytic and photocatalytic degradation of the antibiotic ciprofloxacin and found deactivation data suggesting the formation of an intermediate with antibacterial activity. Gómez et al. (2008) evaluated ecotoxicity to *D. magna* for the mixture generated during the photolysis of three dipyrone metabolites and observed a toxicity increase for all of them. Postigo et al. (2011) investigated the bioluminescence inhibition of the marine bacteria *V. fischeri* exposed to irradiated mixtures generated by photolysis, photocatalysis and photo-Fenton of methadone. In all cases, they found bioluminescence inhibition even after all methadone had disappeared. This is particularly significant for photolytic treatments in which TP cannot undergo further photolysis and still persists in solution at the end of the treatment. Finally, Schulze et al. (2010) observed an increase of toxicity in the green algae *Scenedesmus vacuolatus* exposed to photolyzed diclofenac mixtures. They were able to elucidate and confirm that one of the TP, at least, was responsible for the toxicity increase.

Recent improvements of the analytical tools have allowed the identification, confirmation and quantification of trace levels of micropollutants and their TP by selective and sensitive methods. Mass spectrometry (MS) coupled to either liquid or gas chromatography (LC or GC) for polar or slightly polar and non polar compounds respectively, has experienced a considerable development during the last years (Petrovic et

al., 2010). MS has greatly enhanced its resolution thanks to the use of Orbitrap and time-of-flight (TOF) or quadrupole-TOF (QTOF) mass spectrometers. However, it has been the combination of different MS systems, such as hybrid triple quadrupole-linear ion trap mass spectrometer (QqLIT) and MS/MS systems, which has led to a qualitative and quantitative improvement in the analysis of emerging micropollutants and its TP (Gros et al., 2012). Modern instruments can work in positive and negative ionization modes and are able to select protonated or deprotonated molecular ions as precursor ions to TP elucidation and target compound identification (Kern et al., 2009). In addition, high resolution systems provide the advantage of using direct sample injection, which allows a reduction in time for sample preparation and avoids the use of solvent prepared internal standards which may cause matrix effect problems such as signal enhancement or suppression (Martinez-Bueno et al., 2011). Lately, the use of stir-bar sportive extraction (SBSE) followed by comprehensive two-dimensional gas chromatography coupled to TOF-MS (GC x GC-TOF-MS) has been proposed as the automatic analytical method to efficiently separate and quantify non-polar compounds with detection limits <1 ng/L for most of them (Gomez et al., 2011).

Another important issue is the ecotoxicological assessment of aqueous solutions containing the emerging micropollutant and the TP generated during treatments. Acute and chronic toxicity tests have usually been used for toxicity evaluation through standardized bioassays established by the Organization for Economic Co-operation and Development (OECD) and the International Organization for Standardization (ISO), among others. These tests involve the use of several organisms from different trophic levels (primary producers, primary consumers, secondary consumers and decomposers) such as the algae *Pseudokirchneriella subcapitata*, the crustacean *Daphnia magna*, the fish *Danio rerio* and the marine bacteria *Vibrio fischeri*, among others. The use of a battery of organisms from different trophic levels is required in order

to correctly perform risk assessment because a single organism cannot provide results that can be extended to a whole ecosystem (EC, 2003).

The above mentioned ecotoxicological tests are not specific, but there exist a number of bioassays for specific toxic actions. They include tests to measure estrogenicity, genotoxicity, phytotoxicity, dioxin-like activity and neurotoxicity (Macova et al., 2010). All of them try to explain the interaction between a toxic substance and its target site. This is known as toxicodynamics. The specific mode of toxic action is due to a toxicophore, a substructure in a given molecule such as organophosphate of insecticides. Another dimension of toxicity is toxicokinetics, which involves all the steps from uptake of a compound into an organism to its excretion including biotransformation and the production of metabolites. The removal of chemicals by AOP usually leads to toxicophore degradation with the generation of more hydrophilic molecules. This process is expected to result in lower toxicity, but in some circumstances the breakup of a molecule might cause bioconcentration enhancement (Escher and Fenner, 2011). In this regard, the use of the physicochemical features of toxic substances, such as octanol-water partition coefficient or zeta-potential, might be useful to predict its interaction with the biological systems or living organisms.

Finally, as emerging pollutants are discharged to the environment as complex mixtures, current ecotoxicity investigations also focus on the combined effect of different compounds (Rosal et al., 2010). In fact, a single chemical might display no toxic effect while mixtures with similar concentration could undergo interactions which result in higher toxicity. In particular, the Combination-Index method has been recently suggested to be a more accurate tool than the traditional models of Concentration-Addition and Independent-Action (González-Pleiter et al., 2013). This method has been used for chemicals of different classes to quantify antagonism, synergism and additive effect as a function of the effect level

and test organism used (González-Pleiter et al., 2013; Rodea-Palomares et al., 2010).

2. Objectives and outline of this thesis

The present thesis work aims to study several ozonation and irradiation based processes for the removal of different classes of emerging pollutants from those commonly detected in WWTP effluents. The research effort mainly focuses on the kinetic study, the identification of transformation products, and the energetic and ecotoxicological assessment of micropollutants in order to provide background to identify the most efficient treatment technology.

The specific objectives were:

1. To study the removal kinetics of several emerging micropollutants during ozonation and irradiation processes. In particular, this work focused on two pharmaceuticals (fenofibric acid and propranolol), two synthetic musks (galaxolide and tonalide), a pool of sixteen non-polar or semipolar micropollutants tracked within a real wastewater effluent, and a dendrimer nanoparticle (third-generation amino-terminated poly-amidoamine dendrimer).
2. To elucidate and quantify the transformation products which resulted from oxidation and irradiation treatments in order to propose possible reaction pathways and to compare the energetic efficiency of these mentioned processes. In particular, the efficiency in generating hydroxyl radicals of irradiation and ozone based treatments was considered both in buffered pure water and in a real wastewater matrix.
3. To assess the ecotoxicity of partially oxidized and irradiated mixtures exposed to living organisms from different trophic levels. The results aimed to identify the pollutant removal treatments

leading to a toxicity reduction and those in which a higher toxicity is obtained which could be related to the generation of transformation products.

These objectives are developed through the following chapters, each of which corresponds to a self-standing unit organized around certain target emerging pollutants or a particular wastewater effluent. Except this Chapter 1, which is introductory, and Chapter 7, *Conclusions and future challenges*, the other chapters match with articles published or submitted to peer-review journals prior to PhD defense. A brief description of the following chapters is presented:

Chapter 2 - *Oxidation by-products and ecotoxicity assessment during the photodegradation of fenofibric acid in aqueous solution with UV and UV/H₂O₂ (Journal of Hazardous Materials 194: 30-41, 2011)* - describes the removal of fenofibric acid from aqueous solution by ultraviolet irradiation, either alone or in combination with hydrogen peroxide. It includes the identification of transformation products by LC- ESI-QTOF-MS and the toxicity assessment performed with the algae *Pseudokirchneriella subcapitata*.

Chapter 3 - *Transformation products and reaction kinetics in simulated solar light photocatalytic degradation of propranolol using Ce-doped TiO₂ (Applied Catalysis B: Environmental 129: 13-29, 2012)* – studies the influence of Ce doping TiO₂ photocatalyst applied to photocatalytic removal of the beta-blocker propranolol. Once optimum cerium load and bulk catalyst concentration are determined, elucidation of by-products by LC- ESI-QTOF-MS/MS and evaluation of ecotoxicity using the bacteria *Vibrio fischeri* and the algae *P. subcapitata* are performed with the mixtures obtained during visible light irradiation photolysis and photocatalysis.

Chapter 4 - *Oxidative and photochemical processes for the removal of galaxolide and tonalide from wastewater (Water Research 46: 4435-*

4447, 2012) - assesses hydroxyl radical production of nine oxidative and irradiative based processes for buffer-pure-water and wastewater, and the removal efficiency of two synthetic musk, galaxolide and tonalide. It also presents a concentration profile of galaxolide-lactone, which is an oxidation by-product of galaxolide, and the effect on *Vibrio fischeri*, *P. subcapitata* and *Daphnia magna* exposed to oxidized and irradiated mixtures.

Chapter 5 - *Energy efficiency for the removal of non-polar pollutants during ultraviolet irradiation, visible light photocatalysis and ozonation of a wastewater effluent* (Water Research, DOI 10.1016/j.watres. 2013.06.030) – studies the degradation of sixteen slightly polar and non polar pollutants during ozonation and ultraviolet and visible light irradiation, and visible light photocatalysis. In addition it includes an assessment of the energetic efficiency and toxicity associated with these processes.

Chapter 6 - *Fate and toxicity of amine-terminated PAMAM dendrimers under ozonation and irradiation* (submitted) – determines the occurrence of transformation products formed during ozonation and irradiation processes of a dendrimer nanoparticle, as well as its removal kinetics. Moreover, a wide ecotoxicity study is conducted to evaluate its toxicity endpoints for six living organisms from different trophic levels as well as toxicity evolution with treatment time.

Chapter 7 – *Conclusions and future challenges*- summarizes and remarks the various contribution of this thesis in view of the scientific advances gained in the understanding of the relationship between advanced oxidation processes, the generation of transformation products and the ecotoxicity of emerging pollutants. It is stressed that pollutant removal treatments should be conducted under environmentally sustainable conditions.

3. References

- Andreozzi, R., Caprio, V., Insola, A. and Marotta, R., 1999. Advanced oxidation processes (AOP) for water purification and recovery. *Catalysis Today* 53, 51-59.
- Barceló, D., Petrovic, M., Alemany, J., 2011. Problems and Needs of Sustainable Water Management in the Mediterranean Area: Conclusions and Recommendations, in Damià Barceló and Mira Petrovic (Eds.) *Waste Water Treatment and Reuse in the Mediterranean Region, The Handbook of Environmental Chemistry*, 14 ,295-305.
- Beltran, F.J., 2003. *Ozone reaction kinetics for water and wastewater systems*, CRC Press.
- Beltran, F.J., Aguinaco, A. and Garcia-Araya, J.F., 2010. Kinetic modelling of TOC removal in the photocatalytic ozonation of diclofenac aqueous solutions. *Applied Catalysis B-Environmental* 100, 289-298.
- Boleda, M.R., Majamaa, K., Aerts, P., Gómez, V., Galceran, M.T. and Ventura, F., 2010. Removal of drugs of abuse from municipal wastewater using reverse osmosis membranes. *Desalination and Water Treatment* 21, 122-130.
- Bolong, N., Ismail, A.F., Salim, M.R. and Matsuura, T., 2009. A review of the effects of emerging contaminants in wastewater and options for their removal. *Desalination* 239, 229-246.
- Buffle, M.O., Schumacher, J., Meylan, S., Jekel, M. and von Gunten, U., 2006. Ozonation and advanced oxidation of wastewater: Effect of O₃ dose, pH, DOM and HO center dot-scavengers on ozone decomposition and HO center dot generation. *Ozone-Science & Engineering* 28, 247-259.
- Buxton, G.V., Greenstock, C.L., Helman, W.P. and Ross, A.B., 1988. Critical review of rate constants for reactions of hydrated electrons, hydrogen atoms and hydroxyl radicals. *Physical and Chemical Reference Data* 17, 513-886.
- Caliman, F.A. and Gavrilescu, M., 2009. Pharmaceuticals, personal care products and endocrine disrupting agents in the environment—a review. *CLEAN—Soil, Air, Water* 37, 277-303.
- Corcoran, E., Nellemann, C., Baker, E., Bos, R., Osborn, D. and Savelli, H., 2010. Sick Water? The Central Role of Wastewater Management in Sustainable Development. A Rapid Response Assessment. UN-Habitat/UNEP/GriD-ARENDAL (ed)
- Daneshvar, N., Rabbani, M., Modirshahla, N. and Behnajady, M.A., 2004. Critical effect of hydrogen peroxide concentration in photochemical oxidative degradation of CI Acid Red 27 (AR27). *Chemosphere* 56, 895-900.

- Deblonde, T., Cossu-Leguille, C. and Hartemann, P., 2011. Emerging pollutants in wastewater: A review of the literature. *International Journal of Hygiene and Environmental Health* 214, 442-448.
- E.C., 2003. Technical Guidance Documents in Support of the Commission Directive 93/667/EECC, on risk assessment for new notified substances, the Commission regulation (EC) 1488/94 on Risk substances and the Directive 98/8/EC of the European Parliament and of the Council concerning the placing of biocidal products on the market. Part II, European Chemical Bureau, Ispra, Italy
- Elovitz, M.S. and von Gunten, U., 1999. Hydroxyl radical/ozone ratios during ozonation processes. I. The Rct concept. *Ozone: Science & Engineering* 21, 239-260.
- EMA, 2006. Guideline on the Environmental Risk Assessment of Medicinal Products for Human Use CHMP/SWP/4447/00, The European Agency for the Evaluation of Medicinal Products, London
- Escher, B.I., Baumgartner, R., Koller, M., Treyer, K., Lienert, J. and McArdell, C.S., 2011. Environmental toxicology and risk assessment of pharmaceuticals from hospital wastewater. *Water Research* 45(1), 75-92.
- Escher, B.I. and Fenner, K., 2011. Recent advances in environmental risk assessment of transformation products. *Environmental Science & Technology* 45, 3835-3847.
- Esplugas, S., Bila, D.M., Krause, L.G.T. and Dezotti, M., 2007. Ozonation and advanced oxidation technologies to remove endocrine disrupting chemicals (EDCs) and pharmaceuticals and personal care products (PPCPs) in water effluents. *Journal of Hazardous Materials* 149, 631-642.
- AQUASTAT, 2013. Available at: <http://www.fao.org/nr/water/aquastat/main/index.stm>. Accessed on 25 March 2013.
- FAOSTAT, 2013. Food Balance Sheet. Available from: <http://faostat3.fao.org/home/index.html>. Accessed on 1 April 2013.
- FDA, 1998. Guidance for industry-Environmental assessment of human drugs and biologics applications, FDA, CDER/CBER. CMC 6., rev1
- Ferrari, B., Mons, R., Vollat, B., Fraysse, B., Paxéaus, N., Giudice, R.L., Pollio, A. and Garric, J., 2004. Environmental risk assessment of six human pharmaceuticals: Are the current environmental risk assessment procedures sufficient for the protection of the aquatic environment? *Environmental Toxicology and Chemistry* 23, 1344-1354.
- Fredholm, B.B., Bättig, K., Holmén, J., Nehlig, A. and Zvartau, E.E., 1999. Actions of caffeine in the brain with special reference to factors that contribute to its widespread use. *Pharmacological Reviews* 51, 83-133.

- Friedmann, D., Mendive, C. and Bahnemann, D., 2010. TiO₂ for water treatment: Parameters affecting the kinetics and mechanisms of photocatalysis. *Applied Catalysis B-Environmental* 99, 398-406.
- Gomez, M.J., Herrera, S., Sole, D., Garcia-Calvo, E. and Fernandez-Alba, A.R., 2011. Automatic Searching and Evaluation of Priority and Emerging Contaminants in Wastewater and River Water by Stir Bar Sorptive Extraction followed by Comprehensive Two-Dimensional Gas Chromatography-Time-of-Flight Mass Spectrometry. *Analytical Chemistry* 83, 2638-2647.
- Gómez, M.J., Sirtori, C., Mezcuca, M., Fernández-Alba, A.R. and Agüera, A., 2008. Photodegradation study of three dipyrone metabolites in various water systems: Identification and toxicity of their photodegradation products. *Water Research* 42, 2698-2706.
- González-Pleiter, M., Gonzalo, S., Palomares, I.R., Leganés, F., Rosal, R., Boltes, K., Marco, E. and Piñas, F.F., 2013. Toxicity of five antibiotics and their mixtures towards photosynthetic aquatic organisms: Implications for environmental risk assessment. *Water Research* 47, 2050-2064
- Grassi, M., Rizzo, L. and Farina, A., 2013. Endocrine disruptors compounds, pharmaceuticals and personal care products in urban wastewater: implications for agricultural reuse and their removal by adsorption process. *Environmental Science and Pollution Research*, 1-13.
- Gros, M., Rodríguez-Mozaz, S. and Barceló, D., 2012. Fast and comprehensive multi-residue analysis of a broad range of human and veterinary pharmaceuticals and some of their metabolites in surface and treated waters by ultra-high-performance liquid chromatography coupled to quadrupole-linear ion trap tandem mass spectrometry. *Journal of Chromatography A* 1248, 104-121.
- Hernando, M.D., Mezcuca, M., Fernandez-Alba, A.R. and Barcelo, D., 2006. Environmental risk assessment of pharmaceutical residues in wastewater effluents, surface waters and sediments. *Talanta* 69, 334-342.
- Huber, M.M., Canonica, S., Park, G.Y. and Von Gunten, U., 2003. Oxidation of pharmaceuticals during ozonation and advanced oxidation processes. *Environmental Science & Technology* 37, 1016-1024.
- Ikehata, K., Naghashkar, N.J. and Ei-Din, M.G., 2006. Degradation of aqueous pharmaceuticals by ozonation and advanced oxidation processes: A review. *Ozone-Science & Engineering* 28, 353-414.
- Isidori, M., Lavorgna, M., Nardelli, A., Pascarella, L. and Parrella, A., 2005. Toxic and genotoxic evaluation of six antibiotics on non-target organisms. *Science of the Total Environment* 346, 87-98.
- Kern, S., Fenner, K., Singer, H.P., Schwarzenbach, R.P. and Hollender, J., 2009. Identification of transformation products of organic contaminants in

- natural waters by computer-aided prediction and high-resolution mass spectrometry. *Environmental Science & Technology* 43, 7039-7046.
- Kümmerer, K., 2011. Emerging Contaminants versus Micro-pollutants. *Clean–Soil, Air, Water* 39, 889-890.
- Kumar, K., Gupta, S., Baidoo, S., Chander, Y. and Rosen, C., 2005. Antibiotic uptake by plants from soil fertilized with animal manure. *Journal of Environmental Quality* 34, 2082-2085.
- Lam, M.W., Tantuco, K. and Mabury, S.A., 2003. PhotoFate: A New Approach in Accounting for the Contribution of Indirect Photolysis of Pesticides and Pharmaceuticals in Surface Waters. *Environmental Science & Technology* 37, 899-907.
- Legrini, O., Oliveros, E. and Braun, A., 1993. Photochemical processes for water treatment. *Chemical Reviews* 93, 671-698.
- Litter, M., 2005. Introduction to Photochemical Advanced Oxidation Processes for Water Treatment. *The Handbook of Environmental Chemistry* 2(M).
- Macova, M., Escher, B., Reungoat, J., Carswell, S., Chue, K.L., Keller, J. and Mueller, J., 2010. Monitoring the biological activity of micropollutants during advanced wastewater treatment with ozonation and activated carbon filtration. *Water Research* 44, 477-492.
- Martínez Bueno, M., Uclés, S., Hernando, M. and Fernández-Alba, A., 2011. Development of a solvent-free method for the simultaneous identification/quantification of drugs of abuse and their metabolites in environmental water by LC–MS/MS. *Talanta* 85, 157-166.
- Mendez-Arriaga, F., Torres-Palma, R., Pétrier, C., Esplugas, S., Gimenez, J. and Pulgarin, C., 2009. Mineralization enhancement of a recalcitrant pharmaceutical pollutant in water by advanced oxidation hybrid processes. *Water Research* 43, 3984-3991.
- Michelini, L., Reichel, R., Werner, W., Ghisi, R. and Thiele-Bruhn, S., 2012. Sulfadiazine Uptake and Effects on *Salix fragilis* L. and *Zea mays* L. Plants. *Water, Air, & Soil Pollution* 223, 5243-5257.
- Miège, C., Peretti, A., Labadie, P., Budzinski, H., Le Bizec, B., Vorkamp, K., Tronczyński, J., Persat, H., Coquery, M. and Babut, M., 2012. Occurrence of priority and emerging organic compounds in fishes from the Rhone River (France). *Analytical and Bioanalytical Chemistry*, 404, 2721-2735.
- Munoz, I., Rodriguez, A., Rosal, R. and Fernandez-Alba, A.R., 2009. Life Cycle Assessment of urban wastewater reuse with ozonation as tertiary treatment A focus on toxicity-related impacts. *Science of the Total Environment* 407, 1245-1256.

- Muñoz, I., Peral, J., Antonio Ayllón, J., Malato, S., Passarinho, P. and Domènech, X., 2006. Life cycle assessment of a coupled solar photocatalytic–biological process for wastewater treatment. *Water Research* 40(19), 3533-3540.
- Ortiz de García, S., Pinto Pinto, G., García Encina, P. and Irusta Mata, R., 2013. Consumption and occurrence of pharmaceutical and personal care products in the aquatic environment in Spain. *Science of the Total Environment* 444, 451-465.
- Paul, T., Dodd, M.C. and Strathmann, T.J., 2010. Photolytic and photocatalytic decomposition of aqueous ciprofloxacin: Transformation products and residual antibacterial activity. *Water Research* 44, 3121-3132.
- Pera-Titus, M., Garcia-Molina, V., Banos, M.A., Gimenez, J. and Esplugas, S., 2004. Degradation of chlorophenols by means of advanced oxidation processes: a general review. *Applied Catalysis B-Environmental* 47, 219-256.
- Petrovic, M., Eljarrat, E., De Alda, M.L. and Barceló, D., 2004. Endocrine disrupting compounds and other emerging contaminants in the environment: A survey on new monitoring strategies and occurrence data. *Analytical and Bioanalytical Chemistry* 378, 549-562.
- Petrovic, M., Farré, M., De Alda, M.L., Perez, S., Postigo, C., Köck, M., Radjenovic, J., Gros, M. and Barcelo, D., 2010. Recent trends in the liquid chromatography–mass spectrometry analysis of organic contaminants in environmental samples. *Journal of Chromatography A* 1217, 4004-4017.
- Postigo, C., Sirtori, C., Oller, I., Malato, S., Maldonado, M.I., López de Alda, M. and Barcelo, D., 2011. Photolytic and photocatalytic transformation of methadone in aqueous solutions under solar irradiation: Kinetics, characterization of major intermediate products and toxicity evaluation. *Water Research* 45, 4815-4826.
- Reisz, E., Schmidt, W., Schuchmann, H.-P. and von Sonntag, C., 2003. Photolysis of ozone in aqueous solutions in the presence of tertiary butanol. *Environmental Science & Technology* 37, 1941-1948.
- Richard, C. and Canonica, S. (2005) *Environmental Photochemistry Part II*, pp. 299-323, Springer.
- Rodea-Palomares, I., Petre, A.L., Boltes, K., Leganes, F., Perdigon-Melon, J.A., Rosal, R. and Fernandez-Pinas, F., 2010. Application of the combination index (CI)-isobologram equation to study the toxicological interactions of lipid regulators in two aquatic bioluminescent organisms. *Water Research* 44, 427-438.
- Rodriguez, A., Leton, P., Rosal, R., Dorado, M., Villar, S. and Sanz, J.M., 2006. *Tratamientos avanzados de aguas residuales industriales*, CEIM and Dirección General de Universidades e Investigación de Comunidad de Madrid, Madrid.

- Rosal, R., Gonzalo, M.S., Boltes, K., Leton, P., Vaquero, J.J. and Garcia-Calvo, E., 2009. Identification of intermediates and assessment of ecotoxicity in the oxidation products generated during the ozonation of clofibric acid. *Journal of Hazardous Materials* 172, 1061-1068.
- Rosal, R., Rodríguez, A., Perdigón-Melón, J.A., Petre, A., García-Calvo, E., Gómez, M.J., Agüera, A. and Fernández-Alba, A.R., 2010. Occurrence of emerging pollutants in urban wastewater and their removal through biological treatment followed by ozonation. *Water Research* 44(2), 578-588.
- Rosenfeldt, E.J., Linden, K.G., Canonica, S. and von Gunten, U., 2006. Comparison of the efficiency of center dot OH radical formation during ozonation and the advanced oxidation processes O₃/H₂O₂ and UV/H₂O₂. *Water Research* 40, 3695-3704.
- Sánchez, L., Domènech, X., Casado, J. and Peral, J., 2003. Solar activated ozonation of phenol and malic acid. *Chemosphere* 50, 1085-1093.
- Santos, L.H., Araújo, A., Fachini, A., Pena, A., Delerue-Matos, C. and Montenegro, M., 2010. Ecotoxicological aspects related to the presence of pharmaceuticals in the aquatic environment. *Journal of Hazardous Materials* 175, 45-95.
- Schulze, T., Weiss, S., Schymanski, E., von der Ohe, P.C., Schmitt-Jansen, M., Altenburger, R., Streck, G. and Brack, W., 2010. Identification of a phytotoxic photo-transformation product of diclofenac using effect-directed analysis. *Environmental Pollution* 158, 1461-1466.
- Subedi, B., Du, B., Chambliss, C.K., Koschorreck, J., Rüdell, H., Quack, M., Brooks, B.W. and Usenko, S., 2012. Occurrence of pharmaceuticals and personal care products in German fish tissue: a national study. *Environmental Science & Technology* 46, 9047-9054.
- UN-WATER, 2013. Statistics. Available at: <http://www.unwater.org/statistics.html>. Accessed on 1 April 2013.
- UNESCO, World Water Assessment Programme (WWAP), 2013. Indicators-Level of Stress on the Resource. Available at: <http://www.unesco.org/new/en/natural-sciences/environment/water/wwap/indicators/wwdr-indicators/level-of-stress-on-the-resource/>. Accessed on 5 April 2013.
- UN Millenium Project, 2005. Investing in Development: A Practical Plan to Achieve The Millennium Development Goals. New York
- Vogna, D., Marotta, R., Andreozzi, R., Napolitano, A. and d'Ischia, M., 2004. Kinetic and chemical assessment of the UV/H₂O₂ treatment of antiepileptic drug carbamazepine. *Chemosphere* 54, 497-505.
- von der Ohe, P.C., Dulio, V., Slobodnik, J., De Deckere, E., Kühne, R., Ebert, R.-U., Ginebreda, A., De Cooman, W., Schüürmann, G. and Brack, W., 2011. A new risk assessment approach for the prioritization of 500 classical and

emerging organic microcontaminants as potential river basin specific pollutants under the European Water Framework Directive. *Science of the Total Environment* 409, 2064-2077.

von Gunten, U., 2003. Ozonation of drinking water: Part I. Oxidation kinetics and product formation. *Water Research* 37, 1443-1467.

Westerhoff, P., Yoon, Y., Snyder, S. and Wert, E., 2005. Fate of endocrine-disruptor, pharmaceutical, and personal care product chemicals during simulated drinking water treatment processes. *Environmental Science & Technology* 39, 6649-6663.

Wols, B. and Hofman-Caris, C., 2012. Review of photochemical reaction constants of organic micropollutants required for UV advanced oxidation processes in water. *Water Research* 46, 2815-2827

Yoon, Y., Westerhoff, P., Snyder, S.A., Wert, E.C. and Yoon, J., 2007. Removal of endocrine disrupting compounds and pharmaceuticals by nanofiltration and ultrafiltration membranes. *Desalination* 202, 16-23.

Chapter 2

Oxidation by-products and ecotoxicity assessment during the photodegradation of fenofibric acid in aqueous solution with UV and UV/H₂O₂

Oxidation by-products and ecotoxicity assessment during the photodegradation of fenofibric acid in aqueous solution with UV and UV/H₂O₂*

2.1. Abstract

The degradation of an aqueous solution of fenofibric acid was investigated using ultraviolet (UV) photolysis and UV/H₂O₂ with a low-pressure mercury lamp. We obtained quantum yields at different temperatures and the rate constant for the reaction of fenofibric acid with hydroxyl radicals. The maximum radical exposure per fluence ratio obtained was $1.4 \times 10^{-10} \text{ M L}^{-1} \text{ mW}^{-1}$. Several reaction intermediates were detected by means of exact mass measurements performed by liquid chromatography coupled to quadrupole-time-of-flight mass spectrometry (LC-ESI-QTOF-MS). UV and UV/H₂O₂ pathways involve the decarboxylation of fenofibric acid to 4-chloro-4'-(1-hydroxy-1-methylethyl) benzophenone and other minor products, predominantly chlorinated aromatics. We detected several intermediates from reactions with hydroxyl radicals and some lower molecular weight products from the scission of the carbonyl carbon-to-aromatic-carbon bond. We recorded high toxicity in UV irradiated samples for the growth of *Pseudokirchneriella subcapitata* even

* The contents of this chapter have been published as:

Santiago, J., Agüera, A., del Mar Gómez-Ramos, M., Fernández Alba, A. R., García-Calvo, E., Rosal, R., 2011. Oxidation by-products and ecotoxicity assessment during the photodegradation of fenofibric acid in aqueous solution with UV and UV/H₂O₂. *Journal of Hazardous Materials* 194, 30-41.

after the total depletion of fenofibric acid; this was probably due to the presence of chlorinated aromatics. A degree of toxicity reappeared in highly irradiated UV/H₂O₂ samples, probably because of the formation of ring-opening products. The degree of mineralization was closely related to that of dechlorination and reached values of over 50% after 3-4 min before stabilizing thereafter.

2.2. Introduction

Fenofibric acid, 2-[4-(4-Chlorobenzoyl)phenoxy]-2-methylpropanoic acid, is the active form of fenofibrate, a drug prescribed to reduce plasma triglycerides. Although its use is not widespread, it has often been encountered in wastewater treatment plants (WWTP). Rosal et al. (2010d) reported very low removal efficiency for fenofibric acid in a conventional WWTP located in Madrid with an average annual concentration of 79 ng/L. Stump et al. (1999) obtained concentrations of up to 500 ng/L in the influent of several Brazilian WWTP and calculated a removal efficiency of 45% for conventional activated sludge treatment. Ternes et al. (2003) reported the occurrence of 130 ng/L of fenofibric acid in the effluent of a German WWTP. Acero et al. (2010) found 180 ng/L in the effluent of a WWTP located in Madrid. Fenofibric acid attracts particular attention due to its high toxicity for several aquatic microorganisms (Rosal et al., 2010b). An additional reason for concern is that fenofibric acid and other pharmaceuticals are released in increasing quantities in complex mixtures. Recently, Rodea-Palomares et al. (2010) and Rosal et al. (2010c) used the combination index-isobologram method and reported a synergistic behaviour for fenofibric acid in mixtures involving wastewater.

Advanced oxidation processes (AOP) are effective technologies for the removal of organic pollutants in wastewater. UV-based AOP have the advantage of using a fully commercialized technology due to the widespread use of UV systems for disinfection (Litter, 2005). A drawback of

these processes is the formation of oxidation by-products (Legube, 2003). Over the last few years, it has been shown that the formation of by-products with enhanced toxicity for non-target organisms usually takes place at least under conditions of moderate carbon removal (Rosal et al., 2009a; López-Peñalver et al., 2010). The identification of unknown transformation products is not an easy task. Liquid chromatography-mass spectrometry (LC-MS) combined with a new generation of high sensitivity MS systems provides abundant structural information for the elucidation of chemical structures. The objective of this work was to study the removal of fenofibric acid using UV and UV/H₂O₂ photolysis. We identified oxidation intermediates in order to propose a reaction pathway for the early oxidation stages. We also measured the ecotoxicity of partially oxidized mixtures.

2.3. Materials and methods

2.3.1. Reagents

Fenofibric acid was produced from fenofibrate (Sigma Aldrich, +99% purity) as indicated elsewhere (Rosal et al., 2010b). The product's purity was over 97%, as evaluated by high-performance liquid chromatography (HPLC). Pure water was obtained from a Millipore Mili-Q system with a resistivity of at least 18 MΩ cm at 298 K and a Millipore 0.22 micron Millipak Express filter (Billerica, MA). Hydrogen peroxide, sodium phosphate monobasic dihydrate and sodium hydrogen phosphate, sodium hydroxide and hydrochloric acid were analytical grade reagents used as received. p-chlorobenzoic acid (pCBA), atrazine and 2,9-dimethyl-1,10-phenanthroline (DMP) were purchased from Sigma Aldrich (+99% purity).

2.3.2. Analytical methods

Total organic carbon (TOC) was determined using a Shimadzu TOC-VCSH analyzer. Chlorine was determined using a Dionex DX120 Ion

Chromatograph with a conductivity detector and an IonPac AS9-HC 4 mm × 250 mm analytical column with ASRS-Ultra suppressor. The eluent was 9.0mM Na₂CO₃ flowing at 1.0mL/min. The determination of extinction coefficients and colorimetric analyses was performed in a Shimadzu UV-1800 spectrophotometer. The analyses of fenofibric acid, pCBA and atrazine were performed by HPLC using an Agilent 1200 apparatus equipped with a reversed phase Kromasil 5u 100A C18 analytical column. The mobile phase (flow rate 1 mL/min) was a mixture of water containing 4 mL/L of orthophosphoric acid and 50 mL/L of methanol and acetonitrile in a proportion of 40:60 for pCBA separation and 50:50 for atrazine and fenofibric acid. UV detection was carried out at 280 nm and 228 nm for fenofibric acid, and atrazine and pCBA respectively. The volume injected was 50 µL in all cases. Hydrogen peroxide was measured using the colorimetric methods of Eisenberg (1943) and Baga et al. (1988).

A liquid chromatography-electrospray ionization-quadrupole-time-of-flight mass spectrometry (LC-ESI-QTOF-MS) system, in positive and negative mode, was used to identify the transformation products in the samples. Samples collected at different irradiation times during the experiments were directly analyzed in the LC-TOF-MS system, without previous pre-concentration. The analytes were separated using a HPLC system (vacuum degasser, autosampler and a binary pump Agilent Series 1200, Agilent Technologies) equipped with a reversed-phase XDB-C₁₈ analytical column of 4.6 x 50 mm, 1.8 µm particle size (Agilent Technologies). 0.1% formic acid and 5% MiliQ water in acetonitrile was used as mobile phase A and 0.1% formic acid in water (pH 3.5) as mobile phase B. The elution gradient went from 10% A (3 min) to 100% A in 22 min, and was kept at 100% A for 3 min. The flow rate was 0.5 mL/min and the injection volume 20 µL. The HPLC system was connected to a quadrupole-time-of-flight mass spectrometer (Agilent 6530 Q-TOF MS, Agilent Technologies, Santa Clara, CA). The instrument was operated in the 4GHz High Resolution Mode. Ions were generated using an electrospray

ion source with Agilent Jet Stream Technology. The operation conditions were: superheated nitrogen sheath gas temperature (400°C) at flow rate (12 L/min), nozzle voltage (0 V), capillary, 4000 V; nebulizer, 60 psi; drying gas, 5 L/min; gas temperature, 250 °C; skimmer voltage, 65 V; octapoleRFPeak, 750 V; fragmentor (in source CID fragmentation), 90V. The mass axis was calibrated using the mixture provided by the manufacturer over the m/z 40-3200 range. A second sprayer with a reference solution was used for continuous calibration in positive ion using the following reference masses: 121.0509 and 922.0098 m/z (resolution: 21700 \pm 500 at 922.0098 m/z), and in negative ion using the reference masses: 112.9856 and 966.0007. MS/MS spectra were acquired over the m/z 40-950 range at a scan rate of 0.5 second per spectrum. The collision energy was optimized to obtain the highest number of fragments. The full mass spectra data recorded were processed with Agilent MassHunter Workstation Software (version B.02.00).

2.3.3. Toxicity test and data analysis

The toxicities of fenofibric acid degradations by UV and UV/H₂O₂ treatments were evaluated in accordance with the algal growth inhibition test described in OECD TG 201 and using the *Pseudokirchneriella subcapitata* open system. Prior to the test, hydrogen peroxide was removed using 4 μ L of catalase solution 5000 mg/L (3691 U/mg bovine liver from Sigma-Aldrich) per 1 mL of sample. Cultures were made in OECD growth medium at pH 8.0 \pm 0.2. Algal cells were first cultured in 25 mL agitated flasks, in which growth was evaluated by cell counting. The prescribed amount of cells were then transferred to 96-well clear disposable microplates and exposed to pollutants during the logarithmic growth phase. The total volume occupied was 200 μ L, each well containing 100 μ L of sample and 100 μ L of OECD growth medium. The microplates were placed in an algal growth chamber under continuous fluorescent

illumination (approximately $100 \mu\text{E m}^2 \text{ s}^{-1}$), and incubated at $22 \pm 1 \text{ }^\circ\text{C}$. The cell density was measured using an electronic particle counter (Coulter Counter Z2). The settings were: upper size limit, $8.0 \mu\text{m}$; lower size limit, $2.5 \mu\text{m}$; metered volume, 0.5 mL ; aperture size, $50 \mu\text{m}$. The tests were carried out with duplicate samples for each day of measurement and samples were taken at 24-hour intervals over 72 hours. Specific growth rates were calculated for each sample and treatment in order to obtain the inhibition percentage. EC_{50} value and 95% confidence limits for fenofibric acid were calculated using the concentration – inhibition relationship established by the logistic equation.

2.3.4. Experimental setup and procedure

Irradiation experiments were performed in a Heraeus 700 mL reactor equipped with a 15W Heraeus Noblelight TNN 15/32 low-pressure mercury vapour lamp emitting at 254 nm with a secondary peak at 185 nm. The inner and outer radii were 2.4 and 4.5 cm respectively and the height of irradiated solution was 17 cm. The reactor was covered with black paper to avoid any reflection and in order to maintain a constant temperature, the lamp was fitted in a quartz cooling tube refrigerated by means of a Huber Polystat cc2 thermostatic regulator. pH was kept constant using a 4 mM phosphate buffer; pH was monitored periodically to ensure a constant value within ± 0.1 units. The experiments were carried out in batch mode and samples were withdrawn for analysis at set intervals.

Hydrogen peroxide actinometry experiments were performed to determine fluence rate. With respect to the annular geometry of the photoreactor, we assumed a linear source with emission in planes parallel to the lamp axis (LSPP). In this model the lamp is viewed as a consecutive line of points, each emitting radiation radially in all directions. The equation for the fluence rate is:

$$E'(r) = \frac{E'_o R_o}{r} e^{-\mu(r-R_o)} \quad (1)$$

where μ is the attenuation coefficient, R_o the radius of the internal wall of the photoreactor and E'_o the fluence rate at R_o expressed in mW cm⁻². By applying the LSPP model to the UV photolysis of hydrogen peroxide at high concentration, the exponent becomes negligible and the rate of hydrogen peroxide photolysis allows the fluence rate to be determined at the internal wall of the photoreactor, E'_o :

$$-\frac{dc_{H_2O_2}}{dt} = \Phi_{H_2O_2} \frac{2\pi R_o L E'_o}{V} \quad (2)$$

The total hydrogen peroxide quantum yield, $\Phi_{H_2O_2}$, was considered to be 1 mol E⁻¹ at 254 nm (Nicole et al., 1990). Using 0.05 M of H₂O₂, we determined that the fluence rate was 18.73 ± 0.23 mW cm⁻². For a low attenuation coefficient, the photolytic decomposition of hydrogen peroxide follows a first order rate equation where $\epsilon_{H_2O_2}$ is the molar extinction coefficient of hydrogen peroxide at 254 nm:

$$-\frac{dc_{H_2O_2}}{dt} = 2.303 \frac{2\pi R_o L E'_o \epsilon_{H_2O_2}}{V} (R_1 - R_o) c_{H_2O_2} \quad (3)$$

From experiments at 10⁻⁴ M of H₂O₂, we obtained an effective path of radiation through the reactor of 2.37 ± 0.07 cm, essentially coincident with the physical value of $R_1 - R_o$. More details concerning equations and experimental procedure can be found elsewhere (Beltran et al., 1995).

2.4. Results and discussion

2.4.1. UV photolysis

The molar extinction coefficient of fenofibric acid at pH 6.5 and 254 nm was 9199 ± 150 M⁻¹ cm⁻¹, a value that we did not find elsewhere. As for hydrogen peroxide, atrazine and pCBA, we measured 19.3 ± 0.3, 3768 ± 55 and 2760 ± 94 M⁻¹ cm⁻¹ respectively, in agreement with

previously reported extinction coefficients (Litter et al., 2005; Bolton and Stefan, 2002; Benitez et al., 2004). The photolysis rate of a single target compound at an arbitrary concentration level is given by:

$$-\frac{dc_A}{dt} = \Phi_A \frac{2\pi R_o L E_o'}{V} \left[1 - e^{-\mu(R_1 - R_o)} \right] \quad (4)$$

At high concentrations of the absorbing compound, the integration of the former equation yields the following zero order kinetics:

$$c_A(t) = c_{Ao} - \Phi_A \frac{2\pi R_o L E_o'}{V} t \quad (5)$$

Fig. 2.1 shows the data corresponding to a photolytic decomposition of fenofibric acid. The inset represents a plot of Eq. 5 during the period in which $2.303 \epsilon_A c_A (R_1 - R_o) > 2$, which is its conventional validity condition.

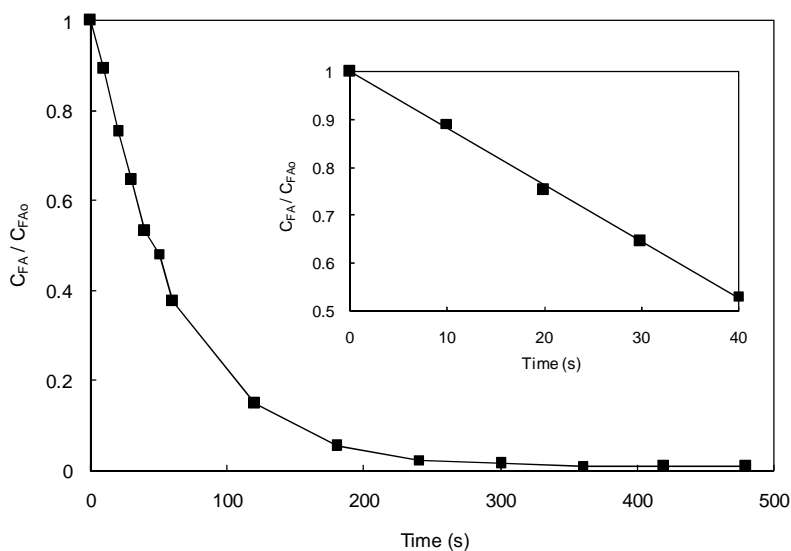


Figure 2.1. Photolytic decomposition of fenofibric acid at 35°C and pH 6.5. The inset represents the period for which the reaction followed zero order kinetics.

We obtained quantum yields for fenofibric acid at 15°C (0.039 ± 0.003 mol E⁻¹), 25°C (0.065 ± 0.003 mol E⁻¹) and 35°C (0.088 ± 0.002 mol E⁻¹). These data correspond to an activation energy for the photolysis rate of 21.5 ± 8.6 kJ mol⁻¹. The same values for the photolysis of atrazine were 0.040 ± 0.003 mol E⁻¹ at 15°C, 0.053 ± 0.002 mol E⁻¹ at 25°C and 0.055 ± 0.001 mol E⁻¹ at 35°C with an activation energy of 11.9 ± 4.7 kJ mol⁻¹. The values found for atrazine were in good agreement with previously reported data (Beltrán et al., 1993). However, the only value found for the quantum yield of fenofibric acid, reported by Miranda et al. (1994), is considerably higher, ~ 0.6 mol E⁻¹, a discrepancy that may be attributed to the different wavelength used (355 nm).

2.4.2. Kinetics of UV/H₂O₂ process

The radical exposure per fluence ratio due to the irradiation, $R_{OH,UV}$, and the stationary-state concentration of HO• radicals was determined according to the method proposed by Rosenfeldt and Linden (2005):

$$R_{OH,UV} = \frac{\int_0^t C_{HO\bullet} dt}{E_o' t} \quad (6)$$

Following Rosenfeldt et al. (2006), we used pCBA as the radical probe compound for determining HO• exposure. The rate of depletion of pCBA by the UV/H₂O₂ process is given by the following equation in which F_{pCBA} is the fraction of total radiation absorbed by pCBA:

$$-\frac{dc_{pCBA}}{dt} = (F_{pCBA} k_{d,pCBA} + k_{HO\bullet,pCBA} c_{HO\bullet}) c_{pCBA} \quad (7)$$

Integrating Eq. 7 gives the following expression:

$$\ln \frac{c_{pCBA,o}}{c_{pCBA}} = F_{pCBA} k_{d,pCBA} t + \int c_{HO\bullet} dt \quad (8)$$

The combination of Eqs. 6-8 allowed $R_{OH,UV}$ to be calculated under different reaction conditions. The results, shown in Fig. 2.2, indicated that $R_{OH,UV}$ was strongly dependent on the presence of hydrogen peroxide, with values of up to $6 \times 10^{-13} \text{ M cm}^2 \text{ mW}^{-1}$ at a plateau reached at about 50 mg/L H_2O_2 . These values bear comparison with those for HO^\bullet radical availability obtained by Rosenfeld et al. (2006) during the irradiation of water from several Swiss lakes; that is to say, volume-based $R_{OH,UV}$ in the $1\text{-}4 \times 10^{-13} \text{ M L}^{-1} \text{ mW}^{-1}$ range for 10 mg/L H_2O_2 under low-pressure mercury vapour irradiation. In our work, we measured $5.7 \times 10^{-11} \text{ M L}^{-1} \text{ mW}^{-1}$ which dropped to $1.8 \times 10^{-11} \text{ M L}^{-1} \text{ mW}^{-1}$ in the presence of 10 mg/L of fenofibric acid. This difference reflects the presence of radical scavengers and UV absorbers in natural water. The inset in Fig. 2.2 shows the oxidation profiles of pCBA without H_2O_2 and in the presence of 10, 50 and 100 mg/L H_2O_2 . Above 200 mg/L, the radical exposure per fluence ratio starts to

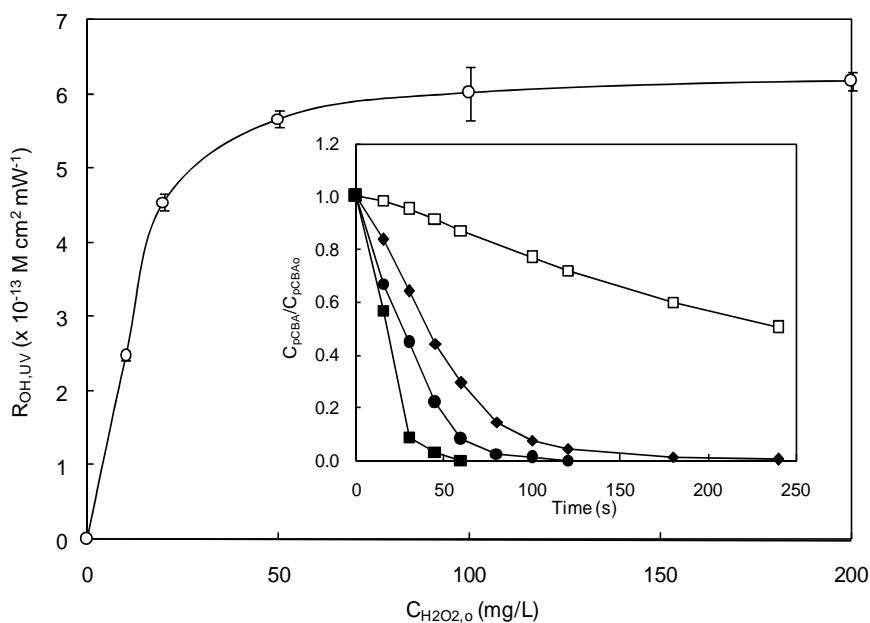


Figure 2.2. $R_{OH,UV}$ for different initial concentrations of hydrogen peroxide and (inset) evolution of the concentration of pCBA for runs without H_2O_2 (\square) and using 10 mg/L H_2O_2 (\blacklozenge), 50 mg/L H_2O_2 (\blacktriangle) and 100 mg/L H_2O_2 (\blacksquare).

decline as a consequence of the well-known effect of overdosing hydrogen peroxide, which reacts with HO• to form hydroperoxyl radicals.

The photolysis rate given by Eq. 3 also holds when two or more compounds are simultaneously photodegraded (Benitez et al., 2004). In this case, the rate expressions for a given couple of solutes can be written in the form of competitive kinetics:

$$\ln \frac{C_{A,o}}{C_A(t)} - F_A k_{d,A} t = \frac{k_{HO\bullet,A}}{k_{HO\bullet,B}} \left[\ln \frac{C_{B,o}}{C_B(t)} - F_B k_{d,B} t \right] \quad (9)$$

The data plotted in Fig.3 correspond to the irradiation of a mixture of fenofibric acid and atrazine using 50, 100 and 200 mg/L H₂O₂. The reason for using atrazine instead of pCBA is that the latter is also a product of the photodegradation of fenofibric acid, as indicated below. The slope of the plot shown in Fig. 2.3 allowed the second order rate constant for the reac-

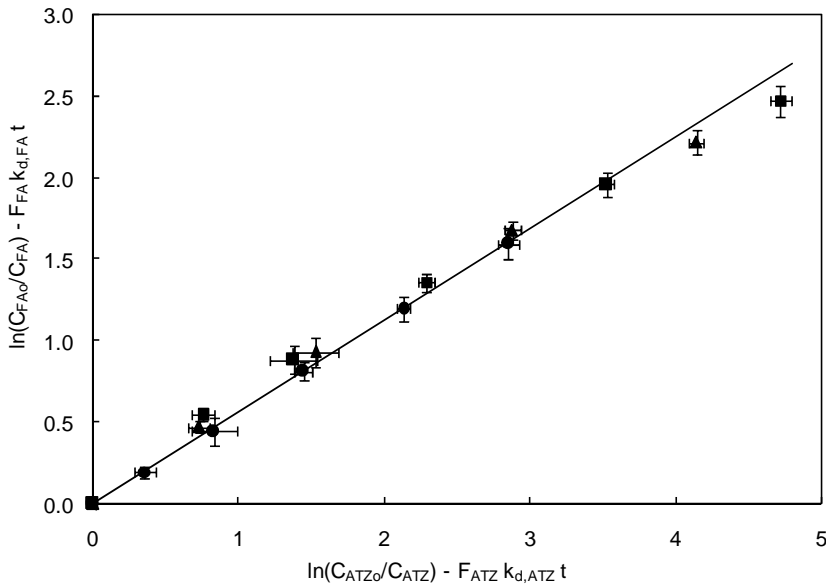


Figure 2.3. Plot of the competitive method of kinetic analysis during UV/H₂O₂ oxidation of mixtures of FA and ATZ using 50 mg/L H₂O₂ (●), 100 mg/L H₂O₂ (■) and 200 mg/L H₂O₂ (▲). (95% confidence intervals are shown for reference.)

tion of fenofibric acid with hydroxyl radicals to be determined. To do so, we used the value of Balci et al. (2009) for the rate constant of atrazine with hydroxyl radicals, which is the only value available that indicates uncertainty. The rate constant for the oxidation of fenofibric acid with HO[•] was $(5.56 \pm 0.22) \times 10^9 \text{ M}^{-1} \text{ s}^{-1}$, a value close to that obtained before in ozonation runs (Rosal et al., 2010a). By performing runs at different pH in the 5.5-7.5 interval, we could also determine that the rate constant for the oxidation of fenofibric acid did not depend on pH, with deviations from the mean not exceeding 5%, while there was almost complete overlapping of confidence intervals. In UV/H₂O₂ runs performed at free pH in the absence of any buffer we noted a continuous trend towards acidification, while in UV photolytic experiments pH increased slightly during the first 2-4 min of irradiation before decreasing thereafter. This behaviour was attributed to the formation of acidic compounds due to the oxidation of intermediates by hydroxyl radicals or other oxidizing species formed during the process.

2.4.3. Identification of reaction intermediates and reaction pathway

Although UV and UV/H₂O₂ can lead to the total removal of fenofibric acid in a few minutes under the experimental conditions tested in this work, this was never accompanied by complete mineralization. The maximum TOC removal observed for UV/H₂O₂ was slightly over 50% after 4 min of UV/H₂O₂ oxidation, but most of the organic carbon removed disappeared during the first minute (Fig. 2.4). The analysis of chloride in solution gave concordant results, with a degree of dechlorination of about 60% after 3 min that increased only up to 66% after 15 min when 20 mg/L of fenofibric acid were irradiated in the presence of 50 mg/L of H₂O₂ (pH 6.5, 25°C). UV irradiation led to a degree of dechlorination typically below 10% and accompanied by very limited TOC removal. Therefore, certain degradation by-products refractory to dechlorination and oxidation persisted after the total removal of the parent compound. This fact

highlights the need to characterize reaction mixtures in order to identify persistent and toxic compounds.

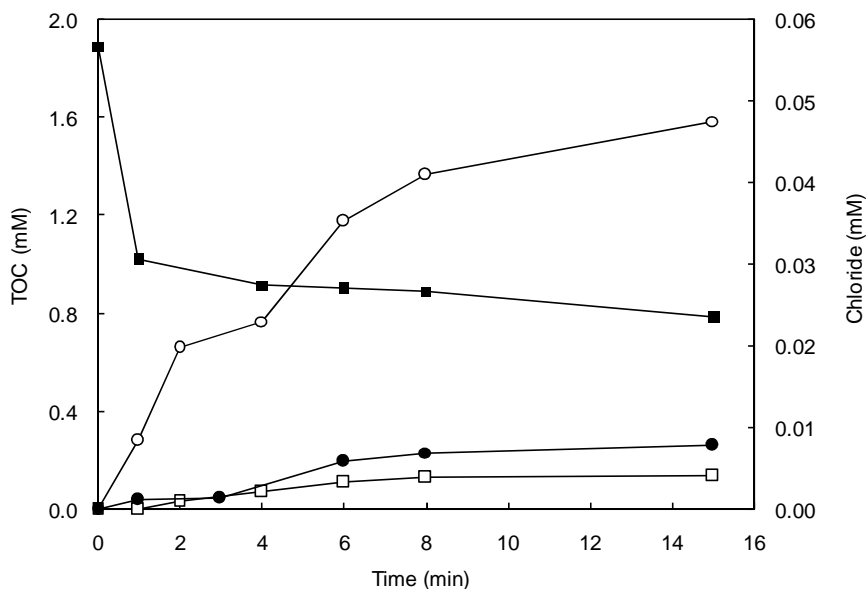


Figure 2.4. Evolution of TOC during UV/H₂O₂ using 50 mg/L H₂O₂ (■, left) and organic carbon in acetate, formiate and oxalate during the same run (●, left). Increase of chloride in solution during UV/H₂O₂ (50 mg/L, ○, right) and UV (□, right).

The identification of fenofibric acid photolysis and oxidation by-products was based on the accurate mass measurements recorded by the LC-ESI-QTOF-MS instrument described above, operating in positive (ESI+) and negative modes (ESI-). These measurements allowed elemental compositions to be proposed for both protonated [M+H]⁺ or deprotonated [M-H]⁻ molecular ions and characteristic ion fragments obtained by in-source fragmentation, which provide a high degree of confidence in structure assignment. Fig 2.5 shows LC-ESI-QTOF-MS/MS spectra of UV/H₂O₂ and UV transformation products of fenofibric acid, while Tables 2.1 and 2.2 list the ion formula and calculated mass of the ions, as well as relative mass error and DBE (double bond and ring equivalents).

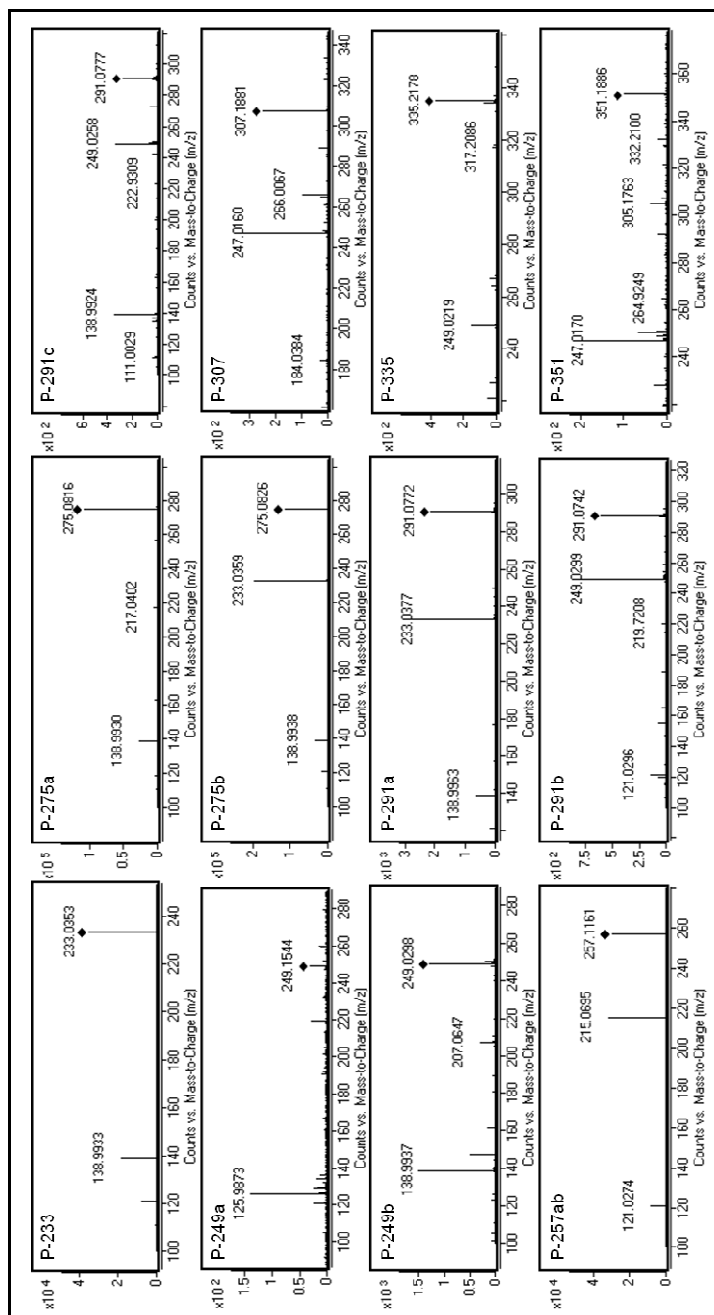


Figure 2.5. LC-ESI-QTOF-MS/MS spectra of UV/H₂O₂ and UV transformation products of fenofibric acid.

Table 2.1. Accurate mass measurements of fenofibric acid and its UV photolysis products by LC-ESI-QTOF-MS and structures proposed for the identified transformation products

Compound	R _t (min)	Ion Mass (m/z)	Ion Formula	Error (ppm)	DBE	Proposed Structure
a) ESI(+)						
Fenofibric acid (FA)	18.76	319.0732	C ₁₇ H ₁₆ ClO ₄	-1.80	10	
		233.0364	C ₁₃ H ₁₀ ClO ₂	1.01	8.5	
		138.9945	C ₇ H ₄ ClO	0.80	5.5	
		121.0284	C ₇ H ₅ O ₂	4.34	5.5	
P-233	17.08	33.0364	C ₁₃ H ₁₀ ClO ₂	0.90	9	
		138.9945	C ₇ H ₄ ClO	1.46	4	
		121.0284	C ₇ H ₅ O ₂	0.02	5.5	
		110.9996	C ₆ H ₄ Cl	3.75	4.5	
P-249a	14.40	249.0313	C ₁₃ H ₁₀ ClO ₃	-1.30	9	
		125.9843	C ₆ H ₃ ClO	4.60	5	
		121.0284	C ₇ H ₅ O ₂	9.07	5.5	
P-249b	15.43	249.0313	C ₁₃ H ₁₀ ClO ₃	1.89	9	
		147.0441	C ₉ H ₇ O ₂	-16.2	6.5	
		138.9945	C ₇ H ₄ ClO	-1.97	5.5	
P-257a	13.06	257.1172	C ₁₆ H ₁₇ O ₃	-1.49	9	
		215.0703	C ₁₃ H ₁₁ O ₃	4.20	8.5	
		121.0284	C ₇ H ₅ O ₂	-2.15	5.5	
P-257b	17.40	257.1172	C ₁₆ H ₁₇ O ₃	-3.70	9	
		215.0703	C ₁₃ H ₁₁ O ₃	3.74	8.5	
		121.0284	C ₇ H ₅ O ₂	-3.62	5.5	
P-275a	18.30	275.0833	C ₁₆ H ₁₆ ClO ₂	-2.11	9	
		257.0728	C ₁₆ H ₁₄ ClO	-2.01	9.5	
		217.0415	C ₁₃ H ₁₀ ClO	-2.39	8.5	
		163.0754	C ₁₀ H ₁₁ O ₂	-3.10	5.5	
		138.9945	C ₇ H ₄ ClO	-4.09	5.5	
		119.0855	C ₉ H ₁₁	-4.83	4.5	
		105.0335	C ₇ H ₅ O	-5.14	5.5	
		73.0284	C ₃ H ₅ O ₂	-7.60	1.5	
59.0491	C ₃ H ₇ O	-9.89	0.5			

Table 2.1. (continued)

Compound	R _i (min)	Ion Mass (m/z)	Ion Formula	Error (ppm)	DBE	Proposed Structure
P-257b	17.40	257.1172	C ₁₆ H ₁₇ O ₃	-3.70	9	
		215.0703	C ₁₃ H ₁₁ O ₃	3.74	8.5	
		121.0284	C ₇ H ₅ O ₂	-3.62	5.5	
P-275a	18.30	275.0833	C ₁₆ H ₁₆ ClO ₂	-2.11	9	
		257.0728	C ₁₆ H ₁₄ ClO	-2.01	9.5	
		217.0415	C ₁₃ H ₁₀ ClO	-2.39	8.5	
		163.0754	C ₁₀ H ₁₁ O ₂	-3.10	5.5	
		138.9945	C ₇ H ₄ ClO	-4.09	5.5	
		119.0855	C ₉ H ₁₁	-4.83	4.5	
		105.0335	C ₇ H ₅ O	-5.14	5.5	
		73.0284	C ₃ H ₅ O ₂	-7.60	1.5	
59.0491	C ₃ H ₇ O	-9.89	0.5			
P-275b	23.24	275.0833	C ₁₆ H ₁₆ ClO ₂	-3.99	9	
		233.0364	C ₁₃ H ₁₀ ClO ₂	2.02	8.5	
		138.9945	C ₇ H ₄ ClO	1.22	5.5	
		121.0284	C ₇ H ₅ O ₂	-1.12	5.5	
		110.9996	C ₆ H ₄ Cl	-1.06	4.5	
P-291a	17.72	291.0782	C ₁₆ H ₁₆ ClO ₃	-4.66	9	
		233.0364	C ₁₃ H ₁₀ ClO ₂	2.45	8.5	
		138.9945	C ₇ H ₄ ClO	-3.99	5.5	
		121.0284	C ₇ H ₅ O ₂	-9.60	5.5	
P-291b	19.74	291.0782	C ₁₆ H ₁₆ ClO ₃	-4.66	9	
		249.0313	C ₁₃ H ₁₀ ClO ₃	2.45	8.5	
		154.9894	C ₇ H ₄ ClO ₂	-3.99	5.5	
		121.0284	C ₇ H ₅ O ₂	-9.60	5.5	
P-291c	20.03	291.0782	C ₁₆ H ₁₆ ClO ₃	-0.56	9	
		249.0313	C ₁₃ H ₁₀ ClO ₃	4.53	8.5	
		138.9945	C ₇ H ₄ ClO	-3.91	5.5	
b) ESI(-) Fenofibric acid (FA)	18.78	317.0586	C ₁₇ H ₁₄ ClO ₄	-1.35	10	
		231.0218	C ₁₃ H ₈ ClO ₂	-0.10	9	
pCBA, P-155	13.90	154.9905	C ₇ H ₄ ClO ₂	0.09	5	
		111.0007	C ₆ H ₄ Cl	-3.18	4	

Table 2.2. Accurate mass measurements of fenofibric acid and its UV/H₂O₂ products by LC-ESI-QTOF-MS and structures proposed for the identified transformation products

Compound	R _t (min)	Ion Mass (m/z)	Ion Formula	Error (ppm)	DBE	Proposed Structure
a) ESI(+)						
Fenofibric acid (FA)	18.76	319.0732	C ₁₇ H ₁₆ ClO ₄	-1.65	10	
		233.0364	C ₁₃ H ₁₀ ClO ₂	1.49	8.5	
		138.9945	C ₇ H ₄ ClO	-1.19	5.5	
		121.0284	C ₇ H ₅ O ₂	-9.21	5.5	
P-233	17.08	233.0364	C ₁₃ H ₁₀ ClO ₂	0.90	9	
		138.9945	C ₇ H ₄ ClO	1.46	4	
		121.0284	C ₇ H ₅ O ₂	0.02	5.5	
		110.9996	C ₆ H ₄ Cl	3.75	4.5	
P-249a	14.40	249.0313	C ₁₃ H ₁₀ ClO ₃	-1.30	9	
		125.9843	C ₆ H ₃ ClO	4.60	5	
		121.0284	C ₇ H ₅ O ₂	9.07	5.5	
P-249b	15.43	249.0313	C ₁₃ H ₁₀ ClO ₃	4.43	9	
		147.0441	C ₉ H ₇ O ₂	-14.2	6.5	
		138.9945	C ₇ H ₄ ClO	-1.87	5.5	
		125.9867	C ₆ H ₃ ClO	4.80	5	
P-257	17.44	257.1172	C ₁₆ H ₁₇ O ₃	9.43	9	
		215.0703	C ₆ H ₃ ClO	4.43	8.5	
		121.0284	C ₇ H ₅ O ₂	-4.25	5.5	
P-275a	18.50	275.0833	C ₁₆ H ₁₆ ClO ₂	-2.12	9	
		138.9945	C ₇ H ₄ ClO	-4.09	5.5	
		110.9996	C ₆ H ₄ Cl	-4.98	4.5	
		59.0491	C ₃ H ₇ O	-9.99	0.5	
P-275b	23.32	275.0833	C ₁₆ H ₁₆ ClO ₂	-2.74	9	
		233.0364	C ₁₃ H ₁₀ ClO ₂	2.02	8.5	
		138.9945	C ₇ H ₄ ClO	1.22	5.5	
		121.0284	C ₇ H ₅ O ₂	-1.12	5.5	
		110.9996	C ₆ H ₄ Cl	-1.06	4.5	
P-291a	17.79	291.0782	C ₁₆ H ₁₆ ClO ₃	-1.27	9	
		233.0364	C ₁₃ H ₁₀ ClO ₂	3.62	8.5	
		138.9945	C ₇ H ₄ ClO	-8.12	5.5	
		121.0284	C ₇ H ₅ O ₂	-9.60	5.5	

Table 2.2. (Continued)

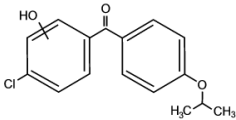
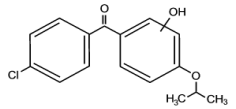
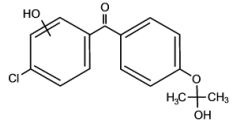
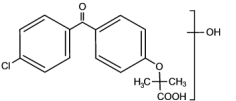
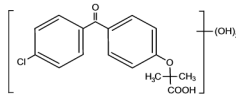
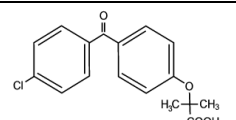
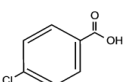
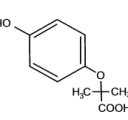
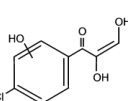
Compound	R _t (min)	Ion Mass (<i>m/z</i>)	Ion Formula	Error (ppm)	DBE	Proposed Structure
P-291b	19.83	291.0782	C ₁₆ H ₁₆ ClO ₃	3.91	9	
		249.0313	C ₁₃ H ₁₀ ClO ₃	4.94	8.5	
		154.9894	C ₇ H ₄ ClO ₂	-3.42	5.5	
		121.0284	C ₇ H ₅ O ₂	1.66	5.5	
P-291c	20.11	291.0782	C ₁₆ H ₁₆ ClO ₃	-0.13	9	
		249.0313	C ₁₃ H ₁₀ ClO ₃	5.72	8.5	
		138.9945	C ₇ H ₄ ClO	-6.03	5.5	
		110.9996	C ₆ H ₄ Cl	3.05	4.5	
P-307	19.11	307.0732	C ₁₆ H ₁₆ ClO ₄	-2.26	9	
		247.0156	C ₁₃ H ₈ ClO ₃	4.87	9.5	
		184.0519	C ₁₂ H ₆ O ₂	-2.26	9	
P-335	16.24	335.0681	C ₁₇ H ₁₆ ClO ₅	2.26	10	
		249.0313	C ₁₃ H ₁₀ ClO ₃	1.92	8.5	
P-351	16.01	351.0630	C ₁₇ H ₁₆ ClO ₆	1.13	10	
		247.0516	C ₁₃ H ₈ ClO ₃	15.6	9.5	
b) ESI(-)						
Fenofibric	18.78	317.0586	C ₁₇ H ₁₄ ClO ₄	-1.78	10	
		231.0218	C ₁₃ H ₈ ClO ₂	-0.60	9	
pCBA, P-155	13.90	154.9905	C ₇ H ₄ ClO ₂	0.05	5	
		111.0007	C ₆ H ₄ Cl	1.17	4	
P-195	9.96	195.0663	C ₁₀ H ₁₁ O ₄	0.61	5	
P-213	14.41	212.9960	C ₉ H ₆ ClO ₄	-3.42	6	
		154.9905	C ₇ H ₄ ClO ₂	-2.18	5	

Table 2.2. (Continued)

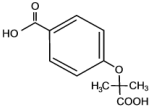
Compound	R _t (min)	Ion Mass (<i>m/z</i>)	Ion Formula	Error (ppm)	DBE	Proposed Structure
P-223	11.51	223.0612	C ₁₁ H ₁₁ O ₅	-0.12	6	
		137.0244	C ₇ H ₅ O ₃	-1.43	5	

Table 2.1 refers to the products of UV photolysis of fenofibric acid, whereas Table 2.2 gives the compounds identified during UV/H₂O₂ treatments. The accurate mass measurements recorded for the protonated and deprotonated fenofibric acid molecule (*m/z* 319.0732 for C₁₇H₁₆ClO₄ and 317.0586 for C₁₇H₁₄ClO₄) yielded excellent agreement between experimental and calculated *m/z* values, with less than 1.7 ppm error. The observation of the characteristic fragmentation of the parent drug provided information for the identification of transformation products. The appearance of fragments characteristic of the parent molecule in the product spectra indicates the prevalence of a certain fraction of the molecule, suggesting that the transformation takes place in another part of the structure.

The proposed reaction pathway for UV photolysis is shown in Fig 2.6a. The primary photoproducts identified in this work were the isomers P-275a and P-275b (C₁₆H₁₆ClO₂, *m/z* 275.0833) and compound P-233 (C₁₃H₁₀ClO₂, *m/z* 233.0364). P-275a (4-chloro-4'-(1-hydroxy-1-methylethyl) benzophenone) and P-275b (4-chloro-4'-isopropoxybenzophenone) correspond to the decarboxylation of fenofibric acid. The photodegradation of fenofibric acid has been attributed to the presence of the easily photo-excited benzophenone group. The first reaction would be a decarboxylation involving a radical species formed via a photo-ionization process upon electron release followed by loss of carbon dioxide (Cermola et al., 2005). P-233 (4-chloro-4'-hydroxybenzophenone) is the result of the

cleavage of the ether with loss of 2-methylpropanoate. As indicated in Fig 7, P-275b is the major identified photoproduct in irradiated mixtures, with minor amounts of P-233 and P-291a. These primary photoproducts agree with those found previously by Cosa (2004), who reported that the excitation of the carboxylate form of fenofibric acid in aqueous buffer at pH 7.4 generates an excited state that decarboxylates to produce a transient biradical intermediate (BRI in Fig. 2.6). This intermediate undergoes intersystem crossing and protonation to yield two products, also identified in this work as P-275a and P-275b. Boscá and Miranda (1999) used laser flash photolysis at 355 nm to study the photodegradation of fenofibric acid. They found the same photoproducts, with similar concentrations of both isomers (P-275a and P-275b). They also encountered P-233, which was attributed to oxygen trapping by an excited state of fenofibric acid or BRI, the later being the option displayed in Fig. 2.6a. In agitated runs under air, the concentration of dissolved oxygen was typically in the 7-8 mg/L range at 25°C. We also detected P-291a, which is probably the consequence of the uptake of oxygen by BRI.

In this work we were also able to detect several reaction products derived from fenofibric acid or its primary products with hydroxyl radicals. The most significant was pCBA (P-155), detected in negative ESI ionization mode ($C_7H_4ClO_2$, m/z 154.9905), whose ion fragment C_6H_4Cl (m/z 111.0007) revealed a non-substituted aromatic moiety. pCBA could be a product of the reaction of HO^\bullet radicals with fenofibric acid and also with photoproducts P-291a, P-291c, P- 275a, P-275b or P-233. For the sake of clarity and to stress the fact that we did not find hydroxylated forms of pCBA, we have only included the first possibility in Fig. 2.6a. The presence of intermediates giving evidence of the hydroxylation of aromatic rings can be explained by the vacuum ultraviolet (VUV) irradiation of low-pressure mercury lamps at 185 nm (about 5% of the total power for the lamp used in this work). The greater effectiveness of VUV irradiation is a consequence (Thomson et al., 2002). It is well-known that 185 nm VUV may also produce

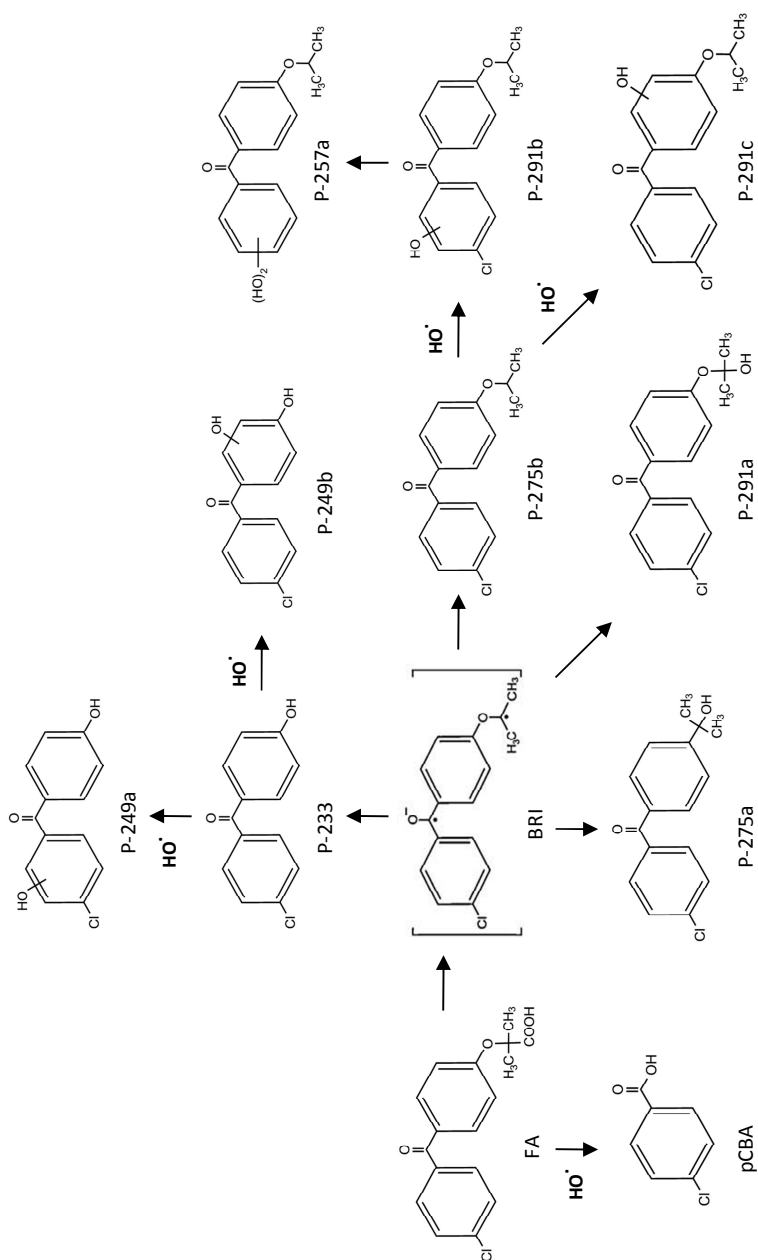


Figure 2.6a. Proposed reaction pathway for fenofibric acid under UV irradiation.

of the formation of hydroxyl radicals via the photolysis of water at 185 nm ozone from dissolved oxygen. We detected small amounts of dissolved ozone but we did not find any reaction product that could be associated with ozone such as ring-opening by ozone cycloaddition (Rosal et al., 2009b).

Fig. 2.6b shows the proposed pathway for the UV/H₂O₂ oxidation of fenofibric acid. The details concerning the identification and structure proposal are given in Table 2.2. The intermediates observed during the photolytic experiments were also identified in UV/H₂O₂ samples. These are compounds P291a, P275a, P275b and P-233, coincident with those indicated before, and two additional intermediates derived from fenofibric acid, P-335 (C₁₇H₁₆ClO₅, *m/z* 335.0681) and P-351 (C₁₇H₁₆ClO₆, *m/z* 351.0630), the elemental composition of which, containing one and two HO groups more than fenofibric acid and without alteration of DBE, corresponded to hydroxylated derivatives. No exact position for hydroxyl groups can be proposed from the fragmentation pattern (Table 2.2). A similar couple of hydroxylation derivatives could be attributed to HO[•] attack on P-233, namely P-249a and P249b. In this case, the fragmentation allowed the hydroxylated ring to be identified. The hydroxylation products from P275b also coincided with those encountered in photolytic runs plus compound P-257 (C₁₆H₁₇O₃, *m/z* 257.1172), the only one identified with the loss of the original chlorine atom. Similar reasoning was applied to the identification of P-307 (C₁₆H₁₆ClO₄, *m/z* 307.0732), a product of HO[•] attack on P-291a. In ESI-, we detected four additional intermediates, the most abundant of which was pCBA. In this case, we were able to detect the other fragment from the scission of the carbonyl carbon to aromatic carbon bond, P-195 (C₁₀H₁₁O₄, *m/z* 195.0663) and the symmetric product P-223 (C₁₁H₁₁O₅, *m/z* 223.0612). Another minor product, P-213 (C₉H₆ClO₄, *m/z* 212.9960), was probably the consequence of the hydroxyl attack and ring opening of fenofibric acid, but it could also be a product of any of the chlorine-containing compound with two aromatic rings listed in Table 2.2.

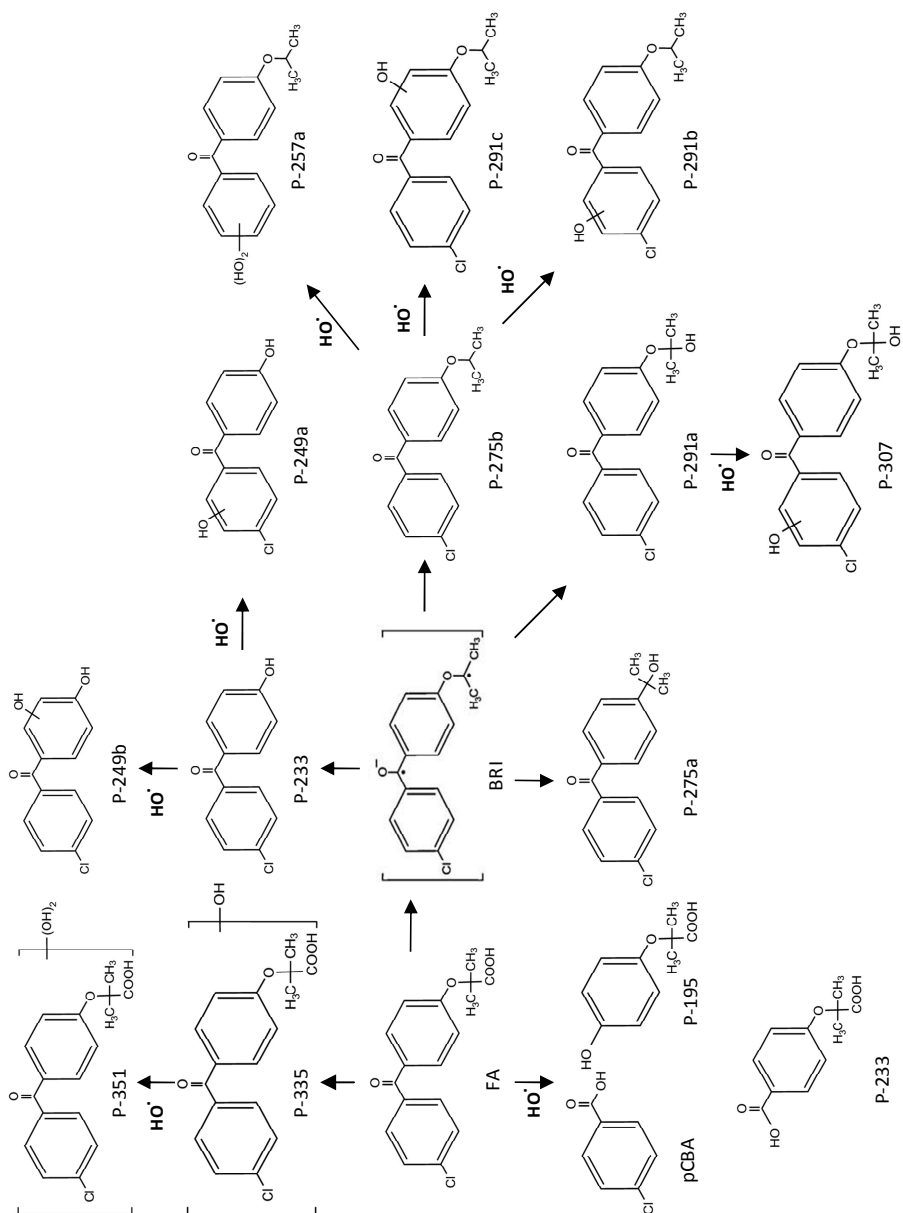


Figure 2.6b. Proposed reaction pathway for fenofibric acid under UV/H₂O₂

2.4.4. Toxicity of partially oxidized mixtures

Fig. 2.7 shows the growth inhibition of *Pseudokirchneriella subcapitata* when exposed to fenofibric acid and partially irradiated or oxidized mixtures as a function of the duration of treatment. The median effect value for the toxicity of fenofibric acid was 7.90 ± 1.61 mg/L, where the boundaries represent 95% confidence intervals. The value was obtained by fitting dose-response data to a logistic function. The results showed that toxicity decreased slightly during the first minute under UV and UV/H₂O₂, but reached a plateau for UV runs with a maximum at about six minutes. Besides, growth inhibition remained in the 20-40% range after the first minute and throughout the run. UV/H₂O₂ oxidation, on the other hand, allowed toxicity to be eliminated completely at about 4 min. After that, we observed a new increase in toxicity with a relative maximum somewhat in advance of that found in irradiation runs. The bars represent standard deviations for four replicated runs. This behaviour was attributed to a balance between the disappearance of the relatively toxic parent compound and the formation of toxic products. Cosa (2004) used molecular a priori analysis based on excited-state lifetimes and singlet oxygen sensitization to predict that the phototoxicity of irradiation products from fenofibric acid should be attributed to P-275a. We found, however, that P-275a was a very minor compound in all reaction mixtures, P-275b being the most abundant intermediate product in all cases. Fig 2.7 shows the chromatographic areas corresponding to the compounds identified in Tables 1 and 2 by lumping certain minor products into a pseudo-component A. The data show that the toxicity of irradiated samples and the recovery of toxicity at higher reaction times in the case of UV/H₂O₂ runs cannot be attributed to the formation or accumulation of a single compound, but are most probably the result of the production of several compounds with a similar chemical structure and toxicity. Is it noteworthy that most intermediates from both UV and UV/H₂O₂ processes retained the chlorine atom and that the reduction of dissolved organic

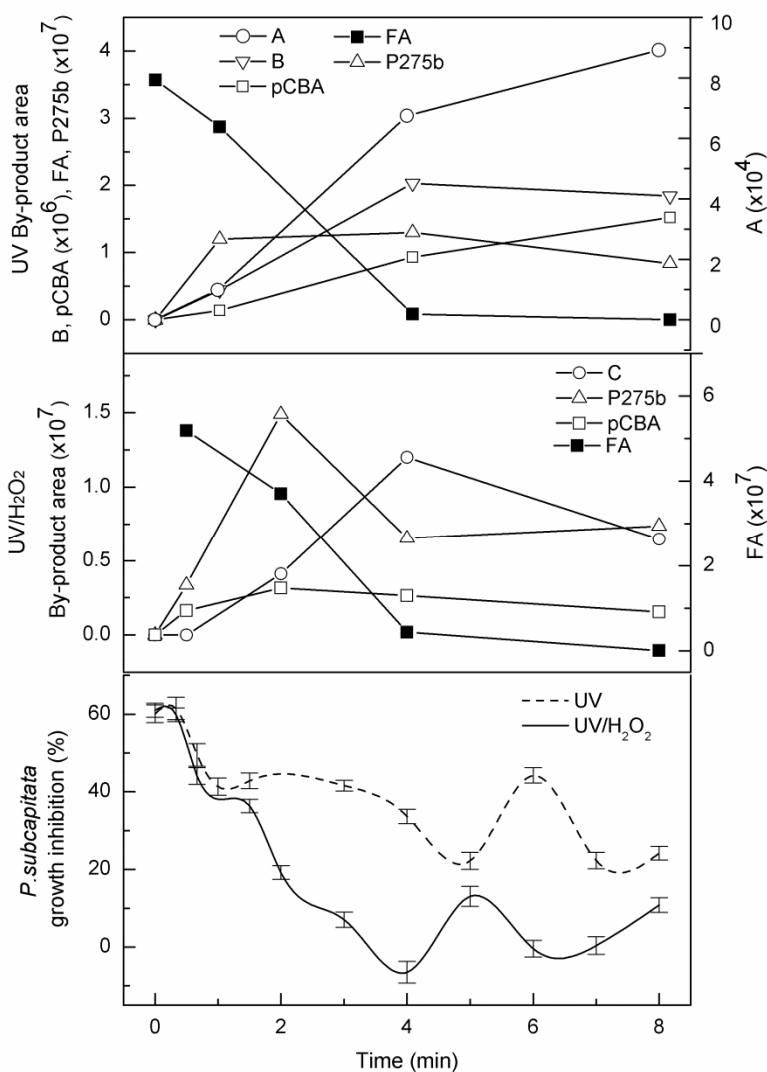


Figure 2.7. Growth inhibition of *Pseudokirchneriella subcapitata* and chromatographic area of transformation products (A = P291a + P291b + P291c, B = P233 + P249a + P249b, C = P307 + P291a + P291b + P291c).

carbon was closely related to the extent of dechlorination. The higher toxicity of the UV irradiated mixtures was most probably the consequence of the presence of a higher concentration of chlorinated aromatics. The

increase of toxicity observed in UV/H₂O₂ runs at high irradiation times was probably the consequence of the formation of ring-opening products, a kind of compound previously associated with high toxicity in partially oxidized mixtures (Rosal et al., 2009a).

2.5. Conclusions

The degradation of an aqueous solution of fenofibric acid using UV photolysis and UV/H₂O₂ led to the complete depletion of fenofibric acid for volume-based UV doses typically below 1 J cm⁻³. Quantum yields for fenofibric acid ranged from 0.039 ± 0.003 mol E⁻¹ (15°C) to 0.088 ± 0.002 mol E⁻¹ (35°C) with a photolytic activation energy of 21.5 ± 8.6 kJ mol⁻¹. The radical exposure per fluence ratio, $R_{OH,UV}$, was measured using pCBA as probe compound and reached a plateau of about 6 × 10⁻¹³ M cm² L mW⁻¹ at about 50 mg/L H₂O₂, before declining thereafter due to the hydroxyl radical scavenger role played by H₂O₂ at high concentration. The presence of fenofibric acid, a compound with intense UV absorption, decreased $R_{OH,UV}$ considerably. Using competitive kinetics with atrazine, we obtained a second order rate constant of (5.56 ± 0.22) × 10⁹ M⁻¹ s⁻¹ for the reaction of fenofibric acid with hydroxyl radicals.

UV photolysis led to a low extent of dechlorination and mineralization reactions, typically below 10%. The maximum TOC removal observed for UV/H₂O₂ was slightly over 50% after 4 min of reaction with most of the organic carbon being removed during the first minute. The absence of complete mineralization resulted in the accumulation of oxidation by-products identified using LC-ESI-QTOF-MS. Exact mass measurements allowed reaction pathways to be proposed for UV and UV/H₂O₂ that start with the decarboxylation of fenofibric acid before yielding 4-chloro-4'-(1-hydroxy-1-methylethyl) benzophenone and other minor products, predominantly chlorinated. We were also able to detect several intermediates from the reactions of primary products with hydroxyl

radicals which, in the case of UV photolysis, were produced by the 185 nm ozone-forming emission of low-pressure mercury lamp. Some additional minor products were detected in ESI negative mode and corresponded to the scission of the carbonyl carbon to the aromatic carbon bond, the most abundant of which was pCBA.

We determined that the toxicity of UV irradiated samples for the 72 h growth of *Pseudokirchneriella subcapitata* was high even after the total depletion of fenofibric acid. This was attributed to the chlorinated aromatic products that dominated reaction mixtures at intermediate reaction times. There were low values for the toxicity of UV/H₂O₂ treated samples in which fenofibric acid was completely depleted. However, a degree of toxicity reappeared in highly irradiated mixtures, probably as a consequence of chlorinated reaction products.

2.6. References

- Acero, J.L., Benitez, F.J., Leal, A.I., Real, F.J. and Teva, F., 2010. Membrane filtration technologies applied to municipal secondary effluents for potential reuse. *Journal of Hazardous Materials*, 177, 390-398.
- Baga, A.N., Johnson, G.R.A., Nazhat, N.B. and Saadallanazhat, R.A., 1988. A Simple Spectrophotometric Determination of Hydrogen-Peroxide at Low Concentrations in Aqueous-Solution. *Analytica Chimica Acta* 204, 349-353.
- Balci, B., Oturan, N., Cherrier, R. and Oturan, M.A., 2009. Degradation of atrazine in aqueous medium by electrocatalytically generated hydroxyl radicals. A kinetic and mechanistic study. *Water Research* 43, 1924-1934.
- Beltran, F.J., Ovejero, G. and Acedo, B., 1993. Oxidation of Atrazine in Water by Ultraviolet-Radiation Combined with Hydrogen-Peroxide. *Water Research* 27, 1013-1021.
- Beltran, F.J., Gonzalez, M., Rivas, F.J. and Jaramillo, J., 1995. Application of Photochemical Reactor Models to Uv Irradiation of Trichloroethylene in Water. *Chemosphere* 31, 2873-2885.
- Benitez, F.J., Acero, J.L., Real, F.J. and Maya, C., 2004. Modeling of photooxidation of acetamide herbicides in natural waters by UV radiation and the combinations UV/H₂O₂ and UV/O₃. *Journal of Chemical Technology and Biotechnology* 79, 987-997.

- Bolton, J.R. and Stefan, M.I., 2002. Fundamental photochemical approach to the concepts of fluence (UV dose) and electrical energy efficiency in photochemical degradation reactions. *Research on Chemical Intermediates* 28, 857-870.
- Bosca, F. and Miranda, M.A., 1999. A laser flash photolysis study on fenofibric acid. *Photochemistry and Photobiology* 70, 853-857.
- Cermola, M., DellaGreca, M., Iesce, M., Previtera, L., Rubino, M., Temussi, F. and Brigante, M., 2005. Phototransformation of fibrate drugs in aqueous media. *Environmental Chemistry Letters* 3, 43-47.
- Cosa, G., 2004. Photodegradation and photosehsitization in pharmaceutical products: Assessing drug phototoxicity. *Pure and Applied Chemistry* 76, 263-275.
- Eisenberg, G., 1943. Colorimetric determination of hydrogen peroxide. *Industrial & Engineering Chemistry Analytical Edition* 15, 327-328.
- Legube, B., 2003. *Haloforms and Related Compounds in Drinking Water*, pp. 95-116, Springer.
- Litter, M., 2005. Introduction to Photochemical Advanced Oxidation Processes for Water Treatment. *The Handbook of Environmental Chemistry* 2(M).
- López-Peñalver, J.J., Sánchez-Polo, M., Gómez-Pacheco, C.V. and Rivera-Utrilla, J., 2010. Photodegradation of tetracyclines in aqueous solution by using UV and UV/H₂O₂ oxidation processes. *Journal of Chemical Technology and Biotechnology* 85, 1325-1333.
- Miranda, M.A., Bosca, F., Vargas, F. and Canudas, N., 1994. Unusual (1, 2) Wittig rearrangement of a carbanion generated in neutral aqueous medium by photodecarboxylation of a phenoxyacetic acid analogue. *Journal of Photochemistry and Photobiology A: Chemistry* 78, 149-151.
- Nicole, I., Delaat, J., Dore, M., Duguet, J.P. and Bonnel, C., 1990. Use of Uv-Radiation in Water-Treatment - Measurement of Photonic Flux by Hydrogen-Peroxide Actinometry. *Water Research* 24, 157-168.
- Rodea-Palomares, I., Petre, A.L., Boltes, K., Leganes, F., Perdigon-Melon, J.A., Rosal, R. and Fernandez-Pinas, F., 2010. Application of the combination index (CI)-isobologram equation to study the toxicological interactions of lipid regulators in two aquatic bioluminescent organisms. *Water Research* 44, 427-438.
- Rosal, R., Gonzalo, M.S., Boltes, K., Leton, P., Vaquero, J.J. and Garcia-Calvo, E., 2009a. Identification of intermediates and assessment of ecotoxicity in the oxidation products generated during the ozonation of clofibrac acid. *Journal of Hazardous Materials* 172, 1061-1068.
- Rosal, R., Gonzalo, M.S., Boltes, K., Letón, P., Vaquero, J.J. and García-Calvo, E., 2009b. Identification of intermediates and assessment of ecotoxicity in the

- oxidation products generated during the ozonation of clofibric acid. *Journal of Hazardous Materials* 172, 1061-1068.
- Rosal, R., Gonzalo, M.S., Rodriguez, A. and Garcia-Calvo, E., 2010a. Catalytic ozonation of fenofibric acid over alumina-supported manganese oxide. *Journal of Hazardous Materials* 183, 271-278.
- Rosal, R., Rodea-Palomares, I., Boltes, K., Fernandez-Pinas, F., Leganes, F., Gonzalo, S. and Petre, A., 2010b. Ecotoxicity assessment of lipid regulators in water and biologically treated wastewater using three aquatic organisms. *Environmental Science and Pollution Research* 17, 135-144.
- Rosal, R., Rodea-Palomares, I., Boltes, K., Fernández-Piñas, F., Leganés, F. and Petre, A., 2010c. Ecotoxicological assessment of surfactants in the aquatic environment: combined toxicity of docusate sodium with chlorinated pollutants. *Chemosphere* 81, 288-293.
- Rosal, R., Rodríguez, A., Perdigón-Melón, J.A., Petre, A., García-Calvo, E., Gómez, M.J., Agüera, A. and Fernández-Alba, A.R., 2010d. Occurrence of emerging pollutants in urban wastewater and their removal through biological treatment followed by ozonation. *Water Research* 44, 578-588.
- Rosenfeldt, E. and Linden, K., 2005. The ROH, UV Concept to Characterize and Model H₂O₂/UV Processes in Natural Waters. IUVA: Third International Congress on Ultraviolet Technologies, Whistler. British Columbia, 24-27.
- Rosenfeldt, E.J., Linden, K.G., Canonica, S. and von Gunten, U., 2006. Comparison of the efficiency of center dot OH radical formation during ozonation and the advanced oxidation processes O₃/H₂O₂ and UV/H₂O₂. *Water Research* 40, 3695-3704.
- Stumpf, M., Ternes, T.A., Wilken, R.D., Rodrigues, S.V. and Baumann, W., 1999. Polar drug residues in sewage and natural waters in the state of Rio de Janeiro, Brazil. *Science of the Total Environment* 225, 135-141.
- Ternes, T.A., Stuber, J., Herrmann, N., McDowell, D., Ried, A., Kampmann, M. and Teiser, B., 2003. Ozonation: a tool for removal of pharmaceuticals, contrast media and musk fragrances from wastewater? *Water Research* 37, 1976-1982.
- Thomson, J., Roddick, F. and Drikas, M., 2002. Natural organic matter removal by enhanced photo-oxidation using low pressure mercury vapour lamps. *Water Science and Technology: Water Supply* 435-443.

Chapter 3

Transformation products and reaction kinetics in simulated solar light photocatalytic degradation of propranolol using Ce-doped TiO₂

Transformation products and reaction kinetics in simulated solar light photocatalytic degradation of propranolol using Ce-doped TiO₂*

3.1. Abstract

The visible light photocatalytic degradation of propranolol was studied using cerium doped titanium dioxide, a catalyst that showed an increased light absorption in the visible region. The experiments were carried out in ultrapure water and in a biologically treated wastewater from the secondary effluent of a treatment plant spiked with propranolol. The best results were obtained for a cerium loading of 0.5 % wt. and a bulk catalyst concentration of 0.14 g/L, with which propranolol became essentially depleted after 1.5 hours of irradiation. The extent of mineralization reached 17.4% after six hours on stream under the same conditions. Both oxidation on catalyst holes and reaction with hydroxyl radicals contribute to propranolol depletion, but for the reaction conditions tested in this study, the first mechanism predominated and counted for 60% of the propranolol rate constant. The runs performed in wastewater matrix led to a very low photocatalytic rate compared with

* The contents of this chapter have been published as:

Santiago-Morales, J., Agüera, A., Gómez, M. M., Fernández-Alba, A. R., Giménez, J., Esplugas, S., Rosal, R., 2012. Transformation products and reaction kinetics in simulated solar light photocatalytic degradation of propranolol using Ce-doped TiO₂. *Applied Catalysis B: Environmental* 129, 13-29.

pure water, which was attributed to the presence of radical scavengers and competing substances. Over thirty reaction intermediates were detected by means of exact mass time-of-flight mass spectrometry (LC-ESI-QTOF-MS/MS) based on the characteristic fragmentation of oxidation by-products. Their relative abundance was also assessed in catalytic and non-catalytic runs. The most abundant transformation products could be attributed to the cleavage of the ether bond of propranolol. Other compounds detected derived from the addition of hydroxyl groups to the aromatic nuclei or to the ring-opening attack of hydroxyl radicals on the naphthol moiety. Finally, the toxicity of oxidized mixtures was determined using the green algae *Pseudokirchneriella subcapitata* and the bioluminescent marine bacterium *Vibrio fischeri*. Although the toxicity of treated mixtures tended to decrease as propranolol was depleted, mixtures treated in pure water may lead to the accumulation of toxic transformation products.

3.2. Introduction

The incomplete removal of pharmaceuticals and other emerging pollutants in conventional wastewater treatment plants (WWTP) has been identified as the main route by which anthropogenic pollutants reach aqueous environments (Kümmerer, 2004). As a consequence, the presence of pharmaceuticals has become ubiquitous in natural waters, even to the extent of entering drinking water facilities (Maycock and Watts, 2011). Some of the adverse effects of these pollutants on ecosystems have been reported but the risk associated with chronic exposure remains essentially unknown (Crane et al., 2006). The presence of anthropogenic pollutants in treated wastewaters also endangers reuse, which is becoming a major issue in view of the growing water scarcity (Muñoz et al., 2009). The occurrence of β -blockers has been repeatedly reported in recent years in the effluents of many WWTP around the world (Ternes, 1998; Huggett et al., 2003; Gabet-Giraud et al., 2010). It has been clearly established that

conventional wastewater treatments using activated sludge are not effective in completely removing propranolol. Maurer et al. reported removal efficiencies in the 28-35% range for propranolol in two WWTP located in the vicinity of Zürich (Maurer et al., 2007). Rosal et al. (2010) monitored the primary and final effluents of a WWTP located in Alcalá de Henares, Madrid, performing monthly analyses on time-composite samples over a one-year sampling period. They obtained average concentrations of atenolol, metoprolol and propranolol of 1025 ng/L, 19 ng/L, and 36 ng/L, respectively, with very low removal efficiencies which did not exceed 15% for atenolol and were even lower for the other two.

Several studies have indicated that advanced oxidation processes (AOP) are a suitable choice for the removal of β -blockers from aqueous solution (Isarain-Chavez et al., 2011; Song et al., 2008). In particular, the oxidation of propranolol has been studied in the past using advanced oxidation processes like ozonation (Benner et al., 2008; Rosal et al., 2008) radiolysis (Song et al., 2008), UV/H₂O₂ (Kim et al., 2009) and electro-Fenton and photoelectro-Fenton (Isarain-Chavez et al., 2011). Heterogeneous photocatalysis belongs to the category of AOP due to the formation of surface reactive oxygen species (ROS) such as the radicals HO[•], O₂^{•-} or HO₂[•]. In this process, the irradiation of certain semiconductors in the presence of oxygen creates a redox environment suitable for the oxidation of diluted organic pollutants (Doll and Frimmel, 2005). The most common photocatalyst is titanium dioxide, the performance of which is very well documented (Malato et al., 2002). Titanium dioxide, however, only absorbs the near-UV part of the solar spectrum (wavelength shorter than 390 nm) corresponding to the band gap of TiO₂, which is about 3.2 eV depending on the anatase/rutile ratio, or even higher for nanoparticles. This fact represents a major drawback for the development of solar photocatalysis, an environmentally friendly process which could reduce the impact of energy consumption related to the use of UV lamps (Muñoz et al., 2005). The photocatalytic efficiency of titanium dioxide can be enhanced by red

shifting its absorption to the visible region (400-800 nm), which can be achieved by doping the anatase matrix with certain cationic or anionic impurities. Rare earth oxides, in particular, enhance the photocatalytic activity of TiO₂ due to the transitions of 4f electrons, which can increase the separation rate of photogenerated charges (Stengl et al., 2009). Cerium has also been identified as one of the most interesting rare earth dopants due to its ability to shift between Ce⁴⁺ (CeO₂) and Ce³⁺ (Ce₂O₃) under oxidizing or reducing conditions and to the facile formation of labile oxygen vacancies as a result of the relatively high mobility of bulk oxygen species. Electronically, the effect of cerium on the TiO₂ bandgap has been interpreted as being due to an n-type impurity band at the interface between the titanium and cerium oxides (Li et al., 2005).

In this study, the use of cerium-doped titanium dioxide was examined as a strategy to increase the degradation rate of the β -blocker propranolol under irradiation in the visible region. The catalyst was prepared by the sol-gel method, a method that has been extensively employed to prepare doped TiO₂ catalysts. Other methods such as hydrothermal, solvothermal or impregnation have been described elsewhere (Akpan and Hameed, 2010). The experiments were carried out in ultrapure water and in a biologically treated wastewater from the secondary effluent of a WWTP spiked with propranolol. Besides obtaining photocatalytic kinetics, a number of reaction intermediates were detected by means of exact mass measurements performed by liquid chromatography coupled to quadrupole-time-of-flight mass spectrometry (LC-ESI-QTOF-MS/MS). Their relative abundance was assessed either in catalytic and non-catalytic runs. Finally, the toxicity of partially oxidized mixtures was determined using the green algae *Pseudokirchneriella subcapitata* and the bioluminescent marine bacterium *Vibrio fischeri*.

3.3. Materials and methods

3.3.1. Materials

Propranolol (PRO) and p-chlorobenzoic acid (pCBA) were purchased from Sigma Aldrich (+99% purity). Titanium isopropoxide, ethanol, diammonium cerium (IV) nitrate, [(NH₄)₂Ce(NO₃)₆], sodium phosphate, sodium hydroxide and hydrochloric acid were analytical grade reagents used as received. Pure water was obtained from a Millipore Milli-Q System with a resistivity of at least 18 MΩ cm at 25°C. Wastewater was collected from the secondary clarifier of a wastewater treatment plant (WWTP) located in Gavà-Viladecans (Barcelona), which receives a mixture of domestic and industrial wastewater from facilities located around the area. This WWTP has a capacity of 300000 equivalent inhabitants and was designed to treat a maximum volume of wastewater of 64000 m³ day⁻¹. The main characteristics of the treated wastewater are shown in Table 3.1.

3.3.2. Catalyst preparation and characterization

The photocatalyst was a cerium doped titanium oxide with different percentages of cerium (0%, 0.5% and 1%) prepared by the sol-gel method. Briefly 10 mL of titanium isopropoxide was dissolved in 50 mL of absolute ethanol (Solution A). In parallel, 92 mg of (NH₄)₂Ce(NO₃)₆ was dissolved in 10 mL distilled water and then added to 40 mL of ethanol and 10 mL of anhydrous acetic acid (Solution B). Solution A was then added dropwise to a beaker containing Solution B. The precipitate was dried at 100 °C and calcined at 670 °C for one hour. The calcination temperature was selected as optimal in the 500-670°C range based on the production of hydroxyl radicals as indicated below. The amounts mentioned produced approximately 2 g of 0.5% Ce-TiO₂ catalyst.

The Brunauer-Emmet-Teller (BET) surface areas were 1.4, 34.1, 56.2 m²/g for 0%, 0.5% and 1% Ce-TiO₂ catalysts respectively. BET surface

Table 3.1. Main wastewater parameters

pH	8.1
Turbidity (NTU)	3.2
Turbidity of 0.45 μm filtered water for experiments (NTU)	0.75
UV Absorbance at 254 nm of filtered wastewater	0.23
Total Suspended Solids (mg/L)	8.0
Conductivity ($\mu\text{S}/\text{cm}$) at 25°C	2750
COD (mg/L)	35
NPOC (mg/L)	12.3
<i>Anions and cations (mg/L)</i>	
Chloride	589
Nitrite	9.9
Nitrate	30.1
Sulfate	205
Phosphate	9.2
Sodium	172
Potassium	45
Magnesium	45
Calcium	124
Ammonium	< 0.5
Alkalinity (mg/L of CaCO_3)	290
<i>Metals (ng/L)</i>	
Chromium	335
Cobalt	840
Copper	320
Manganese	623
Molybdenum	1796
Nickel	3683
Iron	1796
Palladium	161
Silver	12
Tin	88
Titanium	277
Vanadium	25
Zinc	4233
Zirconium	113
<i>Toxicity</i>	
Growth inhibition of <i>P. subcapitata</i> (%)	8.4 \pm 6.9
Bioluminescence inhibition of <i>V. fischeri</i> (%)	45.8 \pm 4.0

area showed a high correlation with cerium loading. This was attributed to the decreasing particle size of crystals as discussed below. All samples showed a well-defined IUPAC type IV isotherm and average pore diameters calculated using the Barrett-Joyner-Halenda (BJH) analysis of the desorption branch showed an increase in pore diameter with cerium loadings from 8.6 nm for 0.5% Ce to 12.0 nm for 1% Ce compared with 3.7 nm for non-doped TiO₂. This behavior may be explained by the decrease in crystallite size due to the incorporation of cerium, as discussed below. The absorbance of the photocatalyst was measured using a UV/VIS/NIR Perkin Elmer Lambda 900 spectrometer equipped with an integrating sphere. The spectra are shown in Fig. 3.1 together with the emission spectrum of the Xenon lamp corrected with Duran tube transmission in order to display an estimate of the radiation spectrum at the inner wall of the photoreactor. The incorporation of a small amount of cerium into TiO₂ significantly increased the absorption of visible light in the 400-600 nm range, which

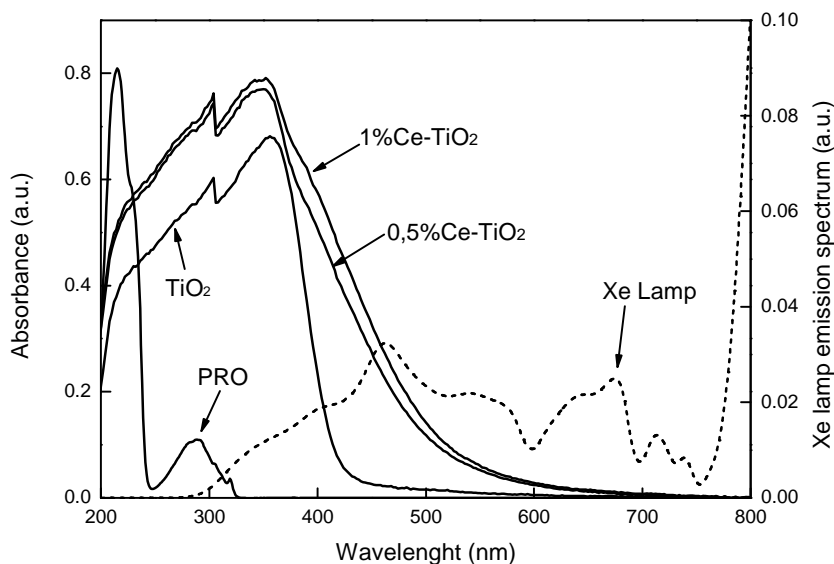


Figure 3.1. Catalyst absorbance for different cerium content: (1) 1.0 %, (2) 0.5 %, (3) 0 % (TiO₂), Xe lamp emission spectrum and propranolol absorption spectrum (5 mg/L).

corresponds to the maximum in the lamp emission spectrum. A further increase of cerium above 0.5% did not result in enhanced radiation absorption. The band gap energies estimated by Tauc's plot were 3.06 ± 0.15 eV, 2.67 ± 0.11 eV and 2.61 ± 0.05 eV for 0%, 0.5% and 1% cerium loadings.

The catalyst was characterized by X-ray diffraction (XRD) using a Seifert 3000P diffractometer (Cu $K\alpha$, $\lambda = 1.5406$ Å). The unit cell parameters of Ce-TiO₂ were calculated considering that TiO₂ anatase belongs to the tetragonal system, whose unit cell parameters comply with the equation $1/d_{hkl}^2 = (h^2+k^2)/a^2 + l^2/c^2$. The diffraction peaks from (1 0 1) and (0 0 4) planes were used, obtaining values of $a = b = 3.78$ Å and $c = 9.49$ Å, essentially coincident with those for pure anatase. We used XRD data and the Scherrer Equation to estimate the size of crystallites in the polycrystalline samples with the Scherrer constant, K_s , rounded up to 1:

$$B(2\theta) = \frac{K_s \lambda}{L \cos \theta} \quad (1)$$

The peak width, B , was determined from the full width at half maximum. The well-defined peak of (2 0 0) plane at $2\theta = 48.1^\circ$ was used to obtain crystallite sizes. With the increase of cerium XRD peaks broadened and their relative intensity decreased. This was attributed to a reduction in the average crystallite sizes, which dropped from 38 nm (0.5 % wt. Ce) to 26 nm (1.0 % wt. Ce). The doping with cerium was shown to induce a crystal lattice expansion that could suppress the growth of anatase crystals and consequently, the average crystallite size decreased (Li et al., 2012).

The size distribution of water suspended particles was obtained using dynamic light scattering (DLS, Malvern Zetasizer Nano ZS). Zeta potential was determined by electrophoretic light scattering in the same Nano ZS instrument. All measurements were conducted at 25 °C using 2 mM phosphate buffer (pH 7.5) as dispersing medium. It was found that the size of catalyst aggregates was not significantly affected by the presence of

cerium in the structure, with sizes in the 400-600 nm range irrespective of the amount of cerium. ζ -potential, however, dropped slightly from -65 ± 10 mV (TiO₂) to -48 ± 6 mV (Ce-TiO₂) in all doped samples, which displayed similar values irrespective of cerium loading.

3.3.3. Analytical methods

Anions were determined using a Metrohm 861 Advance Compact IC with suppressed conductivity detector, a Metrosep A Supp 4-250 analytical column and a Metrosep A Supp 4/5 precolumn with 1.8 mM Na₂CO₃ and 1.7 mM Na HCO₃ as eluents with a flow of 1 mL/min. Cations were quantified by means of a Metrosep C4 Guard/4.0 precolumn and a Metrosep C4-150/4.0 column using 1.7 mM HNO₃ and 0.7 mM dipicolinic acid as eluent with a flow of 0.9 mL/min. Dissolved metals were determined by ICP/MS using a quadrupole mass spectrometer Agilent 7700X operating at 3 MHz in helium cell gas mode. The injection volume was 20 μ L for both methods. Spectrophotometric measurements to obtain UV absorption at 254 nm were carried out in a Perkin-Elmer UV/VIS Lambda 20 (220–700 nm range) spectrophotometer. The determination of chemical oxygen demand (COD), total suspended solids and alkalinity was performed according to the Standard Methods for the examination of Water and Wastewater (APHA, 2005). The dissolved organic carbon, DOC, determined as total content of organic carbon (TOC) and non-purgeable organic carbon (NPOC) was measured using a Shimadzu TOC-VCSH analyzer. NPOC was used for wastewater samples, which had a high content of inorganic carbon. The analyses of propranolol and pCBA were performed by HPLC using a Waters Corporation apparatus equipped with a SEA18 5 μ m 15 x 0.46 Teknokroma column and a Waters 996 photodiode array detector. The mobile phase was a 60:40 mixture of water acidified with phosphoric acid at pH 3.0 and acetonitrile. UV detection was carried

out at 214 nm and 237 nm for propranolol and pCBA respectively. The flow rate was 0.7 mL/min and the injection volume was 10 μ L.

A liquid chromatography-electrospray ionization-quadrupole time-of-flight–mass spectrometry (LC-ESI-QTOF–MS/MS) system in positive mode was used to identify the transformation products from propranolol. Samples collected at different irradiation times during the experiments were directly analyzed without previous pre-concentration. The analytes were separated using a HPLC system (vacuum degasser, autosampler and a binary pump Agilent Series 1200, Agilent Technologies) equipped with a reversed-phase SB-C18 analytical column of 3.0 mm \times 250mm, 5 μ m particle size (Agilent Technologies). 0.1% formic acid and 5% MilliQ water in acetonitrile were used as mobile phase A and 0.1% formic acid in water (pH 3.5) as mobile phase B. The elution gradient went from 10% A (3min) to 100% A in 22 min, to be kept thereafter at 100% A for 3min. The flow rate was 0.5 mL/min and the injection volume 20 μ L. The HPLC system was connected to a quadrupole-time-of-flight mass spectrometer (Agilent 6530 Q-TOF MS, Agilent Technologies, Santa Clara, CA). The instrument was operated in the 4GHz High Resolution Mode. Ions were generated using an electrospray ion source with Agilent Jet Stream Technology. The operation conditions were: superheated nitrogen sheath gas temperature (400 $^{\circ}$ C) at flow rate 12 L/min; nozzle voltage, 0 V; capillary, 4000 V; nebulizer, 60 psi; drying gas, 5 L/min; gas temperature, 250 $^{\circ}$ C; skimmer voltage, 65 V; octapole RF Peak, 750 V; and fragmentor (in source CID fragmentation), 90 V. The mass axis was calibrated using the mixture provided by the manufacturer throughout the m/z 40–3200 range. A second sprayer with a reference solution was used for continuous calibration in positive ion mode using the following reference masses: 121.0509 and 922.0098 m/z (resolution: 21,700 \pm 500 at 922.0098 m/z). MS/MS spectra were acquired throughout the m/z 40–950 range at a scan rate of 0.5 s/spectrum. The collision energy was optimized to obtain the highest number of fragments.

The full mass spectra data recorded were processed with Agilent Mass Hunter Workstation Software (version B.03.01).

3.3.4. Toxicity tests

Multigenerational toxicity was evaluated using an algal growth inhibition test according to the Technical Guideline OECD TG 201 (OECD, 2011). To this end, we cultivated the green alga *P. subcapitata* in 96-well microplates using a total volume of 200 μL . Each well contained 100 μL of sample and 100 μL of growth medium which was prepared using the required amount of concentrated OECD medium (pH adjusted to 8.0 ± 0.1) in order to ensure the same concentration of salts in all samples and controls. The microplates were placed in an algal growth chamber under continuous fluorescent illumination (approximately $100 \mu\text{E m}^{-2} \text{s}^{-1}$), and incubated at $22 \pm 1^\circ\text{C}$. Algal growth was assessed by chlorophyll fluorescence (excitation 444 nm – emission 680 nm) using a Fluoroskan Ascent FL plate luminometer. Algae beads and culture media were purchased from Microbiotest Inc.

Acute toxicity was assessed by measuring the decrease in the constitutive bioluminescence of the marine bacterium *V. fischeri* following the procedure described in ISO 11348-3 (ISO, 2007). The measurements were performed using a Fluoroskan Ascent FL plate luminometer. The incubation period used in this study was 30 min in all cases. Tests were performed at $17.9 \text{C} \pm 0.3^\circ\text{C}$ and the decrease of light was monitored using the previously mentioned microplate luminometer. We used the commercially available Biofix Lumi test (Macherey–Nagel, Germany). The bacterial reagent is supplied freeze-dried and is reconstituted and incubated at 3°C for 5 min before use. The analysis medium was 0.34 M NaCl (2% w/v). The toxicity was measured as the percentage of inhibition with respect to the light emitted in the absence of any toxic influence after 30 min exposure.

3.3.5. Experimental setup and procedure

The photocatalytic reactions were carried out in a Duran tubular photoreactor placed in a Solarbox (Co.fo.me.gra 220V 50Hz) and irradiated by a Xe-OP lamp (Philips 1 kW) with a photon flux of $(6.19 \pm 0,20) \times 10^{-6}$ Einstein s^{-1} (290-400 nm) determined by 2-2-nitrobenzaldehyde actinometry (Allen et al., 2000; Galbavy et al., 2010). The runs were performed at 25°C. The aqueous suspension containing 25 mg/L of propranolol, was continuously driven to the photoreactor from a feeding tank and recirculated to it, at a rate of 0.65 L min^{-1} by means of a pump (Ecoline VC-280 II, Ismatec). The reason for choosing 25 mg/L as initial concentration for propranolol was to facilitate the detection of reaction intermediates and the toxicity assessment of partially oxidized mixtures in view of the toxicity of the parent compound to the microorganisms indicated in the preceding section. All connections and pipes employed were made of Teflon and/or glass material to avoid losses by adsorption. The temperature was controlled using a Huber thermostatic bath. pH was measured with a Crison GLP 22 instrument and kept constant at 7.5 ± 0.1 by using a 2 mM phosphate buffer. The possible adsorption of phosphate was considered negligible in view of the negative charge of the catalytic surface. Dissolved oxygen concentration, with an initial value of 8.0 ± 0.5 mg O_2/L , was measured by a Crison Oxi 330i WTW Oxi Cal-SL sensor. By allowing contact with air in the recirculation chamber, an almost constant concentration of dissolved oxygen was ensured throughout the runs. The catalyst concentration varied in the 0-0.25 mg/L range. Prior to the runs, the catalyst was dispersed in 400 mL of pure water using an ultrasonic homogenizer (Bandelin Sonoplus HO2070) operating at 50 W for 10 min (70% amplitude). The catalyst dispersed in the aqueous phase was allowed to circulate through the photocatalytic system for one hour. The larger particles were removed to avoid deposition within the reaction loop. The concentration of catalyst remaining in suspension was also determined after being dried at 105°C and weighed. The effective concentration of

suspended catalyst was used as bulk concentration for calculations. Propranolol solution from a concentrate was added to the aqueous suspension of the catalyst and stirred for one more hour to reach adsorption-desorption equilibrium. Then the run started. The experiments were carried out in ultrapure water and in spiked wastewater using the secondary effluent of the WWTP described before as a matrix. Samples were withdrawn for analysis at prescribed intervals.

3.4. Results and discussion

3.4.1. Kinetics

The degradation of propranolol takes place through two parallel processes: photolysis and photocatalysis. The photolysis of propranolol, quantified in runs without catalyst, is due to the absorption of radiation of a wavelength lower than 330 nm (Dantas et al., 2010). Fig. 3.2 shows the extent of propranolol depletion with and without catalyst. When using 0.14 g/L of 0.5 % wt. Ce-TiO₂, propranolol completely disappeared in less than 2 h of irradiation, whereas for a similar run in the absence of catalyst, about 50% of the initial propranolol was still in solution. DOC removal also increased from 3% to 17% (after 6 h of irradiation) for runs with the same amount of catalyst with respect to non-catalytic irradiation. This difference was attributed to the photons absorbed by the photocatalyst, which generate holes (h⁺) and intermediate oxygen containing oxidants such as hydroxyl radicals (·OH) which oxidized organic matter. The rate of propranolol removal can be expressed as follows, where r_d and r_i represent the homogeneous rate of photolysis and photocatalysis respectively:

$$-\frac{dc_{PRO}}{dt} = r_d + r_i \quad (2)$$

Assuming that the heterogeneous process follows a Langmuir-Hinshelwood expression (Postigo et al., 2011; Yang et al., 2010), the reaction kinetics for the rate of photocatalysis can be written as follows:

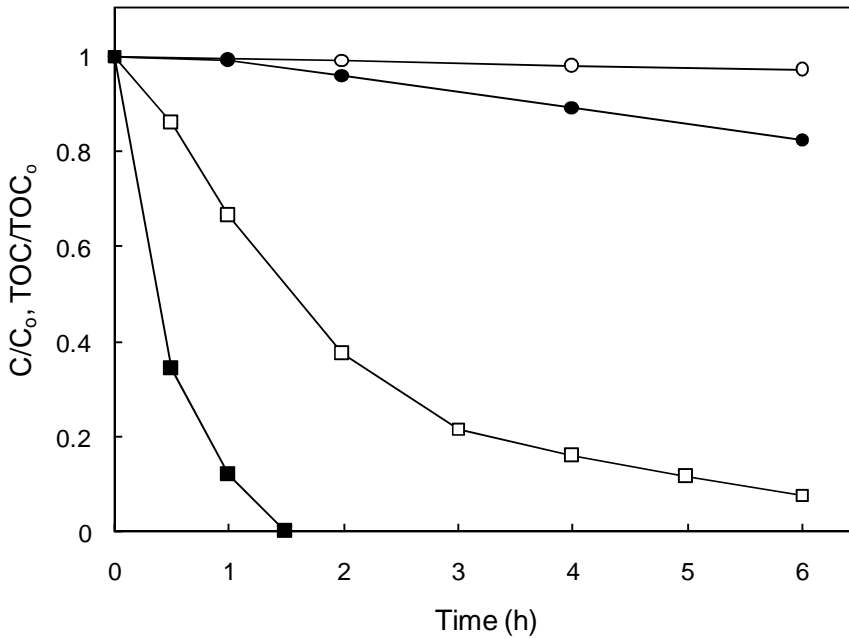


Figure 3.2. Evolution of propranolol (□, ■) and TOC (○, ●) during irradiation (empty symbols) and photocatalytic oxidation (0.14 g/L, Ce-TiO₂ 0.5 % wt. Cerium, filled symbols).

$$r_i = k_T \text{LVRPA}^m \frac{K_{PRO} c_{PRO}}{1 + \sum_i K_i c_i} \quad (3)$$

where K_{PRO} is the equilibrium constant for propranolol adsorption and k_T is a true kinetic constant independent of photon absorption that includes the primary quantum yield for electron-hole generation within the photocatalyst. The kinetic constant takes into account all other factors that may affect the overall quantum yield, with the exception of the substrate concentration and the local volumetric rate of photon absorption (LVRPA). The exponent m of the LVRPA depends on the efficiency of electron-hole formation and recombination at the catalyst surface. The data available indicate that at weak radiation intensities, the rate of photocatalytic oxidation is first-order in radiation intensity and, therefore, $m = 1$ (Ollis,

1991). The sum in the denominator extends to all adsorbable compounds in the mixture including unreacted propranolol. Gora et al. (2006) and Li Puma et al. (2007) determined that the dark equilibrium constants for the TiO₂ adsorption of several compounds were of the same order of magnitude as those observed under irradiation. They also suggested that the transformation products should have equilibrium constants similar to that of the parent compounds, all of them being essentially independent of radiation absorption. The denominator of Eq. 5 takes the following simplified form:

$$1 + \sum_i K_i c_i = 1 + \sum_i K_i c_{i,o} = 1 + K_{PRO} c_{PRO,o} \quad (4)$$

Eq. 3 is valid for any point inside the reactor. The effective radiant power absorbed within the reaction space can be obtained by integrating the LVRPA (Li Puma and Brucato, 2007):

$$\int_V LVRPA dV = 2\pi \iint_{r,z} r(LVRPA) dr dz \quad (5)$$

In a reactor with recirculation with a total volume V and a reactor volume V_r, Eq. 3, yields, after integrating LVRPA, the following first-order rate expression:

$$r_i = \frac{K_{PRO}}{V} \frac{k_T \left(\int_{V_r} LVRPA dV_r \right)}{1 + K_{PRO} c_{PRO,o}} c_{PRO} \quad (6)$$

Finally, the LVRPA can be calculated from the two-flux-absorption-scattering model proposed by Li Puma and Brucato (2007):

$$LVRPA = \kappa c_s I_o e^{-(\kappa+\sigma)c_s \delta \sqrt{1-\omega^2}} \quad (7)$$

The presence of adsorbing compounds does not alter the scattering coefficient, σ , which is equal to that of the photocatalyst particles. In Eq. 7, κ is the specific absorption coefficient of the catalyst, ω the scattering albedo, and I_o the fluence rate at reactor wall. On the other

hand, the absorption coefficient of the medium is a sum of the absorption coefficients of all dissolved compounds and the catalyst: $\kappa c_s + \sum \kappa_i c_i$.

The rate of the photochemical process, r_d , depends on the overall quantum yield and on the LVRPA, in which κc_s of Eq. 7 must be substituted by $\sum \kappa_i c_i$ or $\kappa_{PRO} c_{PRO}$.

$$r_d = \Phi_{PRO} \kappa_{PRO} c_{PRO} I_o e^{-\left(\sigma c_s + \sum_i \kappa_i c_i\right) \delta \sqrt{1-\omega^2}} \quad (8)$$

Assuming again that $\sum \kappa_i c_i$ is essentially coincident with $\kappa_{PRO} c_{PRO}$ due to the contribution of transformation products from the parent compound, both r_i and r_d become first-order in the concentration of propranolol, with the following global rate expression:

$$-\frac{dc_{PRO}}{dt} = (k_d + k_i) c_{PRO} = k c_{PRO} \quad (9)$$

It is interesting to note that, when applied to a polychromatic radiation, all relevant quantities, namely absorption and scattering coefficients and quantum yield, have to be averaged over the useful spectrum of the incident radiation (Braun et al., 1986). Also that first-order rate constants k and k_i depend on the initial concentration of propranolol.

Photocatalytic runs were performed with a Ce-TiO₂ using different cerium loadings: 0, 0.5 and 1.0 % wt., the effective bulk catalyst concentration varying in the 0-0.27 g/L range. Fig. 3.3 shows the increase in the first-order rate constant of propranolol degradation using cerium-doped catalysts with respect to non-doped TiO₂. As indicated in Fig. 3.1, the presence of cerium shifted the absorption towards higher wavelengths, which is probably the reason of their improved performance. The best results were obtained for photocatalysts with a cerium loading of 0.5 % wt. and rate constants roughly twice those of 1.0 % wt. cerium loading. This behaviour was probably due to the role played by Ce⁴⁺ in suppressing electron-hole recombination, which turns into a combination centre at

higher dopant concentrations leading to a decrease in photocatalytic activity (Li et al., 2012). Li et al. (2005) suggested that the presence of Ce⁴⁺ on catalyst surface may promote the production of hydroxyl radicals from dissolved oxygen increasing the efficiency by which a photogenerated electron is transferred. It has also been pointed out that the formation of an amorphous Ce-Ti-O phase at high cerium loadings has a detrimental effect on the dopant role in preventing electron-hole recombination (Silva et al., 2009).

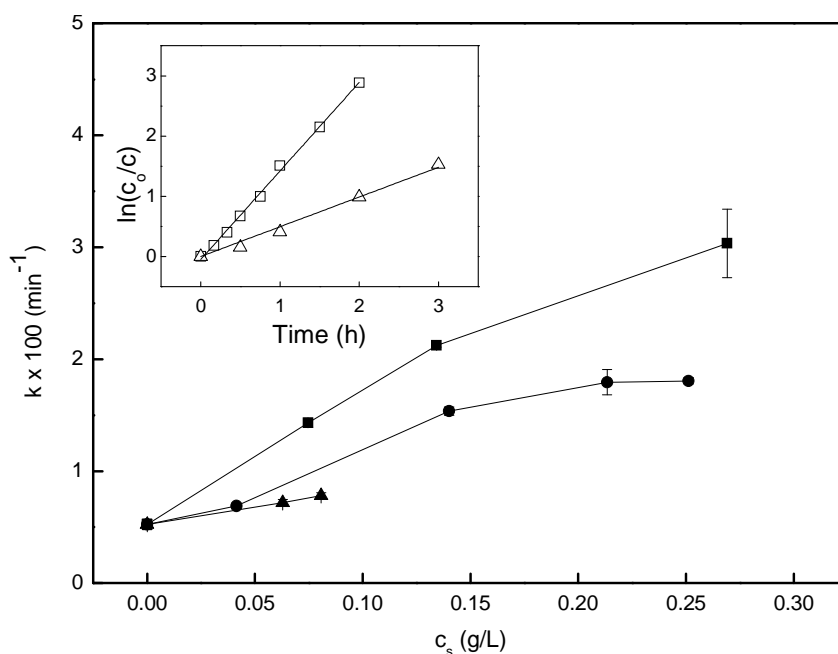


Figure 3.3. First-order rate constant as a function of bulk catalyst concentration for different cerium loadings: 1.0 % wt. (●), 0.5 % wt. (■) and TiO₂ without cerium (▲). Inset: fitting of the logarithmic concentration decay for pure irradiation (without catalyst, Δ) and for 75 mg/L Ce-TiO₂, 0.5 % wt. Ce (□).

On the other hand, the decrease in crystallite size results in the creation of oxygen vacancies which could reduce recombination, this being consistent with our observations concerning crystallite size in doped TiO₂ (Li et al., 2012). The inset in Fig. 3.3 shows the fitting to a first-order rate

equation of catalytic and non-catalytic runs. The rate constant increased with catalyst load in all cases, as indicated in Fig. 3.3, in which the error bars represent 95% confidence intervals. The relationship was essentially linear, as expected from the dependency of rate constants on bulk catalyst concentration, c_s , expressed in Eq. 7.

The degree of mineralization, measured through dissolved organic carbon (DOC), was 8.5% and 17.4% for catalysts with 1.0 and 0.5 of cerium % wt., respectively after six hours of irradiation using a catalyst concentration of 0.14 g/L. The behaviour was similar in other conditions, with the catalyst doped with 0.5 % wt. cerium being the most effective in all cases. Although higher catalyst concentrations (up to 0.27 g/L) led to higher rate constants, we chose the concentration of 0.14 g/L because it fell in the region in which the rate constant increased linearly with catalyst loading. It is well-known that up to a certain catalyst loading the specific reaction rate starts to decline, a fact that can be attributed to the shielding effect or obstruction of light transmission, but also to the appearance of internal mass-transfer limitations within particles (Mehrotra et al., 2003).

The contribution of hydroxyl radicals to propranolol degradation was assessed employing a competitive kinetic approach with pCBA as hydroxyl radical probe. pCBA has been reported for this purpose in UV studies due to its rapid reaction with $\bullet\text{OH}$ ($k_{\bullet\text{OH},\text{pCBA}} = 5 \times 10^9 \text{ M}^{-1} \text{ s}^{-1}$) and its low quantum yield for direct photolysis (0.026 using wavelengths in the 250–350 nm range) and low radiation absorption above 290 nm (Duran cut-off), which implies a low rate of photolysis compared to the $\bullet\text{OH}$ pathway (Rosenfeldt et al., 2006). Besides, no significant adsorption of pCBA has been observed in dark contact with the photocatalyst and, therefore, the direct oxidation of pCBA by holes was considered negligible, the compound being only depleted by bulk hydroxyl radicals. Following Elovitz and von Gunten (1999), the exposure to $\bullet\text{OH}$ could be obtained from kinetic data as follows:

$$\ln \frac{C_{pCBA,o}}{C_{pCBA}} = k_{OH,pCBA} \int c_{\bullet OH} dt \quad (10)$$

Coming back to Eq. 9, the apparent first-order constant for photocatalysis, k_i , is the consequence of two contributions: the oxidation of compounds adsorbed in catalyst holes, $k_{i,h+}$, and the bulk reaction intermediated by hydroxyl radicals $k_{i,\bullet OH}$:

$$-\frac{dc_{PRO}}{dt} = (k_d + k_{i,h+} + k_{i,\bullet OH} c_{\bullet OH}) c_{PRO} \quad (11)$$

Integrating Eq. 11, and combining it with Eq. 10, it is possible to relate the logarithmic concentration decay rates of propranolol and pCBA:

$$\ln \frac{C_{PRO,o}}{C_{PRO}} = (k_d + k_{i,h+}) t + k_{i,\bullet OH} \int c_{\bullet OH} dt = (k_d + k_{i,h+}) t + \frac{k_{i,\bullet OH}}{k_{OH,pCBA}} \ln \frac{C_{pCBA,o}}{C_{pCBA}} \quad (12)$$

The second order rate constant for the reaction of propranolol and hydroxyl radicals, $k_{i,\bullet OH}$, was measured by Benner et al. (2008) who reported a value of $1.0 \pm 0.2 \times 10^{10} \text{ M}^{-1} \text{ s}^{-1}$. By plotting the time-independent terms of Eq. 12 as a function of time (Fig. 3.4), the slope yields the experimental value of $k_d + k_{i,h+}$, the sum of the first-order rate constants for direct photolysis and photocatalytic oxidation of propranolol in catalyst holes, $k_{i,h+}$. The result was $2.50 \times 10^{-2} \pm 4 \times 10^{-4} \text{ min}^{-1}$, and by subtracting the experimental value of k_d ($8.2 \times 10^{-3} \pm 6 \times 10^{-4} \text{ min}^{-1}$), the calculated rate constant for the reaction with holes was $1.6 \times 10^{-2} \pm 1 \times 10^{-3} \text{ min}^{-1}$. It was assumed that a low fraction of radiation is absorbed by the catalyst. On the other hand, the rate constant, k , for the photocatalytic degradation of propranolol under the same conditions was $3.53 \times 10^{-2} \pm 3 \times 10^{-4} \text{ min}^{-1}$ (Fig. 3.3). Combining the former results, $k_i = k_{i,\bullet OH} c_{\bullet OH} = 1.03 \times 10^{-2} \pm 7 \times 10^{-4} \text{ min}^{-1}$ and, therefore, it can be estimated that 60% of the photocatalytic reaction took place through surface holes (h+) for a catalyst load of 0.14 g/L, the rest being mediated by hydroxyl radicals. Yang et al. (2010) calculated that 77.5% of the UV-TiO₂ degradation of propranolol

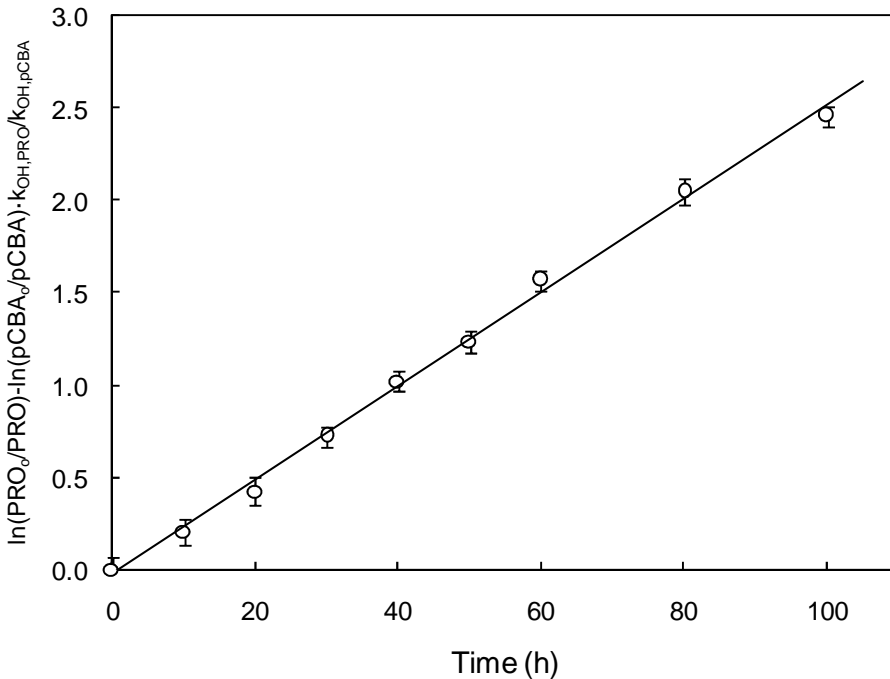


Figure 3.4. Fitting of competitive kinetics (Eq. 12) for the simultaneous treatment of propranolol and pCBA with 0.14 mg/L Ce-TiO₂, 0.5 % wt. Ce.

was due to the reaction with hydroxyl radicals, with 19.2% being due to the reaction with oxidizing catalyst holes. The difference was probably due to the different catalyst load (one order of magnitude greater) which could leave a high catalyst surface area free to produce hydroxyl radicals from water, and to the different light source (UV instead of visible light). Adsorption experiments performed in the dark enabled us to calculate that under the aforementioned conditions, about 20% of the propranolol in solution became adsorbed on the catalyst surface (pH 7.5, buffered). This high adsorption, shared by other β -blockers as noted by Yang et al. (2010) suggest that degradation is prone to occur mainly on the surface of TiO₂ by oxidation with holes. These ideas are supported by the fact that

experimental runs with Ce-TiO₂ resulted in a lower rate constant when performing runs at pH 6 in comparison with pH 7.5 (23% lower).

Photocatalytic degradation runs were also performed using a wastewater matrix with the Ce-TiO₂ (0.5% wt. Ce) and a catalyst bulk concentration of 0.14 g/L. The results are shown in Fig. 3.5. In photolytic runs without catalyst, it was observed that the first-order rate constant, k_d , was higher than that of the runs performed in pure water (85% higher). This was probably due to the consequence of the photolysis of nitrate and nitrite, which has been shown to induce the formation of hydroxyl radicals by absorbing light at 360 nm and 310 nm respectively (Mack and Bolton, 1999). It has also been shown that the presence of organic matter in wastewater effluents may also contribute to the photochemical formation

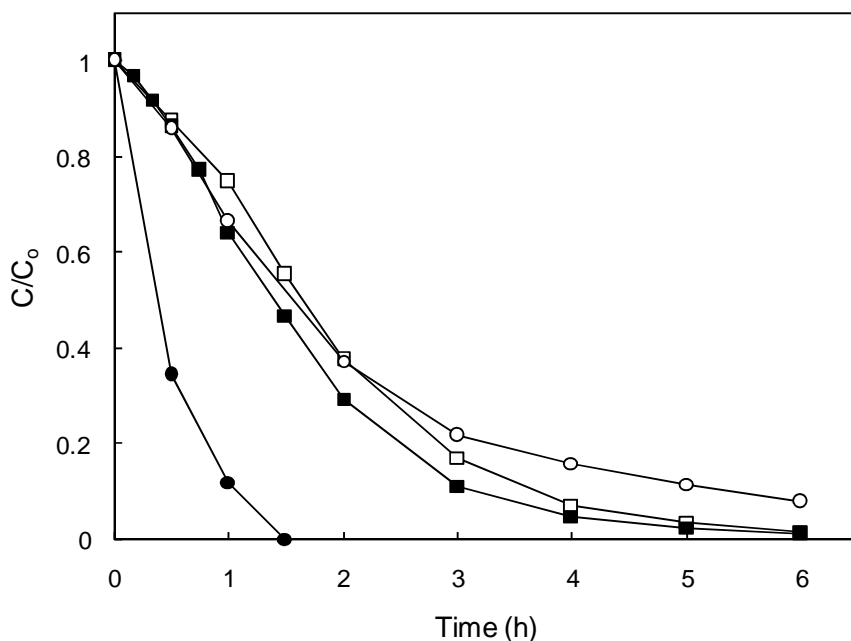


Figure 3.5. Propranolol depletion for irradiation (□) and photocatalytic (■, 0.14 g/L, Ce-TiO₂ 0.5 % wt. Ce) runs in spiked wastewater. For comparison similar runs in pure water are included (○, ●), filled symbols representing photocatalytic experiments.

of hydroxyl radicals (Dong and Rosario-Ortiz, 2012). First-order catalytic rate constants, k , were higher than those of pure photolytic runs (15% higher), but the difference was much lower than that encountered in experiments performed in pure water, in which the catalyst increased the degradation rate by up to four times. This dramatic decrease in the efficiency of the photocatalyst, reflected in k_i values dropping from $1.71 \pm 0.15 \text{ min}^{-1}$ to $0.06 \pm 0.01 \text{ min}^{-1}$, was probably in part a consequence of the presence of radical scavengers in wastewater, such as bicarbonates, phosphates or organic matter. The important role played by catalytic holes in reactions performed in pure water suggests that other compounds in wastewater compete with propranolol for surface adsorption, which would explain this reduction in efficiency. Dimitroula et al. (2012) also found a decrease in the oxidation rate of several micropollutants of one order of magnitude when comparing the reaction in pure water with a wastewater matrix. Ioannou et al. (2011) showed that mineralization practically did not take place at all when irradiating β -blockers with solar light in the presence of TiO_2 . They assumed that photo-generated reactive species were consumed by attacking organic compounds without converting them into carbon dioxide and in the reaction with chlorides and other scavengers. As a consequence, the conversion of propranolol approached zero (from 20-30%) when dissolving it in a secondary treated wastewater effluent. Similar results have been reported elsewhere. Dialynas et al. (2008) reported that the organic matter contained in treated wastewater is considerably refractory towards photocatalytic oxidation, with a very low removal rate of dissolved organic carbon. Our COD results point in the same direction and showed a 13% decrease (28% in pure water), which was essentially the same value obtained without catalyst. However, concerning DOC, we obtained a 14 % decrease after 6 h (0.14 g/L, 0.5 % wt. Ce-TiO₂), only somewhat lower than that in pure water (17%, Fig. 3.2) and considerably higher than that of pure irradiation runs (< 5%).

3.4.2. Identification of reaction intermediates and reaction pathway

The identification of propranolol transformation products was performed on samples with 25 mg/L of propranolol. In catalytic runs, 0.14 g/L of 0.5% wt. Ce-TiO₂ was used. The assignment was based on accurate mass measurements recorded by the LC-QTOF-MS/MS instrument described above, operating in positive mode (ESI+). MS/MS spectra were acquired at optimized collision energies to increase fragmentation and thus improve structural information. These measurements allowed elemental compositions to be proposed for the protonated [M+H]⁺ molecular ions and their characteristic product ions, thus providing a high degree of confidence in structure assignment. Table 3.2 displays the ion formula and calculated mass of the product ions, as well as relative mass error and DBE (double bond and ring equivalents). The second column of the table indicates “c” and “s” for transformation products identified in photocatalytic runs and solar irradiation respectively. “p” stands for the parent compound, propranolol, for which the accurate mass measurements recorded (m/z 260.1645 for C₁₆H₂₂NO₂) offer an excellent agreement of less than 1 ppm error, with calculated m/z value. Propranolol product ions yielded characteristic signals at m/z 218.1176, 183.0804 and 157.0648 that corresponded to cleavages in the aliphatic chain of isopropyl, aminoisopropyl plus water, and C₂H₂ groups, respectively (Table 3.2). These fragments still retained the naphthalene structure. Additionally, product ions at m/z 116.1070, 98.0964, 74.0600, 72.0808 and 56.0495 correspond to transformations in the side chain after cleavage of the ether bond of propranolol. As with propranolol, the characteristic fragmentation of oxidation by-products provided enough information for the identification of over thirty transformation products. The appearance of characteristic fragments in the set of product ions spectra indicates the prevalence of a certain fraction of the molecule and suggests the place it should occupy in the transformation pathway, a proposal which is depicted

Table 3.2. LC-ESI-QTOF-MS/MS mass measurements of propranolol and its transformation products and structures proposed for them (p = parent compound; c = photocatalytic process; s = solar irradiation).

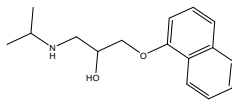
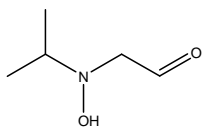
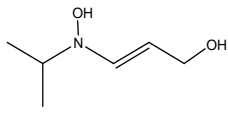
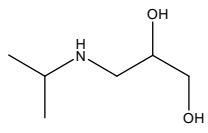
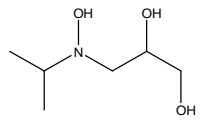
Compound		R _t (min)	Ion Mass (m/z)	Ion formula	Error (ppm)	DBE	Proposed structure
Propranolol - P1	p	14.83	260.1645	C ₁₆ H ₂₂ NO ₂	-0.52	7	
			218.1176	C ₁₃ H ₁₆ NO ₂	1.32	6.5	
			183.0804	C ₁₃ H ₁₁ O	2.52	8.5	
			157.0648	C ₁₁ H ₉ O	-3.12	7.5	
			116.107	C ₆ H ₁₄ NO	-4.85	0.5	
			98.0964	C ₆ H ₁₂ N	1.69	1.5	
			74.06	C ₃ H ₈ NO	-3.25	0.5	
			72.0808	C ₄ H ₁₀ N	-2.69	0.5	
56.0495	C ₃ H ₆ N	-4.69	1.5				
P2	c	2.26	118.0863	C ₅ H ₁₂ NO ₂	-0.89	1	
			76.0394	C ₂ H ₆ NO ₂	1.02	0.5	
			72.0808	C ₄ H ₁₀ N	-3.7	0.5	
			43.0542	C ₃ H ₇	-8.5	0.5	
P3	c	2.31	132.1019	C ₆ H ₁₄ NO ₂	-1.44	1	
			116.107	C ₆ H ₁₄ NO	4.91	0.5	
			74.06	C ₃ H ₈ NO	-0.51	0.5	
			72.0808	C ₄ H ₁₀ N	-7.82	0.5	
			56.0495	C ₃ H ₆ N	-15.77	1.5	
P4	c-s	2.12	134.1176	C ₆ H ₁₆ NO ₂	-0.32	0	
			116.107	C ₆ H ₁₄ NO	2.14	0.5	
			98.0964	C ₆ H ₁₂ N	-3.27	1.5	
			74.06	C ₃ H ₈ NO	-5.68	0.5	
			72.0808	C ₄ H ₁₀ N	-4.49	0.5	
			56.0495	C ₃ H ₆ N	-7.1	1.5	
P5	c	2.09	150.1125	C ₆ H ₁₆ NO ₃	0.67	0	
			132.1019	C ₆ H ₁₄ NO ₂	0.92	0.5	
			114.0913	C ₆ H ₁₂ NO	1.5	1.5	
			88.0757	C ₄ H ₁₀ NO	2.56	0.5	
			74.06	C ₃ H ₈ NO	-0.9	0.5	
			72.0808	C ₄ H ₁₀ N	-4.01	0.5	
			56.0495	C ₃ H ₆ N	3.8	1.5	

Table 3.2. (Continued)

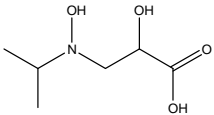
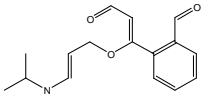
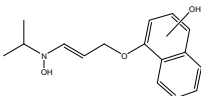
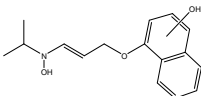
Compound		R _t (min)	Ion Mass (m/z)	Ion formula	Error (ppm)	DBE	Proposed structure
P6	c-s	2.05	164.0917	C ₆ H ₁₄ NO ₄	-1.09	1	
			148.0968	C ₆ H ₁₄ NO ₃	0.05	0.5	
			146.0812	C ₆ H ₁₂ NO ₃	1.02	1.5	
			130.0863	C ₆ H ₁₂ NO ₂	1.87	1.5	
			128.0706	C ₆ H ₁₀ NO ₂	-3.76	2.5	
			118.0863	C ₅ H ₁₂ NO ₂	2.94	0.5	
			100.0757	C ₅ H ₁₀ NO	0.81	1.5	
			88.0757	C ₄ H ₁₀ NO	-2.54	0.5	
			74.0600	C ₃ H ₈ NO	-0.20	0.5	
			56.0495	C ₃ H ₆ N	-14.36	1.5	
			P7	c-s	9.91	266.1387	
248.1281	C ₁₄ H ₁₈ NO ₃	2.05				6.5	
224.0917	C ₁₁ H ₁₄ NO ₄	4.13				5.5	
206.0812	C ₁₁ H ₁₂ NO ₃	1.63				6.5	
145.0648	C ₁₀ H ₉ O	-1.23				6.5	
98.0964	C ₆ H ₁₂ N	-5.45				1.5	
74.06	C ₃ H ₈ NO	4.63				0.5	
72.0808	C ₄ H ₁₀ N	3.69				0.5	
56.0495	C ₃ H ₆ N	-2.69				1.5	
P8	c-s	10.56	274.1438	C ₁₆ H ₂₀ NO ₃	0.25	8	
			232.0968	C ₁₃ H ₁₄ NO ₃	2.19	7.5	
			131.0491	C ₉ H ₇ O	1.02	6.5	
P9	c-s	12.13	274.1438	C ₁₆ H ₂₀ NO ₃	-0.94	8	Structure for compounds: P9-P10 
			143.0491	C ₁₀ H ₇ O	3.09	7.5	
			116.107	C ₆ H ₁₄ NO	0.11	0.5	
			102.0913	C ₅ H ₁₂ NO	1.66	0.5	
			98.0964	C ₆ H ₁₂ N	5.2	1.5	
			72.0808	C ₄ H ₁₀ N	-2.93	0.5	
P10	c-s	12.47	274.1438	C ₁₆ H ₂₀ NO ₃	-0.07	8	
			143.0491	C ₁₀ H ₇ O	1.47	7.5	
			116.107	C ₆ H ₁₄ NO	-0.87	0.5	
			102.0913	C ₅ H ₁₂ NO	1.66	0.5	
			98.0964	C ₆ H ₁₂ N	-2.43	1.5	
			72.0808	C ₄ H ₁₀ N	-9.2	0.5	
56.0495	C ₃ H ₆ N	-11.21	1.5				

Table 3.2. (Continued)

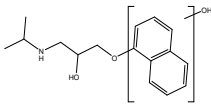
Compound		R _t (min)	Ion Mass (<i>m/z</i>)	Ion formula	Error (ppm)	DBE	Proposed structure
P11	C-S	11.08	276.1594	C ₁₆ H ₂₂ NO ₃	1.1	7	Structure proposed for compounds: P11-P12-P13-P14-P15- P16 
			258.1489	C ₁₆ H ₂₀ NO ₂	-1.7	7.5	
			216.1019	C ₁₃ H ₁₄ NO ₂	3.47	7.5	
			199.0754	C ₁₃ H ₁₁ O ₂	3.21	8.5	
			173.0597	C ₁₁ H ₉ O ₂	-3	7.5	
			157.0648	C ₁₁ H ₉ O	3.17	7.5	
			116.107	C ₆ H ₁₄ NO	-1.2	0.5	
			102.0913	C ₅ H ₁₂ NO	-1.49	0.5	
			98.0964	C ₆ H ₁₂ N	2.34	1.5	
			72.0808	C ₄ H ₁₀ N	4.66	0.5	
58.0651	C ₃ H ₈ N	-7.56	0.5				
P12	C-S	11.56	276.1594	C ₁₆ H ₂₂ NO ₃	-2.25	7	
			258.1489	C ₁₆ H ₂₀ NO ₂	3.2	7.5	
			216.1019	C ₁₃ H ₁₄ NO ₂	2.63	7.5	
			199.0754	C ₁₃ H ₁₁ O ₂	4.56	8.5	
			173.0597	C ₁₁ H ₉ O ₂	1.26	7.5	
			157.0648	C ₁₁ H ₉ O	1.03	7.5	
			116.107	C ₆ H ₁₄ NO	2.37	0.5	
			102.0913	C ₅ H ₁₂ NO	1.11	0.5	
			98.0964	C ₆ H ₁₂ N	3.46	1.5	
			72.0808	C ₄ H ₁₀ N	5.62	0.5	
58.0651	C ₃ H ₈ N	8.23	0.5				
P13	C-S	11.66	276.1594	C ₁₆ H ₂₂ NO ₃	-1.25	7	
			258.1489	C ₁₆ H ₂₀ NO ₂	2.23	7.5	
			216.1019	C ₁₃ H ₁₄ NO ₂	3.02	7.5	
			199.0754	C ₁₃ H ₁₁ O ₂	5.23	8.5	
			173.0597	C ₁₁ H ₉ O ₂	-0.21	7.5	
			157.0648	C ₁₁ H ₉ O	3.21	7.5	
			116.107	C ₆ H ₁₄ NO	2.23	0.5	
			102.0913	C ₅ H ₁₂ NO	3.32	0.5	
			98.0964	C ₆ H ₁₂ N	1.69	1.5	
			72.0808	C ₄ H ₁₀ N	4.56	0.5	
58.0651	C ₃ H ₈ N	5.26	0.5				

Table 3.2. (Continued)

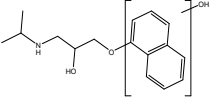
Compound		R _t (min)	Ion Mass (m/z)	Ion formula	Error (ppm)	DBE	Proposed structure
P14	C—S	11.93	276.1594	C ₁₆ H ₂₂ NO ₃	0.14	7	Structure proposed for compounds: P11-P12-P13-P14-P15- P16 
			258.1489	C ₁₆ H ₂₀ NO ₂	1.66	7.5	
			216.1019	C ₁₃ H ₁₄ NO ₂	3.21	7.5	
			173.0597	C ₁₁ H ₉ O ₂	3.32	7.5	
			199.0754	C ₁₃ H ₁₁ O ₂	3.56	8.5	
			157.0648	C ₁₁ H ₉ O	2.39	7.5	
			116.107	C ₆ H ₁₄ NO	3.66	0.5	
			102.0913	C ₅ H ₁₂ NO	2.45	0.5	
			98.0964	C ₆ H ₁₂ N	3.56	1.5	
			72.0808	C ₄ H ₁₀ N	4.99	0.5	
			58.0651	C ₃ H ₈ N	6.02	0.5	
P15	C—S	13.20	276.1594	C ₁₆ H ₂₂ NO ₃	0.77	7	
			258.1489	C ₁₆ H ₂₀ NO ₂	2.05	7.5	
			216.1019	C ₁₃ H ₁₄ NO ₂	3.46	7.5	
			199.0754	C ₁₃ H ₁₁ O ₂	4.56	8.5	
			173.0597	C ₁₁ H ₉ O ₂	-3	7.5	
			157.0648	C ₁₁ H ₉ O	4.56	7.5	
			116.107	C ₆ H ₁₄ NO	2.32	0.5	
			102.0913	C ₅ H ₁₂ NO	1.66	0.5	
			98.0964	C ₆ H ₁₂ N	2.36	1.5	
			72.0808	C ₄ H ₁₀ N	5.32	0.5	
			58.0651	C ₃ H ₈ N	4.56	0.5	
P16	C—S	14.43	276.1594	C ₁₆ H ₂₂ NO ₃	0.08	7	
			258.1489	C ₁₆ H ₂₀ NO ₂	-5.67	7.5	
			199.0754	C ₁₃ H ₁₁ O ₂	2.55	8.5	
			173.0597	C ₁₁ H ₉ O ₂	0.26	7.5	
			145.0648	C ₁₀ H ₉ O	10.57	6.5	
			116.107	C ₆ H ₁₄ NO	1.69	0.5	
			98.0964	C ₆ H ₁₂ N	3.63	1.5	
			72.0808	C ₄ H ₁₀ N	3.99	0.5	
			58.0651	C ₃ H ₈ N	11.59	0.5	
			P17	C—S	6.95	282.1336	
264.123	C ₁₄ H ₁₈ NO ₄	5.94				6.5	
240.0866	C ₁₁ H ₁₄ NO ₅	-1.12				5.5	
204.0655	C ₁₁ H ₁₀ NO ₃	-1.12				7.5	
149.0233	C ₈ H ₅ O ₃	3.09				6.5	
116.107	C ₆ H ₁₄ NO	1.21				0.5	
98.0964	C ₆ H ₁₂ N	-2.53				1.5	
56.0495	C ₃ H ₆ N	4.32				1.5	

Table 3.2. (Continued)

Compound		R _t (min)	Ion Mass (m/z)	Ion formula	Error (ppm)	DBE	Proposed structure
P18	C-S	7.92	282.1336	C ₁₄ H ₂₀ NO ₅	-0.74	6	
			264.123	C ₁₄ H ₁₈ NO ₄	3.02	6.5	
			246.1125	C ₁₄ H ₁₆ NO ₃	2.29	7.5	
			222.0761	C ₁₁ H ₁₂ NO ₄	-0.02	6.5	
			204.0655	C ₁₁ H ₁₀ NO ₃	7.33	7.5	
			116.107	C ₆ H ₁₄ NO	2.01	0.5	
			98.0964	C ₆ H ₁₂ N	-8.32	1.5	
			72.0808	C ₄ H ₁₀ N	2.1	0.5	
56.0495	C ₃ H ₆ N	-6.41	1.5				
P19	C-S	8.77	282.1336	C ₁₄ H ₂₀ NO ₅	-0.71	6	
			264.123	C ₁₄ H ₁₈ NO ₄	-6.2	6.5	
			240.0866	C ₁₁ H ₁₄ NO ₅	1.24	5.5	
			222.0761	C ₁₁ H ₁₂ NO ₄	-5.15	6.5	
			178.0863	C ₁₀ H ₁₂ NO ₂	20.01	5.5	
			98.0964	C ₆ H ₁₂ N	5.72	1.5	
			72.0808	C ₄ H ₁₀ N	0.34	0.5	
			56.0495	C ₃ H ₆ N	-6.69	1.5	
P20	C-S	9.78	282.1336	C ₁₄ H ₂₀ NO ₅	-1.89	6	
			264.123	C ₁₄ H ₁₈ NO ₄	2.33	6.5	
			149.0233	C ₈ H ₅ O ₃	9.04	6.5	
			116.107	C ₆ H ₁₄ NO	26.75	0.5	
			98.0964	C ₆ H ₁₂ N	-4	1.5	
			72.0808	C ₄ H ₁₀ N	2.1	0.5	
			56.0495	C ₃ H ₆ N	-11.68	1.5	
			P21	C	8.74	292.1543	
274.1438	C ₁₆ H ₂₀ NO ₃	6.69				7.5	
264.1594	C ₁₅ H ₂₂ NO ₃	4.68				5.5	
161.0597	C ₁₀ H ₉ O ₂	-11.89				6.5	
116.107	C ₆ H ₁₄ NO	2.23				0.5	
72.0808	C ₄ H ₁₀ N	4.02				0.5	
P22	C-S	8.95	292.1543	C ₁₆ H ₂₂ NO ₄	-1.01	7	
			274.1438	C ₁₆ H ₂₀ NO ₃	-1.86	7.5	
			264.1594	C ₁₅ H ₂₂ NO ₃	3.95	5.5	
			187.0754	C ₁₂ H ₁₁ O ₂	0.17	7.5	
			161.0597	C ₁₀ H ₉ O ₂	-10.8	6.5	
			133.0648	C ₉ H ₉ O	-9.39	5.5	
			116.107	C ₆ H ₁₄ NO	2.23	0.5	
			98.0964	C ₆ H ₁₂ N	-2.35	1.5	
			72.0808	C ₄ H ₁₀ N	-1.23	0.5	
			56.0495	C ₃ H ₆ N	-6.39	1.5	

Table 3.2. (Continued)

Compound		R _t (min)	Ion Mass (m/z)	Ion formula	Error (ppm)	DBE	Proposed structure
P23	C-S	9.69	292.1543	C ₁₆ H ₂₂ NO ₄	-4.98	7	
			274.1438	C ₁₆ H ₂₀ NO ₃	1.22	7.5	
			132.1019	C ₆ H ₁₄ NO ₂	9.47	0.5	
			116.107	C ₆ H ₁₄ NO	-0.56	0.5	
			98.0964	C ₆ H ₁₂ N	1.5	1.5	
			72.0808	C ₄ H ₁₀ N	-11.77	0.5	
			56.0495	C ₃ H ₆ N	-4.91	1.5	
P24	C-S	10.17	292.1543	C ₁₆ H ₂₂ NO ₄	0.27	7	
			274.1438	C ₁₆ H ₂₀ NO ₃	-0.91	7.5	
			232.0968	C ₁₃ H ₁₄ NO ₃	0.18	7.5	
			246.1494	C ₁₅ H ₂₀ NO ₂	0.61	6.5	
			215.0703	C ₁₃ H ₁₁ O ₃	8.24	8.5	
			197.0597	C ₁₃ H ₆ O ₂	-0.22	9.5	
			185.0597	C ₁₂ H ₆ O ₂	10.25	8.5	
			157.0648	C ₁₁ H ₉ O	-2.55	7.5	
			116.107	C ₆ H ₁₄ NO	3.21	0.5	
			72.0808	C ₄ H ₁₀ N	3.63	0.5	
			56.0495	C ₃ H ₆ N	-19.19	1.5	
P25	C-S	12.23	292.1543	C ₁₆ H ₂₂ NO ₄	0.47	7	
			274.1438	C ₁₆ H ₂₀ NO ₃	0.89	7.5	
			159.0441	C ₁₀ H ₇ O ₂	4.15	7.5	
			131.0491	C ₉ H ₇ O	-2.23	6.5	
			116.107	C ₆ H ₁₄ NO	3.02	0.5	
			103.0542	C ₈ H ₇	-0.72	5.5	
			98.0964	C ₆ H ₁₂ N	5.22	1.5	
			72.0808	C ₄ H ₁₀ N	-4.01	0.5	
			56.0495	C ₃ H ₆ N	-5.92	1.5	
P26	C-S	5.07	294.1700	C ₁₆ H ₂₄ NO ₄	-2.4	6	
			276.1594	C ₁₆ H ₂₂ NO ₃	1.76	6.5	
			234.1125	C ₁₃ H ₁₆ NO ₃	-5.56	6.5	
			199.0754	C ₁₃ H ₁₁ O ₂	-2.7	8.5	
			173.0597	C ₁₁ H ₉ O ₂	-1.03	7.5	
			116.107	C ₆ H ₁₄ NO	5.32	0.5	
			98.0964	C ₆ H ₁₂ N	3.38	1.5	
			74.06	C ₃ H ₈ NO	-7.14	0.5	
			72.0808	C ₄ H ₁₀ N	2.56	0.5	
			56.0495	C ₃ H ₆ N	-12.3	1.5	

Table 3.2. (Continued)

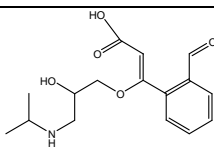
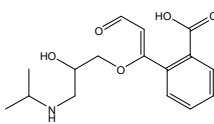
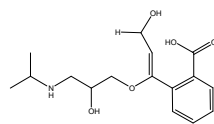
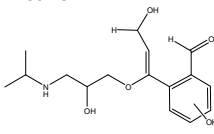
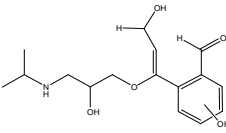
Compound		R _t (min)	Ion Mass (m/z)	Ion formula	Error (ppm)	DBE	Proposed structure
P27	C-S	11.18	308.1492	C ₁₆ H ₂₂ NO ₅	0.53	7	
			290.1387	C ₁₆ H ₂₀ NO ₄	4.02	7.5	
			249.0757	C ₁₃ H ₁₃ O ₅	1.19	7.5	
			175.039	C ₁₀ H ₇ O ₃	2.91	7.2	
			147.0446	C ₉ H ₇ O ₂	-1.72	6.5	
			131.0491	C ₉ H ₇ O	3.72	6.5	
			116.107	C ₆ H ₁₄ NO	3.23	0.5	
			98.0964	C ₆ H ₁₂ N	2.86	1.5	
			72.0808	C ₄ H ₁₀ N	10.23	0.5	
			56.0495	C ₃ H ₆ N	4.02	1.5	
P28	C-S	12.02	308.1492	C ₁₆ H ₂₂ NO ₅	0.53	7	
			290.1387	C ₁₆ H ₂₀ NO ₄	-1.89	7.5	
			249.0757	C ₁₃ H ₁₃ O ₅	-0.9	7.5	
			175.039	C ₁₀ H ₇ O ₃	1.41	7.5	
			157.029	C ₁₀ H ₅ O ₂	-4.07	8.5	
			131.0491	C ₉ H ₇ O	3.12	6.5	
			116.107	C ₆ H ₁₄ NO	1.02	0.5	
			98.0964	C ₆ H ₁₂ N	3.21	1.5	
			72.0808	C ₄ H ₁₀ N	1.23	0.5	
			56.0495	C ₃ H ₆ N	-3.76	1.5	
P29	C-S	3.37	310.1649	C ₁₆ H ₂₄ NO ₅	1.36	6	
			292.1543	C ₁₆ H ₂₂ NO ₄	1.23	7	
			274.1438	C ₁₆ H ₂₀ NO ₃	-3.02	7.5	
			256.1338	C ₁₆ H ₁₈ NO ₂	6.15	8.5	
			250.1079	C ₁₃ H ₁₆ NO ₄	6.23	6.5	
			232.0974	C ₁₃ H ₁₄ NO ₃	0.43	7.5	
			228.1388	C ₁₅ H ₁₈ NO	5.44	7.5	
			215.0708	C ₁₃ H ₁₁ O ₃	-1.39	8.5	
			199.0759	C ₁₃ H ₁₁ O ₂	-5.85	8.5	
			197.0603	C ₁₃ H ₉ O ₂	-3.7	9.6	
			116.107	C ₆ H ₁₄ NO	1.23	0.5	
			114.0913	C ₁₃ H ₁₂ NO	4.01	1.5	
			98.0964	C ₆ H ₁₂ N	4.24	1.5	
72.0808	C ₄ H ₁₀ N	-17.23	0.5				
P30	C-S	4.44	310.1649	C ₁₆ H ₂₄ NO ₅	-1.09	6	Structure proposed for compounds: P30-P32 
			292.1543	C ₁₆ H ₂₂ NO ₄	0.99	7	
			250.1074	C ₁₃ H ₁₆ NO ₄	-1.25	6.5	
			215.0803	C ₁₃ H ₁₁ O ₃	2.33	8.5	
			116.107	C ₆ H ₁₄ NO	1.65	0.5	
			72.0808	C ₄ H ₁₀ N	4.63	0.5	
			56.0495	C ₃ H ₆ N	-9.32	1.5	

Table 3.2. (Continued)

Compound		R _t (min)	Ion Mass (m/z)	Ion formula	Error (ppm)	DBE	Proposed structure
P31	c—s	5.97	310.1649	C ₁₆ H ₂₄ NO ₅	1.79	6	Structure proposed for compounds: P30-P32 
			292.1543	C ₁₆ H ₂₂ NO ₄	0.36	7	
			274.1438	C ₁₆ H ₂₀ NO ₃	1.98	7.5	
			264.1600	C ₁₅ H ₂₂ NO ₃	5.09	5.5	
			215.0803	C ₁₃ H ₁₁ O ₃	4.57	8.5	
			177.0552	C ₁₀ H ₉ O ₃	-0.66	6.5	
			161.0603	C ₁₀ H ₉ O ₂	-2.85	6.5	
			133.0653	C ₉ H ₉ O	12.43	5.5	
			116.107	C ₆ H ₁₄ NO	-0.14	0.5	
			98.0964	C ₆ H ₁₂ N	9.53	1.5	
			72.0808	C ₄ H ₁₀ N	-7.18	0.5	
			56.0495	C ₃ H ₆ N	-14.39	1.5	
			P32	c—s	6.49	310.1649	
292.1543	C ₁₆ H ₂₂ NO ₄	0.56				7	
274.1438	C ₁₆ H ₂₀ NO ₃	5.05				7.5	
264.1600	C ₁₅ H ₂₂ NO ₃	5.49				5.5	
250.1079	C ₁₃ H ₁₆ NO ₄	9.11				6.5	
215.0803	C ₁₃ H ₁₁ O ₃	-2.77				8.5	
177.0552	C ₁₀ H ₉ O ₃	-0.02				6.5	
161.0603	C ₁₀ H ₉ O ₂	6.1				6.5	
133.0653	C ₉ H ₉ O	1.7				5.5	
116.107	C ₆ H ₁₄ NO	-1.37				0.5	
98.0964	C ₆ H ₁₂ N	-10.7				1.5	
72.0808	C ₄ H ₁₀ N	2.93				0.5	
56.0495	C ₃ H ₆ N	-3.48				1.5	

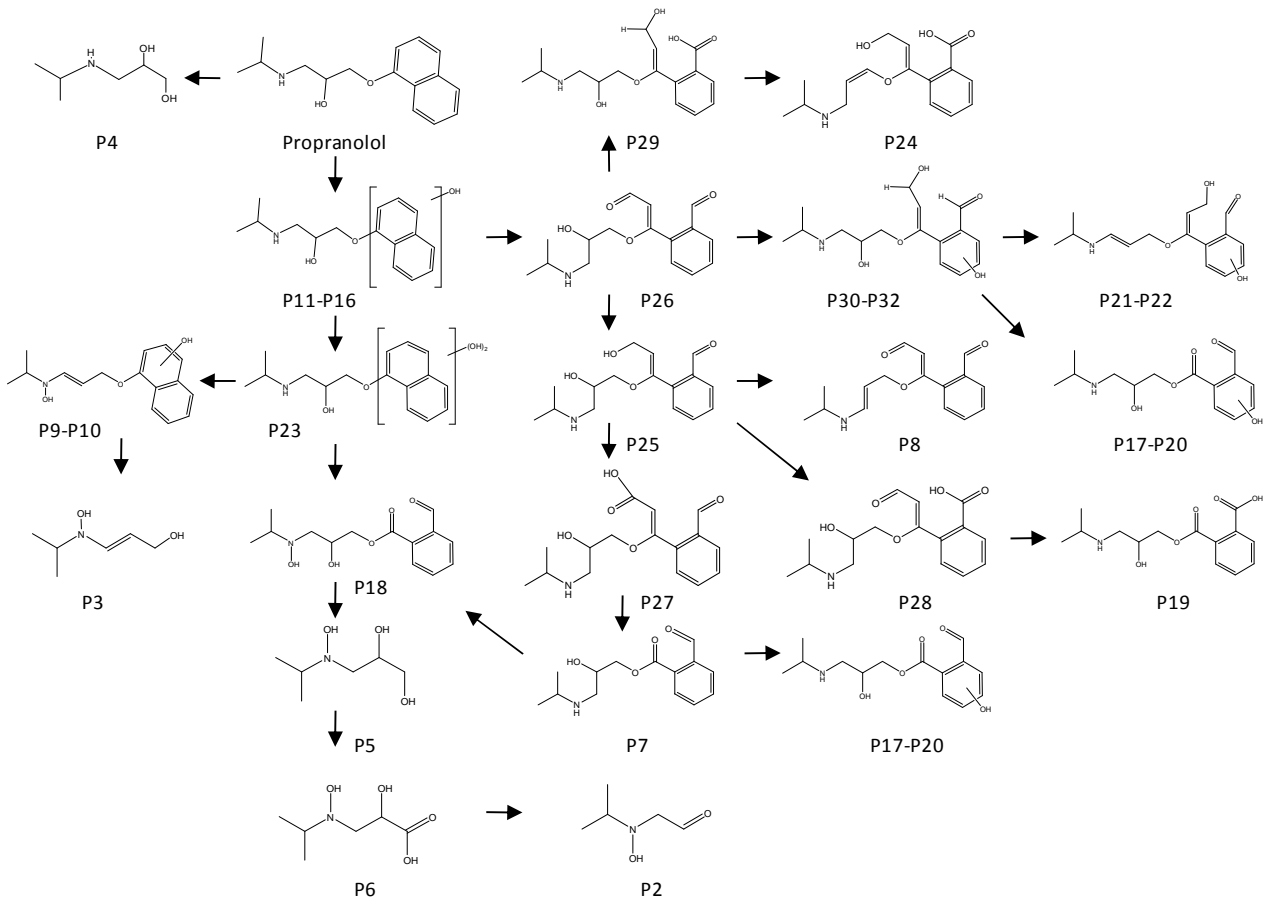


Figure 3.6. Proposed degradation pathway for propranolol.

in Fig. 3.6. Compounds P2, P3, P5 and P21 were only encountered in samples from photocatalytic runs, the rest having been detected in all samples.

The relative abundance of the main identified compounds is given in Fig. 3.7. The most abundant transformation product obtained in photocatalytic runs was P4 (m/z 134.1176, C₆H₁₆NO₂), which is attributed to the cleavage of the ether bond of propranolol. Yang et al. (2010) studied the TiO₂ photocatalytic degradation of propranolol (and other β -blockers) and found that the main degradation products corresponded to hydroxylated forms or the parent molecule. They detected several monohydroxylated and polyhydroxylated isomers as well as the product of the ether cleavage. The latter resulted in the formation of naphthol and an intermediate whose protonated form was detected at m/z 134 assumed to be an aminodiol with ion formula (C₆H₁₆NO₂), which corresponds with P4. The addition of hydroxyl groups to the aromatic nuclei was probably the first step in the degradation pathway. The first photoproducts identified in this study were the isomers P11-P16 (C₁₆H₂₂NO₃, m/z 276.1594), which represent the addition of 16 mass units to the parent compound, imputable to monohydroxylated intermediates. P11-P16, however, represented only a very low amount of the whole set of transformation products detected in photocatalytic runs, none of them being among the fourteen displaying higher chromatographic areas and included in Fig 3.7 a and b. In contrast, P11, P13 and P14 were measured in relatively high amounts in the photoproducts of solar irradiation (Fig. 3.7 c and d). The main products of photocatalysis retaining the structure of propranolol were P26 (m/z 294.1700, C₁₆H₂₄NO₄), P27 (m/z 308.1492, C₁₆H₂₂NO₅), and P29 (m/z 310.1649, C₁₆H₂₄NO₅) all of which are the consequence of the ring-opening attack of hydroxyl radicals on the naphthol moiety.

Some other fragments from the ether bond cleavage were detected in photocatalytic runs, namely P2 (m/z 118.0863, C₅H₁₂NO₂), P3

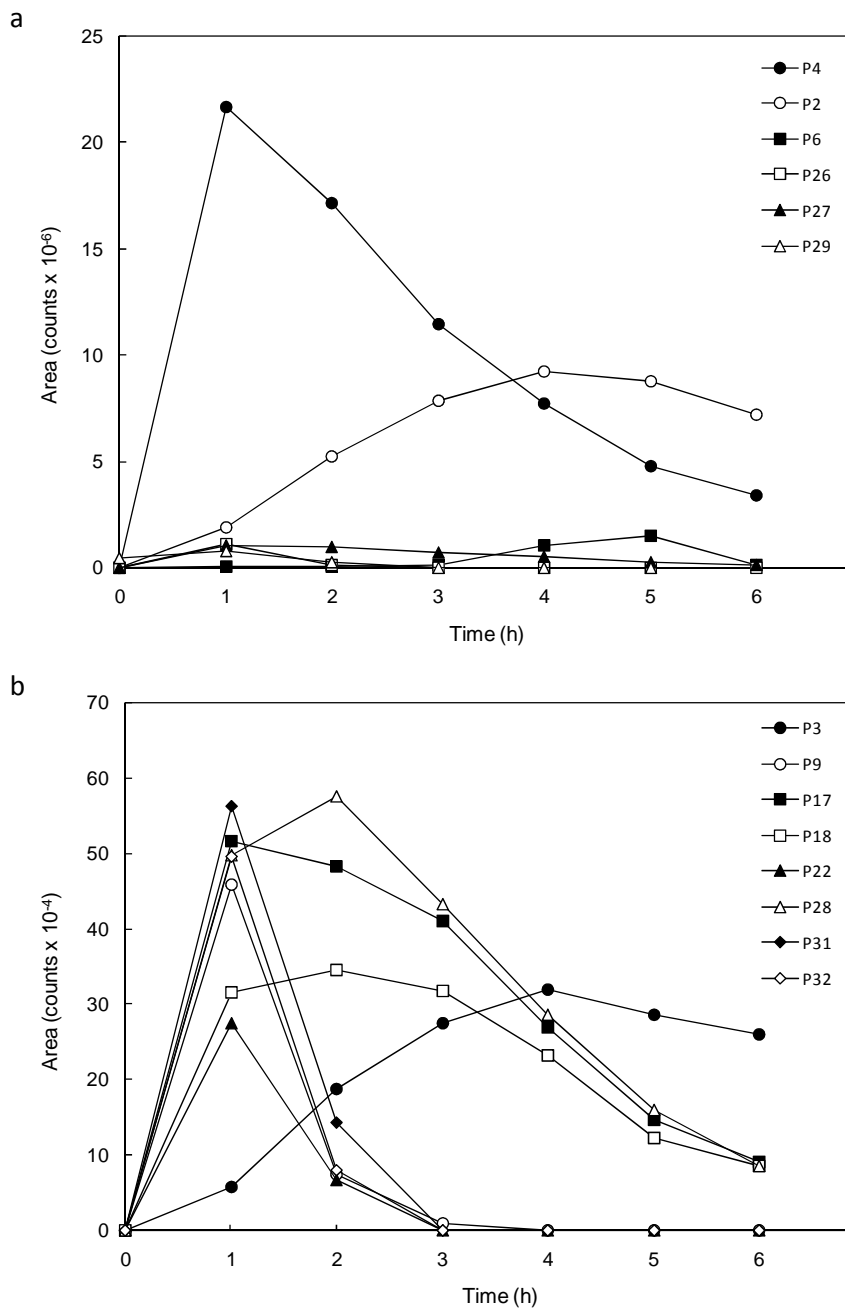


Figure 3.7. Chromatographic areas of the main transformation product from photocatalytic (a, b) and solar irradiation runs (c, d).

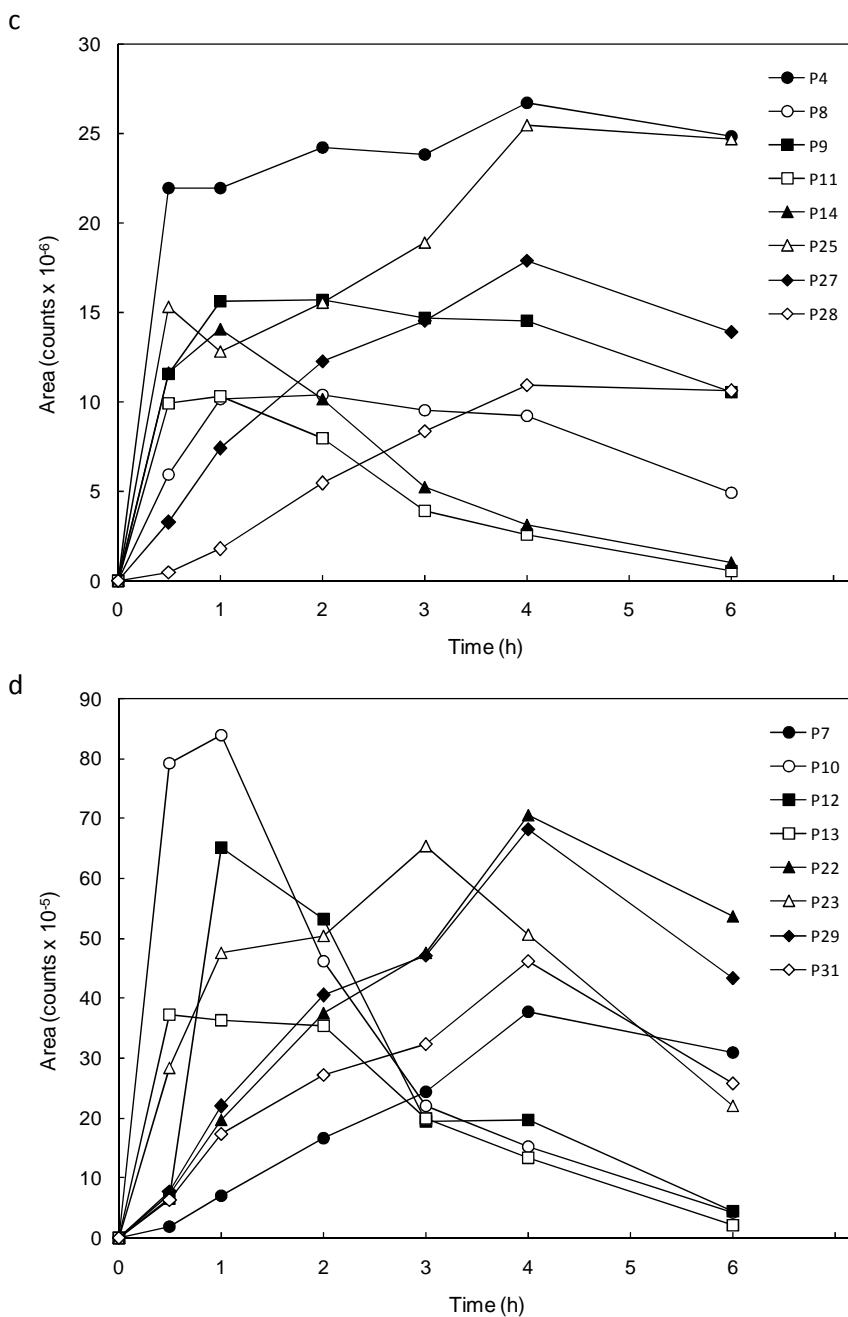


Figure 3.7. Chromatographic areas of the main transformation product from photocatalytic (a, b) and solar irradiation runs (c, d). (Continued)

(m/z 132.1019, $C_6H_{14}NO_2$), P5 (m/z 150.1125, $C_6H_{16}NO_3$) and P6 (m/z 164.0917, $C_6H_{14}NO_4$), some of which were absent in non-catalytic runs. Non-catalytic solar irradiation yielded a considerably higher amount of the more complex transformation products. These included, the hydroxylated transformation products P9 and P10 (m/z 274.1438, $C_{16}H_{20}NO_3$), with a hydroxyl group in the aromatic moiety but in which the amine had been oxidized to a hydroxylamine. P25 (m/z 292.1543, $C_{16}H_{22}NO_4$) is a naphthol ring-opening product which was detected in much higher amounts in solar runs than in photocatalytic oxidation. In general, solar irradiation led to a higher accumulation of hydroxylated and polyhydroxylated intermediates (such as P23, m/z 292.1543, $C_{16}H_{22}NO_4$) in spite of a lower formation of ether cleavage products. This might be attributed to the higher oxidizing power of the photocatalytic system, which prevents the accumulation of the first oxidation intermediates. Moreover, compounds such as P4, P9 and P28, among others, tended to accumulate in the solar irradiated mixture, while exhibiting a maximum in photocatalytic runs followed by a decrease after a period of 1-3 h on stream. This is a consequence of the enhanced oxidation capacity of the photocatalytic system in comparison with pure solar irradiation.

Liu and William (2007) and Liu et al. (2009) studied the photodegradation of propranolol by radiation in the 295-800 nm range and determined that the main transformation product was an isomer of m/z 292 (protonated), for which they proposed a ring-opening structure. In this study, we also found a series of ring-opening products, namely P21, P22, P24 or P25 as well as a hydroxylation derivative, P23, all of them with m/z 292.1543, P25 being similar to Liu's proposal except for a different ring-opening position. Romero et al. (2010) studied the TiO_2 photocatalytic degradation of propranolol using visible light radiation (Romero et al., 2011). They identified four reaction intermediates, of which m/z 266, 282 and 292 corresponded to our compounds P7, P18 and P25. For the others, at m/z 308, we proposed a different structure (P27-P28, $C_{16}H_{22}NO_5$) with a

carboxylic acid instead of a hydroxylamine. This is justified by the presence of the characteristic fragments C₆H₁₂N and C₁₀H₇O₃ that could not be explained otherwise. It is interesting to note that similar compounds can be obtained as a consequence of biological degradation. Marco Urrea et al. (2010) studied the biological advanced oxidation of propranolol using the extracellular oxidizing species produced by the fungus *Trametes versicolor*. The main degradation products were identified as monohydroxylated derivatives from the hydroxyl radical attack on the naphthalene moiety and would correspond to our P11-P16 set.

3.4.3. Toxicity of partially oxidized mixtures

Fig. 3.8 shows the growth inhibition of *Pseudokirchneriella subcapitata* when exposed to propranolol and partially irradiated mixtures. Growth was completely inhibited both in pure water and spiked wastewater for untreated propranolol solutions, as their concentration was considerably higher than the EC₅₀ value, which is 0.77 mg/L (Liu et al., 2009). The irradiation of propranolol decreased the toxicity towards the growth of *P. subcapitata* leading to essentially non-toxic mixtures after 2 h in the presence of 0.14 g/L of Ce-TiO₂ (0.5 Ce wt. %). For non-catalytic irradiation, the detoxification led to growth inhibition of < 5% after 4 h (Fig. 3.8a). The effect of the presence of the catalyst was much more marked when using spiked wastewater as matrix. In this case, irradiation led to growth inhibition of still 16% after 6h, whereas the photocatalytic process removed most of the toxicity within the first two hours (Fig. 3.8b). In Fig. 3.8b, we also represented the toxicity of irradiated wastewater that inhibited algal growth by 8%, which increased up to some 25% for prolonged exposures. It is interesting to note that during the first hour of treatment of propranolol spiked wastewater, there was no noticeable effect on mixture toxicity, which is due to the lower rate of oxidation or photodegradation in the presence of the compounds dissolved in wastewater.

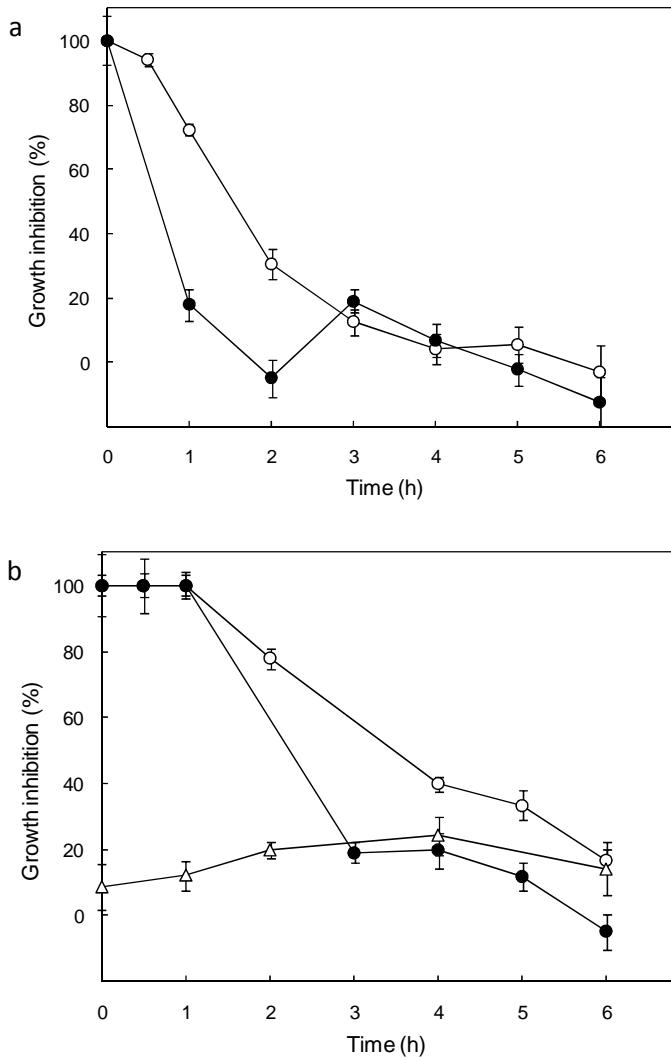


Figure 3.8. Growth inhibition of *P. subcapitata* during irradiation (○) and photocatalytic treatment of propranolol (●, 0.14 g/L, Ce-TiO₂ 0.5 % wt. cerium) in (a) pure water and (b) spiked wastewater. (Δ): toxicity of non-spiked wastewater during irradiation.

Fig. 3.9 shows the results obtained for the marine bacteria *Vibrio fischeri*. Escher et al. (2006) determined a median effect value of 81 mg/L for 30 min contact time of propranolol with *V. fischeri*. Propranolol toxicity is much lower than for the green alga and represented a 15% inhibition for

the untreated solution in pure water. The toxic effect of propranolol also increased the background toxicity of wastewater, but only to a modest 10% till about 55% bioluminescence inhibition. The non-catalytic irradiation of propranolol, either in pure water or in wastewater, resulted in a moderate toxicity reduction.

The photocatalytic degradation of propranolol in pure water, however, led to a sharp bioluminescence decrease, which reached almost 80%. The fact that a similar treatment in wastewater matrix did not cause a similar toxicity peak was probably due to the accumulation of transformation products such as P17 or P28. The results with *P. subcapitata* (Fig 3.8a) also show that photocatalytic treatments induce a significant increase in toxicity after about 3 h of treatment. The higher toxicity of partially oxidized mixtures was probably the consequence of the formation of ring-opening products, as these are the kinds of compound that have been associated in the past with increased toxicity in partially

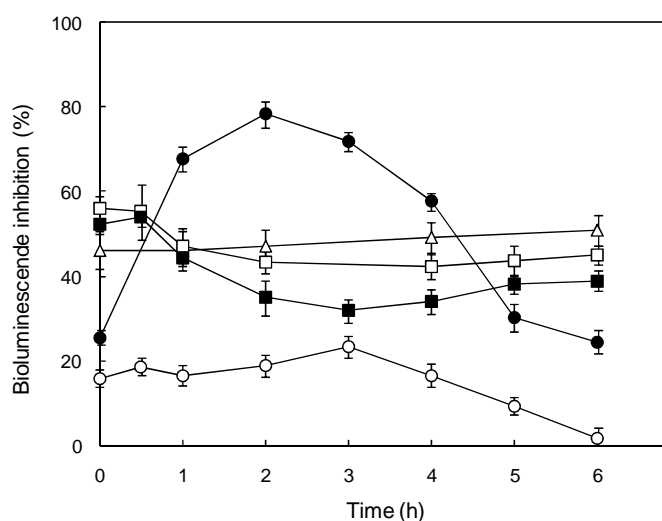


Figure 3.9. Bioluminescence inhibition (30 min) of *V. fischeri* during irradiation (○, □) and photocatalytic treatment of propranolol (●, ■, 0.14 g/L, Ce-TiO₂ 0.5 % wt. cerium) in pure water (circles) and spiked wastewater (squares). (Δ): toxicity of non-spiked wastewater during irradiation.

oxidized mixtures (Rosal et al., 2009; Santiago et al., 2011).

Liu et al. (2009) used the alga *Pseudokirchneriella subcapitata* and the rotifer *Brachionus calyciflorus* to conclude that propranolol yields phototransformation products that would generally be less toxic because of their higher polarity and hydrophilicity compared to the parent compound. On the other hand, the formation of toxic or non-degradable compounds during the early stages of propranolol irradiation or photocatalytic oxidation has been suggested elsewhere. Romero et al. (2011) showed that the biodegradability of visible light irradiated samples increased with time, but only after a period of several hours. During the photocatalytic treatment of propranolol using TiO_2 , Ioannou et al. (2011) found that the toxicity of treated mixtures to *Daphnia magna* increased during the first part of the reaction to progressively decrease thereafter. This implies the formation of toxic transformation compounds that could be eliminated upon prolonged irradiation.

3.5. Conclusions

The visible light photocatalytic degradation of propranolol can be carried out using cerium doped titanium dioxide. The results showed that, for a cerium loading of 0.5 % wt. with a bulk catalyst concentration of 0.14 g/L, propranolol became essentially depleted after 1.5 hours of irradiation. In contrast, 8% of initial propranolol remained in solution after 6 h of photolytic (non-catalytic) treatment. The effect was related to an increased light absorption in the visible region of cerium doped TiO_2 .

The contribution of hydroxyl radicals to propranolol degradation was assessed using pCBA as hydroxyl radical probe. A kinetic competition approach allowed determination of the rate constant for the photocatalytic oxidation of propranolol in catalyst holes. Thus, it was estimated that 60% of the photocatalytic reaction took place through surface holes (h^+), the rest being mediated by hydroxyl radicals.

Experiments carried out in biologically treated wastewater spiked with propranolol showed a very low rate for the photocatalytic process compared with pure water. This could be attributed to the presence of radical scavengers but also to substances competing for surface adsorption.

Over thirty reaction intermediates were detected by means of exact mass measurements performed by LC-ESI-QTOF-MS/MS. The main transformation products could be attributed to the cleavage of the ether bond of propranolol, while other compounds derived from the addition of hydroxyl groups to the aromatic nuclei or to the ring-opening attack of hydroxyl radicals on the naphthol moiety.

The toxicity of oxidized mixtures determined using the green algae *P. subcapitata* and bioluminescent marine bacterium *V. fischeri* showed the formation of toxic transformation products, which accumulated in runs performed in pure water, for which the photocatalytic reaction rate was much higher.

3.6. Nomenclature

C_i, C_j	concentration of a given organic compound, mol L ⁻¹
C_s	bulk concentration of solids in the liquid phase, kg L ⁻¹
$C_{\bullet OH}$	concentration of hydroxyl radicals, mol L ⁻¹
B	peak width in XRD, nm
I_o	fluence rate at reactor wall, W m ⁻²
k_{dr}, k_{ir}, k	first order rate constants, s ⁻¹
$k_{\bullet OH}$	second order rate constant for the reaction with hydroxyl radicals, M ⁻¹ s ⁻¹
k_{ht}	first-order rate constant for the reaction with catalyst holes, s ⁻¹
k_T	kinetic constant of the photocatalytic process, mol W ⁻¹ s ⁻¹ (if $m = 1$)
K	equilibrium constant, L mol ⁻¹
K_S	Scherrer constant, dimensionless

L	crystallite size, nm
$LVRPA$	Local Volumetric Rate of Photon Absorption, $W L^{-1}$
r_d	rate of direct photolysis, $mol L^{-1} s^{-1}$
r_i	homogeneous rate of photocatalysis, $mol L^{-1} s^{-1}$

Greek letters

δ	optical path, m
κ	specific absorption coefficient, $m^{-2} kg^{-1}$
κ_i	extinction coefficient for compound i , $M^{-1} m^{-1}$
λ	wavelength, Å or nm
σ	specific scattering coefficient, $m^{-2} kg^{-1}$
ω	scattering albedo, $\sigma/(\sigma+\kappa)$, dimensionless

3.7. References

- Akpan, U. and Hameed, B., 2010. The advancements in sol-gel method of doped-TiO₂ photocatalysts. *Applied Catalysis A: General* 375, 1-11.
- Allen, J.M., Allen, S.K. and Baertschi, S.W., 2000. 2-Nitrobenzaldehyde: a convenient UV-A and UV-B chemical actinometer for drug photostability testing. *Journal of Pharmaceutical and Biomedical Analysis* 24, 167-178.
- American Public Health Association (APHA), 2005. American Water Works Association (AWWA) & Water Environment Federation (WEF), Standard Methods for the Examination of Water and Wastewater, 21st Edition, Washington, D.C.
- Benner, J., Salhi, E., Ternes, T. and von Gunten, U., 2008. Ozonation of reverse osmosis concentrate: Kinetics and efficiency of beta blocker oxidation. *Water Research* 42, 3003-3012.
- Braun, A.M., Maurette, M.-T. and Oliveros, E., 1986. *Technologie photochimique*, Presses polytechniques romandes Lausanne, Switzerland.
- Crane, M., Watts, C. and Boucard, T., 2006. Chronic aquatic environmental risks from exposure to human pharmaceuticals. *Science of the Total Environment* 367, 23-41.
- Dantas, R.F., Rossiter, O., Teixeira, A.K.R., Simoes, A.S.M. and da Silva, V.L., 2010. Direct UV photolysis of propranolol and metronidazole in aqueous solution. *Chemical Engineering Journal* 158, 143-147.

- Dialynas, E., Mantzavinos, D. and Diamadopoulos, E., 2008. Advanced treatment of the reverse osmosis concentrate produced during reclamation of municipal wastewater. *Water research* 42, 4603-4608.
- Dimitroula, H., Daskalaki, V.M., Frontistis, Z., Kondarides, D.I., Panagiotopoulou, P., Xekoukoulotakis, N.P. and Mantzavinos, D., 2012. Solar photocatalysis for the abatement of emerging micro-contaminants in wastewater: Synthesis, characterization and testing of various TiO₂ samples. *Applied Catalysis B: Environmental* 117, 283-291.
- Doll, T.E. and Frimmel, F.H., 2005. Removal of selected persistent organic pollutants by heterogeneous photocatalysis in water. *Catalysis Today* 101, 195-202.
- Dong, M.M. and Rosario-Ortiz, F.L., 2012. Photochemical formation of hydroxyl radical from effluent organic matter. *Environmental Science & Technology* 46, 3788-3794.
- Elovitz, M.S. and von Gunten, U., 1999. Hydroxyl radical/ozone ratios during ozonation processes. I. The Rct concept. *Ozone: Science & Engineering* 21, 239-260.
- Escher, B.I., Bramaz, N., Richter, M. and Lienert, J., 2006. Comparative ecotoxicological hazard assessment of beta-blockers and their human metabolites using a mode-of-action-based test battery and a QSAR approach. *Environmental Science & Technology* 40, 7402-7408.
- Gabet-Giraud, V., Miège, C., Choubert, J., Ruel, S.M. and Coquery, M., 2010. Occurrence and removal of estrogens and beta blockers by various processes in wastewater treatment plants. *Science of the Total Environment* 408, 4257-4269.
- Galbavy, E.S., Ram, K. and Anastasio, C., 2010. 2-Nitrobenzaldehyde as a chemical actinometer for solution and ice photochemistry. *Journal of Photochemistry and Photobiology A: Chemistry* 209, 186-192.
- Gora, A., Toepfer, B., Puddu, V. and Li Puma, G., 2006. Photocatalytic oxidation of herbicides in single-component and multicomponent systems: Reaction kinetics analysis. *Applied Catalysis B: Environmental* 65, 1-10.
- Huggett, D., Khan, I., Foran, C. and Schlenk, D., 2003. Determination of beta-adrenergic receptor blocking pharmaceuticals in United States wastewater effluent. *Environmental Pollution* 121, 199-205.
- Ioannou, L., Hapeshi, E., Vasquez, M., Mantzavinos, D. and Fatta-Kassinos, D., 2011. Solar/TiO₂ photocatalytic decomposition of β -blockers atenolol and propranolol in water and wastewater. *Solar Energy* 85, 1915-1926.
- Isarain-Chavez, E., Cabot, P.L., Centellas, F., Rodriguez, R.M., Arias, C., Garrido, J.A. and Brillas, E., 2011. Electro-Fenton and photoelectro-Fenton degradations of the drug beta-blocker propranolol using a Pt anode: Identification and

- evolution of oxidation products. *Journal of Hazardous Materials* 185, 1228-1235.
- Kim, I., Yamashita, N. and Tanaka, H., 2009. Photodegradation of pharmaceuticals and personal care products during UV and UV/H₂O₂ treatments. *Chemosphere* 77, 518-525.
- Kümmerer, K., 2004. *Pharmaceuticals in the environment: sources, fate, effects and risks*, Springer Verlag.
- Li, F., Li, X., Hou, M., Cheah, K. and Choy, W., 2005. Enhanced photocatalytic activity of Ce³⁺-TiO₂ for 2-mercaptobenzothiazole degradation in aqueous suspension for odour control. *Applied Catalysis A: General* 285, 181-189.
- Li Puma, G. and Brucato, A., 2007. Dimensionless analysis of slurry photocatalytic reactors using two-flux and six-flux radiation absorption–scattering models. *Catalysis Today* 122, 78-90.
- Li Puma, G., Toepfer, B. and Gora, A., 2007. Photocatalytic oxidation of multicomponent systems of herbicides: Scale-up of laboratory kinetics rate data to plant scale. *Catalysis Today* 124, 124-132.
- Li, S., Wang, Q., Chen, T., Zhou, Z., Wang, Y. and Fu, J., 2012. Study on cerium-doped nano-TiO₂ coatings for corrosion protection of 316 L stainless steel. *Nanoscale Research Letters* 7, 1-9.
- Liu, Q.-T. and Williams, H.E., 2007. Kinetics and degradation products for direct photolysis of β -blockers in water. *Environmental Science & Technology* 41, 803-810.
- Liu, Q.T., Williams, T.D., Cumming, R.I., Holm, G., Hetheridge, M.J. and Murray Smith, R., 2009. Comparative aquatic toxicity of propranolol and its photodegraded mixtures: algae and rotifer screening. *Environmental Toxicology and Chemistry* 28, 2622-2631.
- Mack, J. and Bolton, J.R., 1999. Photochemistry of nitrite and nitrate in aqueous solution: a review. *Journal of Photochemistry and Photobiology A: Chemistry* 128, 1-13.
- Malato, S., Blanco, J., Vidal, A. and Richter, C., 2002. Photocatalysis with solar energy at a pilot-plant scale: an overview. *Applied Catalysis B: Environmental* 37, 1-15.
- Marco-Urrea, E., Radjenović, J., Caminal, G., Petrović, M., Vicent, T. and Barceló, D., 2010. Oxidation of atenolol, propranolol, carbamazepine and clofibrac acid by a biological Fenton-like system mediated by the white-rot fungus *Trametes versicolor*. *Water research* 44, 521-532.
- Maurer, M., Escher, B.I., Richle, P., Schaffner, C. and Alder, A.C., 2007. Elimination of beta-blockers in sewage treatment plants. *Water Research* 41, 1614-1622.

- Maycock, D.S. and Watts, C.D., 2011. In J.O.N. (ed), Encyclopedia of Environmental Health, Elsevier, Burlington, pp. 472-484,
- Mehrotra, K., Yablonsky, G.S. and Ray, A.K., 2003. Kinetic studies of photocatalytic degradation in a TiO₂ slurry system: Distinguishing working regimes and determining rate dependences. *Industrial & Engineering Chemistry Research* 42, 2273-2281.
- Muñoz, I., Rieradevall, J., Torrades, F., Peral, J. and Domènech, X., 2005. Environmental assessment of different solar driven advanced oxidation processes. *Solar Energy* 79, 369-375.
- Muñoz, I., Rodríguez, A., Rosal, R. and Fernández-Alba, A.R., 2009. Life Cycle Assessment of urban wastewater reuse with ozonation as tertiary treatment: a focus on toxicity-related impacts. *Science of the Total Environment* 407, 1245-1256.
- OECD, 2011. Test No. 201: Freshwater Alga and Cyanobacteria, Growth Inhibition Test. OECD Guidelines for the Testing of Chemicals. Section 2 OECD Publishing.
- Ollis, D.F., 1991. Photochemical conversion and storage of solar energy, pp. 593-622, Springer.
- Postigo, C., Sirtori, C., Oller, I., Malato, S., Maldonado, M.I., López de Alda, M. and Barcelo, D., 2011. Photolytic and photocatalytic transformation of methadone in aqueous solutions under solar irradiation: Kinetics, characterization of major intermediate products and toxicity evaluation. *Water research* 45, 4815-4826.
- Romero, V., De la Cruz, N., Dantas, R.F., Gimenez, P.M.J. and Esplugas, S., 2011. Photocatalytic treatment of metoprolol and propranolol. *Catalysis Today* 161, 115-120.
- Rosal, R., Rodriguez, A., Perdigon-Melon, J.A., Mezcua, M., Hernando, M.D., Leton, P., Garcia-Calvo, E., Agüera, A. and Fernandez-Alba, A.R., 2008. Removal of pharmaceuticals and kinetics of mineralization by O₃/H₂O₂ in a biotreated municipal wastewater. *Water Research* 42, 3719-3728.
- Rosal, R., Gonzalo, M.S., Boltes, K., Letón, P., Vaquero, J.J. and García-Calvo, E., 2009. Identification of intermediates and assessment of ecotoxicity in the oxidation products generated during the ozonation of clofibrac acid. *Journal of Hazardous Materials* 172, 1061-1068.
- Rosal, R., Rodríguez, A., Perdigón-Melón, J.A., Petre, A., García-Calvo, E., Gómez, M.J., Agüera, A. and Fernández-Alba, A.R., 2010. Occurrence of emerging pollutants in urban wastewater and their removal through biological treatment followed by ozonation. *Water research* 44, 578-588.
- Rosenfeldt, E.J., Linden, K.G., Canonica, S. and von Gunten, U., 2006. Comparison of the efficiency of center dot OH radical formation during ozonation and

the advanced oxidation processes O₃/H₂O₂ and UV/H₂O₂. *Water Research* 40, 3695-3704.

Santiago, J., Agüera, A., del Mar Gómez-Ramos, M., Fernández Alba, A.R., García-Calvo, E. and Rosal, R., 2011. Oxidation by-products and ecotoxicity assessment during the photodegradation of fenofibric acid in aqueous solution with UV and UV/H₂O₂. *Journal of Hazardous Materials* 194, 30-41.

Silva, A.M.T., Silva, C.G., Drazic, G. and Faria, J.L., 2009. Ce-doped TiO₂ for photocatalytic degradation of chlorophenol. *Catalysis Today* 144, 13-18.

Song, W.H., Cooper, W.J., Mezyk, S.P., Greaves, J. and Peake, B.M., 2008. Free radical destruction of beta-blockers in aqueous solution. *Environmental Science & Technology* 42, 1256-1261.

International Organization for Standardization, 2007. Water Quality-Determination of the Inhibitory Effect of Water Samples on the Light Emission of *Vibrio fischeri* (Luminescent Bacteria Test). ISO 11348-3 revised version. Geneva, Switzerland.

Stengl, V., Bakardjieva, S. and Murafa, N., 2009. *Materials Chemistry and Physics* 114, 217-226.

Ternes, T.A., 1998. Occurrence of drugs in German sewage treatment plants and rivers. *Water Research* 32, 3245-3260.

Yang, H., An, T.C., Li, G.Y., Song, W.H., Cooper, W.J., Luo, H.Y. and Guo, X.D., 2010. Photocatalytic degradation kinetics and mechanism of environmental pharmaceuticals in aqueous suspension of TiO₂: A case of beta-blockers. *Journal of Hazardous Materials* 179, 834-839.

Chapter 4

Oxidative and photochemical processes for the removal of galaxolide and tonalide from wastewater

Oxidative and photochemical processes for the removal of galaxolide and tonalide from wastewater^{*}

4.1. Abstract

Synthetic musks have been reported in wastewaters at concentrations as high as tens of micrograms per litre. The two most significant polycyclic musk fragrance compounds are 1,3,4,6,7,8-hexahydro-4,6,6,7,8,8-hexamethylcyclopenta(g)-2-benzopyran (HHCb, trade name galaxolide[®]) and 7-acetyl-1,1,3,4,4,6 hexamethyltetrahydronaphthalene (AHTN, trade name tonalide[®]). We report the result of several irradiation and advanced oxidation processes carried out on samples of the effluent of a wastewater treatment plant located in Alcalá de Henares, Madrid. Wastewater samples were pre-ozonated and spiked with 500 ng/L of tonalide or galaxolide in order to obtain final concentrations in the same order as the raw effluent. The treatments assayed were ozonation with and without the addition of hydrogen peroxide (O_3 , O_3/H_2O_2), ultraviolet (254 nm low pressure mercury lamp) and xenon-arc visible light irradiation alone and in combination with ozone (UV, O_3/UV , Xe, O_3/Xe) and visible light photocatalytic oxidation using a Ce-doped titanium dioxide

^{*} The contents of this chapter have been published as:

Santiago-Morales, J., Gómez, M. J., Herrera, S., Fernández-Alba, A. R., García-Calvo, E., Rosal, R., 2012. Oxidative and photochemical processes for the removal of galaxolide and tonalide from wastewater. *Water research* 46, 4435-4447.

photocatalyst performed under continuous oxygen or ozone gas bubbling ($O_2/Xe/Ce-TiO_2$, $O_3/Xe/Ce-TiO_2$). In all cases, samples taken at different contact times up to 15 min were analyzed. An analytical method based on stir-bar sorptive extraction (SBSE), followed by comprehensive two-dimensional gas chromatography (SBSE-GC×GC-TOF-MS), was used for the automatic searching and evaluation of the synthetic musks and other nonpolar or semipolar contaminants in the wastewater samples. In all cases tonalide was more easily removed than galaxolide. The best results for the latter (more than 75% removal after 5 min on stream) were obtained from ozonation (O_3) and visible light photocatalytic ozonation ($O_3/Xe/Ce-TiO_2$). A significant removal of both pollutants (~60% after 15 min) was also obtained during visible light photocatalysis ($O_2/Xe/Ce-TiO_2$). UV radiation was able to deplete tonalide (+90%) after 15 min but only reduced the concentration of galaxolide to about half of its initial concentration. The toxicity of treated samples decreased for O_3/UV and $O_3/Ce-TiO_2$, but increased during irradiation processes UV, Xe and $Xe/Ce-TiO_2$. Ozone treatments tend to decrease toxicity up to a certain dosage, from which point the presence of toxic transformation products has adverse effects on aquatic microorganisms.

4.2. Introduction

Synthetic musks are currently manufactured and used in large amounts for incorporation in a wide variety of personal care products. Their role is to fix fragrances by slowing down the release of volatiles (Reiner and Kannan, 2006). Synthetic musks comprise a wide variety of substances, of which only nitro, polycyclic and macrocyclic derivatives have achieved any commercial importance. They are artificial substances which do not occur in the nature and do not share chemical or structural relationship with natural musks. Currently, nitro musks, a family comprising musk xylene and musk ketone, are being gradually displaced by polycyclic derivatives, which account for about three-quarters of the

worldwide market (Sommer, 2004). Of these, 1,3,4,6,7,8-hexahydro-4,6,6,7,8,8-Hexamethyl cyclopenta(g)-2-benzopyran (HHCB, galaxolide®) and 7-acetyl 1,1,3,4,4,6-hexamethyltetrahydronaphthalene (AHTN, tonalide®) are by far the two largest volume products, representing about 95% of the EU market and 90% of the US market for all polycyclic musks (Clara et al., 2011).

The widespread use of synthetic musks leads to their release to the environment in large amounts through the discharge of wastewater treatment plants (WWTP). Rosal et al. (2010a) measured values of up to 25 µg/L of HHCB and 1.9 µg/L of AHTN in the influent of a wastewater treatment plant, very high figures compared with the 30 ng/L found for celestolide and 6 ng/L for traseolide. As a consequence, HHCB is one of the most abundant xenobiotic in untreated wastewater together with caffeine, its metabolite paraxanthine and the non-steroidal anti-inflammatory drug acetaminophen. According to their non-polar character, the removal efficiency of these compounds is high in conventional activated sludge WWTP, but their high concentration still leads to occurrences in the microgram per litre range in treated effluents (Bester, 2004; Ternes et al., 2007; Lv et al., 2010). In comparison, the average concentration of musk xylene and musk ketone has been found in the 50–100 ng/L range (Rosal et al., 2010a). Synthetic musks have also been detected in similar concentrations in environmental samples (Gómez et al., 2012). Bester (2005) reported concentrations of up to 600 ng/L of polycyclic musks in the River Ruhr at the discharge point of a WWTP. In the part of the same river where drinking water is extracted, he found 60 ng/L HHCB and 10 ng/L AHTN. These are typical values for rivers in populated areas. In Korean surface waters, Lee et al. (2010) reported concentrations in the 100–272 ng/L range for HHCB and 30–52 ng/L for AHTN. Synthetic musks are persistent compounds, a fact stressed by Schmid et al. (2007) who investigated their presence in lipid-based fish tissue from remote Alpine lakes. Although at levels far below those for fish from lakes and rivers

receiving effluents of WWTP, HHCB and AHTN as well as other nitro and polycyclic musks were nonetheless still detectable on account of their entrance by atmospheric precipitation.

It has been shown that the biotransformation of HHCB into HHCB-lactone takes place in WWTP operating with activated sludge (Bester, 2004). The same author reported 20–30 ng/L HHCB-lactone in the River Ruhr at considerable distances from WWTP discharge points (Bester, 2005). HHCB-lactone was found in all samples taken from the River Henares (Madrid, Spain), with a profile along the river course similar to its parent compound HHCB. HHCB-lactone was found in the water samples at a comparable concentration or even higher than those for HHCB (Gómez et al. 2012). This metabolite has been identified in fish and water samples by other groups (Franke et al., 1999; Kallenborn et al., 2001). HHCB-lactone was found in all wastewater samples in the United States at concentrations in the 146-4000 ng/L range and in sludge at 3.16-22.0 mg/kg dry weight (Reiner et al., 2007). Besides its biological origin, some HHCB-lactone is included in the technical galaxolide product, so it can also be found at the plant entrance. While HHCB and AHTN concentrations decreased during treatment, the concentrations of HHCB-lactone increased in water after treatment from an average of 505 ng/L (897 ng/L) in the influent to 1620 ng/L (1740 ng/L) in the effluent of two WWTP receiving domestic (domestic and industrial) discharges in New York State (Reiner et al., 2007). Recently, Janzen et al. (2011) identified HHCB-lactone as transformation product from the ozonation of HHCB in pure water.

In spite of concern due to their persistence and potential to bioaccumulate, the toxicity and environmental risks of these chemicals have been usually regarded as low (Salvito, 2005). However, it has been demonstrated that nitro musks can behave as co-genotoxicants (Mersch-Sundermann et al., 2001) and musk xylene has been included in the Candidate List of Substances of Very High Concern of the European

Chemicals Agency. Luckenbach and Epel (2005) showed that nitro and polycyclic musks can inhibit the activity of multidrug efflux transporters responsible for multixenobiotic resistance in the gills of a marine mussel (*Mytilus californianus*). Nitro musks were more effective inhibitors than polycyclic musks, with combined IC_{50} values of $0.82 \pm 0.53 \mu\text{M}$ for nitro musks and $2.34 \pm 0.82 \mu\text{M}$ for polycyclic musks. Moreover, a long term inhibition of efflux transporters results in the continued accumulation of normally excluded toxicants even after direct exposure to the musk has ended.

In this work, an analytical method based on stir-bar sorptive extraction (SBSE), followed by comprehensive two-dimensional gas chromatography (SBSE-GC \times GC-TOF-MS) was used for the evaluation of synthetic musks (Balthussen et al., 1999). This technique has recently been proposed as a tool for the multiresidue analysis of priority and emerging contaminants in waters with excellent results in terms of separation efficiency, analysis time and detection limits (Prieto et al., 2007; Gómez et al., 2011). The depletion of HHCB and AHTN in biologically treated wastewaters spiked with environmentally relevant concentrations of both compounds was tracked. The treatments assayed were ozonation with and without the addition of hydrogen peroxide (O_3 , O_3/H_2O_2), ultraviolet (254 nm low pressure mercury lamp) and xenon-arc visible light irradiation alone and in combination with ozone (UV, O_3/UV , Xe, O_3/Xe) and visible light photocatalytic oxidation using a cerium-doped titanium dioxide photocatalyst performed under continuous oxygen or ozone gas bubbling ($O_2/Xe/Ce-TiO_2$, $O_3/Xe/Ce-TiO_2$). In all cases, we analyzed samples taken at different contact times up to 15 min and monitored their toxicity for the microcrustacean *Daphnia magna*, the green alga *Pseudokirchneriella subcapitata* and the marine bacterium *Vibrio fischeri*.

4.3. Methodology

4.3.1. Materials

Galaxolide and tonalide were purchased from Dr. Ehrenstorfer (Augs-burg, Germany). The reagents used for the analyses were analytical grade methanol and sodium chloride (> 99.5 %) supplied by J.T. Baker (Deventer, Holland) and analytical grade water from Fluka (Buchs, Switzerland). The solutions in pure water were prepared with water obtained from a Milipore Mili-Q system with a resistivity of at least $18 \text{ M}\Omega \text{ cm}^{-1}$ at 25 °C. The rest of the chemicals (purity > 95%) were purchased from Sigma-Aldrich. Wastewater samples were taken from the output of the secondary clarifier of a WWTP located in Alcalá de Henares (Madrid). The plant treats a mixture of domestic and industrial wastewater from facilities located near the city and has a nominal capacity of $3000 \text{ m}^3/\text{h}$ of raw wastewater. Additional details are given elsewhere (Rosal et al., 2010a). Prior to the runs, wastewater aliquots were filtered using $0.45 \mu\text{m}$ glass fibre filters, analyzed and, for runs involving the use of ozone, pre-ozonated according to the procedure described below. For runs involving catalyst in suspension, treated samples were filtered prior to the analyses using the same $0.45 \mu\text{m}$ glass fibre filters. The main wastewater parameters are listed in Table 4.1. The samples were spiked before treatments with 500 ng/L of galaxolide or tonalide to ensure final concentrations below one microgram per liter, which represents the lower range of concentration in treated wastewater (Rosal et al., 2010a).

The photocatalyst was a ceria-doped TiO_2 with 0.5% wt. of cerium prepared by sol–gel method. The synthesis was as follows. Solution A was prepared by adding 10 mL $\text{Ti}(\text{O-Pr})_4$ to 50 mL ethanol. Solution B was prepared by dissolving 0.1842 g of $(\text{NH}_4)_2\text{Ce}(\text{NO}_3)_6$ in 10 mL ultrapure water and then immediately adding 40 mL ethanol and 10 mL glacial acetic acid under vigorous stirring. Solution A was then added dropwise to solution B, sonicated, dried at 100 °C and calcined in air at 670°C for 1 h. The catalyst

had a surface area (BET) of 29 m²/g and average pore size (BJH, desorption) of 6.3 nm. The catalyst had a mean particle size of 547 ± 33 nm as determined by Dynamic Light Scattering and a ζ-potential of -49.6 ± 0.7 mV, which dropped to -16.7 ± 0.8 mV when dispersed in raw wastewater

Table 4.1. Wastewater characterization parameters for raw and pre ozonated effluent

Parameters	raw wastewater	pre-ozonated effluent
pH	7.79 (in situ)	n.a.
TSS (mg/L)	20 (as received)	n.a.
Dissolved oxygen (mg/L)	8.7 (in situ)	n.a.
Conductivity (μS/cm)	875	802
Turbidity (NTU)	2.5	1.4
COD (mg/L)	28	20
NPOC (mg/L)	8.1	4.7
Hardness (mg/L CaCO ₃)	219	221
N-NO ₃ (mg/L)	9.8	10.5
N-NH ₄ (mg/L)	0.8	0.7
SUVA 254 nm	1.7 × 10 ⁻²	8.7 × 10 ⁻³
<i>Anions and cations</i>		
Sulphate (mg/L)	79.9	80.1
Chloride (mg/L)	80.6	81.9
Phosphate (mg/L)	2.6	2.7
Sodium (mg/L)	70.5	70.2
Potassium (mg/L)	14.9	15.8
Magnesium (mg/L)	21.6	21.6
Calcium (mg/L)	52.2	53.0
<i>Metals (μg/L)</i>		
Chromium	13	
Cobalt	1.8	
Copper	1.7	
Lead	0.49	
Manganese	0.92	
Molybdenum	4.3	
Nickel	12.3	
Strontium	560	
Tin	0.29	
Titanium	0.93	
Vanadium	1.1	
Zinc	34	

n.a.: not analyzed

and to -14.0 ± 0.9 mV in pre-ozonated wastewater. The catalyst absorbed radiation from 290 nm (Pyrex cut-off). The band gap energy of the photocatalyst as obtained by UV/VIS spectroscopy was 2.63 eV (470 nm), 90 nm higher than anatase. The unit cell parameters of Ce-TiO₂ were calculated from X-ray diffraction (XRD) considering that TiO₂ anatase belongs to the tetragonal system, whose unit cell parameters comply with the equation $1/d_{hkl}^2 = (h^2+k^2)/a^2 + l^2/c^2$. The diffraction peaks from (1 0 1) and (0 0 4) planes were used, obtaining values of $a = b = 3.78$ Å and $c = 9.49$ Å, which essentially coincide with those for pure anatase.

4.3.2. Experimental setup and procedure

A scheme of the experimental setup for ozonation and irradiation is given in Fig. 4.1. Ozone was produced by a corona discharge and continuously bubbled throughout the run. Further details are given elsewhere (Rosal et al., 2008a). Irradiation experiments were performed

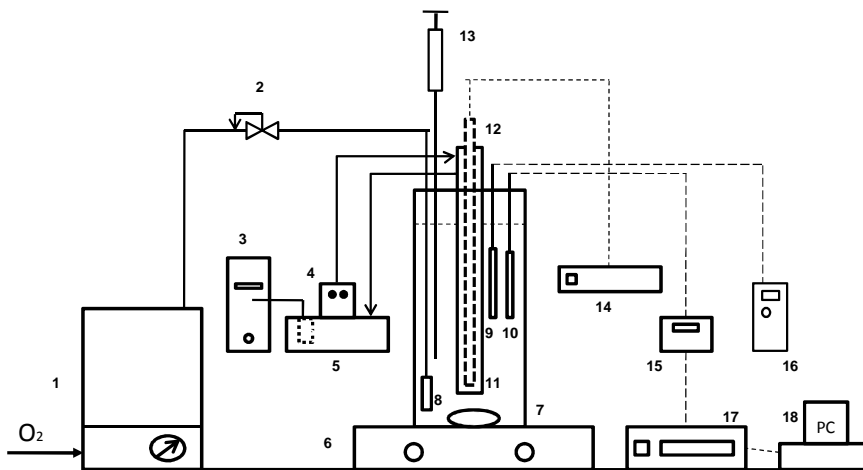


Figure 4.1. Experimental equipment: 1, ozone generator; 2, flow control; 3, cooling device; 4, thermostat; 5, bath; 6, magnetic stirrer; 7, reactor; 8, diffuser; 9, pH electrode; 10, ozone sensor; 11, cooling tube; 12, lamp; 13, sampling device; 14, power supply; 15, ozone analyzer; 16, pH control unit; 17, data acquisition unit; 18, PC.

using a 15W Heraeus Noblelight TNN 15/32 low-pressure mercury vapour lamp emitting at 254 nm and a Heraeus TQ Xe 150, Xe-arc lamp with spectral emission in the visible region. For visible light irradiation, an additional Pyrex tube acted as a filter absorbing wavelengths lower than 290 nm. The lamp sleeve was equipped with a quartz cooling tube in which the lamps were fitted and was refrigerated by means of a thermostatic bath. The temperature was kept at 25°C in all cases. Actinometric measurements allowed the fluence rates per unit volume to be determined: $6.01 \times 10^{-6} \text{ E L}^{-1} \text{ s}^{-1}$ for the low pressure mercury lamp and $1.05 \times 10^{-6} \text{ E L}^{-1} \text{ s}^{-1}$ for the Xe-arc lamp. As chemical actinometers, hydrogen peroxide for the mercury lamp and 2-nitrobenzaldehyde for the Xe-arc lamp, were used, the latter method basically recording the near UV part of the spectra in the 290-400 nm range (Nicole et al., 1990; Allen et al., 2000).

The experiments were carried out in batch mode in a vessel (1.3 L) agitated with a magnetic stirrer at 900 min^{-1} . Samples were taken for analysis at prescribed intervals. In ozonation runs the dissolved ozone was removed using sodium thiosulfate except for those samples used to measure the concentration of HHCB, AHTN and HHCB-lactone, in which ozone was stripped by bubbling nitrogen in order to avoid interferences with the analytical procedure. For all experiments pH was controlled at 7.5 within ± 0.1 units and close to the value measured in raw wastewater. The catalyst, when used, was loaded at a concentration of 200 mg/L and agitated 30 min prior to the run in order to equilibrate surface charge. In ozonation runs, galaxolide and tonalide were dissolved in wastewater previously ozonated under the same conditions used for the runs until ozone appeared in solution. The reason for this procedure was to avoid interferences due to the presence of organic compounds which react rapidly with ozone (Rosal et al., 2010b). This would have kept ozone absent from the bulk and reaction would have taken place at the interface or in the liquid film. In these conditions, the exposure to hydroxyl radicals is not defined as it refers to the bulk (Buffle et al., 2006a). Besides, non-polar

compounds tend to accumulate at the gas-liquid interface, so it was preferred to spike wastewater by the moment of appearing ozone in solution. Additional runs were performed in pure water using a 2 mM phosphate buffer at pH 7.5 prepared from 0.2 M $\text{NaH}_2\text{PO}_4 \cdot 2\text{H}_2\text{O}$ and 0.2 M Na_2HPO_4 solutions to avoid pH drift. Table 4.2 summarizes the experimental conditions used in this work.

Table 4.2. Summary of experimental conditions used in this work.

No. and description	Process conditions
<i>Processes involving homogeneous ozone</i>	
1 O_3	Gas flow $0.19 \text{ N m}^3 \text{ h}^{-1}$ $C_{\text{O}_3(\text{g})} 22 \text{ g Nm}^{-3}$
2 $\text{O}_3/\text{H}_2\text{O}_2$	H_2O_2 (30 %) 30 $\mu\text{L/L}$ at 0 min and 7.5 min Ozone as in (1)
3 O_3/UV	15W Heraeus Noblelight TNN 15/32 mercury lamp Fluence rate $6.01 \times 10^{-6} \text{ E L}^{-1} \text{ s}^{-1}$ (254 nm)
4 O_3/Xe	Heraeus TQ Xe 150, Xe-arc lamp Fluence rate $1.05 \times 10^{-6} \text{ E L}^{-1} \text{ s}^{-1}$ (290-400 nm)
<i>Catalytic and Photocatalytic processes</i>	
5 $\text{O}_3/\text{Ce-TiO}_2$	200 mg/L catalyst agitated 30 min prior to the run Ozone as in (1)
6 $\text{O}_3/\text{Xe/Ce-TiO}_2$	Ozone as in (1) Irradiation as in (4) Catalyst as in (5)
7 Xe/Ce-TiO_2	Concentration of dissolved oxygen 31-33 mg/L kept throughout the treatment Irradiation as in (4) Catalyst as in (5)
8 Xe/Ce-TiO_2 (Raw wastewater)	Matrix: 0.45 μm filtered effluent Irradiation as in (4) Catalyst as in (5) Dissolved oxygen as in (7)
<i>Photolytic processes without ozone</i>	
9 UV	Irradiation as in (3)
10 UV (Raw wastewater)	Matrix: 0.45 μm filtered effluent Irradiation as in (3)
11 Xe	Irradiation as in (4)
12 Xe (Raw wastewater)	Matrix: 0.45 μm filtered effluent Irradiation as in (4)

4.3.3. Analyses

The analyses of water samples were carried out by stir-bar sorptive extraction (SBSE) followed by comprehensive two-dimensional gas chromatography (GC×GC-TOF-MS). Treated and untreated wastewater samples were extracted with 20 mm (length) x 0.5 mm (film thickness) PDMS commercial stir bars (Gerstel, Muelheim an der Ruhr, Germany). The coated stir bars were thermally desorbed using a thermal desorption unit (Gerstel) connected to a programmed temperature vaporization (PTV) system injector CIS-4 (Gerstel) by a heated transfer line at 300 °C. The PTV injector was installed in a GC×GC-TOF-MS system (Agilent 7890A gas chromatograph, equipped with an additional oven and a quad-jets modulator (two cold jets and two hot jets). Liquid nitrogen used for cooling was automatically filled from a 60 L Dewar liquid nitrogen storage tank. The first column was a 10 m x 0.18 mm i.d., 0.2 µm film thickness Rtx-5 coated with 5% diphenyl 95% dimethyl polysiloxane (Restek). The second column was a 1 m x 0.1 mm i.d., 0.10 µm film thickness Rxi-17 coated with 50% diphenyl 50% dimethylpolysiloxane (Restek). The MS system was a Pegasus 4D TOF (LECO Corporation). Details concerning the performance of the analytical method as well as sample preparation can be found elsewhere (Gómez et al., 2011). A hybrid triple quadrupole/Linear Ion Trap mass spectrometer system (5500 QTRAP® LC/MS/MS, AB Sciex Instruments, Foster City, CA) coupled to an HPLC, Agilent 1200 (Agilent Technologies, Wilmington, DE, USA) with an electrospray interface was used for the structural elucidation of HHBC-lactone using ozonated or irradiated mixtures of HHBC diluted in pure water. The analytical column employed was a reversed-phase C8 of 150 mm x 4.6 mm and 5 µm particle size (Agilent ZorbaxEclipse XDB). Details on the analytical procedure have been given elsewhere (Martínez-Bueno et al., 2011). The analyses of p-chlorobenzoic acid (pCBA) were performed by HPLC using an Agilent 1200 apparatus equipped with a reversed phase Kromasil 5u 100A C18 analytical column. The mobile phase (flow rate 1mL/min) was a 40:60 mixture of

water containing 4mL/L of orthophosphoric acid and 50 mL/L of methanol and acetonitrile. UV detection was carried out at 280 nm.

Non Purgeable Organic Carbon (NPOC) was determined by means of a Shimadzu TOC-VCSH total carbon organic analyzer. Anions were determined using a Metrohm 861 Advance Compact IC with suppressed conductivity detector and a Metrosep A Supp 7-250 analytical column with 36 mM Na₂CO₃ as eluent with a flow of 0.8 mL min⁻¹. Cations were quantified by means of a Metrosep C3 column using 5.0 mM HNO₃ as eluent with a flow of 1 mL min⁻¹. The content of trace metals in the wastewater was assessed by Inductively Coupled Plasma-Mass Spectrometry using a quadrupole mass spectrometer Agilent 7700X operating at 3 MHz in helium cell gas mode. The concentration of ozone dissolved in the aqueous phase was monitored with an amperometric Mettler Toledo 358/210 dissolved ozone sensor calibrated using the Indigo Colorimetric Method (SM 4500-O3 B). The signal was transmitted to a Mettler Toledo Thornton M300 and finally monitored and recorded using an Agilent 34970 Data Acquisition Unit connected to a computer. The concentration of ozone in gas phase was determined using an Anseros Ozomat GM6000 Pro photometer calibrated against potassium iodide.

The catalyst was characterized by x-ray diffraction (XRD) using a Seifert 3000P diffractometer (Cu K α , $\lambda = 1.5406 \text{ \AA}$). The BET specific surface was determined by nitrogen adsorption at 77 K using a SA 3100 Beckman Coulter Analyzer. The size distribution of catalyst particles (< 5000 nm) was obtained using dynamic light scattering (DLS, Malvern Zetasizer Nano ZS). Zeta potential was measured via electrophoretic light scattering combined with phase analysis light scattering in the same instrument. The measurements were conducted at 25°C using 2 mM phosphate buffer at pH 7.5 as the dispersing medium. The absorbance of the photocatalyst was measured using a UV/VIS/NIR Perkin Elmer Lambda 900 spectrometer equipped with integrating sphere.

4.3.4. Toxicity assessment

The toxicities of raw, spiked and treated wastewater samples were assessed using the following bioassays: multigenerational growth inhibition of the green alga *Pseudokirchneriella subcapitata*, the inhibition of the constitutive luminescence of the marina bacterium *Vibrio fischeri*, and the immobilization of the microcrustacean *Daphnia magna*. This amounts to the combination of acute and multigenerational assays and the combined use of prokaryotic and eukaryotic organisms at two trophic levels. Phenol, ZnSO₄ and K₂Cr₂O₇ have been used as toxicity standards and all tests have been replicated to ensure reproducibility and in order to obtain acceptable confidence intervals.

The algal growth inhibition test followed the procedure described in OECD TG 201 *P. subcapitata* open system (OECD, 2011). Prior to the test hydrogen peroxide was removed using 5 µL of catalase solution 5000 mg/L (3691 U/mg bovine liver obtained from Sigma-Aldrich) per 1 mL of sample. This procedure removed excess H₂O₂ in O₃/H₂O₂ and the H₂O₂ that could have been produced as secondary oxidant in other processes. The cultures used the OECD growth medium at pH adjusted to 8.0 ± 0.1. Algal cells were first cultured in 25 mL agitated flasks. The prescribed amount of cells was transferred to 96-well clear disposable microplates and exposed to pollutants during the logarithmic growth phase. The total volume occupied was 220 µL, each well containing 180 µL of sample, 20 µL of a concentrated OECD growth medium and 10 µL of microalgae. The microplates were placed in an algal growth chamber under continuous fluorescent illumination (approximately 100 µE m² s⁻¹), and incubated at 22 ± 1 °C. The growth of *P. subcapitata* was monitored daily for 72 h and assessed by chlorophyll fluorescence (Excitation 444 nm – Emission 680 nm) using a Fluoroskan Ascent FL plate fluorometer-luminometer.

Bioassays with the photo luminescent bacteria *V. fischeri* were carried out according to ISO 11348-3 standard protocol (International

Organization for Standardization, 2007). This bioassay measures the decrease in bioluminescence due to the presence of a toxic substance. The commercial Biofix Lumi test (Macherey-Nagel, Germany) was used. The measurements were performed at $16.5 \pm 0.8^\circ\text{C}$ using a Fluoroskan Ascent FL plate luminometer. The effect of toxics was measured as percentage of inhibition with respect to the light emitted in the absence of any toxic influence after 30 min exposure. In treated wastewater, the reference was always the same wastewater after adjusting osmotic pressure.

Acute immobilization tests with *D. magna* were conducted following the standard protocol described in the European Guideline OECD TG 202 (OECD, 2004). The *D. magna* bioassay used a commercially available test kit (Daphtoxkit F™ magna, Creasel, Belgium). The dormant eggs were incubated in standard culture medium imitating natural fresh water at $20 \pm 1^\circ\text{C}$ under continuous illumination of 6000 lx in order to induce hatching. Between hatching and test steps, the daphnids were fed with the microalga *Spirulina* to avoid mortality during tests. Neonates were incubated for 48 h in the dark at 20°C , the pH of samples being adjusted to the tolerance interval of this organism (Seco et al. 2003). Acute toxicity was assessed by observing the mobility of *D. magna*: the neonates were considered immobilized if they lay on the bottom of the test plate and did not resume swimming within 15 s.

4.4. Results and discussion

4.4.1. Efficiency of hydroxyl radical formation during ozonation and irradiation processes

The removal of dissolved organics by ozone is due to the combination of direct and indirect reactions, the latter essentially being reactions with hydroxyl radicals. Elovitz and von Gunten (1999) proposed a parameter R_{ct} to characterize the ozonation process by measuring the

exposure to hydroxyl radicals. They defined a ratio between integral ct -exposures to hydroxyl radicals and ozone as follows:

$$R_{ct} = \frac{\int_0^t c_{HO^\bullet} dt}{\int_0^t c_{O_3} dt} \quad (1)$$

The parameter can be readily obtained using a *p*-chlorobenzoic acid (*p*CBA) as probe compound since its direct ozonation rate constant is negligible. The R_{ct} parameter depends on matrix composition and can be applied to evaluate the efficiency of ozonation and ozone-based disinfection processes in natural waters (Elovitz and von Gunten, 1999). Its suitability for wastewaters has been shown in previous works (Rosal et al., 2008b & 2010a). It has also been determined that hydroxyl radical exposure may be very high during the initial phase of ozonation runs. In fact, before ozone appears in solution during the fast kinetic regime, there is a significant exposure which cannot be measured using Eq. 1. The initial phase also contributes to a high proportion of the ozone consumption but, as a consequence of the low concentration of dissolved ozone, it accounts for a small or negligible proportion of the overall ozone-exposure. R_{ct} decays thereafter and attains a steady state once the slow kinetic regime has been achieved (Buffle et al., 2006b). This two-period pattern is particularly clear in waters with low concentration of radical scavengers for which R_{ct} can be several orders of magnitude higher during the first ozonation period.

In this work, R_{ct} was measured before and after the second minute on stream, which was the time necessary to ensure slow kinetic regime in all ozonation runs (Rosal et al., 2010a). The corresponding data are given in the lower part of Fig. 4.2 for O_3 and O_3/H_2O_2 homogeneous systems; for catalytic, $O_3/Ce-TiO_2$, and photocatalytic, $O_3/Xe/Ce-TiO_2$ ozonation and for the photolytic treatments O_3/Xe and O_3/UV . The results depicted in Fig 4.2 were obtained by spiking wastewater with up to 1 mg/L of *p*CBA in phosphate buffered pure water, identified as “pure water”, and in pre-

ozonated wastewater prepared as described above. In pure water runs, the rapid decay of pCBA meant sufficient data could not be obtained in order to evaluate R_{ct} under slow kinetic regime. Generally, R_{ct} values were much lower in wastewater than in pure water due to the presence of bicarbonates and other radical scavengers. As expected, O_3/H_2O_2 and O_3/UV resulted in higher values of R_{ct} as both H_2O_2 and UV accelerate the decomposition of ozone and provide an additional source of hydroxyl radicals. The combined use of ozone and radiation (O_3/UV) led to the highest R_{ct} values, in both pure water and in wastewater, whereas for the rest the values observed were in the 10^{-7} - 10^{-8} range and exhibited the typical two-phase pattern described before. The combined use of ozone

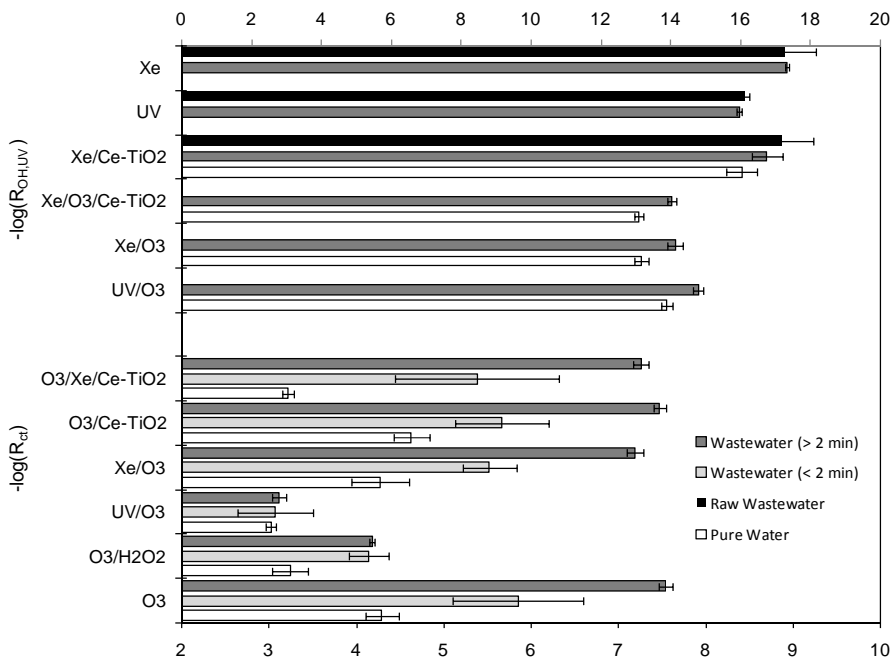


Figure 4.2. Radical exposure parameters R_{ct} and $R_{OH,UV}$ for ozone and radiation-based processes in pure water and wastewater. (Note that higher values of $-\log(R_{ct})$ or $-\log(R_{OH,UV})$ represent lower generation of hydroxyl radicals.)

and visible radiation (O₃/Xe) including photocatalysis (O₃/Xe/Ce-TiO₂) did not result in any significant reduction of R_{ct} in wastewater samples, although the effect of Ce-TiO₂ was apparent in pure water, with R_{ct} for O₃/Xe/Ce-TiO₂ one order of magnitude higher for non-catalytic O₃/Xe and catalytic O₃/Ce-TiO₂ ozonation. Most probably, the presence of oxidizable compounds and radical scavengers reduced the production of the hydroxyl radicals detected by pCBA.

The presence of HHCB and AHTN in spiked treated wastewater does not introduce any significant change in the slow/rapid kinetic regime pattern. These compounds were added in very small concentrations and their rate constant for the direct ozonation reaction were not high. Nöthe et al. (2007) determined rate constants for the reaction of HHCB and AHTN with molecular ozone of 8 M⁻¹ s⁻¹ and 140 M⁻¹ s⁻¹, respectively. The removal of both compounds due to stripping was not significant for the experimental conditions used in this work.

The radical exposure per fluence ratio due to irradiation, $R_{OH,UV}$, was determined according to the method proposed by Rosenfeldt et al. (2006):

$$R_{OH,UV} = \frac{\int_0^t c_{HO^\bullet} dt}{E_0 t} \quad (2)$$

where $R_{OH,UV}$ is the hydroxyl radical exposure per UV fluence expressed in (M L mW⁻¹) and E_0 the average UV fluence rate per unit volume (mW L⁻¹). pCBA was used as probe compound to determine the exposure to hydroxyl radicals as indicated elsewhere (Santiago et al., 2011). As shown in Fig. 4.2, $R_{OH,UV}$ was higher for photocatalytic and photolytic ozonation as a consequence of the dual mechanism of hydroxyl radical generation. The low, but quantifiable values obtained for $R_{OH,UV}$ under UV-filtered Xe irradiation were probably the result of the photolysis of nitrate (and nitrite), which is known to result in the formation of hydroxyl radicals (Mack and Bolton, 1999). Otherwise, no measurable formation of hydroxyl

radicals should be expected. In pure photolytic and photocatalytic processes Xe, UV and Xe/Ce-TiO₂, $R_{OH,UV}$ were almost constant throughout the runs in the 10⁻¹⁶ order; i.e., they did not exhibit the two-phase pattern observed in ozonation. The combined use of ozone and radiation reduced $R_{OH,UV}$ by about three orders of magnitude.

4.4.2. Removal of galaxolide and tonalide

In the wastewater samples used in this work, the concentrations of HHCB and AHTN were 1849 ng/L and 438 ng/L, respectively, dropping after pre-ozonation to 590 ng/L (HHCB) and 98 ng/L (AHTN). This represented a removal of ~ 70% for both compounds during the fast ozonation period before the ozone in solution was recorded. Fig. 4.3 (a and b) shows the variation in the relative concentrations of HHCB and AHTN in spiked wastewater throughout the treatments assayed in this work. For the sake of clarity, experimental errors are indicated as bars only in the case of xenon irradiation runs since this treatment did not result in any significant degradation of HHCB or AHTN. Error bars were calculated from the initial concentrations of HHCB and AHTN in samples directly taken from the reactor in the nine treatments assayed and therefore represent the variability associated with sample preparation and the analytical procedure. In all cases AHTN was more easily removed than HHCB, with a final concentration below 100 ng/L (representing > 90% removal efficiency) for O₃, O₃/UV, O₃/H₂O₂, O₃/Xe and for UV irradiation alone. The best removal efficiencies were obtained for HHCB in O₃, O₃/Xe and O₃/Xe/Ce-TiO₂, while UV-based processes, particularly UV photolysis gave poorer results with depletion close to 50% after 15 min of irradiation. It is interesting to note that catalytic ozonation did not result in better removal efficiencies for either compound, probably because of the low affinity of the catalyst surface with these non-polar compounds. The absence of adsorption of HHCB and AHTN was assessed by performing adsorption experiments under non-oxidizing conditions and analyzing samples taken

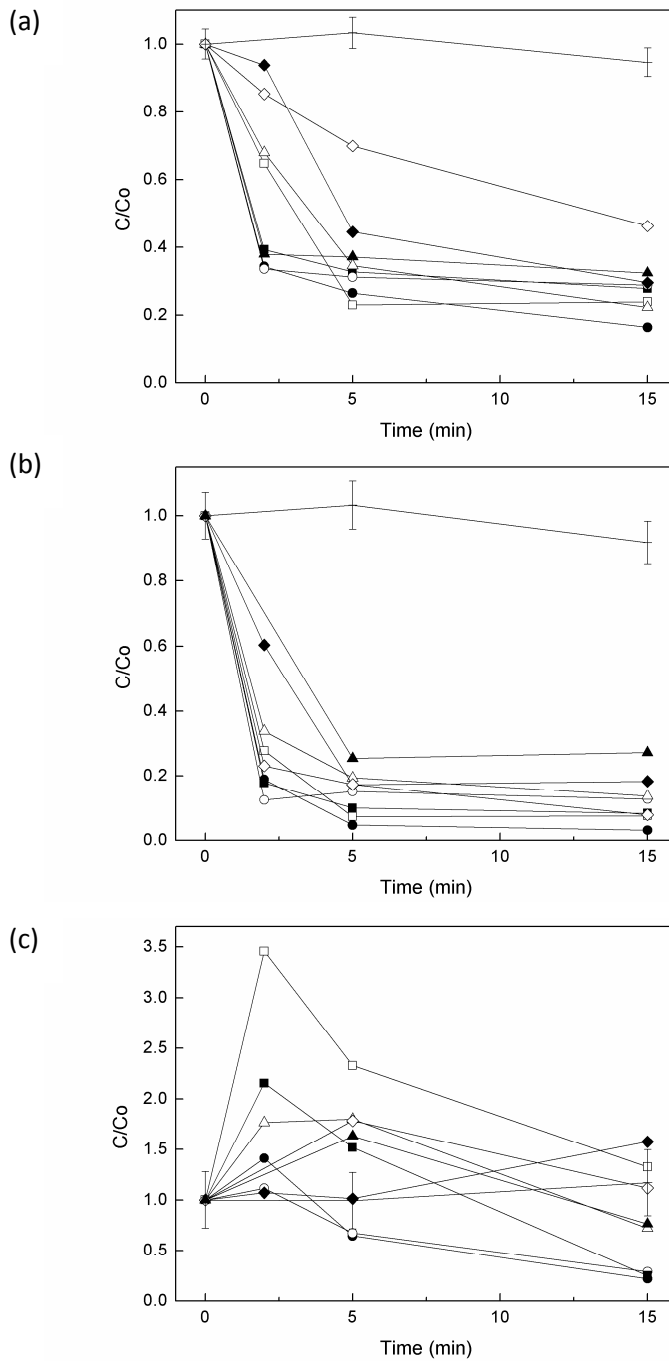


Figure 4.3. Concentration profiles for HHCB (a), AHTN (b) and HHCB-lactone (c) during the different treatments assayed: O_3 (●), O_3/H_2O_2 (○), O_3/UV (■), O_3/Xe (□), $O_3/Ce-TiO_2$ (▲), $O_3/Xe/Ce-TiO_2$ (Δ), $Xe/Ce-TiO_2$ (◆), UV (◇), Xe (+)

after the same period used for reactions. Xe/Ce-TiO₂ photocatalysis resulted in depletion of 71 % and 83% for HHCB and AHTN, respectively, in 15 min on stream, which was close to the values for ozone and UV irradiation-based treatments, which were considerably more efficient at generating hydroxyl radicals. Fig. 4.3c also shows the evolution of HHCB-lactone, the concentration of which was 250 ng/L in the spiked preozonated wastewater (103 ng/L in RWW). In most runs, but particularly for O₃/UV and O₃/Xe the concentration of HHCB-lactone increased during the first minutes on stream. This proved that HHCB-lactone was formed as an intermediate transformation product during the ozone treatment of effluents containing HHCB, but also during UV irradiation as observed in Fig. 4.3c. O₃, O₃/UV and O₃/H₂O₂ reduced HHCB-lactone concentrations by up to 25% of its initial value after 15 min.

Fig 4.4a displays the GC×GC contour plot with all the main compounds detected in the wastewater effluent represented as dots in a bidimensional plot in which the first (x-axis) and second (y-axis) dimensions represent retention times in a non-polar (Rtx-5) column and a polar (Rxi-17) column respectively. In this particular case, the signal-to-noise ratio was set to 10. For this application, in which several thousand compounds could be present in similar concentrations in the mixture, the choice of the second column was particularly critical as noted and discussed elsewhere (Gómez et al., 2011). The two-dimensional chromatogram allows both targeted and non-targeted compounds to be separated and identified. Fig. 4.4a also shows the mass spectra identification of HHCB, AHTN and HHCB-lactone, which in fact represent two isomers (cis- and trans- each with two enantiomers that could be resolved with the GC×GC technique at high dilution rates) with slightly different retention times, but perfectly separated in the bidimensional chromatogram. It can be observed that the deconvoluted mass spectra of the compounds in the acquired sample match the reference library spectra perfectly with a similarity score above 900. It is important to note that the resolution reached with the GC×GC

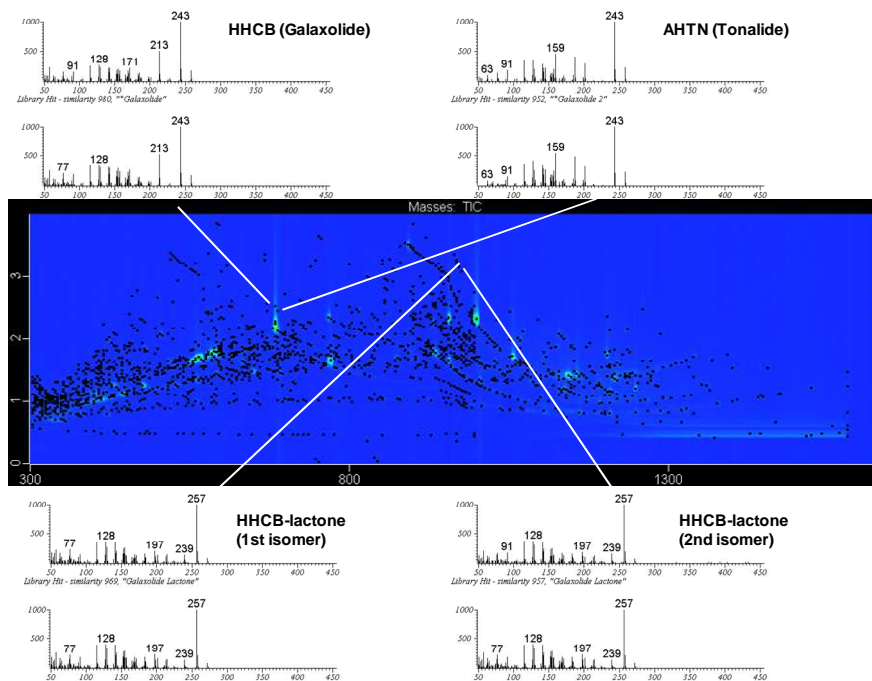


Figure 4.4. (a) GCxGC-TOFMS contour plot of spiked wastewater before treatment, showing the peaks and the spectra library searches for HHCB, AHTN and HHCB lactone. (b) GCxGC-TOFMS bubble plot showing temporal variation of target compounds.

technique allows most compounds to be separated from matrix components, a feature which is essential for their further identification in TOF-MS. The identification of HHCB-lactone was based on accurate mass measurements recorded by the LC-TOF-MS instrument described above operating in positive mode (ESI+). These measurements allowed elemental composition to be proposed for the protonated $[M+H]^+$ molecular ions and their characteristic ion fragments, so providing a high degree of confidence in structure assignment. The accurate mass measurements recorded for the protonated HHCB-lactone (m/z 273.1850 for $C_{18}H_{25}O_2$) offer an excellent agreement of 0.2 ppm error with calculated m/z value. The main fragments (at m/z 255.1743, 225.1274 and 197.1325) correspond to the

breaking of the benzopyrone moiety of HHCB-lactone with errors < 0.1, 4.8 and 6.5 ppm respectively.

The sequence of chromatograms represented in Fig. 4.4b displays the evolution of the target compounds HHCB, AHTN and HHCB-lactone during O_3/H_2O_2 . In order to visualize peak intensity in the two-dimensional image, a bubble-type plot was used in which the bubble radius is proportional to the relative area of the peak represented. It is relative because for each sample the maximum radius size is proportional to the most concentrated compound in it. The absence of background in Fig. 4.4b is due to the filtering of the mass-spectra in order to display target compounds only.

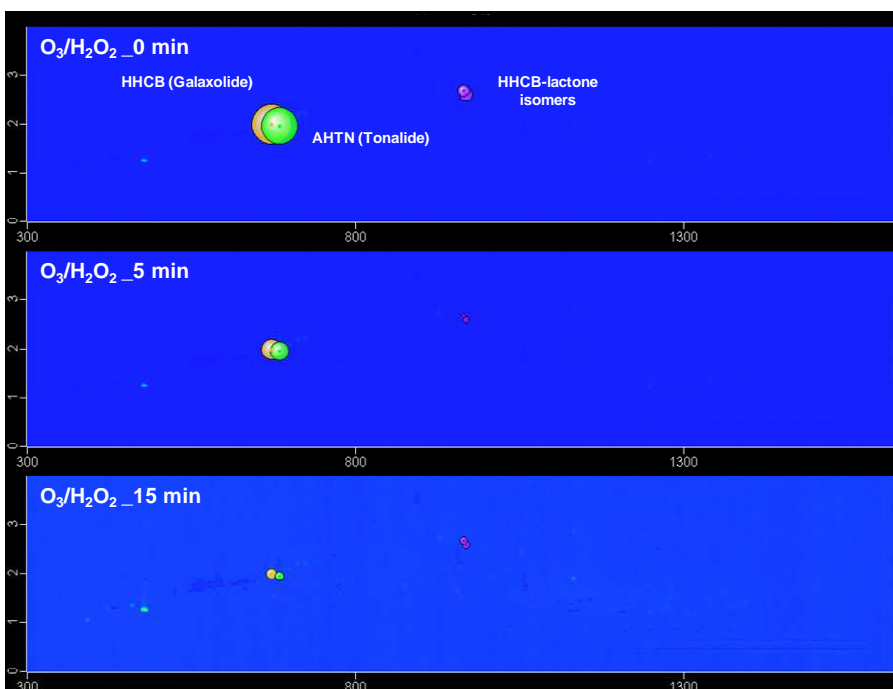


Figure 4.4. (b)- continued

4.4.3. Toxicity of raw and treated samples

Under the conditions of moderate TOC removal encountered in practical forms of AOP, the formation of transformation products with enhanced toxicity for aquatic organisms seems to be the rule rather than the exception (Rosal et al., 2009; Gómez-Ramos et al., 2011). Accordingly, in the runs reported in this work, organic carbon removal was not high. Measured as NPOC, it ranged from 2-15% after 15 min on stream except for O_3/H_2O_2 for which it reached ~40% in accordance with the oxidizing capacity of this system. Xe irradiation was also an exception, as no significant mineralization took place. The evolution of the toxicity of treated wastewater to *P. subcapitata* is shown in Fig. 4.5. The dotted line

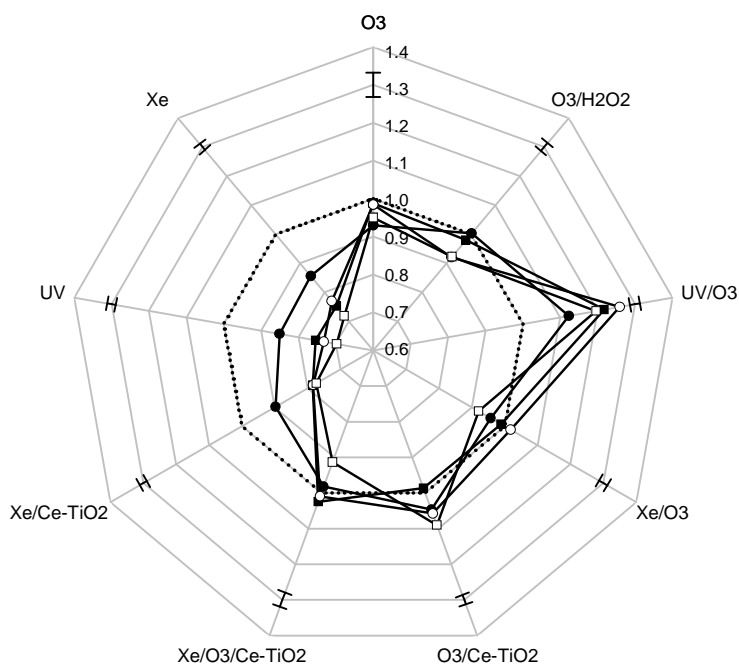


Figure 4.5. Toxicity of treated samples: relative growth rate of *P. subcapitata* (higher values correspond to lower toxicity; 1 = control). Time on stream: (●) 2 min, (■) 5 min, (○) 10 min, (□) 15 min. Dotted line: untreated pre-ozonated wastewater. (The bars represent confidence intervals.)

represents the growth rate of the green alga under control conditions. Values above 1 represent non-toxic mixtures or toxicity reduction, whereas lower values indicate growth inhibition.

During Xe and UV (Hg lamp) irradiation and Xe/CeTiO₂ photocatalysis, the toxicity of the reaction mixture increased during the treatment, attaining in the case of UV a value as low as 60% of algal growth (UV 15 min, with respect to spiked pre-ozonated wastewater before irradiation). This reflects the formation and accumulation of toxic transformation products. Conversely, ozonation runs, and particularly O₃/UV led to higher algal growth and therefore a reduction in the toxicity of the reaction mixture. It is interesting to note that catalytic ozonation, O₃/CeTiO₂, a non-photolytic process with modest hydroxyl radical generation, led to mixtures in which toxicity always decreased over treatment time. For more intense processes such as O₃/H₂O₂ or homogeneous ozonation, the toxicity of the mixtures treated during 15 min was higher than that of non-treated spiked wastewater. In O₃/H₂O₂, in particular, the toxicity increased in all samples except the first, taken after 2 min. In photolytic ozonation, O₃/Xe, O₃/Xe/CeTiO₂ and O₃/UV a higher toxicity was observed in samples treated for longer periods. This indicates that efforts to reduce dissolved carbon concentrations are not necessarily followed by a fall in toxicity in treated effluents. On the contrary, the effect may be an increase in the concentration of toxic compounds. After 5 min, the concentration of the target compounds HHBC and AHTN did not suffer significant reductions, while the toxicity of samples treated for an additional 10 min period generally increased. Whenever significant changes in toxicity were encountered, most of the variations in the algal growth rate took place during the first 2 min on stream. These facts indicated that prolonged irradiation or ozonation treatments bring no benefits in terms of HHBC/AHTN removal or toxicity reduction.

Raw filtered wastewater was relatively toxic to *D. magna*, with an immobilization percentage of 15% for a contact time of 48 h. The toxicity of ozonated wastewater dropped to ~5%, the toxicity level observed after most treatments (Fig. 4.6). Only ozonation and UV or Xe irradiation of pre-ozonated wastewater led to lower immobilization, but the differences were not high, remaining close to the experimental error. It is interesting to note that the UV irradiation of raw, non pre-ozonated wastewater reduced toxicity by 5% up to a 10% immobilization, an effect that can only be attributed to the photolysis of toxic compounds in wastewater: the effect of UV on the other two species tested in this work, was the opposite.

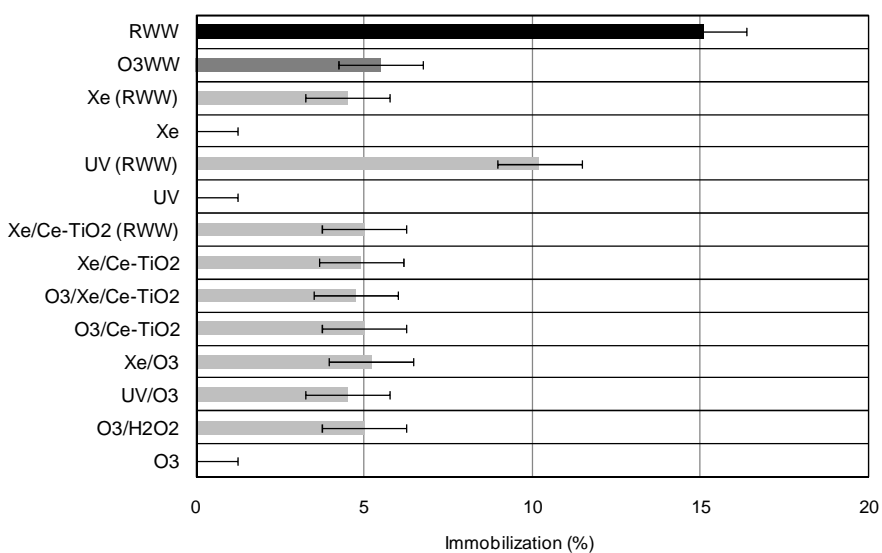


Figure 4.6. Toxicity assessed by immobilization of *D. magna*. RWW: Raw wastewater, O3WW: pre-ozonated wastewater before treatment.

A greater effect was observed using the marine bacteria *V. fischeri*, whose constitutive luminescence decayed considerably during UV, Xe and Xe/Ce-TiO₂ treatments. This is represented in Fig. 4.7 as relative bioluminescence, with lower values corresponding to more intense toxic effect. The lowest toxicities were observed for O₃/UV, O₃/Xe and O₃/Ce-

TiO₂ treatments, in good agreement with the results obtained for *P. subcapitata*. Again, for O₃/H₂O₂, O₃ a decrease in toxicity was followed by an upturn at 2 min processing time. Once more, further treatment would be justified neither to remove micropollutants nor for its effect on the toxicity of treated effluent.

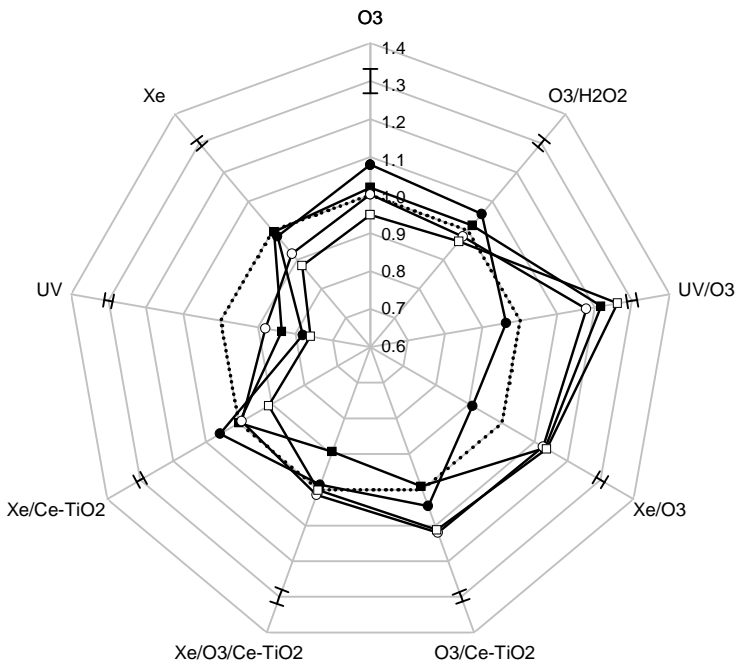


Figure 4.7. Toxicity of treated samples: relative luminescence of *V. fischeri* (higher values correspond to lower toxicities; 1 = control). Time on stream: (●) 2 min, (■) 5 min, (○) 10 min, (□) 15 min. Dotted line: untreated pre-ozonated wastewater. (The bars represent confidence intervals.)

The background toxicity of wastewater decreased with pre-ozonation both for *P. subcapitata* and *V. fischeri*. The relative (to pre-ozonated wastewater) growth inhibition of raw wastewater for *P. subcapitata* was 0.76 ± 0.04 , whereas the bioluminescence inhibition of *V. fischeri* was 1.32 ± 0.10 , which represented a 25-30% toxicity reduction in both cases. This effect must be due to the reaction of ozone with

compounds with high direct ozonation rate constants, as it took place before ozone appeared in solution. Contrary to the generation of toxic transformation products observed with treatments like UV or high contact time ozonation, a low ozone dosage allowed the target pollutant to be removed without producing compounds which were toxic for microorganisms.

A significant part of wastewater toxicity could be attributed to dissolved toxic metals, particularly zinc, mercury and other heavy metals. In this case, the amount of dissolved zinc in raw wastewater (34 $\mu\text{g/L}$) was close to the median effect value (EC_{50}) of 60 $\mu\text{g/L}$ in *P. subcapitata* reported by Franklin et al. (2007). On the other hand *D. magna* and *V. fischeri* are relatively insensitive to zinc as their EC_{50} lie in the mg/L range (Vesela et al., 2007; Ytreberg et al., 2010). In fact, ozone may lead to the separation of dissolved metals in the form of insoluble oxides. The parallel effect obtained for *V. fischeri* and *P. subcapitata* using pre-ozonated wastewater under different treatments, suggests that its toxicity was associated to the presence of organic pollutants that were eventually able to be removed by oxidation processes.

4.5. Conclusions

The combined use of ozone and radiation (O_3/UV) or hydrogen peroxide ($\text{O}_3/\text{H}_2\text{O}_2$) increased R_{ct} by three orders of magnitude. Ozone-radiation combined treatments also increased $R_{OH,UV}$ due to the effect of a dual source of hydroxyl radicals.

AHTN was more easily removed than HHCB, with best removal efficiencies for O_3 , O_3/UV , $\text{O}_3/\text{H}_2\text{O}_2$, O_3/Xe and for UV irradiation alone. The depletion of HHCB was higher in ozone-driven treatments, while UV-based processes, particularly UV photolysis gave poorer results. Xe/Ce-TiO₂ photocatalysis, whose efficiency in generating hydroxyl radicals was

relatively low, led to AHTN and HHCB degradation close to those obtained during ozonation treatments.

The concentration of HHCB-lactone increased during ozonation treatments at least during the first minutes, thus proving that HHCB-lactone is formed as an intermediate transformation product from HHCB. For this reason, most ozone treatments only resulted in moderate reductions in HHCB-lactone concentration. In the best case the depletion of initial HHCB-lactone reached about 75% for O_3 , O_3/UV and O_3/H_2O_2 .

Radiative treatments, particularly germicidal UV, but also Xe/CeTiO₂ photocatalysis, led to an increase in toxicity for *P. subcapitata* and *V. fischeri*. This was most probably a consequence of the formation and accumulation of toxic transformation products from the oxidation of wastewater components.

Ozonation treatments, including O_3/UV but also catalytic ozonation $O_3/Ce-TiO_2$, O_3/Xe and $O_3/Xe/Ce-TiO_2$ resulted in initial toxicity reduction for short contact times, but the toxicity of treated wastewater to *P. subcapitata* and *V. fischeri* increased thereafter.

The results showed that prolonged irradiation or ozonation treatments offer no advantages in terms of HHCB/AHTN removal or toxicity reduction.

4.6. References

- Allen, J.M., Allen, S.K., Baertschi, S.W., 2000. 2-Nitrobenzaldehyde: a convenient UV-A and UV-B chemical actinometer for drug photostability testing. *Journal of Pharmaceutical and Biomedical Analysis* 24, 167–178.
- Baltussen, E., Sandra, P., David, F., Cramers, C.A., 1999. Stir bar sorptive extraction (SBSE), a novel extraction technique for aqueous samples: theory and principles. *Journal of Microcolumn Separations*. 11, 737-747.
- Bester, K., 2005. Polycyclic musks in the Ruhr catchment area—transport, discharges of waste water, and transformations of HHCB, AHTN and HHCB-lactone. *J. Environmental Monitoring* 7, 43–51.

- Bester, K., 2004. Retention characteristics and balance assessment for two polycyclic musk fragrances (HHCB and AHTN) in a typical German sewage treatment plant. *Chemosphere* 57, 863–870.
- Buffle, M.O., Schumacher, J., Meylan, S., Jekel, M., von Gunten, U., 2006a. Ozonation and advanced oxidation of wastewater: effect of O₃ Dose, pH, DOM and HO[•]-scavengers on ozone decomposition and HO[•] generation. *Ozone: Science & Engineering* 28, 247–259.
- Buffle, M.O., Schumacher, J., Salhi, E., Jekel, M., von Gunten, U., 2006b. Measurement of the initial phase of ozone decomposition in water and wastewater by means of a continuous quench-flow system: application to disinfection and pharmaceutical oxidation. *Water Research* 40, 1884–1894.
- Clara, M., Gans, O., Windhofer, G., Krenn, U., Hartl, W., Braun, K., Scharf, S., Scheffknecht, C., 2011. Occurrence of polycyclic musks in wastewater and receiving water bodies and fate during wastewater treatment. *Chemosphere* 82, 1116–1123.
- Elovitz, M.S., von Gunten, U., 1999. Hydroxyl radical/ozone ratios during ozonation processes I. The R_{ct} concept. *Ozone: Science & Engineering* 21, 239–260.
- Franke, S., Meyer, C., Heinzel, N., Gatermann, R., Hühnerfuss, H., Rimkus, G., König, W.A., Francke, W., 1999. Enantiomeric composition of the polycyclic musks HHCB and AHTN in different aquatic species. *Chirality* 11, 795–801.
- Franklin, N. M., Rogers, N. J., Apte, S. C., Batley, G. E., Gadd, G. E., Casey, P. S., 2007. Comparative toxicity of nanoparticulate ZnO, bulk ZnO, and ZnCl₂ to a freshwater microalga (*Pseudokirchneriella subcapitata*): the importance of particle solubility. *Environmental Science & Technology* 41, 8484–8490.
- Gómez, M.J., Herrera, S., Solé, D., García-Calvo, E., Fernández-Alba, A., 2011. Automatic searching and evaluation of priority and emerging contaminants in wastewater and river water by stir bar sorptive extraction followed by comprehensive two-dimensional gas chromatography-time-of-flight mass spectrometry. *Analytical Chemistry* 83, 2638–2647.
- Gómez, M.J., Herrera, S., Solé, D., García-Calvo, E., Fernández-Alba, A.R., 2012. Spatio-temporal evaluation of organic contaminants and their transformation products along a river basin affected by urban, agricultural and industrial pollution. *Science of the Total Environment* 420, 134-145
- Gómez-Ramos, M.M., Mezcuca, M., Agüera, A., Fernández-Alba, A.R., Gonzalo, S., Rodríguez, A., Rosal, R., 2011. Chemical and toxicological evolution of the antibiotic sulfamethoxazole under ozone treatment in water solution. *The Journal of Hazardous Materials* 192, 18–25.
- International Organization for Standardization, 2007. Water Quality-Determination of the Inhibitory Effect of Water Samples on the Light Emission of *Vibrio fischeri* (Luminescent Bacteria Test). ISO 11348-3 revised version, Geneva, Switzerland.

- Janzen, N., Dopp, E., Hesse, J., Richards, J., Türk, J., Bester, K., 2011. Transformation products and reaction kinetics of fragrances in advanced wastewater treatment with ozone. *Chemosphere* 85, 1481–1486.
- Kallenborn, R., Gatermann, R., Nygard, T., Knutzen, J., Schlabach, M., 2001. Synthetic musks in Norwegian marine fish samples collected in the vicinity of densely populated areas. *Fresenius Environmental Bulletin* 10, 832–842.
- Lee, I.S., Lee, S.H., Oh, J.E., 2010. Occurrence and fate of synthetic musk compounds in water environment. *Water Research* 44, 214–222.
- Luckenbach, T., Epel, D., 2005. Nitromusk and polycyclic musk compounds as long-term inhibitors of cellular xenobiotic defense systems mediated by multi-drug transporters. *Environmental Health Perspectives* 113, 17–24.
- Lv, Y., Yuan, T., Hu, J., Wang, W., 2010. Seasonal occurrence and behavior of synthetic musks (SMs) during wastewater treatment process in Shanghai, China. *Science of The Total Environment* 408, 4170–4176.
- Mack, J., Bolton, J.R., 1999. Photochemistry of nitrite and nitrate in aqueous solution: a review, *Journal of Photochemistry and Photobiology A: Chemistry* 128, 1–13.
- Martínez-Bueno, M.J., Uclés, S., Hernando, M.D., Fernández-Alba, A.R., 2011. Development of a solvent-free method for the simultaneous identification/quantification of drugs of abuse and their metabolites in environmental water by LC–MS/MS. *Talanta*, 85, 157–166.
- Mersch-Sundermann, V., Schneider, H., Freywald, C., Jenter, C., Parzefall, W., Knasmüller, S., 2001. Musk ketone enhances benzo(a)pyrene induced mutagenicity in human derived HepG2 cells. *Mutation Research* 495, 89–96.
- Nicole, I., De Laat, J., Dore, M., Duguet, J.P., Bonnel, C., 1990. Use of UV radiation in water treatment: measurement of photonic flux by hydrogen peroxide actinometry. *Water Research* 24, 157–168.
- Nöthe, T., Hartmann, D., von Sonntag, J., von Sonntag, C., Fahlenkamp, H., 2007. Elimination of the musk fragrances galaxolide and tonalide from wastewater by ozonation and concomitant stripping. *Water Science and Technology* 55, 287–292.
- OECD, 2004. Test No. 202: *Daphnia sp.* Acute Immobilisation Test, OECD Guidelines for the Testing of Chemicals, Section 2, OECD Publishing.
- OECD, 2011. Test No. 201: Freshwater Alga and Cyanobacteria, Growth Inhibition Test, OECD Guidelines for the Testing of Chemicals, Section 2, OECD Publishing.
- Prieto, A., Zuloaga, O., Usobiaga, A., Etxebarria, N., Fernández, L. A., 2007. Development of a stir bar sorptive extraction and thermal desorption-gas chromatography-mass spectrometry method for the simultaneous

- determination of several persistent organic pollutants in water samples. *Journal of Chromatography A* 1174, 40–49.
- Reiner, J.L., Berset, J.D., Kannan, K., 2007. Mass flow of polycyclic musks in two wastewater treatment plants. *Archives of Environmental Contamination and Toxicology* 52, 451–457.
- Reiner, J.L., Kannan, K., 2006. A survey of polycyclic musks in selected household commodities from the United States. *Chemosphere* 62, 867–873.
- Rosal, R., Rodríguez, A., Gonzalo, M.S., García-Calvo, E., 2008a. Catalytic ozonation of naproxen and carbamazepine on titanium dioxide. *Applied Catalysis B: Environmental* 84, 48–57.
- Rosal, R., Rodríguez, A., Perdigón-Melón, J.A., Mezcua, M., Agüera, A., Hernando, M.D., Letón, P., García-Calvo, E., Fernández-Alba, A.R., 2008b. Removal of pharmaceuticals and kinetics of mineralization by O_3/H_2O_2 in a biotreated municipal wastewater. *Water Research* 42, 3719–3728.
- Rosal, R., Gonzalo, M.S., Boltes, K., Letón, P., Vaquero, J.J., García-Calvo, E., 2009. Identification of intermediates and ecotoxicity assessment of the oxidation products generated during the ozonation of clofibric acid. *Journal of Hazardous Materials* 172, 1061–1068.
- Rosal, R., Rodríguez, A., Perdigón-Melón, J.A., Petre, A., García-Calvo, E., Gómez, M.J., Agüera, A., Fernández-Alba, A.R., 2010a. Occurrence of emerging pollutants in urban wastewater and their removal through biological treatment followed by ozonation. *Water Research* 44, 578–588.
- Rosal, R., Gonzalo, M.S., Rodríguez, A., García-Calvo, E., 2010b. Catalytic ozonation of fenofibric acid over alumina-supported manganese oxide. *Journal of Hazardous Materials* 183, 271–278.
- Rosenfeldt, E.J., Linden, K.G., Canonica, S., von Gunten, U., 2006. Comparison of the efficiency of OH radical formation during ozonation and the advanced oxidation processes O_3/H_2O_2 and UV/H_2O_2 . *Water Research* 40, 3695–3704.
- Salvito, D., 2005 Synthetic Musk Compounds and Effects on Human Health? *Environmental Health Perspectives* 113, 802–803.
- Santiago, J., Agüera, A., Gómez-Ramos, M.M., Fernández Alba, A.R., García-Calvo, E., Rosal, R., 2011. Oxidation by-products and ecotoxicity assessment during the photodegradation of fenofibric acid in aqueous solution with UV and UV/H_2O_2 . *Journal of Hazardous Materials* 194, 30–41.
- Schmid, P., Kohler, M., Gujer, E., Zennegg, M., Lanfranchi, M., 2007. Persistent organic pollutants, brominated flame retardants and synthetic musks in fish from remote alpine lakes in Switzerland. *Chemosphere* 67, S16–S21.
- Seco, J.I., Fernández-Pereira, C., Vale, J., 2003. A study of the leachate toxicity of metal-containing solid wastes using *Daphnia magna*. *Ecotoxicology and Environmental Safety* 56, 339–350.

- Sommer, C., 2004. The role of musks and musk compounds in the fragrance industry, in Gerhard G. Rimkus (Ed.) Synthetic Musk Fragrances in the Environment. The Handbook of Environmental Chemistry, Vol. 3, Part X, pp. 1–16
- Ternes, T.A., Bonerz, M., Herrmann, N., Teiser, B., Andersen, H.R., 2007. Irrigation of treated wastewater in Braunschweig, Germany: An option to remove pharmaceuticals and musk fragrances. *Chemosphere* 66, 894–904.
- Vesela, S., Vijverberg, J., 2007. Effect of body size on toxicity of zinc in neonates of four differently sized *Daphnia* species, *Aquatic Ecology* 41, 67–73.
- Ytreberg, E., Karlsson, J., Eklund, B., 2010. Comparison of toxicity and release rates of Cu and Zn from anti-fouling paints leached in natural and artificial brackish seawater. *Science of the Total Environment* 408, 2459 – 2466.

Chapter 5

Energy efficiency for the removal of non-polar pollutants during ultraviolet irradiation, visible light photocatalysis and ozonation of a wastewater effluent

Energy efficiency for the removal of non-polar pollutants during ultraviolet irradiation, visible light photocatalysis and ozonation of a wastewater effluent*

5.1. Abstract

This study aims to assess the removal of a set of non-polar pollutants in biologically treated wastewater using ozonation, ultraviolet (UV 254 nm low pressure mercury lamp) and visible light (Xe-arc lamp) irradiation as well as visible light photocatalysis using Ce-doped TiO₂. The compounds tracked include UV filters, synthetic musks, herbicides, insecticides, antiseptics and polyaromatic hydrocarbons. Raw wastewater and treated samples were analyzed using stir-bar sorptive extraction coupled with comprehensive two-dimensional gas chromatography (SBSE–CG x GC–TOF–MS). Ozone treatment could remove most pollutants with a global efficiency of over 95% for 209 μM ozone dosage. UV irradiation reduced the total concentration of the sixteen pollutants tested by an average of 63% with high removal of the sunscreen 2-ethylhexyl trans-4-methoxycinnamate (EHMC), the synthetic musk 7-acetyl-1,1,3,4,4,6-hexa-

* The contents of this chapter have been pre-published online as:

Santiago-Morales, J., Gómez, M. J., Herrera-López, S., Fernández-Alba, A. R., García-Calvo, E., Rosal, R. Energy efficiency for the removal of non-polar pollutants during ultraviolet irradiation, visible light photocatalysis and ozonation of a wastewater effluent. *Water Research*, DOI 10.1016 /j.watres. 2013.06.030

methyltetrahydronaphthalene (tonalide, AHTN) and several herbicides. Visible light Ce-TiO₂ photocatalysis reached ~70% overall removal with particularly high efficiency for synthetic musks. In terms of power usage efficiency expressed as nmol kJ⁻¹, the results showed that ozonation was by far the most efficient process, ten-fold over Xe/Ce-TiO₂ visible light photocatalysis, the latter being in turn considerably more efficient than UV irradiation. In all cases the efficiency decreased along the treatments due to the lower reaction rate at lower pollutant concentration. The use of photocatalysis greatly improved the efficiency of visible light irradiation. The collector area per order decreased from $9.14 \pm 5.11 \text{ m}^2 \text{ m}^{-3} \text{ order}^{-1}$ for visible light irradiation to $0.16 \pm 0.03 \text{ m}^2 \text{ m}^{-3} \text{ order}^{-1}$ for Ce-TiO₂ photocatalysis. The toxicity of treated wastewater was assessed using the green alga *Pseudokirchneriella subcapitata*. Ozonation reduced the toxicity of treated wastewater, while UV irradiation and visible light photocatalysis limited by 20-25% the algal growth due to the accumulation of reaction by-products. Three transformation products were identified and tracked along the treatments.

5.2. Introduction

A wide variety of anthropogenic organic pollutants has been detected in surface waters during the last two decades. Most of them are pharmaceutical, personal care and household cleaning products, which, among others, constitute a new class of micropollutants usually referred to as emerging contaminants (Kümmerer, 2011). They are a result from human activities and are continuously released to the aquatic environment where their occurrence and concentration is quite variable depending on the proximity of urban or rural centres and their corresponding discharge points. In wastewater and receiving bodies they appear at concentrations in the ng/L to µg/L range (Rosal et al., 2010; Gómez et al., 2012). Most of them are not particularly toxic and due to their relatively low environmental concentration their risk has often been disregarded, but

little attention has been paid to the formation of toxic transformation products. Some pollutants are regulated and a subject of increasing concern as they have, for example, been found in fish tissues above their Environmental Quality Standards (Miège et al., 2012). The establishment of these standards is a fundamental part of the environmental strategy of the European Union against water pollution in compliance with the Water Framework Directive (2000/60/EC of the European Parliament and Council) and other legal statutes (Decision 2455/2001/EC, Directive 2008/105/EC). The outcome is a list of substances endangering aquatic ecosystems, with the last proposal (Proposal COM 2011, 876 final, 31.1.2012) establishing 48 priority substances of which 21 are considered priority hazardous substances. It includes pesticides, biocides, chemicals, metals, polybrominated diphenyl ethers and polyaromatic hydrocarbons. Most emerging pollutants, such as pharmaceutical and personal care products, are not yet included in monitoring programs of the European Union although they could be future candidates due to the scientific consensus on their risk.

Current wastewater treatment plants (WWTP) are the main way of anthropogenic pollutants to enter the aquatic environment. Because of this continuous release of organic pollutants, their occurrence is becoming ubiquitous and might affect not only aquatic organisms but also endanger the reclamation of water in a moment when it appears as a chief strategy to fight against water scarcity. A suitable strategy could include an additional treatment after the biological process in order to remove contaminants and to improve surface water quality with respect to direct reuse (Muñoz et al., 2009). Several studies have noted that advanced oxidation processes (AOP) are an available technology that may successfully remove emerging and recalcitrant micropollutants from wastewater (Esplugas et al., 2007). AOP treatments are capable of generating highly oxidative species but they require chemicals, energy supply or both, and their energy efficiency is the subject matter of discussions (Katsoyiannis et al., 2011). It has also been shown that the formation of refractory by-

products makes it difficult to achieve a high mineralization level (Krichevskaya et al., 2011). Moreover the degradation of the initial contaminants does not ensure any toxicity reduction target as transformation products can be even more toxic than their parent compounds (Shang et al., 2006; Santiago-Morales et al., 2013). There is a lack of investigations involving both energetic and ecotoxicity assessment as a step to allow its implementation in wastewater reuse scenarios using Life Cycle Assessment tools. Life cycle assessment is a well-known methodology to evaluate potential environmental impacts and has been previously proposed for water treatment processes (Zhang et al., 2010). The emissions to the aquatic environment should take into account aquatic ecotoxicity, whereas emissions to soil require the assessment of terrestrial and human ecotoxicity (Huijbregts et al., 2000). One of the limitations of this approach is the scarcity of information on the toxicity of treated samples and the difficulty of precisely establishing the required dosage of radiation or oxidants (Rodríguez et al., 2012).

In this study, we focused on the removal of non-polar micropollutants from biologically treated wastewater using irradiation and oxidation processes. Hydrophobic compounds pose an environmental threat because of their capacity to bioaccumulate in sediments and aquatic biota (Van der Oost et al., 2003). Also, the oxidative treatment of hydrophobic compounds produces oxidized transformation products with increased mobility (Santiago-Morales et al., 2012). The treatments studied were ozonation (O_3), ultraviolet (low pressure mercury lamp) and visible light (Xe-lamp) irradiation, the latter with and without photocatalyst (Ce/TiO₂). We analyzed treated samples with a method based on stir-bar sorptive extraction (SBSE) coupled with comprehensive two-dimensional gas chromatography (SBSE–CG x GC–TOF–MS) in order to track the most relevant non-polar pollutants in wastewater. SBSE–CG x GC–TOF–MS has been previously shown to display excellent results in the multianalysis of priority and emerging pollutants in water (Gómez et al., 2011). For all

treatments, we followed the toxicity of treated samples for the green alga *Pseudokirchneriella subcapitata*.

5.3. Methodology

5.3.1. Materials

Wastewater was sampled from the secondary clarifier of a 3000 m³ h⁻¹ WWTP placed in Alcalá de Henares, Madrid. This plant receives a mixture of domestic and industrial wastewater from industrial facilities located around the city. The biological treatment used a traditional A2O multistage configuration with nitrification-denitrification and enhanced phosphorus removal by phosphorus-accumulating microorganisms. The samples were stored in a refrigerator (< 4°C) inside glass bottles and filtered using 0.45 µm glass fibre filters before runs and analyses. The samples of photocatalytic runs received an additional filtration at the end to remove the suspended catalyst. Table 5.1 shows the main wastewater parameters. All the analytical standards (purity >95%) included in this study were purchased from Sigma-Aldrich (Steinheim, Germany) or from Dr. Ehrenstorfer (Augsburg, Germany). Hydrochloric acid and sodium hydroxide (purity >95 %) used for pH adjustment were purchased from Sigma-Aldrich. The photocatalyst was a ceria-doped TiO₂ with 0.5 % wt, described in a previous work (Santiago Morales et al., 2012). It has a band gap of 2.63 eV, a surface area of 29 m² g⁻¹ and X-ray diffraction experiments showed that its crystallographic phase corresponds to anatase crystals. The catalyst suspended in wastewater displayed a ζ-potential of 16.7 ± 0.8 mV and a mean particle size of 547 ± 33 nm determined by dynamic light scattering (DLS).

Table 5.1. Analysis of wastewater

<i>Parameter</i>		
pH	7.8 (in situ)	
Dissolved oxygen (mg L ⁻¹)	8.7 (in situ)	
TSS (mg L ⁻¹)	20 (as received)	
Turbidity (NTU)	2.5	
Conductivity (µS cm ⁻¹)	875	
NPOC (mg L ⁻¹)	8.1	
COD (mg L ⁻¹)	28	
Hardness (mg CaCO ₃ L ⁻¹)	219	
N-NO ₃ (mg L ⁻¹)	9.8	
SUVA-254 (L mg ⁻¹ m ⁻¹)	1.7	
<i>Anions and cations (mg L⁻¹)</i>		
Sulphate	79.9	
Chloride	80.6	
Phosphate	2.6	
Potassium	14.9	
Magnesium	21.6	
Calcium	52.2	
Sodium	70.5	
<i>Metals (µg L⁻¹)</i>		
Chromium	13	
Nickel	12.3	
Cobalt	1.8	
Strontium	560	
Copper	1.7	
Tin	0.29	
Lead	0.49	
Titanium	0.93	
Manganese	0.92	
Vanadium	1.1	
Molybdenum	4.3	
Zinc	34	
<i>Micropollutants (ng/L)</i>		
2-Ethylhexyl trans-4-methoxycinnamate (EHMC)		23.6 ± 8.1
Oxybenzone		14.4 ± 1.7
1,3,4,6,7,8-hexahydro-4,6,6,7,8,8-hexamethylcyclopenta(g)-2-benzopyran, Galaxolide (HHBC)	4212.4 ± 339.6	
Musk ketone		84.9 ± 6.7
7-acetyl-1,1,3,4,4,6-hexamethyltetrahydronaphthalene, Tonalie (AHTN)	461.3 ± 32.7	
Butyl hydroxytoluene (BHT)		164.6 ± 24.4
Atrazine		183.5 ± 9.6
Metolachlor		208.4 ± 31.4
Terbutryn		8.3 ± 1.8
Terbutylazine		5.5 ± 0.8
Chlorpyrifos-ethyl		2.4 ± 0.4
Diazinon		59.5 ± 11.0
Clorophene		3.6 ± 1.4
Triclosan		101.2 ± 20.6
Phenanthrene		2.5 ± 0.6
Pyrene		1.4 ± 0.3

TSS = Total suspended solids, NPOC = Non-purgeable organic carbon, COD = Chemical oxygen demand, SUVA-254 = Specific ultraviolet absorbance at 254 nm

5.3.2. Experimental setup and procedure

The irradiation experiments used a Heraeus TQ Xe 150 Xe-arc lamp with spectral emission in the visible region and 15 W Heraeus Noblelight TNN 15/32 low-pressure mercury vapour lamp (UV) emitting at 254 nm. The lamps were placed inside a quartz jacketed sleeve refrigerated using a thermostatic bath. The reaction temperature was closely controlled at 25°C in all cases. For visible light irradiations an additional borosilicate glass tube was used to absorb wavelengths < 290 nm. Fluence rates per unit volume were $6.01 \times 10^{-6} \text{ E L}^{-1} \text{ s}^{-1}$ (254 nm) for the UV lamp and $1.05 \times 10^{-6} \text{ E L}^{-1} \text{ s}^{-1}$ (290-400 nm) for the Xe-arc lamp. The chemical actinometers used were hydrogen peroxide and 2-nitrobenzaldehyde, which allowed us to obtain the indicated values for the UV and Xe lamps, respectively (Nicole et al., 1990; Allen et al., 2000).

Ozone was continuously bubbled during the run from a corona discharge ozone generator with a gas flow of $0.19 \text{ Nm}^3 \text{ h}^{-1}$ and concentration of ozone of 22 g Nm^{-3} . The ozone dosage, O_D , was determined, from the integration of the ozone absorption rate equation:

$$O_D(t) = E k_L a \left(C_{O_3}^* t - \int_0^t C_{O_3} dt \right) \quad (1)$$

where $C_{O_3}^*$ is equilibrium concentration of dissolved ozone and $k_L a$ the volumetric mass transfer coefficient. The enhancement factor, E , can be estimated from Hatta number as indicated in a previous work (Rosal et al., 2010). Details on the experimental methodology can be found elsewhere (Rosal et al., 2008). All experiments were performed in batch mode in a 1.3 L vessel magnetically stirred at 900 min^{-1} and the samples were withdrawn at prescribed intervals for analyses. To remove dissolved ozone from the samples we used nitrogen bubbling. This method avoids chemical quenchers and for the experimental conditions used it has been verified that the concentration of dissolved ozone falls below 3% in less than 30 s (Rosal et al., 2010). Throughout all the experiments pH was kept at $7.5 \pm$

0.1 units. The catalyst was used at a concentration of 200 mg L⁻¹ and stirred for 30 min before each run to ensure surface charge equilibration. The concentration of dissolved oxygen throughout photocatalytic treatments was 31-33 mg/L kept by constant oxygen bubbling.

5.3.3. Analyses

The analyses of micropollutants were performed using stir bar sorptive extraction (SBSE) coupled with comprehensive two dimensional gas chromatography (GC x GC–TOF–MS). This technique allows the simultaneous separation and determination of difficult to resolve constituents in complex mixtures at very low concentrations. This technique is based on the use of 20 mm (length) x 0.5 mm (film thickness) PDMS commercial stir bars (Gerstel, Muelheim an der Ruhr, Germany) loaded overnight and subsequently desorbed in a thermal desorption unit (Gerstel) connected to a programmed temperature vaporization (PTV) system injector CIS-4 (Gerstel) by a heated transfer line at 300 °C. The PTV injector was placed in a GC x GC–TOF–MS system Agilent 7890A gas chromatograph equipped with an additional oven and a quad-jets modulator (two cold jets and two hot jets). Liquid nitrogen used for cooling was automatically delivered from a 60 L Dewar liquid nitrogen storage tank. The first column (non-polar) was a 10 m x 0.18 mm i.d., 0.2 mm film thickness Rtx-5 coated with 5% diphenyl 95% dimethylpolysiloxane (Restek). The second column (semipolar) was a 1 m x 0.1 mm i.d., 0.10 mm film thickness Rxi-17 coated with 50% diphenyl 50% dimethylpolysiloxane (Restek). The MS system was a Pegasus 4D TOF (LECO Corporation). The method detection limits (MDLs) and method quantification limits (MQLs) in wastewater of the compounds analyzed in this study ranged between 0.02 to 3.07 ngL⁻¹ and 0.06 to 10.23 ngL⁻¹ respectively. Sample preparation details of the analytical method as well as the performance might be obtained elsewhere (Gómez et al., 2011).

A Metrohm 861 Advance Compact IC with suppressed conductivity detector allowed quantifying cations using a Metrosep C3 column with 5.0 mM HNO₃ eluent at 1 mL min⁻¹. Anions were determined in the same equipment using a Metrosep A Supp 7-250 analytical column with 36 mM Na₂CO₃ as eluent at 0.8 mL min⁻¹. Non Purgeable Organic Carbon (NPOC) was analyzed in a Shimadzu TOC-VCSH total carbon organic analyzer. Absorbance measurements were performed in a Shimadzu UV-1800 spectrophotometer. Trace metals were quantified by Inductively Coupled Plasma-Mass Spectrometry using a quadrupole mass spectrometer Agilent 7700X operating at 3 MHz in helium cell gas mode. The concentration of ozone dissolved in the aqueous phase was measured with an amperometric Mettler Toledo 358/210 dissolved ozone sensor calibrated using the Indigo Colorimetric Method (SM 4500-O3 B). The signal was transmitted to a Mettler Toledo Thornton M300 and finally monitored and recorded using an Agilent 34970 Data Acquisition Unit connected to a computer. The concentration of ozone in gas phase was determined using an Anseros Ozomat GM6000 Pro photometer calibrated against potassium iodide. The BET specific surface was evaluated by nitrogen adsorption at 77 K using an SA 3100 Beckman Coulter Analyzer. The catalyst was characterized by X-ray diffraction (XRD) using a Seifert 3000P diffractometer (Cu K α , $\lambda = 1.5406 \text{ \AA}$). DLS measurements were conducted in Malvern Zetasizer Nano ZS equipment. ζ -potential was measured via electrophoretic light scattering combined with phase analysis light scattering in the same instrument.

The toxicity of partially oxidized mixtures was assessed using the multigenerational growth inhibition of the green alga *Pseudokirchneriella subcapitata* according to OECD TG 201 (OECD, 2011). Algae were cultured in OECD growth medium at pH adjusted to 8.0 ± 0.2 . A culture kept in 25 mL agitated flasks was inoculated three days before each test. The exposed cultures were kept in 96-well clear microplates with a total dosed volume of 210 μ L, each well containing 180 μ L of sample, 20 μ L of a concentrated

OECD growth medium and 10 μL of microalgae. During 72 h algae were grown in a chamber under continuous fluorescent illumination of $100 \mu\text{E m}^{-2} \text{s}^{-1}$ at $22 \text{ }^\circ\text{C}$. The chlorophyll content was measured daily by fluorescence (Excitation 444nm – Emission 680 nm) using a Fluoroskan Ascent FL plate fluorometer-luminometer as substitute parameter for algal biomass production.

5.4. Results and discussion

5.4.1. Removal of micropollutants

We detected and quantified 16 micropollutants in the wastewater samples. The list includes 6 personal care products, namely the UV filters 2-ethylhexyl trans-4-methoxycinnamate (EHMC) and oxybenzone, the synthetic musks 1,3,4,6,7,8-hexahydro-4,6,6,7,8,8-hexamethylcyclopenta(g)-2-benzopyran (galaxolide, HHBC), 7-acetyl-1,1,3,4,4,6-hexamethyltetrahydronaphthalene (tonalide, AHTN) and musk ketone and the food additive (antioxidant) butyl hydroxitoluene (BHT). We also detected 8 pesticides/biocides and 2 polycyclic aromatic hydrocarbons (PAH): atrazine, metolachlor, terbutryn, terbuthylazine, chlorpyrifos-ethyl, diazinon, chlorophene, triclosan, phenanthrene and pyrene (Table 5.1). It is interesting to note that atrazine and metolachlor are excluded from of EC Regulation 1107/2009 (or the former Annex I of Council Directive 91/414/EEC). The abundance of HHBC and AHTN in treated wastewater complies with data published elsewhere and it is due to their very large consumption incorporated in a wide variety of personal care products in which they act as a fragrance fixative (Santiago-Morales et al., 2012). The other contaminants analyzed with concentrations in the order of hundreds of ng L^{-1} were the herbicides atrazine and metolachlor, frequently used in the past in gardening, the antioxidant additive BHT, and the antiseptic triclosan, included in a number of personal care products such as toothpastes.

The results of the irradiation and ozonation treatments on these pollutants are shown in (Table 5.2). Ozone was capable of removing most of the analyzed pollutants, particularly HHBC, AHTN and all the pesticides, with a global efficiency of +95% for an ozone dosage (calculated according to Eq. 1) of $209 \pm 38 \mu\text{M}$. The data for HHBC (97% removal) showed a higher degradation than found by Rosal et al. (2010) who encountered 83% removal for $340 \mu\text{M}$ ozone dosage. This could be explained by a lower COD for the wastewater used in this work. Snyder et al. (2006) observed 80-90% removal for HHBC in river water and in WWTP effluents using ozone dosages comparable to that of this work. It is interesting to note that EHMC and musk ketone were not significantly removed by ozone. This is in good agreement with data reported elsewhere: for the ozonation of musk ketone Rosal et al. (2010) reported no degradation for 220 mM ozone

Table 5.2. Removal of pollutants for irradiation, photocatalytic and ozonation treatments (expressed as $c(t)/c_0$). Reaction conditions: UV used a 15W low pressure mercury lamp with fluence rate $6.01 \times 10^{-6} \text{ E L}^{-1} \text{ s}^{-1}$ (254 nm); Xe and Xe-TiO₂ used a Heraeus TQ Xe 150 Xe-arc lamp with fluence rate $1.05 \times 10^{-6} \text{ E L}^{-1} \text{ s}^{-1}$ (290-400 nm); the catalyst concentration was 200 mg/L; ozone gas flow and concentration were $0.19 \text{ N m}^3 \text{ h}^{-1}$ and 22 g Nm^{-3} .

No.	Compound	UV		Xe		Xe/Ce-TiO ₂		O ₃
		2 min	15 min	2 min	15 min	2 min	15 min	22 min
1	EHMC	0.38	0.50	0.94	0.77	1.00	0.87	1.00
2	Oxybenzone	0.70	0.52	1.08	1.01	1.00	1.07	0.75
3	Galaxolide (HHBC)	0.47	0.46	1.00	1.01	0.53	0.22	0.03
4	Musk ketone	0.60	0.08	1.00	0.84	0.49	0.36	1.10
5	Tonalide (AHTN)	0.12	0.02	0.85	0.99	0.31	0.15	0.02
6	BHT	0.34	0.26	1.02	0.50	0.72	0.40	0.34
7	Atrazine	0.48	< 0.02	0.91	1.00	0.82	0.85	< 0.02
8	Metolachlor	0.37	0.003	0.94	1.00	0.67	0.72	< 0.002
9	Terbutryn	0.23	< 0.02	1.08	1.07	0.54	0.22	< 0.02
10	Terbutylazine	0.43	< 0.10	0.94	0.91	0.74	0.68	< 0.10
11	Chlorpyrifos-ethyl	0.86	0.63	1.00	1.10	0.67	0.25	< 0.17
12	Diazinon	0.82	0.04	0.96	0.93	1.02	1.01	< 0.002
13	Chlorophene	< 0.02	< 0.02	0.81	0.86	0.85	0.72	< 0.02
14	Triclosan	0.03	0.02	1.17	0.90	0.63	0.47	0.02
15	Pyrene	0.67	0.52	1.06	0.99	1.09	1.00	< 0.06
16	Phenanthrene	0.37	0.55	0.77	1.01	1.04	1.20	0.65

dosage whereas Snyder et al. (2006) found depletions of <1 % and 17% for low and high ozone dosages, respectively. Triclosan was almost completely removed by ozone while pyrene fell below its quantification limit. UV irradiation reduced the total concentration of the sixteen pollutants tested by an average of 63%. A remarkable fact is that musk ketone and EHMC were removed up to 92% and 50% respectively after 15 min, with substantial degradation taking place during the first 2 min (Table 5.2). 254 nm UV irradiation also resulted in high removal efficiencies for AHTN, atrazine, metolachlor, terbutryn, diazinon, chlorophene and triclosan (all of which were removed +99% in 15 min).

The rate of photolysis of a given compound at any concentration, c_p , can be calculated assuming for the photoreactor the model of linear source with emission in planes parallel to the lamp axis (LSPP). Details on the derivation can be found elsewhere (Beltrán, 2003):

$$-\frac{d c_p}{dt} = F_p \Phi_p \frac{2\pi R_o L E_o'}{V} \left[1 - e^{-\mu(R_1 - R_o)} \right] \quad (2)$$

μ is the attenuation coefficient and F_p the fraction of the absorbed radiation absorbed by a given compound, P :

$$\mu = 2.303 \sum \varepsilon_i c_i \quad (3)$$

$$F_p = \frac{\varepsilon_p c_p}{\sum \varepsilon_i c_i} \quad (4)$$

Φ_p is the quantum yield, R_o the inner radius of the photoreactor, L the length of the lamp, V the irradiated volume, E_o' the fluence rate at R_o (expressed in W cm^{-2}) and ε_p and ε_i the molar extinction coefficients of compound P and a generic compound in the mixture. Using the experimental values of $\sum \varepsilon_i c_i = 0.137 \text{ cm}^{-1}$ and $(R_1 - R_o) = 2.58 \text{ cm}$, the value for $\mu (R_1 - R_o)$ was 0.814, constant throughout the runs because the absorbance of wastewater (and the attenuation coefficient) did not change appreciably during treatments. In what follows, the initial value for F_p was used for

Table 5.3. Properties of micropollutants

Function	Substance	CAS No.	Molecular formula	pK _a	Log K _{ow} ^d	Log D _{ow} ^e
UV filter / sunscreen	2-Ethylhexyl trans-4-methoxycinnamate	5466-77-3	C ₁₈ H ₂₆ O ₃	- ^a	5.8	5.8
UV filter / sunscreen	Oxybenzone	131-57-7	C ₁₄ H ₁₂ O ₃	9.7 ^a	3.79	3.79
Synthetic musk	Galaxolide (HHBC)	1222-05-5	C ₁₈ H ₂₆ O	- ^b	5.9	5.90
Synthetic musk	Musk ketone	81-14-1	C ₁₄ H ₁₈ N ₂ O ₅	- ^a	4.3	4.30
Synthetic musk	Tonalide (AHTN)	21145-77-7	C ₁₈ H ₂₆ O	- ^b	5.7	5.70
Food additive / antioxidant	Butyl hydroxytoluene (BHT)	128-27-0	C ₁₅ H ₂₄ O	12.23 ^c	5.1	5.10
Herbicide	Atrazine ^{PH}	1912-24-9	C ₈ H ₁₄ ClN ₅	12.3 ^a	2.61	2.61
Herbicide	Metolachlor	51218-45-2	C ₁₅ H ₂₂ ClNO ₂	12.55 ^a	3.13	3.13
Herbicide	Terbutryn ^{PH}	886-50-0	C ₁₀ H ₁₉ N ₅ S	9.7 ^c	3.74	3.74
Herbicide	Terbutylazine	5915-41-3	C ₉ H ₁₆ ClN ₅	12 ^c	3.21	3.21
Insecticide	Chlorpyrifos-ethyl ^{PH}	2921-88-2	C ₉ H ₁₁ Cl ₃ NO ₃ PS	- ^a	4.96	4.96
Insecticide	Diazinon	333-41-5	C ₁₂ H ₂₁ N ₂ O ₃ PS	12.4 ^a	3.81	3.81
Disinfectant	Chlorophene	120-32-1	C ₁₃ H ₁₁ ClO	9.6 ^a	3.6	3.60
Antiseptic	Triclosan	3380-34-5	C ₁₂ H ₇ Cl ₃ O ₂	7.8 ^b	4.76	4.64
Combustion by-product	Pyrene ^{PHS}	129-00-0	C ₁₆ H ₁₀	-	4.88	4.88
Combustion by-product	Phenanthrene ^{PHS}	85-01-8	C ₁₄ H ₁₀	-	4.46	4.46

a) ACD/Ilab Web service Advanced_Chemistry_Development_Inc.; b) Rosal et al. 2010; c) U.S_National_Library_of_Medicine; d) Gómez et al. 2011; e) log D_{ow}: logarithm of pH-dependent or apparent octanol–water distribution coefficient, D_{ow} [for basic compounds, this coefficient can be determined by the following equation using pK_a for the corresponding conjugate acid (Rosal et al., 2010): $D_{ow} = \frac{K_{ow}}{1+10^{pK_a-pH}}$]; PS: priority substance; PHS: priority hazardous substance. PS and PHS are according to the Proposal COM 2011,876 final 31.1.2012 of European Parliament and Council

Table 5.4. Properties of micropollutants (continued)

Substance	Spectrum range	$\phi_{254\text{ nm}}$ ($\times 10^{-3}$)	$\epsilon_{254\text{ nm}}$ ($\text{M}^{-1}\text{ cm}^{-1}$)	$\phi_{>290\text{ nm}}$ ($\times 10^{-3}$)	$\epsilon_{>290\text{ nm}}$ ($\text{M}^{-1}\text{ cm}^{-1}$)	k_{O_3} ($\text{M}^{-1}\text{ s}^{-1}$)	k_{OH} ($\times 10^9\text{ M}^{-1}\text{ s}^{-1}$)
2-Ethylhexyl trans-4-methoxycinnamate	< 340 nm ¹	-	1550 ¹¹	-	25300 ¹¹	-	-
Oxybenzone	< 400 nm ²	0.13 ^a	6653 ¹²	0.13 ¹²	5900 ¹²	5.0·10 ⁶ ²³	-
Galaxolide (HHBC)	< 300 nm ^b	-	486 ^b	-	20.4 ^b	140 ²⁴	4.72 ³²
Musk ketone	-	-	-	-	-	-	1.49 ³³
Tonalide (AHTN)	< 340 nm ^b	120 ^a	12613 ^b	120 ²⁰	849 ^b	8 ²⁴	5.00 ²⁴
Butyl hydroxytoluene (BHT)	< 295 nm ³	-	316 ³	-	39.8 ³	-	-
Atrazine	< 290 nm ^b	53 ¹²	3768 ¹²	53 ^a	0	6 ²⁵	2.54 ³⁵
Metolachlor	< 305 nm ⁴	302 ¹⁵	615 ⁴	302 ^a	9.6 ⁴	1.11 ²⁶	6.70 ²⁶
Terbutryn	< 290 nm ⁵	79 ¹⁶	4210 ⁵	79 ^a	0	-	-
Terbutylazine	< 290 nm ⁶	94 ¹⁷	3830 ¹⁷	94 ^a	0	8.9 ²⁸	2.80 ²⁷
Chlorpyrifos-ethyl	< 310 nm ⁷	16 ¹⁸	900 ¹⁸	52 ¹⁸	330 ¹⁸	-	4.90 ³⁵
Diazinon	< 320nm ⁸	86 ⁸	3558 ⁴	58 ⁸	89 ⁴	1602 ²⁸	9.00 ⁸
Chlorophene	< 300 nm ⁹ (based on dichlorophene)	-	-	-	-	-	10.0 ²⁹
Triclosan	< 300 nm (acid form) < 320 nm (basic form) ¹⁰	480 ²²	3300 ¹⁰	740 ²¹	1500 ¹⁰	1.81·10 ⁸ ³⁰	5.40 ³¹
Pyrene	< 384 nm ¹⁴	3.83 ³⁹	13461 ¹⁴	2.1 ¹⁴	7179 ¹⁴	3.60·10 ⁴ ³⁸	10.0 ³⁶
Phenanthrene	< 355 nm ¹⁴	6.9 ¹⁹	45753 ¹⁴	3.5 ¹⁴	1222 ¹⁴	1.0·10 ⁴ ³⁸	13.4 ³⁷

1) Kikuchi et al., 2010; 2) Serpone et al., 2002; 3) NIST, 2012; 4) Feigenbrugel et al., 2005; 5) Gonzalez et al., 2007; 6) Palm et al., 1997; 7) Moffat et al. 2011; 8) Shemer and Linden, 2006; 9) Ghauch and Tuqan, 2009; 10) Lindström et al., 2002; 11) Panday, 2002; 12) Serpone et al., 2002;; 12) Santiago et al., 2011;; 14) Ram and Anastasio, 2009; 15) Wu et al., 2007; 16) Zwiener et al., 1995; 17) Nick et al., 1992; 18) Wan et al., 1994; 19) Beltrán et al., 1995; 20) European Union, 2008; 21) Latch et al., 2003; 22) Chung et al., 2007; 23) Huber et al., 2003; 24) Nöthe et al., 2007; 25) Acero et al., 2000; 26) Acero et al., 2003; 27) Camel and Bermond, 1998; 28) Ku et al., 1998; 29) Sires et al., 2007; 30) Suarez et al., 2007; 31) Latch et al., 2009; 32) Ward, 2010; 33) Hirsch, 2011; 35) Balci et al., 2009; 35) Wu and Linden, 2010; 36) Haag and Yao, 1992; 37) Beltrán, 2003; 38) Trapido et al., 1995; 39) Lehto et al., 2000; a) Quantum yield 254 nm \approx Quantum yield >290 nm; b) Measured in this work. c) $\phi_{>290\text{ nm}}$ and $\epsilon_{>290\text{ nm}}$ corresponds to averaged values between 290 nm and the maximum absorbance wavelength.

integrating Eq. 2 to get the concentration of irradiated compounds as a function of volume based fluence ratio, E'_{Vo} (expressed in $W\ m^{-3}$):

$$\frac{C_o - C_P}{t} = k = F_p \Phi_p E'_{Vo} \left[1 - e^{-\mu(R_i - R_o)} \right] \quad (5)$$

where k is the rate constant in $mol\ L^{-1}\ min^{-1}$. The two sides of Eq. 3 were plotted for each micropollutant for which quantum yields and molar extinction coefficients were available (See Table 5.4). The results are displayed in Fig. 5.1 in which the dashed line indicates the theoretical degradation rates obtained from Eq. 3. The points located below this line represent compounds with experimental rate constants lower than those theoretically calculated using their specific absorbance and quantum yield. The opposite stands for values above the theoretical line. The graph shows that all pollutants disappeared at rates close to their theoretical values

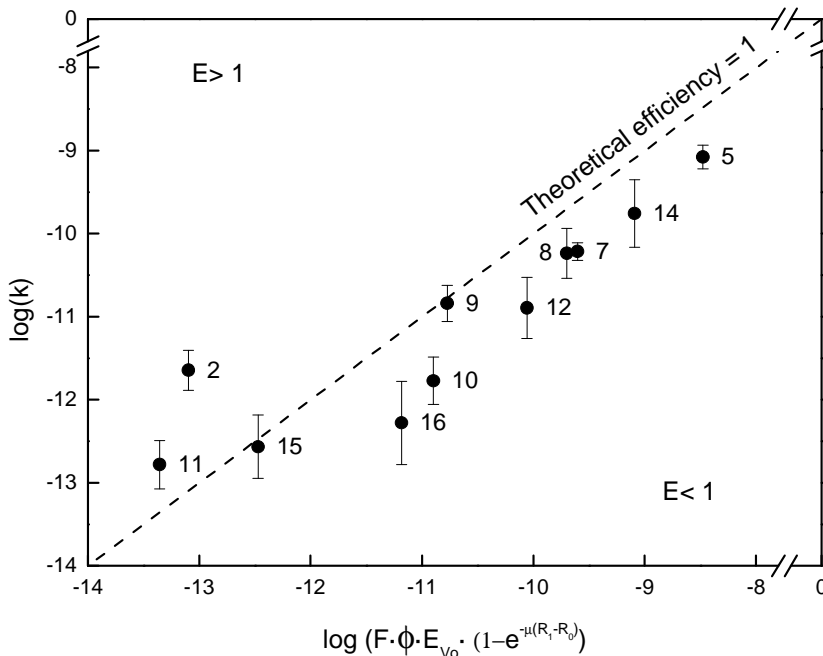


Figure 5.1. First-order constant rate for micropollutant removal during UV irradiation as a function of their theoretical rate of photolysis (Eq. 4). For compound identification see Table 5.2.

with experimental values slightly overestimated by theoretical calculations. This drift is most probably due to a decrease in F_p during irradiation. For compounds with a degradation rate above theoretical prediction (oxybenzone and chlorpyrifos-ethyl) other degradation mechanisms could be involved such as the reaction with hydroxyl radicals generated by photolysis of nitrate and nitrite or the photosensitization by dissolved organic matter (Mack and Bolton, 1999; Werner et al., 2005).

Visible light Xe-lamp driven photolysis led to a reduced removal of micropollutants, with an average of 1.4% for those tested in this work. However, visible light irradiation (filtered from wavelengths < 290 nm) was able to reduce the concentration of 4 (of 16) micropollutants in the 14-50% range. Remarkably, BHT became depleted by 50%. EHMC and musk ketone also displayed relatively high removal rates with depletion percentages in the 20% range after only 15 min of irradiation. These data indicate the relevance of natural irradiation in the environmental degradation of these pollutants.

Visible light Ce-TiO₂ photocatalysis was much more efficient and reached ~70% overall removal after 15 minutes. The main contribution was the high removal efficiency observed for the synthetic musks HHBC, AHTN and musk ketone (in the 64-85% range). Some other compounds, like oxybenzone, diazinon and the two polyaromatic hydrocarbons (phenanthrene and pyrene) did not suffer any significant degradation. Fig. 5.2 displays the photocatalytic removal efficiency of the tested micropollutants as a function of their octanol-water partition coefficient, K_{ow} (Table 5.3). (Because all compounds are non-polar, their dissociation constants are not significant for calculating the octanol-water partition coefficient.) For a group of pollutants, located in the shadowed region of Fig. 5.2, there is a clear relationship between photocatalytic removal efficiency and K_{ow} . Another group of five compounds showed no degradation or very low removal ratios (< 15%), namely EHMC, oxyben-

zone, diazinon, phenanthrene and pyrene. The insert of Fig. 5.2 also includes the percentage of dark adsorption taking place before irradiation. Diazinon (12) significantly adsorbed on the surface of the Ce-TiO₂ catalyst probably due to its positive charge at the pH of wastewater, which would allow electrostatic interaction with the deprotonated catalyst surface. The surface interaction of chlorophene (13), adsorbing > 20%, was most probably due to the electroneutral interaction with the separated proton in the proximity of TiO₂ surface (Friedmann et al., 2010). D'Oliveira et al. (1993) encountered a linear relationship between apparent first-order rate constants, Hammett constants and octanol-water partition coefficients for several chlorophenols during TiO₂ photocatalysis. In their work, K_{ow} showed a positive correlation with apparent rate constants, a similar behaviour as that reported here. The same result was indicated for several

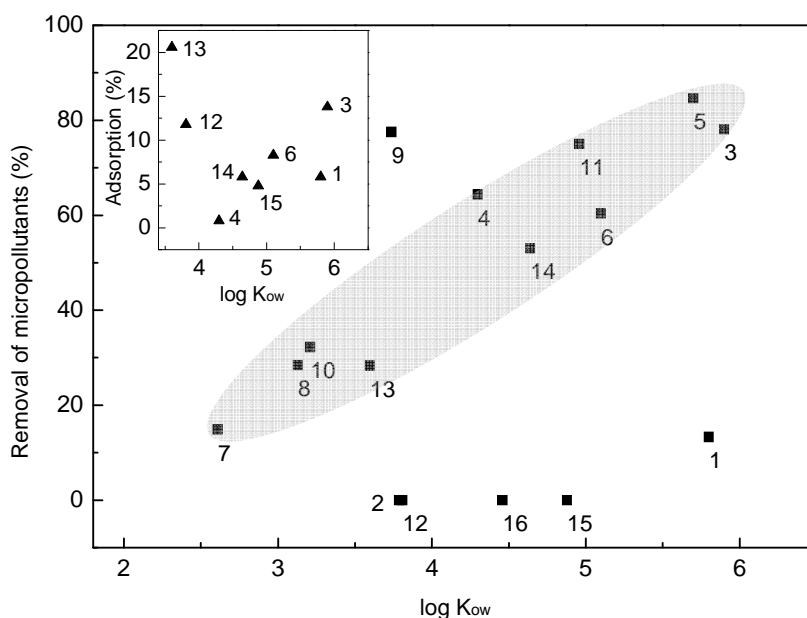


Figure 5.2. Photocatalytic removal of micropollutants as a function of the apparent octanol-water partition coefficient, K_{ow} . Insert: pollutant adsorption on catalyst surface for photocatalytic runs. The numbers refer to compounds as listed in Table 5.2.

pesticides by Tanaka and Reddy (2002). All these findings suggest that photocatalytic degradation of non-polar compounds might be mainly governed by the adsorption on the catalyst surface. The indirect reaction, which takes place by mediation of photogenerated radical species with soluble compounds, would be less efficient in this case than hole-based oxidation.

It is interesting to note that the depletion of the tested organic compounds by ozone is not directly related to the second order direct or indirect ozonation rate constants (See Table 5.4). There are several reasons for it derived from the intrinsic complexity of ozonation reactions. First, ozonation is a heterogeneous process, which takes part not only in the bulk, but also at the gas-liquid interface. Moreover, at the beginning of run there was no ozone in solution, and then the reactions took place at the gas-liquid interface or within the liquid film. Non-polar organics tend to accumulate at the surface, while more polar or dissociated compounds remain in the bulk, thus there is a preferential reactivity of the former during the first minutes. The fact that compounds with similar reaction rate became depleted at very different actual rates depending on their polarity has already been observed in a previous work (Rosal et al., 2010). Ozonation can be a direct reaction or hydroxyl radical-mediated process in which the availability of hydroxyl radicals determines the governing path. Radical reactions are highly influenced by the presence of interfering compounds. For example, it has been demonstrated that the reaction of aromatic compounds with hydroxyl radical is inhibited by dissolved natural organic matter, the probable reason being that hydroxyl radical formation occurs in micro-environmental sites remote from the aromatic compounds (Lindsey and Tarr, 2000). Moreover, the partition coefficient of a hydrophobic compound to dissolved organic matter also plays a significant role, up to the point that the presence of natural organic matter dramatically hinders the degradation of hydrophobic compounds even at too low concentrations to significantly scavenge hydroxyl radicals.

Besides the depletion of the compounds shown in Tables 5.1 and 5.2, we also tracked three relevant metabolites of three of them, namely HHBC-lactone from HHBC, AHTN-COOH (3,5,5,6,8,8-hexamethyl-5,6,7,8-tetrahydronaphthalene-2-carboxylic acid) from AHTN and 2-amino musk ketone from musk ketone. They were identified by GC x GC-TOF-MS and their concentrations during irradiation are displayed in Fig. 5.3 for irradiation runs. AHTN-COOH and 2-amino musk ketone were tentatively assigned according to mass spectra found in the literature (Valdersnes et al., 2006; Gatermann et al., 1998). HHBC-lactone is a biotransformation product of HHBC produced in WWTP operating with activated sludge (Bester, 2004). Apart from its biological origin, HHBC-lactone is a component of technical HHBC and was identified in river water samples at a comparable concentration or even higher than those for HHBC (Gómez et al., 2012). We also detected 2-amino musk ketone at levels higher than those of its parent compound. 2-amino musk ketone is the most common metabolite of musk ketone and is a suspected endocrine disruptor able to interact with oestrogen receptors (Champagne, 2008). AHTN-COOH has recently been shown to come out from AHTN reaction with sodium hypochlorite as a disinfection by-product (Kuhlich et al., 2011). The concentration of the three transformation products were significantly reduced by UV irradiation, particularly that of 2-amino musk ketone, which disappeared completely after 15 min. Xe/Ce-TiO₂ reached removal efficiencies within 25-50%, while visible light irradiation did not induce any significant depletion. Fig. 5.3 also shows the depletion of HHBC, AHTN and musk ketone during UV, Xe and Xe/Ce-TiO₂ irradiation processes. Concerning ozonation runs, the more polar character of TP and their higher removal rates make them more difficult to be detected and quantified. The identification of TP from galaxolide has been recently considered in detail in a recent paper in which we used liquid chromatography/hybrid quadrupole time-of-flight mass spectrometry (Herrera et al., 2013). In this

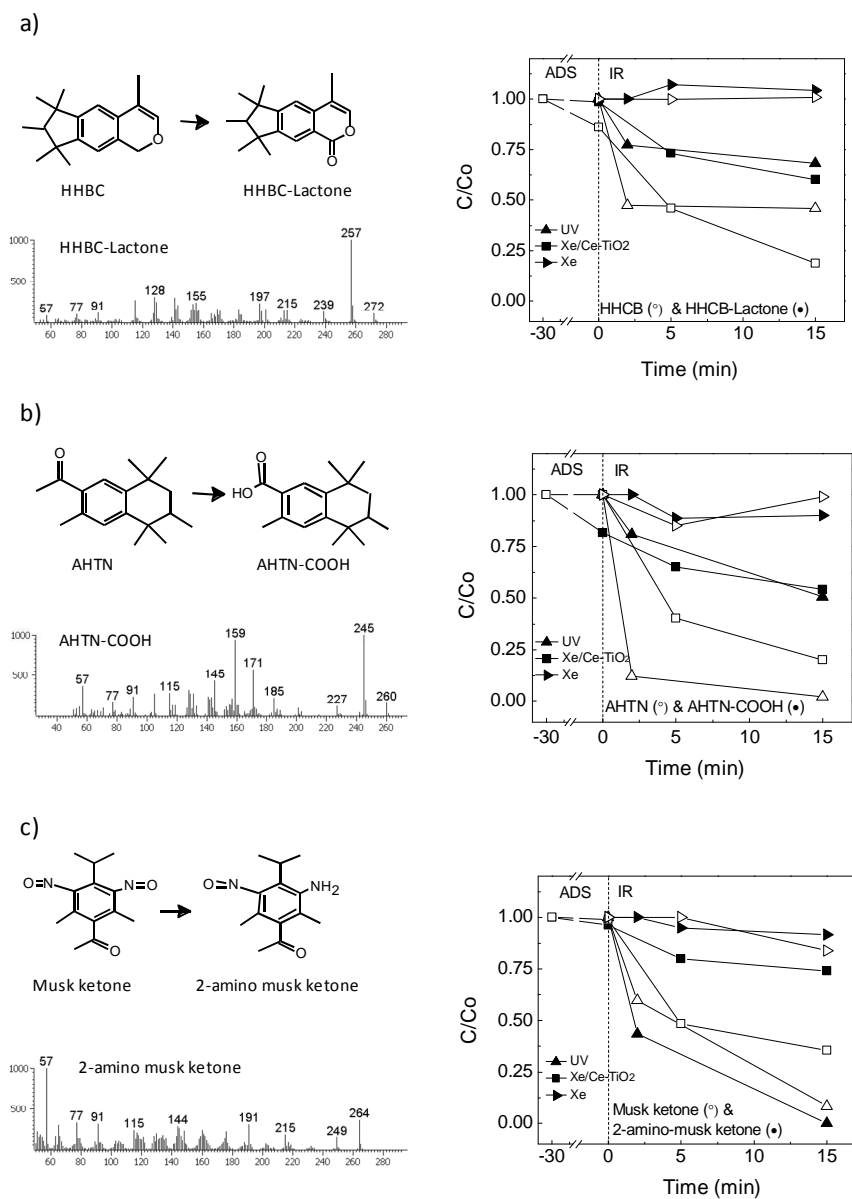


Figure 5.3. Concentration profile for the photodegradation of HHBC (a), AHTN (b), and musk ketone (c), shown by empty symbols, and its main transformation products, HHBC-Lactone (a), AHTN-COOH (b) and 2-amino musk ketone (c) displayed with filled symbols. (ADS: adsorption, IR: irradiation.) The left part of the figure shows the mass spectra identification of HHBC-Lactone (a), AHTN-COOH (b) and 2-amino musk ketone (c).

work we could detect HHCB-lactone in ozonated samples because its concentration was relatively high (103 ng/L). In a previous research we showed that during the first minutes of ozonation, HHCB-lactone could increase because it is also a transformation product formed during the ozone treatment of HHCB (Santiago-Morales et al., 2012). In this work, we obtained > 98% removal of HHCB-lactone after 22 min on stream. Pure irradiation treatments (UV, Xe) did not lead to any significant removal of the organic carbon initially present in the wastewater sample while Xe/Ce-TiO₂ photocatalysis reduced the amount of dissolved carbon 9% after 15 min. Ozonation led to a maximum mineralization of 40%, with NPOC removal below 15% after 15 min on stream. Moderate TOC removal is typical for most practical forms of AOP and favours the formation of organic transformation products, giving way to more complex reaction mixtures. In similar conditions we reported several cases of enhanced toxicity for aquatic organisms (Rosal et al., 2009; Gómez-Ramos et al., 2011).

The toxicity of treated samples for the green algae are displayed in Fig. 5.4 expressed as growth rate relative to untreated wastewater. Ozonation was the only treatment that could reduce the toxicity with respect to raw wastewater. The UV irradiation and Xe/Ce-TiO₂ visible light photocatalysis led to a growth rate reduction of up to 20-25% after 15 min of irradiation. The plot in Fig. 5.4 is accompanied with 95% confidence intervals, which show significant toxic responses at least after 5 min, while pure visible light irradiation has no effect at all. The enhancement in wastewater toxicity during irradiation processes is most probably due to the generation of transformation products that may be more toxic than the parent ones. It is interesting to note that UV and Xe irradiation did not reduce NPOC and that for Xe/Ce-TiO₂ the reduction was only 9%, a modest figure in comparison with the ozone treatment which reached NPOC removal of 40%. Additionally, synergistic effects between mixture components might make favour toxic responses in complex mixtures. The

generation of a high number of transformation products from every single parent pollutant would be a cause for concern (Boltes et al., 2012; Santiago-Morales et al., 2013).

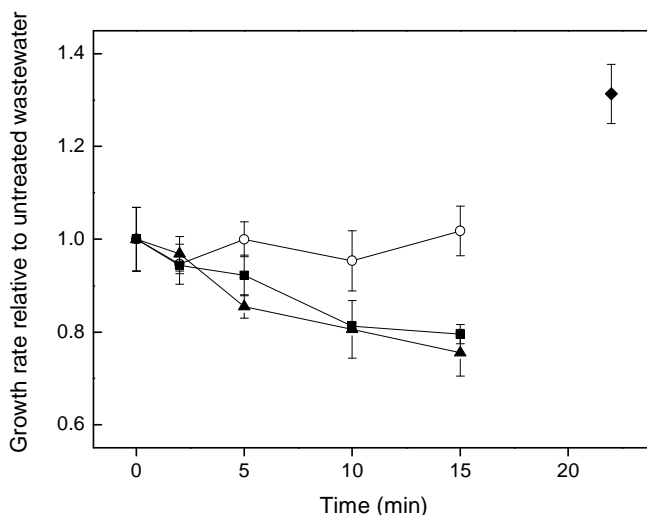


Figure 5.4. Toxicity of irradiated and ozonated wastewater samples. Ozonation (◆), UV (■), Xe (○), Xe/Ce-TiO₂ (▲).

UV and visible light irradiation treatments are initially quite different, but the similar generation of TP and the comparable toxicity pattern suggest a deeper analogy. During UV irradiation at 254 nm it is expected a certain oxidative contribution from hydroxyl radicals originated during the photolysis of nitrate (Lam et al., 2003). Also from water photolysis as the low-pressure mercury lamp used in this work yielded about 5% of its total power at 185 nm, in the vacuum UV. Visible light photocatalysis may also generate hydroxyl radicals by catalyst photoexcitation even though the direct oxidation on catalyst holes would eventually dominate. The lower capacity of irradiation processes to generate highly oxidant species would be the underlying reason for the main differences observed.

5.4.2. Energy efficiency

Water transferred power (WTP , expressed in $W\ m^{-3}$) was used to quantify the amount of energy entering a volume of water per unit time. The energy could be supplied in several forms such as radiation, electricity or chemical energy. For irradiation processes, WTP was obtained from the fluence rate, E_o' , the irradiated area A and the volume of treated water V :

$$WTP = \frac{E_o' A}{V} \quad (6)$$

For ozonation, WTP was calculated using standard enthalpy of formation of O_3 to convert ozone dosage into chemical energy:

$$WTP_{O_3} = \frac{F C \Delta H}{V} \quad (7)$$

F is the gas flow ($Nm^3\ s^{-1}$), C the $O_3(g)$ concentration ($g\ Nm^{-3}$), ΔH the formation enthalpy of ozone ($2.97\ kJ\ g^{-1}$) and V the volume of treated water. The results of WTP for the irradiation and ozonation processes used in this work are listed in Table 5.5. It is interesting to note that UV irradiation supplied one and two orders of magnitude more power than visible light irradiation and ozonation respectively. For the derivation of Table 5.5 we assumed gas-to-liquid ozone transfer efficiency of 75% as discussed else-where (Muñoz et al., 2009). The energy transferred to treated water, WTE is WTP multiplied by time. Fig. 5.5 shows the influence of the water transferred energy WTE ($kJ\ m^{-3}$) for photochemical and oxidation treatments on the depletion of total micropollutant concentration. Ozonation was by far the most efficient treatment in terms of the amount of micro-pollutants removed per unit of energy transferred to the water. The sample used for ozone treatments was taken once ozone appeared in solution and reasonably reached a plateau. This choice represents an ozone dosage not much higher than that required for rapid direct ozone reactions to complete and would be a reasonable minimum ozone dosage for wastewater treatment.

Photocatalytic Xe/Ce-TiO₂ required considerably lower energy than UV to remove the same amount of micropollutants. The contribution of dark adsorption on catalyst surface to pollutant depletion (~10%) is also shown in Fig. 5.5. As indicated before, the non-catalytic degradation by visible light resulted negligible.

The efficiency of energy usage can be quantified using the concept of transferred energy efficiency (*TEE*). *TEE* (nmol kJ⁻¹) is the ratio between concentration removal of micropollutants (nmol L⁻¹) and *WTE*. A higher value means better energy usage efficiency. The values of *TEE* are also shown as labels in Fig. 5.5. Ozonation was the most efficient process with *TEE* of 503 nmol kJ⁻¹, five-fold higher than Xe/Ce-TiO₂ visible light photocatalysis. In this work, the sample of the ozonation runs was withdrawn once ozone dissolved concentration achieved a plateau at 22 min on stream. Ozonation could lead to even better results in terms of efficiency

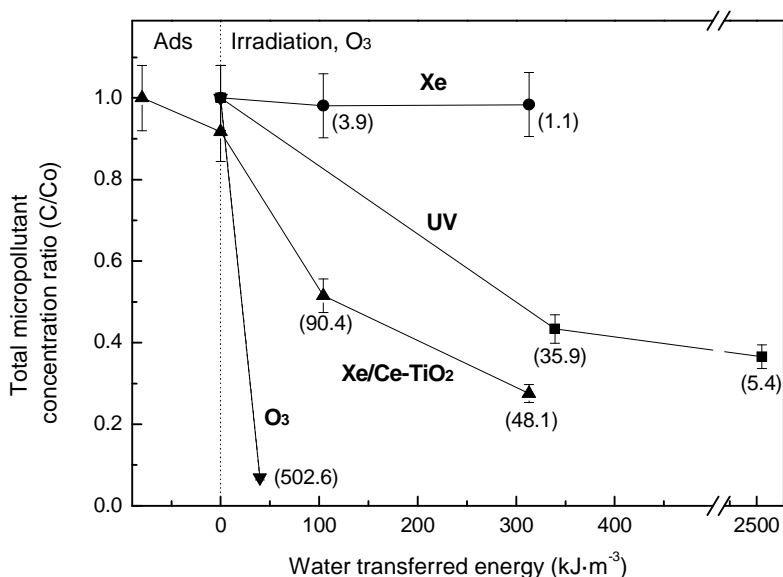


Figure 5.5. Removal of the total concentration of micropollutants as a function of the energy transferred to water during Xe, Xe/Ce-TiO₂, UV and O₃ treatments. Transferred energy efficiency (*TEE*, nmol kJ⁻¹) is shown in labels.

for lower contact times because, for lower ozone dosages, the amount of transferred energy would be proportionally lower. In any case it is necessary to consider that the minimum ozone dosage would correspond to that required to reach the slow kinetic regime. Therefore there is no reason for great differences. Concerning irradiation treatments, Xe/Ce-TiO₂ photocatalysis showed a better efficiency than UV and Xe. The data also show a decrease in energy efficiency with treatments time due to the lower reaction rate as pollutant concentration dropped.

Low-pressure mercury vapour lamp irradiation and ozonation are energy-intensive treatments in which electric energy can represent a large fraction of the operating costs. Bolton et al. (2001) defined a concept for measuring the energy consumption during the depletion of organic compounds at low concentrations by electrically driven processes called electrical energy per order, E_{EO} (kWh m⁻³ order⁻¹). It assumes overall first order kinetic expression and represents the electric energy needed to remove a given pollutant by one order of magnitude in a unit volume of water according to the following equation (written for batch operation):

$$E_{EO} = \frac{Pt}{V \log \left(\frac{c_i}{c_f} \right)} \quad (8)$$

P is the electric power, t the time, V the volume of reaction and c_i and c_f the initial and final concentration respectively.

For solar driven systems the electrical cost of irradiation does not apply because Xe-lamp is assumed to represent a true solar irradiation in a solar collector. In this case, the cost is dominated by the capital investment in the collector and the efficiency is best described in terms of irradiated area. Collector area per order, A_{CO} (m² m⁻³ order⁻¹), is the collector area needed to obtain one-order-magnitude degradation of a given contaminant (or group of contaminants) per unit of volume receiving

“standardized” incident solar fluence rate (E'_{SO}) of 1000 W m^{-2} over a period t_o (1h):

$$A_{CO} = \frac{AE'_s t}{V \log\left(\frac{c_i}{c_f}\right) E'_{SO} t_o} \quad (9)$$

A is the collector area and E'_s (W m^{-2}) and the average solar fluence rate during the period t of the treatment. Actinometry measurements allowed the determination of the volume based average fluence rate, E'_{VO} :

$$E'_{VO} = \frac{AE'_s}{V} \quad (10)$$

Finally, the volume based average fluence rate, E'_{VO} , can be replaced in Eq. 9 to obtain the collector-area-per-order expression used in this work:

$$A_{CO} = \frac{E'_{VO} t}{\log\left(\frac{c_i}{c_f}\right) E'_{SO} t_o} \quad (11)$$

Both “figures-of-merit”, E_{EO} and A_{CO} , for the treatments used in this work are exposed in Table 5.5. Ozonation led to E_{EO} of $0.18 \text{ kWh m}^{-3} \text{ order}^{-1}$, which represents a much lower electric consumption than UV irradiation. This consumption agreed with the figures reported by Katsoyiannis et al. (2011), in the $0.0035\text{-}0.9 \text{ kWh m}^{-3} \text{ order}^{-1}$ range, and Rodríguez et al. (2012) who obtained $0.03\text{-}0.26 \text{ kWh m}^{-3} \text{ order}^{-1}$ for continuous ozonation in a double column arrangement. Most of this variation in ozone efficiency could be explained by the balance between direct and hydroxyl-mediated oxidation processes and the effect of radical scavengers on the latter (Katsoyiannis et al., 2011). Kim and Tanaka (2011) calculated E_{EO} in the $0.03\text{-}0.09 \text{ kWh m}^{-3} \text{ order}^{-1}$ range in a process in which they got over 90% removal for most of a set of 37 pharmaceuticals and personal care products. More refractory compounds require higher dosages and conse-

Table 5.5. Water-transferred power (WTP), electrical energy per order (EEO) and collector area per order (ACO) for the different treatments

<i>Treatment</i>	WTP (W m^{-3})
UV irradiation (254 nm)	2828
Visible light irradiation (Xe lamp 290-400 nm)	348
Ozonation ^a	29.5
	E_{EO} ($\text{kWh m}^{-3} \text{ order}^{-1}$)
UV irradiation (254 nm)	2.56 ± 1.85
Ozonation ^a	0.18
	A_{CO} ($\text{m}^2 \text{ m}^{-3} \text{ order}^{-1}$)
Visible light irradiation (Xe lamp 290-400 nm)	9.14 ± 5.11
Xe/Ce-TiO ₂ photocatalysis	0.16 ± 0.03

a) Assuming gas-to-liquid ozone transfer efficiency of 75% (Muñoz et al., 2009).

quently other authors found lower efficiencies for the removal of dyes with O₃, O₃/H₂O₂, H₂O₂/UV and TiO₂/UV-A, which were in the 0.23-0.68 kWh m⁻³ order⁻¹ range (Arslan et al., 1999; Alaton et al., 2002). For UV treatment, we calculated the required energy considering an electric efficiency of 40% and a quartz transmittance of 92% (254 nm). The obtained E_{EO} was $2.56 \pm 1.85 \text{ kWh m}^{-3} \text{ order}^{-1}$, a figure in good agreement with previously reported data for the irradiation of river water and wastewater (Bolton and Stephan, 2002; Benotti et al. 2009; Zoschke et al., 2012). Lower values are associated with treatments in pure water, in which there are less absorbing species (Table 5.6).

Concerning Xe-lamp irradiated treatments, we assumed the same conditions would stand for a solar collector, with a borosilicate glass transmittance of 86.1% for wavelength range 290-400 nm taken from ASTM G173-03 Reference Solar Spectra and the transmittance data for DURAN glass. The experiments led to collector areas per order of $9.14 \pm 5.11 \text{ m}^2 \text{ m}^{-3} \text{ order}^{-1}$ for Xe irradiation and $0.16 \pm 0.03 \text{ m}^2 \text{ m}^{-3} \text{ order}^{-1}$ for

Table 5.6. Electrical energy per order per order, E_{EO} (kWh m^{-3} order) and and collector area per order, A_{CO} ($m^2 m^{-3}$ order $^{-1}$) in the literature.

	Treatment	This work	Literature value	Conditions	References
E_{EO} (kWh m^{-3} order $^{-1}$)	UV	2.56 ± 1.85	0.2^a to 1.3^b	^a Ultrapure water, ^b Raw water 2-methyl isoborneol and geosmin	(Zoschke et al., 2012)
			0.628	Atrazine (~100 ppb), MQ water	(Bolton and Stefan, 2002)
			0.3-0.5	Deionised water 0.001 mM N-nitrosodimethylamine	(Stefan and Bolton, 2002)
			~1-50	Atenolol–TCEP (ng L $^{-1}$) in river water	(Benotti et al., 2009)
	O ₃	0.18	0.0035 (SMX) 0.9 (NDMA)	Sulfamethoxazole [$k_{O_3} 2.5 \cdot 10^6 M^{-1} s^{-1}$ (pH 7), $k_{OH} 5 \cdot 10^9 M^{-1} s^{-1}$] N-nitrosodimethylamine [$k_{O_3} 0.052 M^{-1} s^{-1}$, $k_{OH} 4.5 \cdot 10^8 M^{-1} s^{-1}$]	(Katsoyiannis et al., 2011)
			0.03-0.09	Number of removed PPCPs > 90% / total number of PPCP 24/37 - 35/37	(Kim and Tanaka, 2011)
			0.684	Dyebath effluent	(Alaton et al., 2002)
			0.23	Dyehouse, pH 11	(Arslan et al., 1999)
			0.03-0.26	Two ozonation columns, 0.30 L min $^{-1}$, 90% removal	(Rodríguez et al., 2012)
	A_{CO} ($m^2 m^{-3}$ order $^{-1}$)	Xe	9.14 ± 5.11	NF	NF
Xe-CeTiO ₂		0.16 ± 0.03	12-37.5 8.7-5.5	Oxalic acid degradation (10 mM): PTC-CPC, 50 mg/L TiO ₂ PTC-CPC, 1 g/L TiO ₂	(Bandala and Estrada, 2007)
			14 9.6	Carbaryl degradation (0.25mM): PTC 0.05g/L TiO ₂ CPC 0.5g/L TiO ₂	
		8.6-11.2	Pebble bet, Different Dyes, 20-50 mg/L deionised water	(Rao et al., 2012)	

PTC: parabolic trough collector; CPC Concentrating Parabolic Collector); NF: not found

Xe/Ce-TiO₂. These results indicate that Ce-TiO₂ photocatalysis greatly improved the treatment efficiency of solar radiation. The collector area determined in this work for the photocatalytic process was one order-magnitude lower than that found elsewhere for the treatments of oxalic acid, the pesticide carbaryl and certain dyes (Bandala and Estrada, 2007; Rao et al., 2012). This fact could be due to the method of radiation measurement, which in our case was a chemical actinometry instead of radiometer calculations, and also due to the difference in target compounds, which were considerably more refractory for the cited references. (A more detailed reference to results reported in the literature can be found in Table 5.6.)

5.5. Conclusions

Ozone treatment achieved a global efficiency over 95% for the removal of the non-polar pollutants studied in this work for $209 \pm 37 \mu\text{M}$ ozone dosage. Particularly HHBC, AHTN, the agrochemicals atrazine, metolachlor, terbutryn, terbuthylazine, chlorpyrifos-ethyl, diazinon, chlorophene, the antiseptic triclosan and the polyaromatic compound pyrene were all removed over 99%.

The irradiation with 254 nm UV reduced the total concentration of the tracked pollutants by an average of 63% with the highest removal for the synthetic musks AHTN and musk ketone and all the herbicides (> 98%) except chlorpyrifos-ethyl (37%).

Visible light Ce-TiO₂ photocatalysis reached ~70% overall removal after 15 minutes of irradiation with the best results for the synthetic musks HHBC, AHTN and musk ketone (removal efficiencies in the 64-85% range). For a significant group of pollutants there was a clear positive relationship between photocatalytic removal efficiency and K_{ow} .

The efficiency in the use of energy was compared using the ratio between pollutant depletion (nmol) and the energy transferred to water (kJ). Ozonation was by far the most efficient treatment, one order of magnitude ahead of Xe/Ce-TiO₂, which was the irradiation process requiring less energy to remove the same amount of micropollutants.

Expressed in terms of energy per order, ozonation was again preferred, with $0.18 \pm 0.06 \text{ kWh m}^{-3} \text{ order}^{-1}$, while UV irradiation at 254 nm consumed $2.56 \pm 1.85 \text{ kWh m}^{-3} \text{ order}^{-1}$. Visible light irradiation photocatalysis led to collector areas per order of $0.16 \pm 0.03 \text{ m}^2 \text{ m}^{-3} \text{ order}^{-1}$. The result is lower than other published data for solar degradation of water pollutants, probably reflecting the ability of Ce-TiO₂ to remove non-polar pollutants.

The toxicity of treated wastewater decreased during ozone treatments while irradiation processes led to a toxicity increase due to the accumulation of toxic transformation products, three of which were identified and tracked along the runs. UV irradiation and Xe/Ce-TiO₂ photocatalysis led to a relatively high toxic response for the growth of the green alga *P. subcapitata*.

5.6. References

- Acero, J.L., Stemmler, K., von Gunten, U., 2000. Degradation kinetics of atrazine and its degradation products with ozone and OH radicals: a predictive tool for drinking water treatment. *Environmental Science & Technology* 34, 591-597.
- Acero, J.L., Benitez, F.J., Real, F.J., Maya, C., 2003. Oxidation of acetamide herbicides in natural waters by ozone and by the combination of ozone/hydrogen peroxide: Kinetic study and process modeling. *Industrial & Engineering Chemistry Research* 42, 5762-5769.
- Advanced Chemistry Development Inc., PhysChem Properties in: ACD/I-Lab, Available at: ilab.acdlabs.com. Accessed on September 2012
- Alaton, I.A., Balcioglu, I.A., Bahnemann, D.W., 2002. Advanced oxidation of a reactive dye bath effluent: comparison of O₃, H₂O₂/UV-C and TiO₂/UV-A processes. *Water Research* 36, 1143-1154.

- Allen, J.M., Allen, S.K., Baertschi, S.W., 2000. 2-Nitrobenzaldehyde: a convenient UV-A and UV-B chemical actinometer for drug photostability testing. *Journal of Pharmaceutical and Biomedical Analysis* 24, 167-178.
- Arslan, I., Balcioglu, I.A., Tuhkanen, T., 1999. Advanced oxidation of synthetic dyehouse effluent by O₃, H₂O₂/O₃ and H₂O₂/UV processes. *Environmental Technology* 20, 921-931.
- Balci, B., Oturan, N., Cherrier, R., Oturan, M.A., 2009. Degradation of atrazine in aqueous medium by electrocatalytically generated hydroxyl radicals. A kinetic and mechanistic study. *Water Research* 43, 1924-1934.
- Bandala, E.R., Estrada, C., 2007. Comparison of solar collection geometries for application to photocatalytic degradation of organic contaminants. *Journal of Solar Energy Engineering* 129, 22-27.
- Beltrán, F.J., Ovejero, G., García-Araya, J.F., Rivas, J., 1995. Oxidation of polynuclear aromatic hydrocarbons in water. 2. UV radiation and ozonation in the presence of UV radiation. *Industrial & Engineering Chemistry Research* 34, 1607-1615.
- Beltran, F.J., 2003. Ozone reaction kinetics for water and wastewater systems, Lewis Publishers, CRC Press, Boca Raton, pp. 193-205.
- Benotti, M.J., Stanford, B.D., Wert, E.C., Snyder, S.A., 2009. Evaluation of a photocatalytic reactor membrane pilot system for the removal of pharmaceuticals and endocrine disrupting compounds from water. *Water Research* 43, 1513-1522.
- Bester, K., 2004. Retention characteristics and balance assessment for two polycyclic musk fragrances (HHCB and AHTN) in a typical German sewage treatment plant. *Chemosphere* 57, 863-870.
- Boltes, K., Rosal, R., García-Calvo, E., 2012. Toxicity of mixtures of perfluorooctane sulfonic acid with chlorinated chemicals and lipid regulators. *Chemosphere* 86, 24-29.
- Bolton, J.R., Stefan, M.I., 2002. Fundamental photochemical approach to the concepts of fluence (UV dose) and electrical energy efficiency in photochemical degradation reactions. *Research on Chemical Intermediates* 28, 857-870.
- Bolton, J.R., Bircher, K.G., Tumas, W., Tolman, C.A., 2001. Figures-of-merit for the technical development and application of advanced oxidation technologies for both electric-and solar-driven systems (IUPAC Technical Report). *Pure and Applied Chemistry* 73, 627-638.
- Camel, V., Bermond, A., 1998. The use of ozone and associated oxidation processes in drinking water treatment. *Water Research* 32, 3208-3222.
- Champagne, P., 2008. Personal care products. In: Alok Bhandari, Rao Y. Surampalli, Craig D. Adams, Pascale Champagne, Say Kee Ong, and R. D. Tyagi (Eds.),

Contaminants of Emerging Environmental Concern. American Society of Civil Engineers, Reston, pp. 86-140.

- D'Oliveira, J.C., Minero, C., Pelizzetti, E. and Pichat, P., 1993. Photodegradation of dichlorophenols and trichlorophenols in TiO₂ aqueous suspensions: kinetic effects of the positions of the Cl atoms and identification of the intermediates. *Journal of Photochemistry and Photobiology A: Chemistry* 72, 261-267.
- Esplugas, S., Bila, D.M., Krause, L.G.T., Dezotti, M., 2007. Ozonation and advanced oxidation technologies to remove endocrine disrupting chemicals (EDCs) and pharmaceuticals and personal care products (PPCPs) in water effluents. *Journal of Hazardous Materials* 149, 631-642.
- European Union, 2008. European Union Risk Assessment Report. 1-(5,6,7,8-Tetrahydro-3,5,5,6,8,8-hexamethyl-2-naphthyl)ethan-1-one (AHTN) , European Communities, Luxembourg.
- Feigenbrugel, V., Loew, C., Calvé, S.L., Mirabel, P., 2005. Near-UV molar absorptivities of acetone, alachlor, metolachlor, diazinon and dichlorvos in aqueous solution. *Journal of Photochemistry and Photobiology A: Chemistry* 174, 76-81.
- Friedmann, D., Mendive, C., Bahnemann, D., 2010. TiO₂ for water treatment: Parameters affecting the kinetics and mechanisms of photocatalysis. *Applied Catalysis B Environmental* 99, 398-406.
- Gatermann, R., Hühnerfuss, H., Rimkus, G., Attar, A., Kettrup, A., 1998. Occurrence of musk xylene and musk ketone metabolites in the aquatic environment. *Chemosphere* 36, 2535-2547.
- Ghauch, A., Tuqan, A., 2009. Reductive destruction and decontamination of aqueous solutions of chlorinated antimicrobial agent using bimetallic systems. *Journal of Hazardous Materials* 164, 665-674.
- Gómez, M.J., Herrera, S., Solé, D., García-Calvo, E., Fernández-Alba, A.R., 2011. Automatic searching and evaluation of priority and emerging contaminants in wastewater and river water by stir bar sorptive extraction followed by comprehensive two-dimensional gas chromatography-time-of-flight mass spectrometry. *Analytical Chemistry* 83, 2638-2647.
- Gómez, M.J., Herrera, S., Solé, D., García-Calvo, E., Fernández-Alba, A.R., 2012. Spatio-temporal evaluation of organic contaminants and their transformation products along a river basin affected by urban, agricultural and industrial pollution. *Science of the Total Environment* 420, 134-145.
- Gómez-Ramos, M.M., Mezcuca, M., Agüera, A., Fernández Alba, A.R., Gonzalo, S., Rodríguez, A., Rosal, R., 2011. Chemical and toxicological evolution of the antibiotic sulfamethoxazole under ozone treatment in water solution. *Journal Hazardous Materials* 192, 18-25.

- Gonzalez, C., Touraud, E., Spinelli, S., Thomas, O., 2007. Organic Constituents in: Olivier Thomas and Christopher Burgess (Eds.) UV-visible Spectrophotometry of Water and Wastewater, Elsevier Science Limited, Amsterdam
- Haag, W.R., Yao, C.C.D., 1992. Rate constants for reaction of hydroxyl radicals with several drinking water contaminants. *Environmental Science & Technology* 26, 1005-1013.
- Herrera, S., Hernando, M.D., Gómez, M.J., Santiago-Morales, J., Rosal, R., Fernández-Alba, A.R., 2013. Investigation of Galaxolide degradation products generated under oxidative and irradiation processes by liquid chromatography/hybrid quadrupole time-of-flight mass spectrometry and comprehensive two-dimensional gas chromatography/time-of-flight mass spectrometry. *Rapid Communications in Mass Spectrometry* 27, 1237-1250.
- Hirsch, C.M., 2011. The removal of synthetic musks and other personal care product chemicals from reclaimed wastewater using radical reactions, M.Sc. Thesis, California State University, Long Beach
- Huber, M.M., Canonica, S., Park, G.Y., von Gunten, U., 2003. Oxidation of pharmaceuticals during ozonation and advanced oxidation processes. *Environmental Science & Technology* 37, 1016-1024.
- Huijbregts, M.A.J., Thissen, U., Guinée, J.B., Jager, T., Kalf, D., van de Meent, D., Ragas, A.M., Sleswijk, A.W., Reijnders, L., 2010. Priority assessment of toxic substances in life cycle assessment. Part I: Calculation of toxicity potentials for substances with the nested multi-media fate, exposure and effects model USES-LCA. *Chemosphere* 41, 541-573.
- Kümmerer, K., 2011. Emerging Contaminants, In: Peter Wilderer (Ed.), *Treatise on Water Science*, Elsevier, Oxford, pp. 69-87.
- Katsoyiannis, I.A., Canonica, S., von Gunten, U., 2011. Efficiency and energy requirements for the transformation of organic micropollutants by ozone, O₃/H₂O₂ and UV/H₂O₂. *Water Research* 45, 3811-3822.
- Kikuchi, A., Yukimaru, S., Oguchi, N., Miyazawa, K., Yagi, M., 2010. Excited triplet state of a UV-B absorber, octyl methoxycinnamate. *Chemistry Letters* 39, 633-635.
- Kim, I., Tanaka, H., 2011. Energy Consumption for PPCPs Removal by O₃ and O₃/UV. *Ozone Science & Engineering* 33, 150-157.
- Ku, Y., Chang, J.L., Shen, Y.S., Lin, S.Y., 1998. Decomposition of diazinon in aqueous solution by ozonation. *Water Research* 32, 1957-1963.
- Kuhlich, P., Göstl, R., Teichert, P., Piechotta, C., Nehls, I., 2011. Transformations of polycyclic musks AHTN and HHCb upon disinfection with hypochlorite: two new chlorinated disinfection by-products (CDBP) of AHTN and a possible source for HHCb-lactone. *Analytical and Bioanalytical Chemistry* 399, 3579-3588.

- Krichevskaya, M., Klauson, D., Portjanskaja, E., Preis, S., 2011. The Cost evaluation of advanced oxidation processes in laboratory and pilot-scale experiments. *Ozone Science & Engineering* 33, 211-223.
- Lam, M.W., Tantuco, K., Mabury, S.A., 2003. PhotoFate: A new approach in accounting for the contribution of indirect photolysis of pesticides and pharmaceuticals in surface waters. *Environmental Science & Technology* 37,899-907.
- Latch, D.E., Packer, J.L., Arnold, W.A., McNeill, K., 2003. Photochemical conversion of triclosan to 2, 8-dichlorodibenzo-p-dioxin in aqueous solution. *Journal of Photochemistry and Photobiology A: Chemistry* 158, 63-66.
- Latch, D.E., Packer, J.L., Stender, B.L., Van Overbeke, J., Arnold, W.A., McNeill, K., 2009. Aqueous photochemistry of triclosan: formation of 2, 4-dichlorophenol, 2, 8-dichlorodibenzo-p-dioxin, and oligomerization products. *Environmental Toxicology and Chemistry* 24, 517-525.
- Lehto, K.M., Vuorimaa, E., Lemmetyinen, H., 2000. Photolysis of polycyclic aromatic hydrocarbons (PAHs) in dilute aqueous solutions detected by fluorescence. *Journal of Photochemistry and Photobiology A: Chemistry* 136, 53-60.
- Lindsey, M. E., Tarr, M. A., 2000. Inhibition of hydroxyl radical reaction with aromatics by dissolved natural organic matter. *Environmental Science & Technology* 34, 444-449.
- Mack, J., Bolton, J.R., 1999. Photochemistry of nitrite and nitrate in aqueous solution: a review. *Journal of Photochemistry and Photobiology A: Chemistry* 128, 1-13.
- Miège, C., Peretti, A., Labadie, P., Budzinski, H., Le Bizec, B., Vorkamp, K., Tronczyński, J., Persat, H., Coquery, M., Babut, M., 2012. Occurrence of priority and emerging organic compounds in fishes from the Rhone River (France). *Analytical and Bioanalytical Chemistry* 404, 2721-2735.
- Moffat, A., Osselton, D., Widdop, B. and Galichet, L.Y., 2011. Chlorpyrifos in: *Analysis of Drugs and Poisons*. Available at: <http://mntnviewfarm.net/drugs-poisons-0356.html>. Accessed on December 2012
- Muñoz, I., Rodríguez, A., Rosal, R., Fernández-Alba, A.R., 2009. Life cycle assessment of urban wastewater reuse with ozonation as tertiary treatment: a focus on toxicity-related impacts. *Science of the Total Environment* 407, 1245-1256.
- Nick, K., Schöler, H., Mark, G., Söylemez, T., Akhlaq, M., Schuchmann, H., von Sonntag, C., 1992. Degradation of some triazine herbicides by UV radiation such as used in the UV disinfection of drinking water. *Aqua- Journal of Water Supply: Research and Technology* 41, 82-87.

- Nicole, I., Delaat, J., Dore, M., Duguet, J.P., Bonnel, C., 1990. Use of UV-radiation in water treatment. Measurement of photonic flux by hydrogen-peroxide actinometry. *Water Research* 24, 157-168.
- NIST, N.I.o.S.a.T., NIST chemistry webbook, NIST standard reference database number 69, U.S. Secretary of Commerce on behalf of the United States of America. Available at: <http://webbook.nist.gov/chemistry/>. Accessed on December 2012
- Nöthe, T., Hartmann, D., Fahlenkamp, H., Von Sonntag, C., von Sonntag, J., 2007. Elimination of the musk fragrances galaxolide and tonalide from wastewater by ozonation and concomitant stripping. *Water Science and Technology* 55, 287-292.
- OECD, 2011. Test No. 201: Freshwater Alga and Cyanobacteria, Growth Inhibition Test, OECD Guidelines for the Testing of Chemicals, Section 2, OECD Publishing.
- Palm, W.U., Elend, M., Krueger, H.U., Zetzsch, C., 1997. OH radical reactivity of airborne terbutylazine adsorbed on inert aerosol. *Environmental Science & Technology* 31, 3389-3396.
- Panday, R., 2002. A photochemical investigation of two sunscreen absorbers in a polar and a non-polar medium. M.Sc. Thesis, University of Natal, Durban.
- Ram, K., Anastasio, C., 2009. Photochemistry of phenanthrene, pyrene, and fluoranthene in ice and snow. *Atmospheric Environment* 43, 2252-2259.
- Rao, N.N., Chaturvedi, V., Li Puma, G., 2012. Novel pebble bed photocatalytic reactor for solar treatment of textile wastewater. *Chemical Engineering Journal* 184, 90-97.
- Rodea-Palomares, I., Petre, A.L., Boltes, K., Leganés, F., Perdígón-Melón, J.A., Rosal, R., Fernández-Piñas, F., 2010. Application of the combination index (CI)-isobologram equation to study the toxicological interactions of lipid regulators in two aquatic bioluminescent organisms. *Water Research* 44, 427-438.
- Rodríguez, A., Muñoz, I., Perdígón-Melón, J.A., Carbajo, J.B., Martínez, M.J., Fernández-Alba, A.R., García-Calvo, E., Rosal, R., 2012. Environmental optimization of continuous flow ozonation for urban wastewater reclamation. *Science of the Total Environment* 437, 68-75.
- Rosal, R., Rodríguez, A., Gonzalo, M.S., García-Calvo, E., 2008. Catalytic ozonation of naproxen and carbamazepine on titanium dioxide. *Applied Catalysis B Environmental* 84, 48-57.
- Rosal, R., Gonzalo, M.S., Boltes, K., Letón, P., Vaquero, J.J., García-Calvo, E., 2009. Identification of intermediates and assessment of ecotoxicity in the oxidation products generated during the ozonation of clofibric acid. *Journal of Hazardous Materials* 172, 1061-1068.

- Rosal, R., Rodríguez, A., Perdígón-Melón, J.A., Petre, A., García-Calvo, E., Gómez, M.J., Agüera, A., Fernández-Alba, A.R., 2010. Occurrence of emerging pollutants in urban wastewater and their removal through biological treatment followed by ozonation. *Water Research* 44, 578-588.
- Sanches, S., Leitão, C., Penetra, A., Cardoso, V., Ferreira, E., Benoliel, M., Crespo, M., Pereira, V., 2011. Direct photolysis of polycyclic aromatic hydrocarbons in drinking water sources. *Journal of Hazardous Materials* 192, 1458-1465.
- Santiago, J., Agüera, A., del Mar Gómez-Ramos, M., Fernández Alba, A.R., García-Calvo, E., Rosal, R., 2011. Oxidation by-products and ecotoxicity assessment during the photodegradation of fenofibric acid in aqueous solution with UV and UV/H₂O₂. *Journal of Hazardous Materials* 194, 30-41.
- Santiago-Morales, J., Gómez, M.J., Herrera, S., Fernández-Alba, A.R., García-Calvo, E., Rosal, R., 2012. Oxidative and photochemical processes for the removal of galaxolide and tonalide from wastewater. *Water Research* 46, 4435-4447.
- Santiago-Morales, J., Agüera, A., Gómez, M.M., Fernández-Alba, A.R., Giménez, J., Esplugas, S., Rosal, R., 2013. Transformation products and reaction kinetics in simulated solar light photocatalytic degradation of propranolol using Ce-doped TiO₂. *Applied Catalysis B Environmental* 129, 13-29.
- Serpone, N., Salinaro, A., Emeline, A.V., Horikoshi, S., Hidaka, H., Zhao, J., 2002. An in vitro systematic spectroscopic examination of the photostabilities of a random set of commercial sunscreen lotions and their chemical UVB/UVA active agents. *Photochemical & Photobiological Sciences* 1, 970-981.
- Shang, N.C., Yu, Y.H., Ma, H.W., Chang, C.H., Liou, M.L., 2006. Toxicity measurements in aqueous solution during ozonation of monochlorophenols. *Journal of Environmental Management* 78, 216-222.
- Shemer, H., Linden, K.G., 2006. Degradation and by-product formation of diazinon in water during UV and UV/H₂O₂ treatment. *Journal of Hazardous Materials* 136, 553-559.
- Sires, I., Garrido, J.A., Rodriguez, R.M., Brillas, E., Oturan, N., Oturan, M.A., 2007. Catalytic behavior of the Fe³⁺/Fe²⁺ system in the electro-Fenton degradation of the antimicrobial chlorophene. *Applied Catalysis B: Environmental* 72, 382-394.
- Snyder, S.A., Wert, E.C., Rexing, D.J., Zegers, R.E., Drury, D.D., 2006. Ozone oxidation of endocrine disruptors and pharmaceuticals in surface water and wastewater. *Ozone Science & Engineering* 28, 445-460.
- Stefan, M.I., Bolton, J.R., 2002. UV direct photolysis of N-nitrosodimethylamine (NDMA): kinetic and product study. *Helvetica Chimica Acta* 85, 1416-1426.
- Suarez, S., Dodd, M.C., Omil, F., von Gunten, U., 2007. Kinetics of triclosan oxidation by aqueous ozone and consequent loss of antibacterial activity:

- relevance to municipal wastewater ozonation. *Water Research* 41, 2481-2490.
- Tanaka, K., Reddy, K., 2002. Photodegradation of phenoxyacetic acid and carbamate pesticides on TiO₂. *Applied Catalysis B: Environmental* 39, 305-310.
- Trapido, M., Veressinina, Y., Munter, R., 1995. Ozonation and advanced oxidation processes of polycyclic aromatic hydrocarbons in aqueous solutions—a kinetic study. *Environmental Technology* 16, 729-740.
- U.S National Library of Medicine, ChemIDplusAdvanced. Available at: <http://chem.sis.nlm.nih.gov/chemidplus/>. Accessed on December 2012.
- Valdersnes, S., Kallenborn, R., Sydnnes, L.K., 2006. Identification of several Tonalide® transformation products in the environment. *International Journal of Environmental Analytical Chemistry* 86, 461-471.
- Van der Oost, R., Beyer, J., Vermeulen, N.P.E., 2003. Fish bioaccumulation and biomarkers in environmental risk assessment: a review. *Environmental Toxicology and Pharmacology* 13, 57-149.
- Wan, H.B., Wong, M.K., Mok, C.Y., 1994. Comparative study on the quantum yields of direct photolysis of organophosphorus pesticides in aqueous solution. *Journal of Agricultural and Food Chemistry* 42, 2625-2630.
- Ward, C.P., 2010. Direct and indirect photochemical degradation of two polycyclic musk fragrances and two polycyclic aromatic hydrocarbons in natural waters, M.Sc. Thesis, The Ohio State University.
- Werner, J.J., McNeill, K., Arnold, W.A., 2005. Environmental photodegradation of mefenamic acid. *Chemosphere* 58, 1339-1346.
- Wong-Wah-Chung, P., Rafiqah, S., Voyard, G., Sarakha, M., 2007. Photochemical behaviour of triclosan in aqueous solutions: kinetic and analytical studies. *Journal of Photochemistry and Photobiology A: Chemistry* 191, 201-208.
- Wu, C., Shemer, H., Linden, K.G., 2007. Photodegradation of metolachlor applying UV and UV/H₂O₂. *Journal of Agricultural and Food Chemistry* 55, 4059-4065.
- Wu, C., Linden, K.G., 2010. Phototransformation of selected organophosphorus pesticides: Roles of hydroxyl and carbonate radicals. *Water Research* 44, 3585-3594.
- Zhang, Q.H., Wang, X.C., Xiong, J.Q., Chen, R., Cao, B., 2010. Application of life cycle assessment for an evaluation of wastewater treatment and reuse project—case study of Xi'an. *Bioresource Technology* 101, 1421-1425.
- Zoschke, K., Dietrich, N., Börnick, H., Worch, E., 2012. UV-based advanced oxidation processes for the treatment of odour compounds: Efficiency and by-product formation. *Water Research* 46, 5365-5373.
- Zwiener, C., Weil, L., Niessner, R., 1995. UV- und UV/Ozon-Abbau von Triazinherbiziden in einer Pilotanlage-Bestimmung von Ratenkonstanten und Quantenausbeuten der UV-Photolyse. *Vom Wasser* 84, 47-60.

Chapter 6

**Fate and toxicity of amine-terminated
PAMAM dendrimers under ozonation and
irradiation**

Fate and toxicity of amine-terminated PAMAM dendrimers under ozonation and irradiation *

6.1. Abstract

This article deals with the degradation of a third-generation (G3) poly(amidoamine) (PAMAM) dendrimer under ozonation and irradiation, visible and ultraviolet, processes. The identification and quantification of G3 PAMAM dendrimer and its transformation products has been performed by liquid chromatography–electrospray ionization–hybrid quadrupole time-of-flight–mass spectrometry. The dendrimer was completely depleted by ozone in less than 1 min, while the effect of ultraviolet irradiation was attributed to hydroxyl-mediated oxidation rather than to direct photolysis. The mineralization was limited and the transformation products were the consequence of a retro-Michael fragmentation pathway. The oxidation of these fragments originated highly oxidized structures with abundance of carboxylic acids. We studied the toxicity of oxidized and irradiated mixtures for six different organisms in three different trophic levels: the acute toxicity for the bacterium *Vibrio fischeri* and the microcrustacean *Daphnia magna*, the multigenerational growth inhibition of the alga *Pseudokirchneriella subcapitata*, and the seed germination phytotoxicity of *Licopersicon esculentum*, *Lactuca sativa* and

* The contents of this chapter have been submitted as:

Santiago-Morales, J., Rosal, R., Hernando, M.D., Ulaszewska, M.M., García-Calvo, E., Fernández-Alba, A.R. Fate and toxicity of amine-terminated PAMAM dendrimers under ozonation and irradiation.

Lolium perenne. Both ozonation and irradiation produce transformation products that are more toxic than the parent dendrimer for certain species. The toxicity increase was particularly apparent for *D. magna* in ozonated mixtures and could be attributed to the formation of low molecular weight oxidized species such as carboxylic acids, including formic acid. The toxicity of G3 dendrimer was linked to a strong increase of intracellular ROS measured by DCF and Bodipy fluorescence. Meanwhile, the DCF signal indicated that ROS-damaged cells coexisted with other apparently normal, intense lipid peroxidation localized in certain intracellular bodies of algal cells.

6.2. Introduction

The use of manufactured nanomaterials has been rapidly increasing during the last years in a wide variety of applications. In view of the concern associated with their environmental risk, the Organization for Economic Co-operation and Development (OECD) recently published a list of nanomaterials for which toxicology measurement and risk assessment are necessary (OECD, 2010). These are carbon products, metals, metal oxides, nanoclays and dendrimers. This work focuses on the latter, which are hyperbranched nanoscale polymers possessing uniform size, defined molecular weight, large internal cavities and a high number of surface groups that make them particularly tunable in terms of solution chemistry (Svenson and Tomalia, 2005). These features make them suitable for several applications such as pharmaceutical and cosmetic additives, drug vectors or analytical carriers (Baker and Majoros, 2008).

The occurrence of dendrimers in the environment has not yet been reported but they are likely to be detected at least in view of their excretion profiles: it has been reported that the elimination of G3 and G5 PAMAM in mice via urine ranged from 1 to 5% of injected dose (ID) per gram of tissue while for G7 PAMAM it achieved a maximum 74 % ID/g 4h

after injection (Roberts et al., 1996). Kobayashi and Brechbiel (2005), however, observed that macromolecular contrast agents based on PAMAM lower generations (G2-G4) were mainly excreted via kidney, whereas the higher ones (G7-G10) were processed in liver.

The ecotoxicity of PAMAM dendrimers is limited to few studies in which EC_{50} ranged from 0.13 μM of ethylenediamine core G6 PAMAM for *Daphnia magna* (48 h) to 194 μM of G2 PAMAM dendrimer for a 30 min exposure *Vibrio fischeri* assay (Suárez et al., 2011). In general, positively charged dendrimers lead to higher toxic effects and for the same generation, dendrimers with hydroxyl or carboxylic-acid terminal groups showed a much higher EC_{50} than their amine-terminated counterparts (Kitchens et al., 2007). Once released to the environment, dendrimers would undergo transformation by biotic and abiotic processes, the latter including irradiation and oxidation in wastewater treatment facilities.

The aim of this work was to explore the effect of ozonation and germicidal ultraviolet (UV, 254 nm) on G3 amine-terminated PAMAM dendrimer. In addition, we studied the photochemical stability of this dendrimer under visible light irradiation driven by an arc-Xenon lamp in order to reproduce the situation that could take place in an aquatic ecosystem. We paid special attention to the generation of transformation products (TP) and the toxicity associated with their mixtures, the rationale being that it has been observed that TP of organic pollutants are often more toxic than their parent compounds (Schmitt-Jansen et al., 2007; Santiago-Morales et al., 2012).

The identification of G3 dendrimer and its TP has been performed by liquid chromatography–electrospray ionization–hybrid quadrupole time-of-flight–mass spectrometry (LC-ESI-QTOF-MS). This analytical technique allows the resolution of these complex molecular structures using multiply charged tracer ions and their $^{13}\text{C}/^{12}\text{C}$ isotopic distribution (Hernando et al., 2012). The toxicity assessment of partially oxidized and irradiated mixtures

was conducted using six different organisms belonging to three different trophic levels. The bioassays used were the inhibition of the constitutive luminescence of the bacterium *Vibrio fischeri* (decomposer), the immobilization of the microcrustacean *Daphnia magna* (primary consumer), the multigenerational growth inhibition of the green alga *Pseudokirchneriella subcapitata*, and the seed germination tests for the plants *Lycopersicon esculentum*, *Lactuca sativa* and *Lolium perenne*.

6.3. Methodology

6.3.1. Materials

Amine terminated G3 PAMAM-(NH₂)₃₂ dendrimer (CAS Number 153891-46-4) aqueous solution was purchased from Dendritech (Midland, USA). The dilutions were prepared using pure water obtained from a Millipore Mili-Q system with a resistivity of at least 18 MΩcm⁻¹ at 25 °C. Sodium hydroxide and hydrochloric acid (purity >95 %) were used for pH adjustments. Phenol, ethanol (95% v/v), sodium nitropusside, sodium citrate and sodium hypochlorite used as described below were analytical grade reagents from Sigma-Aldrich. Methanol and acetonitrile (HPLC-grade) were supplied by Merck. Water used for LC-MS analysis was generated from a Direct-Q™ 5 Ultrapure water system (Millipore). Formic acid (98% purity) was purchased from Fluka. The fluorescence dyes 2',7'-dichlorofluorescein diacetate (H₂DCFDA) and C4-Bodipy were obtained from Invitrogen Molecular Probes.

6.3.2. Experimental setup and procedure

Ozone was produced by a corona discharge and continuously bubbled by means of a porous glass disk with a gas flow of 0.21 Nm³ h⁻¹ at a concentration of 12 g Nm⁻³. Further details are given elsewhere (Rosal et al., 2008a). The irradiation experiments were conducted using a 15 W Heraeus Noblelight TNN 15/32 low-pressure mercury vapour lamp (254

nm) and a Heraeus TQ Xe 150 Xe-arc lamp emitting in the visible region. Both were located inside a quartz sleeve jacketed and thermostated at 25°C. In the case of visible light irradiations, an additional borosilicate glass tube was used to cut-off wavelengths < 290 nm. Fluence rates per unit volume were $6.01 \times 10^{-6} \text{ E L}^{-1} \text{ s}^{-1}$ (254 nm) for UV lamp and $1.05 \times 10^{-6} \text{ E L}^{-1} \text{ s}^{-1}$ (290-400 nm) for Xe-arc lamp determined by chemical actinometry of hydrogen peroxide and 2-nitrobenzaldehyde for UV and Xe lamps, respectively (Nicole et al., 1990; Allen et al., 2000). All experiments were conducted in batch mode in 1.3 L vessel magnetically stirred at 900 min^{-1} and pH was kept at 7.0 ± 0.2 units throughout the run.

6.3.3. Analyses

The structural elucidation of TP was carried out using a hybrid quadrupole time-of-flight mass spectrometer TripleTOF 5600 system (AB SCIEX) with an ESI (electrospray ionization) source coupled to an Agilent 1200 Series HPLC system. The TripleTOF 5600 system combines high resolving power and mass accuracy with a mass range up to 40000 Da. The optimized ion source-dependent parameters were: ion spray voltage floating, 5500 V (ion spray voltage); temperature, 550°C; curtain gas flow rate, 25 psi (flow of N₂ to the curtain gas interface located between the curtain plate and the orifice) and ion source gas (GS1 and GS2) at a pressure of 40 psi (GS1 controls the nebulizer gas, N₂, and GS2, the heater gas, N₂). Flow injection analysis compound optimization was performed in full scan positive ion mode using a declustering potential of 20 V and collision energy of 10 eV. Mass calibration and resolution adjustments were performed automatically with a 10^{-5} M solution of poly(propylene glycol). The QTOF system accomplishes external calibration with a $0.167 \text{ pmol } \mu\text{L}^{-1}$ solution of reserpine through both an automated instrument calibration and an auto-batch calibration. The MS was operated with a resolution power of approx. 20000 *fwhm* (full width at half maximum) in full scan at *m/z* 609.28066 (C₃₃H₄₀N₂O₉, reserpine).

The LC analysis was performed with a reversed-phase C5 analytical column (150 mm length x 4.6 mm i.d. and 5 μm particle size, 300Å, Phenomenex). Mobile phases A and B were, respectively HPLC-grade water and acetonitrile with 5% of water, both with 0.1% formic acid. A linear gradient was set from 90% to 70% of A in 20 min, decreased up to 0% in 2 min and then maintained for 2 min. The re-equilibration time was set for 5 minutes. The injection volume was 20 μL . Data acquisition and processing were carried out using Analyst® TF 1.5.1 and PeakView™ (AB SCIEX) software. PeakView incorporates tools for compound identification (Mass Calculator, Isotope Distribution Calculator and Formula Finder) based on the accurate mass measurement.

Total Organic Carbon (TOC) was determined using a Shimadzu TOC-VCSH total carbon organic analyzer. Carboxylic acids, nitrite and nitrate were analyzed by means of a Dionex DX120 Ion Chromatograph equipped with a conductivity detector and a cation suppressor coupled to a column IonPac 4 x 250 mm AS9-HC. Ammonia was measured using the method of Solorzano (1969). The concentration of ozone dissolved in the aqueous phase was measured with an amperometric Mettler Toledo 358/210 dissolved ozone sensor calibrated using the Indigo Colorimetric Method (SM 4500-O3 B). The concentration of ozone in gas phase was determined using an Anseros Ozomat GM6000 Pro photometer calibrated against potassium iodide. Zeta potential was measured using electrophoretic light scattering in a Malvern Zetasizer instrument.

6.3.4. Toxicity determinations

The green alga *P. subcapitata* was used to conduct multigenerational growth inhibition test following the procedure displayed in OECD TG 201 open system. Algae were cultured in OECD growth medium at pH adjusted to 8.0 ± 0.2 . The exposed cultures were run in 96-well microplates with a total dosed volume of 250 μL , each well containing

225 μL of the sample in OECD growth medium and 25 μL of microalgae ($\sim 2 \times 10^4$ cells/mL). Algae were grown in a chamber under continuous fluorescent illumination of $100 \mu\text{E m}^{-2} \text{s}^{-1}$ at $23 \text{ }^\circ\text{C}$. The chlorophyll content was measured by fluorescence (Excitation 450 nm – Emission 672 nm) using a Fluoroskan Ascent FL plate fluorometer-luminometer.

The production of ROS was assessed at 72 h treating the cells with H_2DCFDA , the intracellular oxidation of which originates 2,7-dichlorofluorescein (DCF), which serves as an indicator for hydrogen peroxide and related ROS. A volume of 10 μL of a 10 mM H_2DCFDA stock solution was added to each well. After 1 h of incubation at room temperature DCF was measured by fluorescence. C4-Bodipy was used for evaluating lipid peroxidation as it is oxidized by peroxy radicals yielding a green fluorescence after incubating for 30 min with a final concentration of C4-Bodipy of about 5 μM . For micrographs, DCF and Bodipy fluorescence was recorded using a confocal fluorescence microscope (Spectral Leica TCS SP5) with excitation at 488 nm; chlorophyll/DCF and chlorophyll/C4-Bodipy, while emissions were recorded at 665 nm and 535 nm, respectively.

The phytotoxicity was assessed using the seed germination test for one monocotyledon *Lolium perenne* (English ryegrass) and two dicotyledons, *Lycopersicon esculentum* var. “Marmande” (tomato) and *Lactuca sativa* var. “Maravilla de Verano” (lettuce) corresponding to the families *Solanaceae* and *Asteraceae* respectively. Certificated non-treated seeds from organic farming were used. The assays were conducted according to US EPA procedures (EPA, 1996). Prior to placing seeds, a volume of 5 mL of sample adjusted at $\text{pH } 7 \pm 0.2$ was added to 9 cm diameter Petri dishes containing a cellulose filter paper disk. Seed surface was sterilized with sodium hypochlorite. Ten sterilized seeds with three replicates were placed on each paper disk. The Petri dishes were incubated in the dark at 23°C for six days to ensure $> 65\%$ germination of control seeds with roots of at least 20 mm long. The results were expressed using a germination index (GI) in

which N_s and N_c are numbers of germinated seeds, and L_s and L_c average root lengths for sample and control respectively (Komilis et al., 2005):

$$GI = \frac{N_s L_s}{N_c L_c} \quad (1)$$

The photoluminescence inhibition of bacteria *V. fischeri* was carried out according to the ISO 11348-3 standard protocol using the commercial Biofix Lumi test (Daphtoxkit F™ magna, Creasel, Belgium) acquired from Macherey Nagel, Germany. The inhibition was measured at 16.5 ± 1.1 °C in a Fluoroskan Ascent FL plate luminometer. Toxic inhibition was determined with respect to light emitted in the absence of any toxic influence after 30 min exposure.

The immobilization of *D. magna* was tested using the commercial test kit Daphtoxkit (Creasel, Belgium) according to the European Guideline OECD TG 202. The incubation of dormant eggs in a standard culture medium was conducted in a 6000 lux chamber at 20 °C \pm 1 °C to induce hatching. The bioassay was performed for 48 h in the dark at 20°C. The neonates were counted as immobile when they did not display swimming movements within 15 s.

The analysis of toxicity data was performed using the add-on package 'drc' version 2.3-0 for the open source program and environment R (<http://www.r-project.org>). The best fitting of experimental data for *V. fischeri*, *D. magna* and *P. subcapitata* was the five parameter log-logistic function:

$$E(x) = c + \frac{d - c}{[1 + e^{b[\log(x) - \log(EC_{50})]}]g} \quad (2)$$

where $E(x)$ indicates the average response at dosage x , c and d are the lower and upper horizontal asymptotes, respectively, b the relative slope at EC_{50} and g the asymmetry curve parameter. For plant germination bioassays, Brain and Cousens' model was chosen because of the hormesis effect observed (Fig. 6.8):

$$E(x) = c + \frac{d - c + fx}{[1 + e^{b[\log(x) - \log(EC_{50})]}]g} \quad (3)$$

This model is a variation from the four-parameter log-logistic one in which $g = 1$ and where f represents the size of the hormesis effect: the larger the value the larger the hormesis effect is. This parameter is positive in the presence of hormesis. Parameters b and e have no straightforward biological meaning, while d and c retain those of Eq. 2. EC_{50} , EC_{20} , EC_{10} and their confidence intervals (CI) were estimated using the described 'drc' packages and fitting models.

6.4. Results

G3 PAMAM-(NH₂)₃₂ dendrimer at an initial concentration of 100 mg L⁻¹ (14.5 μM) was treated by ozone and ultraviolet and visible light irradiation. During the first minute of UV irradiation, the initial concentration of G3 PAMAM-(NH₂)₃₂ was reduced by 30% reaching about 95%

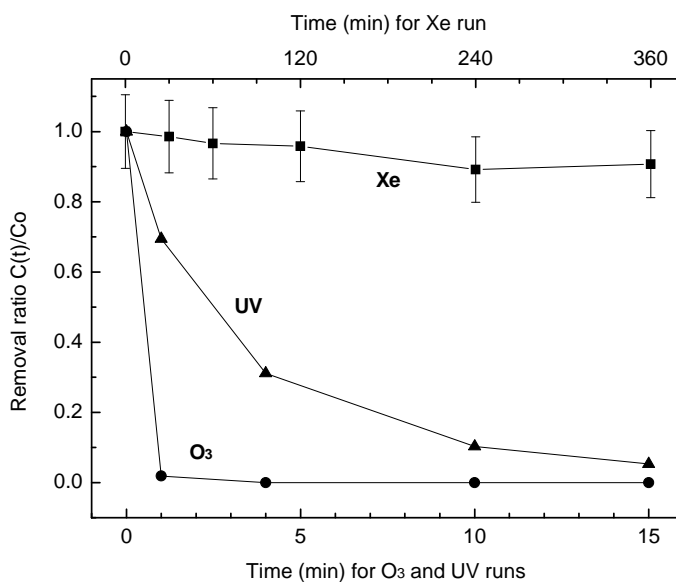


Figure 6.1. G3 PAMAM-(NH₂)₃₂ removal during ozone (O₃), ultraviolet (UV) and visible light irradiation (Xe).

after 15 min. Visible light (> 290 nm) irradiation also resulted in low but significant (for 240 min) dendrimer depletion, which was otherwise lower than 10%. The results of dendrimer depletion are displayed in Fig. 6.1, which represents runs performed at pH 7.0 and 25°C in pure water.

The evolution of TOC, carboxylic anions (formiate and oxalate) and nitrogen species (nitrate, nitrite and ammonia) were monitored during reactions. While neither UV nor visible light irradiation led to measurable TOC reduction or ion release, the results for ozonation are shown in Fig. 6.2. No significant mineralization took place during the first 15 min of ozonation, a period after which TOC started to display a slow decline. TOC

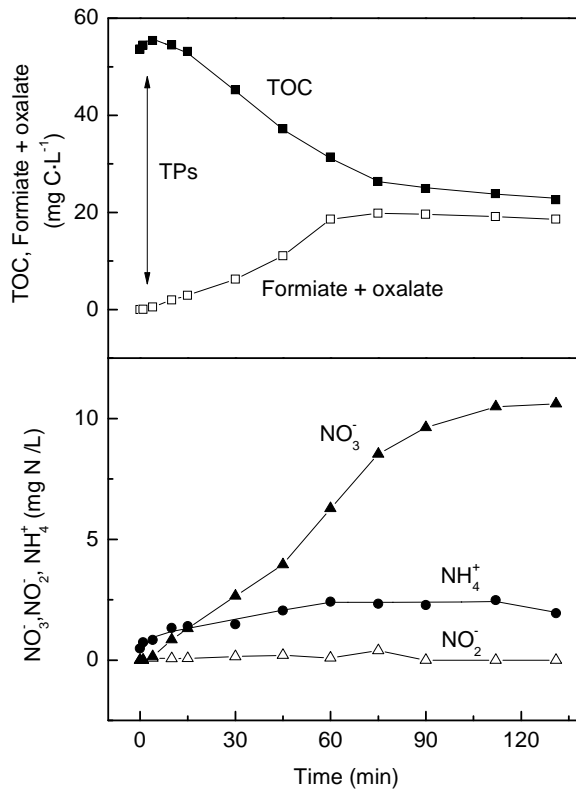
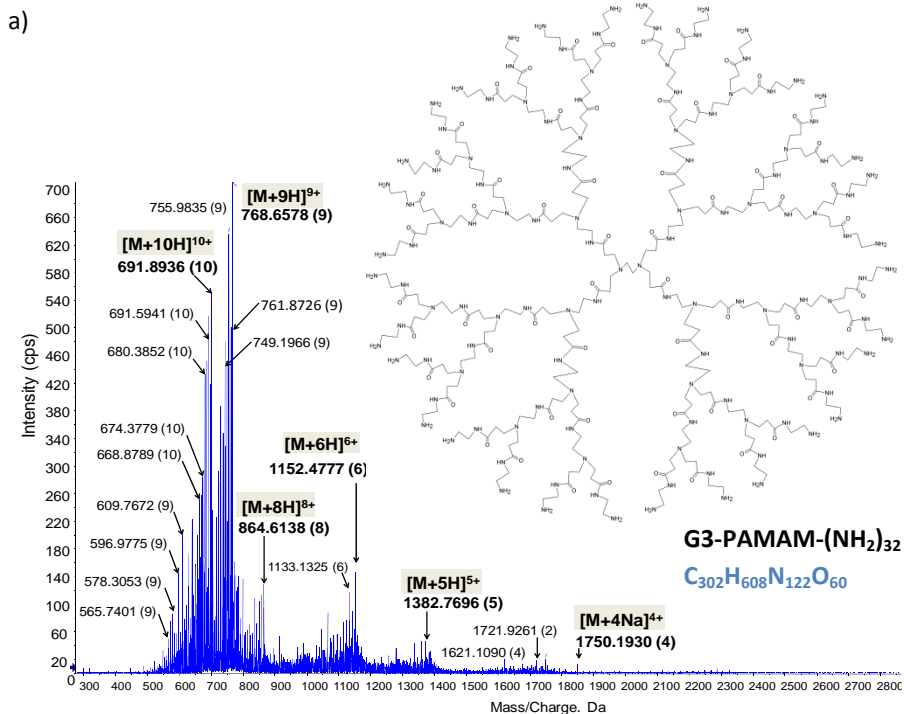


Figure 6.2. Nitrogen release, TOC evolution and carboxylic acids produced during the ozonation of G3 PAMAM-(NH₂)₃₂.

removal was 50.8% after 75 min, after which additional ozone exposure for 56 min more only led to an extra 7% removal. The concentration of carboxylic anions increased with time up to 75 min to stabilize thereafter, with an evolution parallel to TOC. Concerning nitrogen, an initial release of ammonia was observed during ozonation, its concentration increasing up to 2.4 mgN L⁻¹. Nitrite was detected in low concentration (< 0.4 mgN L⁻¹) but nitrate constantly rose during the whole ozone treatment up to about 10 mgN L⁻¹.

G3 PAMAM-(NH₂)₃₂ dendrimer contains an ethylenediamine core bonded with four tertiary amine branches (corresponding to the generations 0, 1, and 2) and 32 surface groups of primary amines. The multiple-charging phenomenon observed in this dendrimer, by means of electrospray ionization, has provided key advantages. Accurate mass measurement below ±2.5 ppm for the selected diagnostic ions as well as assignment of elemental composition and charge state, through resolution of isotopic clusters ¹³C/¹²C, provided high confidence in the determination of PAMAM G3. Fig 6.3 shows a LC-ESI-QTOF-MS mass spectrum of G3-PAMAM-(NH₂)₃₂ in full scan mode, characterized by a charge state distribution of the protonated molecular ion up to +10 (*MW*, 3254.29). Mass error for the most abundant isotopic clusters +10, +9 and +6, selected as diagnostic ions, was in the (-2.3) - 1.9 ppm range. From the entire list of feasible molecular formulas, ranked according to the best results of mass error and ¹³C/¹²C isotope distribution, the molecular formula (C₃₀₂H₆₀₈N₁₂₂O₆₀+9H)⁹⁺ was attributed to the protonated molecule [M+9H]⁹⁺ at *m/z* 768.6578 (mass error of -2.3 ppm). Isotopic distribution of [M+9H]⁹⁺ was characterized by a peak-spacing of 0.11 *m/z* unit (approx. 20000 *fwhm*), sufficient to achieve charge state assignment. This enhanced resolution is also key for providing reliance in the structural elucidation of unknowns. Fig. 6.4a shows an overlay of seven chromatograms (corresponding to the TIC, *total ion chromatogram*) of samples withdrawn at different times of ozonation, where the depletion of G3-PAMAM-(NH₂)₃₂



b)

- Spectrum from + QTOF MS (250 - 3000) from 8.189 to 8.945 min
- Isotopic Distribution for C₃₀₂H₆₀₈N₁₂₂O₆₀H₉⁹⁺

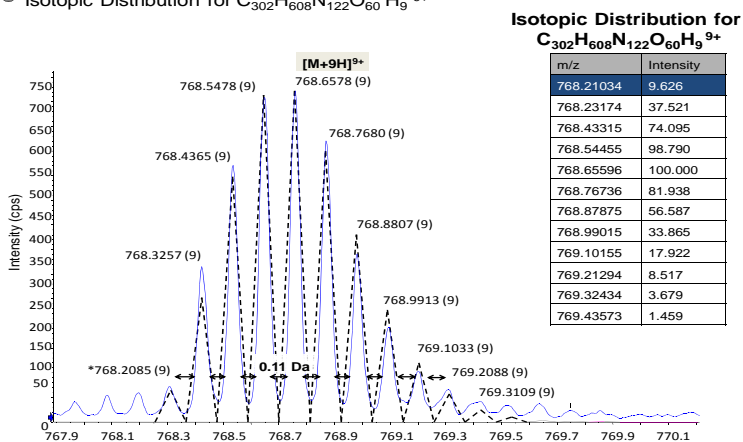


Figure 6.3. (a) LC-ESI-QTOF-MS full scan spectrum of PAMAM dendrimer of third-generation G3. (b) Resolution of isotopic cluster $[M+9H]^{9+}$. ¹³C/¹²C isotopic distribution and isotopic peak spacing.

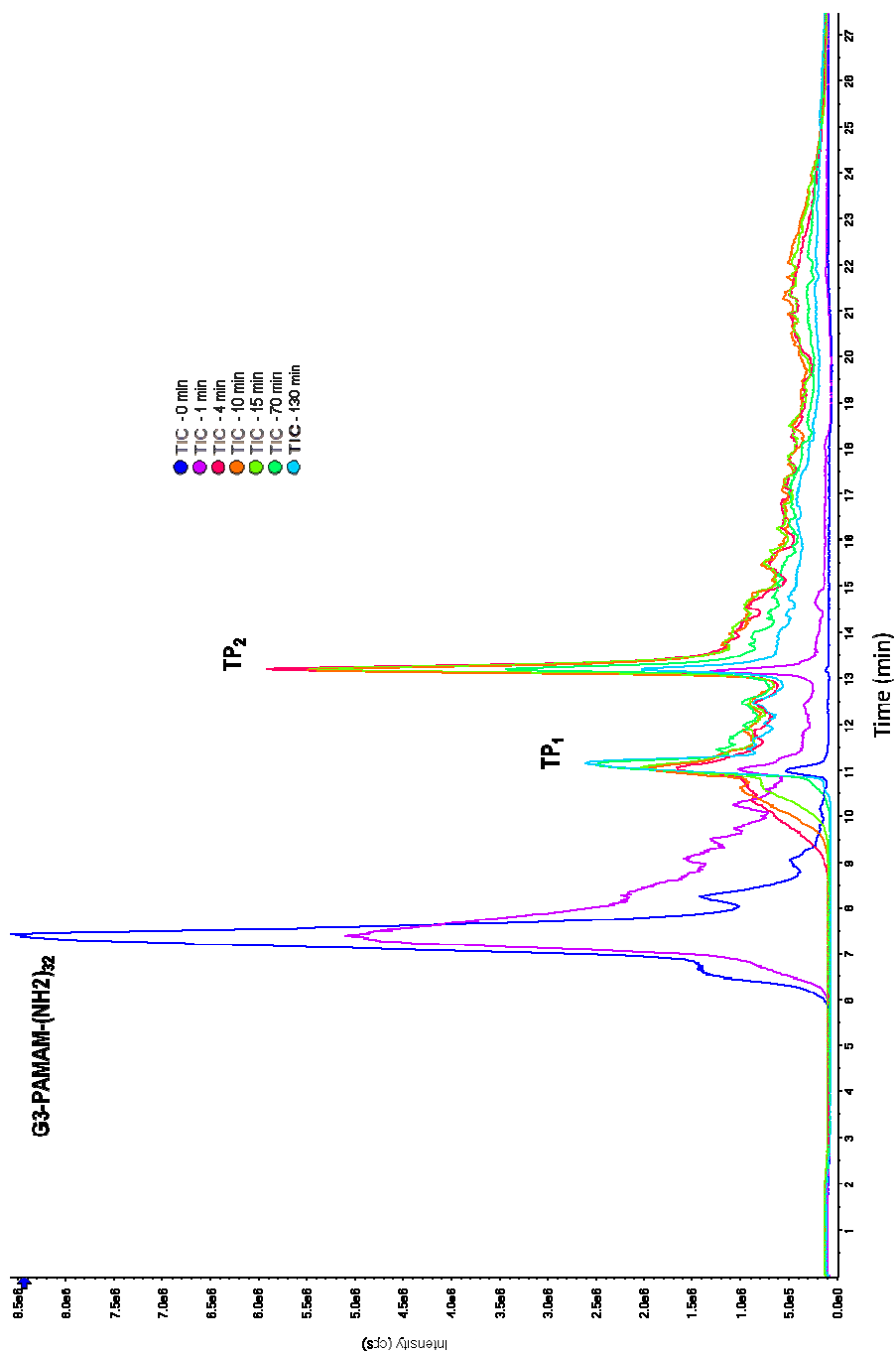


Figure 6.4. (a) Total ion chromatograms (TIC) of samples collected at different times of treatment (up to 130 min) showing depletion of G3-PAMAM-(NH₂)₃₂ and formation of two TP.

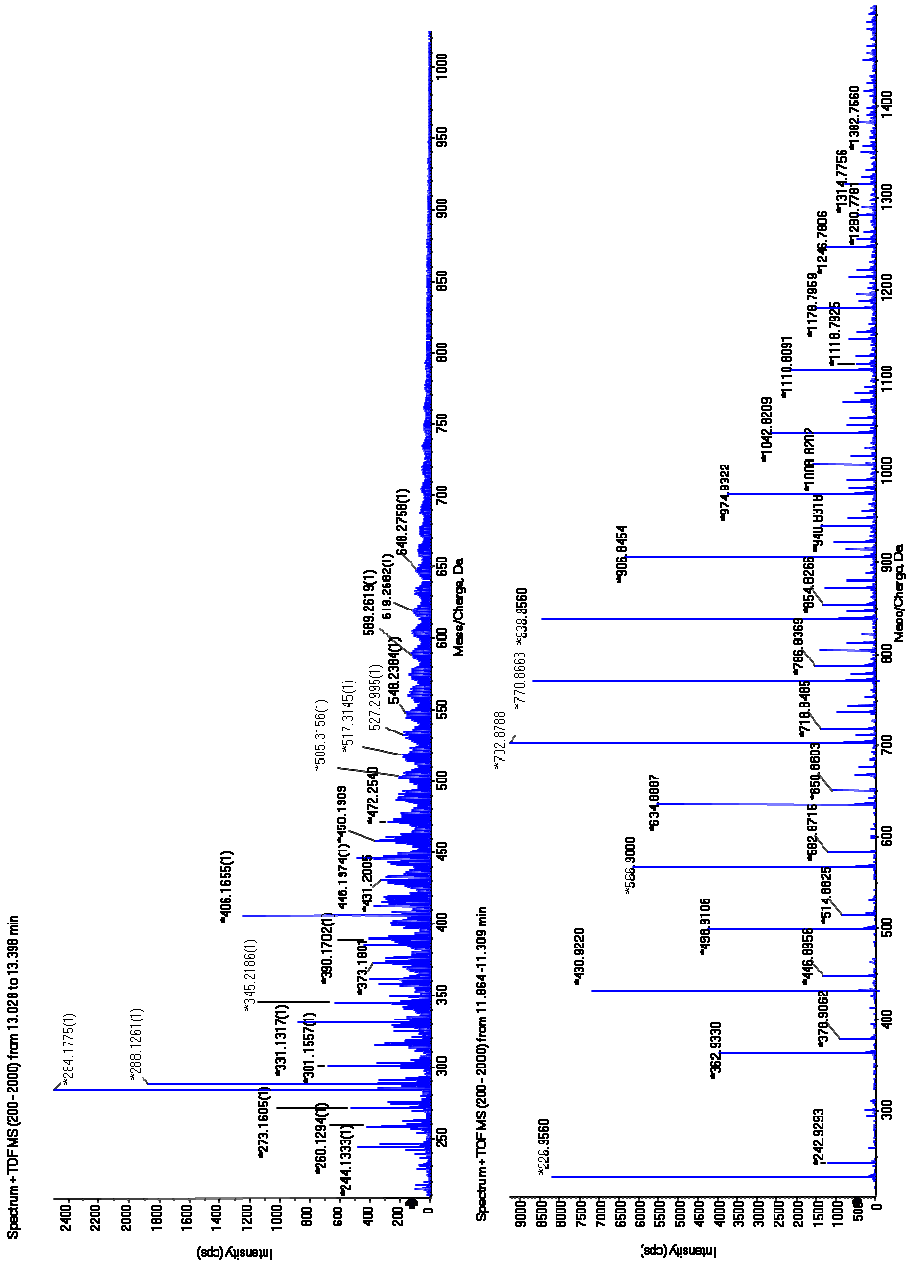


Figure 6.4. (b) LC-ESI-QTOF-MS full scan spectrum of TP1 (130 min ozonation) and TP2 (15 min ozonation).

(peak at retention time, Rt, 7.5 min) and the formation of two TP are displayed. TP₁ (at Rt 11.0 min) showed a maximum in the signal intensity after 130 min on stream but lower (over 3 times) than the TP₂ (at Rt 13.1 min), after 4 min of treatment. Fig. 6.4b shows the full scan mass spectrum of TP₁ and TP₂ observed under ozonation. After 15 min of UV irradiation, another minor TP (TP₃) was detected. The discussion concerning the structural elucidation of these TP is given in the following section.

The toxicological endpoints EC₅₀, EC₂₀ and EC₁₀ of G3 PAMAM-(NH₂)₃₂ are shown in Table 6.1. The toxic effect of G3 PAMAM dendrimer increased for the tested organisms in the following order *P. subcapitata* > *D. magna* > *L. esculentum* ≈ *L. sativa* > *L. perenne* > *V. fischeri*. Fig. 6.5 displays the results of the toxicity assessment of the mixtures obtained from G3 PAMAM-(NH₂)₃₂ in ozonation or irradiation assays; i.e.: partially ozonated and irradiated mixtures. During ozonation runs, both the growth inhibition of *P. subcapitata* and the immobilization of *D. magna* initially decreased in parallel with dendrimer depletion. After 15 min, however, the toxicity to *D. magna* increased again up to 100% immobilization at 71 min. The opposite effect was observed for *L. sativa* and *L. esculentum*, for which a toxicity increase (GI decrease) was observed during the first part of the ozonation runs. In the case of *V. fischeri*, for which neither the dendrimer nor its transformation mixtures were particularly toxic, a certain toxicity increase was observed at intermediate times, with luminescence inhibition near 30% after 15 min. During UV irradiation, a toxicity reduction was observed for *D. magna*, with low or no effect for *P. subcapitata* and *V. fischeri*. GI for *L. esculentum* and *L. sativa* (and with less significant results for *L. perenne*) increased during the first few minutes on stream to decrease thereafter in more deeply oxidized mixtures. Visible light irradiation significantly affected *D. magna*, with 30% immobilization increase. No toxicity changes were observed for *P. subcapitata* and *V. fischeri* and for the three plant seeds. In all cases, samples irradiated up to 6 h did not lead to significant effects on GI.

Table 6.1. Dose-Effect Relationship Parameters for the bioassays used in this work. In parenthesis 95% confidence intervals. EC₅₀, EC₂₀ and EC₁₀ are expressed in milligrams per liter. GI: Germination Index. ^a Clear microplate (upper and lower irradiation), ^b Black bottom microplate (upper irradiation)

	<i>V.fischeri</i>	<i>Pseudokirchneriella subcapitata</i>	<i>Daphnia magna</i>	<i>Lolium perenne</i>	<i>Licopersicon esculentum</i>	<i>Lactuca sativa</i>
EC50	-	0.41 ^a (0.39-0.43) ^a 0.15 ^b (0.13-0.17) ^b	1.45 (0.49-2.40)	259 (230-289)	191 (170-212)	185 (135-234)
EC20	833 (335- 1331)	0.23 ^a (0.20-0.26) ^a 0.078 ^b (0.058-0.098) ^b	0.231 (0.025-0.437)	169 (147-191)	117 (105-129)	123 (92-154)
EC10	100 (37-163)	0.129 ^a (0.083-0.176) ^a 0.050 ^b (0.031-0.070) ^b	0.076 (0.001-0.140)	143 (120-165)	97 (86 – 108)	108 (79-138)
Model	Log-Logistic	Log-Logistic	Log-Logistic	Brain-Cousens (hormesis) f = 0.23 ± 0.10	Brain-Cousens (hormesis) f = 0.41 ± 0.11	Brain-Cousens (hormesis) f = 1.55 ± 0.61
Notes	Conc. range: 0-1000 mg L ⁻¹ 21.9 ± 0.1% inhibition at 1000 mg L ⁻¹	Conc. range: 0-2.5 mg L ⁻¹ Microplate	Conc. range: 0-100 mg L ⁻¹	GI Conc range: 0-1000mg/L	GI Conc range: 0-1000mg/L	GI Conc range: 0-1000mg/L

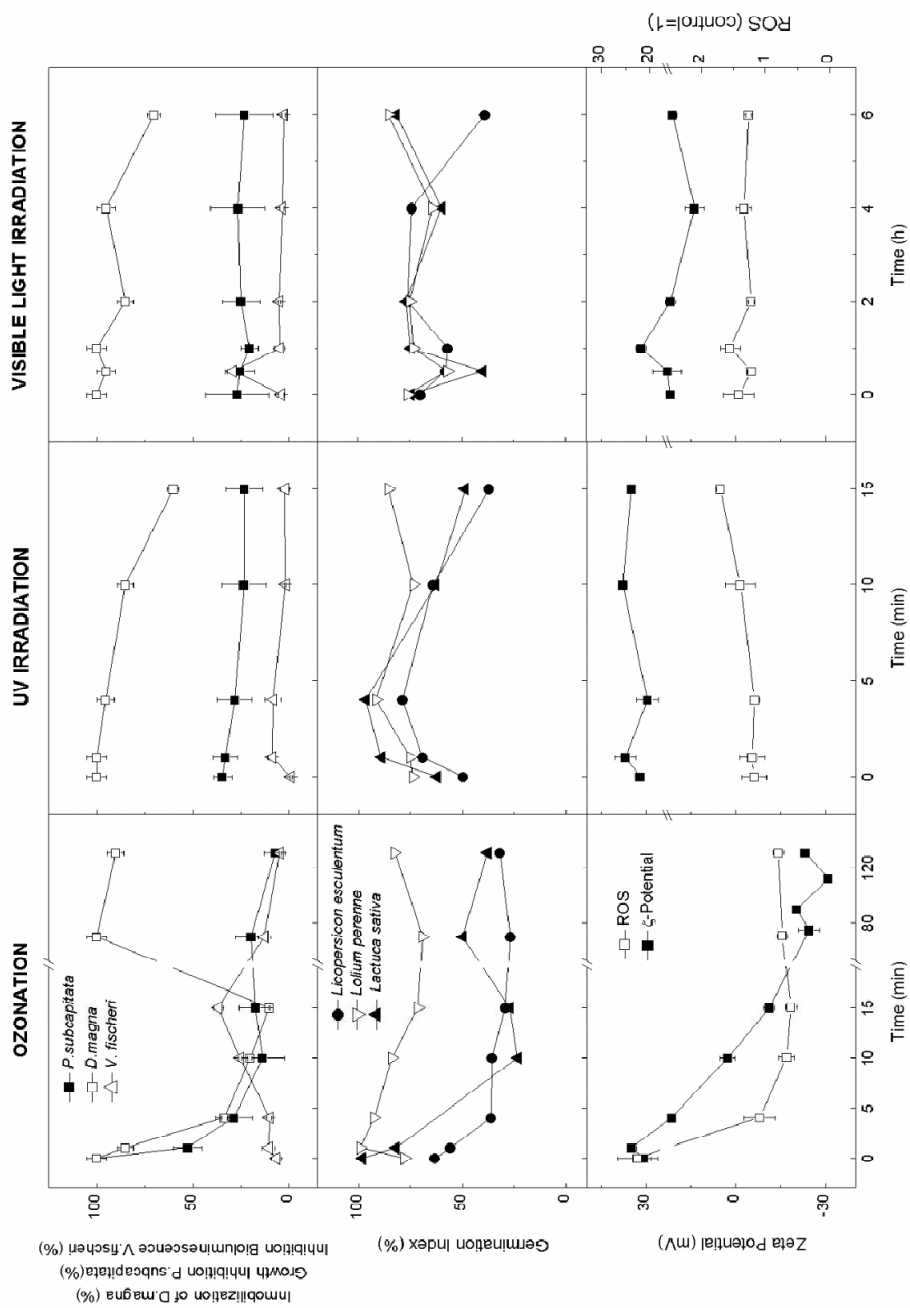


Figure 6.5. Toxicity assessment of ozonated and irradiated mixtures

With respect to zeta potential also shown in Fig 6.4, it decreased during ozonation runs from $+30.8 \pm 2.6$ mV at 0 min to -11.3 ± 1.8 mV at 15 min, dropping to -23.2 ± 1.8 mV at 131 min. Irradiation treatments kept positive zeta potential values for G3 PAMAM-(NH₂)₃₂ with only minor variations during treatments. The same behavior was found for ROS production, measured by DCF fluorescence, which rapidly decreased during the first minutes of ozonation. ROS production slightly increased during UV irradiation with statistically significant data after at least 15 min of irradiation (Fig. 6.5).

Figs. 6.9 and 6.10 show confocal microscopy images of cells of *P. subcapitata* exposed to G3 PAMAM-(NH₂)₁₆ during 72 h. Intense DCF and Bodipy signals came out as a consequence of the production of ROS and lipid peroxidation, respectively. DCF fluorescence appeared in certain damaged cells and aggregates, which coexisted with cells with apparently no damage. C4-Bodipy fluorescence appeared at certain specific places within green algae and with high intensity in aggregates of cells and cell debris.

6.5. Discussion

Ozone was capable of removing +98% of dendrimer during the first minute on stream, which corresponded to an ozone dosage of 47.9 ± 4.2 μ M. The reaction was rapid as evidenced by the fact that ozone was not detected in solution during the first 12 min on stream. Irradiation treatments did not lead to a significant mineralization, but UV irradiation removed 85% of the initial dendrimer after 10 min. As explained below, this could be a consequence of the vacuum ultraviolet (185 nm, VUV) irradiation of low-pressure mercury lamps, which represented about 5% of the total power emitted for the lamp used in this work. The effect of VUV irradiation is due to the photolysis of water with subsequent formation of

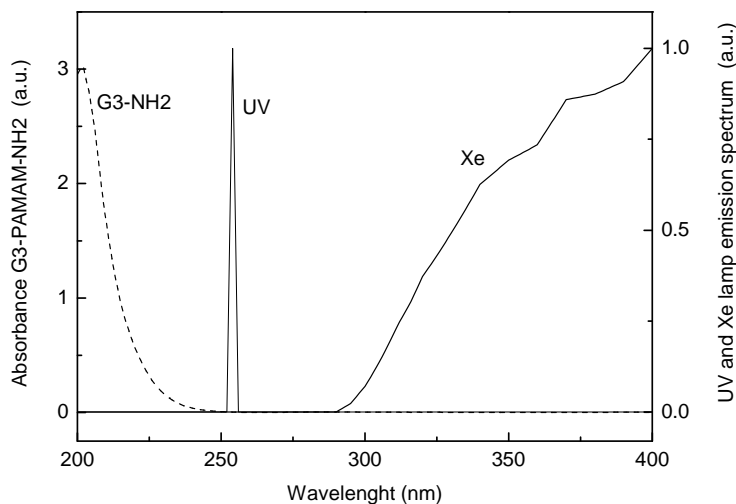


Figure 6.6. G3 PAMAM-(NH₂)₃₂ absorption spectrum and Xe and UV lamp emission spectra.

hydroxyl radicals (Thomson et al., 2002). This observation is further supported by the minimum overlap of G3 PAMAM-(NH₂)₃₂ absorption spectrum and lamp emission spectra as shown in Fig. 6.6. The maximum TOC decrease corresponds to a 57% of the initial organic carbon introduced with the dendrimer (52.4 mgC L⁻¹). The nitrogen liberated as nitrate represents 43% of the dendrimer nitrogen both figures indicating that the mineralization of organic carbon and the release of nitrogen as nitrate run in parallel as graphically displayed in Fig. 6.2. The rate of mineralization decreased as the reaction proceeded. This is shown in Fig. 6.7, which displays the logarithmic decay of TOC with exposure to dissolved ozone. The pseudo-second order rate constant of the ozonation process, R , fell from 32.8 M⁻¹ s⁻¹ from 15 to 45 min, approximately, to 1.1 M⁻¹ s⁻¹ for contact times over 75 min. Mineralization is not a single chemical process but represents a series of reactions that are slower for highly oxidized molecules, such as carboxylic acids. Parameter R is not constant except for a limited period of time and characterizes the progress

of the ozonation process by connecting ozone profiles and TOC decay (Rosal et al., 2008b).

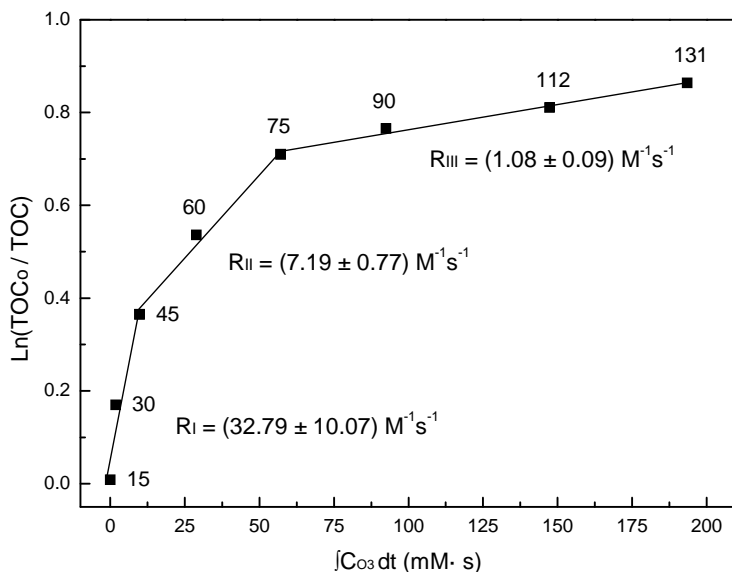


Figure 6.7. Logarithmic decay of TOC as a function of the integral exposure to dissolved ozone. R_i represent the second order rate constants for the mineralization process.

PeakView software was used for exploring and processing LC-ESI-QTOF-MS mass spectral data to elucidate the chemical structure of TP_1 and TP_2 with the following scheme: (i) selection of an ion with the highest m/z ratio for further assignment of a molecular formula with an acceptable mass error, (ii) molecular formula assignment to the ions of lower m/z ratio, mostly those with a relative intensity higher than 20% (fragment ions presumably formed in the ionization source from the intact ionic molecule, the TP) and, (iii) to assemble and elucidate the structure of the TP from the structures proposed for the diagnostic ions. Table 6.2 presents the empirical formulas of the diagnostic ions and the proposals of chemical structures of TP generated under ozonation and UV irradiation. Formula-Finder allowed assignment of empirical formulas from a list of candidates.

Mass accuracy below ± 2 ppm is generally accepted in the case of compounds of low molecular mass (Lacorte and Fernández-Alba, 2006). For chemicals of higher molecular weight there are no well-established criteria regarding mass accuracy for structural elucidation. For instance, in the analysis of peptides and proteins, the influence of mass resolution and peak shapes, gives rise to errors as high as ~ 10 -100 ppm (Strupat, 2005; Joyner et al., 2013). At least three ions with mass error below 10 ppm were required to characterize TP. To elucidate the major TP (TP₂), the monocharged ions at m/z 505.3156 (8.9 ppm), 517.3145 (6.5 ppm) and 527.2995 (7.7 ppm) were selected, despite their relative intensity 10-15%, but within mass error tolerance. Additionally the ions at m/z 273.1605 (15.7 ppm), 284.1775 (13.7 ppm), 288.1261 (-15.9 ppm), 345.2186 (14.1 ppm) of higher relative intensity (28-100 %) were also taken into consideration. The ion at m/z 527.2995 was assigned to a unique elemental composition $C_{24}H_{41}N_5O_8^{*+}$, which may lead to several structures. To overcome this constraint, a detailed examination of tentative structures stoichiometrically coherent with a polyamidoamine dendrimer, was carried out using the structure elucidation tool. MS fragmentation pattern of PAMAM from generation G0 to G3 by LC-ESI-QTOF-MS/MS was discussed in a previous article (Ulaszewska et al., 2013). Most of the product ions arose from retro-Michael pathway, involving neutral losses of amino amide branch (114 Da) or part of this branch (102 Da). The ion at m/z 527.2995 may result from hydrogen migration and α -cleavage reaction at the most exterior tertiary amines and sequential losses of amino amide branches resulting in a structure similar to a dendrimer of generation G0 with an ethylenediamine core and a dendron of the layer corresponding to a G1. The oxidation of this structure resulted in the formation of carboxylic acids, also observed for the ions at m/z 505.3156 ($C_{22}H_{43}N_5O_8^{*+}$) and 517.3145 ($C_{23}H_{43}N_5O_8^{*+}$). It has been suggested that the initiation of photo-oxidation of polyamides, predominantly occurs through a radical attack, ascribing the initiation to the direct scission of the C-N bond of the amide group

Table 6.2. Identification of transformation products (TP) of PAMAM dendrimer of third generation by LC-ESI-QTOF-MS analysis. Mass measured of major diagnostic ions detected under ozonation and UV irradiation, mass error (ppm), elemental composition and proposed structures. TP1: ozonation, 15 min of treatment; TP2: ozonation 130 min of treatment; TP3: UV irradiation, 15 min of treatment.

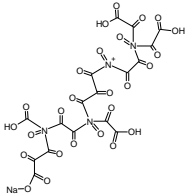
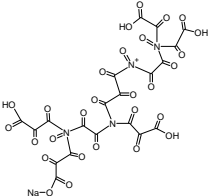
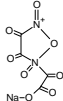
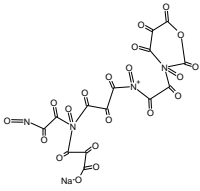
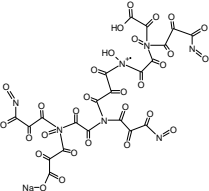
TP R _t (min)	Measured mass of major diagnostic ions	Relative peak intensity (%)	Elemental composition	Calculated mass	Error (ppm)	Proposed structures of diagnostic ions
TP1 11.00	702.8788	100	C ₁₇ H ₄ N ₄ O ₂₆ Na ⁺	702.9011	-31.7	
	770.8663	89.8	C ₂₀ H ₄ N ₄ O ₂₈ Na ⁺	770.8909	-31.9	
	226.9560	89.6	C ₄ N ₂ O ₈ Na ⁺	226.9552	3.5	
	566.9000	72.5	C ₁₄ N ₄ O ₂₉ Na ⁺	566.9003	-0.5	
	838.8560	92.1	C ₂₁ H ₂ N ₇ O ₂₉ Na ⁺	838.8794	-27.8	

Table 6.2. (Continued)

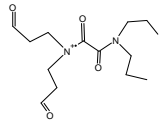
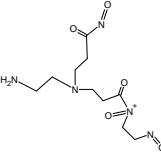
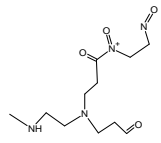
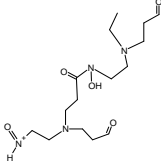
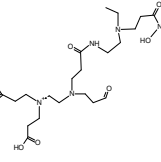
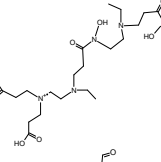
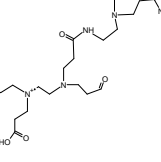
TP R _t (min)	Measured mass of major diagnostic ions	Relative peak intensity (%)	Elemental composition	Calculated mass	Error (ppm)	Proposed structures of diagnostic ions
TP2 13.1	284.1775	100	C ₁₄ H ₂₄ N ₂ O ₄ ⁺⁺	284.1736	13.7	
	288.1261	65.8	C ₁₀ H ₁₈ N ₅ O ₅ ⁺	288.1307	-15.9	
	273.1605	28.3	C ₁₁ H ₂₁ N ₄ O ₄ ⁺	273.1562	15.7	
	345.2186	28.3	C ₁₅ H ₂₉ N ₄ O ₅ ⁺	345.2137	14.1	
	517.3145	12.5	C ₂₃ H ₄₃ N ₅ O ₈ ⁺⁺	517.3111	6.5	
	505.3156	10.8	C ₂₂ H ₄₃ N ₅ O ₈ ⁺⁺	505.3111	8.9	
	527.2995	10	C ₂₄ H ₄₁ N ₅ O ₈ ⁺⁺	527.2954	7.7	

Table 6.2. (Continued)

TP R _t (min)	Measured mass of major diagnostic ions	Relative peak intensity (%)	Elemental composition	Calculated mass	Error (ppm)	Proposed structures of diagnostic ions
TP₃ 13.0	345.2078	65.5	C ₁₄ H ₂₇ N ₅ O ₅ ⁺⁺	345.3954	19.1	
	346.2093	10	C ₁₄ H ₂₈ N ₅ O ₅ ⁺	346.2090	0.8	
	367.1890	23.3	C ₁₄ H ₂₆ N ₅ O ₅ Na ⁺	367.1831	16.0	
	368.1922	6.6	C ₁₄ H ₂₇ N ₅ O ₅ Na ⁺	368.1909	3.5	
	457.2671	5	C ₁₉ H ₃₈ N ₄ O ₇ Na ⁺	457.2638	7.2	

(Forsström et al., 2000). Thus, the decomposition of a polymeric structure causes scission of the molecule into fragments of lower mass. Other studies have confirmed that the most susceptible hydrogens of the N-alkylamides, are the hydrogens at the N-vicinal methylene group and that

this would be the position where alkyl radicals and hydroperoxides will preferentially be formed (Lanska et al., 1991). The oxidation of secondary amines and tertiary amines resulting in the formation of amine oxide is suggested by means of the ions at m/z 505.3156, 517.3145, 345.2186 ($C_{15}H_{29}N_4O_5^+$) and 288.1261 ($C_{10}H_{18}N_5O_5^+$), 273.1605 ($C_{11}H_{21}N_4O_4^+$), respectively. The ions at m/z 273.1605 and 345.2186 confirmed the formation of highly oxidized intermediates affecting the ethylenediamine core.

The most plausible structure for the minor TP (TP_1) formed after 130 min under ozonation, suggests a higher oxidation state. The ion at m/z 838.8560 was assigned to $C_{21}H_2N_7O_{29}Na^{++}$ with a mass error of -27.8 ppm. Mass error exceeding 50 ppm was obtained for any lower percentage composition of oxygen, discarding this approach. The added oxygen in the elemental composition is present mainly as carbonyl and carboxyl groups, as well as amine oxides. With better mass accuracy, the ions at m/z 226.9560 ($C_4N_2O_8Na^+$, 3.5 ppm) and 566.9000 ($C_{14}N_4O_{29}Na^+$, -0.5 ppm) also appears to be consistent with a high oxidation state and the fragmentation pattern observed in TP_2 . The ion at m/z 226.9560 could be associated with an intermolecular cyclization of the ethylenediamine core, reported in previous studies (Hernando et al., 2012; Ulaszewska et al., 2013). The ion at m/z 566.9000 could be rationalized assuming the formation of an anhydride from two terminal carboxyl groups. The ions at m/z 770.8663 ($C_{20}H_4N_4O_{28}Na^+$, -31.9 ppm) and 702.8788 ($C_{17}H_4N_4O_{26}Na^+$, -31.7 ppm) resulted from the ion at m/z 838.8560 due to the successive scission of the C-N bond of the amide group. Several other mono-charged species that appear in the spectrum at m/z 1110.8091, 1042.8209, 974.8322, 906.8454, 634.8887, 498.9106, 430.9220, 362.9330 did not provide acceptable mass errors for a reliable characterization. On the other hand, all those ions showed a sequential loss of 68 Da, which once more would support the formation of carboxylic acids during ozonation (HCOONa).

The full scan mass spectrum of TP₃, the TP detected in UV irradiation runs, yielded the ions at m/z 457.2671, 368.1922, 367.1890, 346.2093 and 345.2078, which were assigned to elemental formula consistent with dendrimer composition. With a mass error of 7.2 ppm, the elemental composition C₁₉H₃₈N₄O₇Na⁺ was assigned as the most probable for the ion at m/z 457.2671, evidencing a lower degree of oxidation, also supported with the ions 345.2078 (C₁₄H₂₇N₅O₅⁺, 19.1 ppm), 346.2093 (C₁₄H₂₈N₅O₅⁺, 0.8 ppm) and their respective sodium adducts 367.1890 (C₁₄H₂₆N₅O₅Na⁺, 16 ppm), 368.1922 (C₁₄H₂₇N₅O₅Na⁺, 3.5 ppm). Table 6.2 presents the proposed structures for these diagnostic ions. The formation of carboxylic acids and amine oxides could be explained again as a consequence of the VUV irradiation of the low-pressure mercury lamps.

Few studies have reported the toxicity assessment of PAMAM dendrimers (Ulaszewska et al., 2012). Specifically, no information exists about the toxicity of G3 PAMAM-(NH₂)₃₂ for the organisms commonly used in ecotoxicity tests and, therefore, comparisons can only be established with close dendrimer generations. The effect was particularly high for the green alga, for which all endpoints fell below 1 mg/L. The result (0.059 μM) is in good agreement with the EC₅₀ 1.4 mg/L (0.099 μM) previously reported for G4 PAMAM for Suárez et al. (2011). For *P. subcapitata*, it was reported that EC₅₀ for G1 PAMAM-(NH₂)₈ was 8.9 mg/L (4.1 μM). The higher toxicity for G3 can be rationalized in terms of the negative surface charge of PAMAM dendrimers measured as ζ-potential, which was -0.89 ± 0.23 mV for G1, and +31.08 ± 2.24 mV for G3. A higher positive charge could lead to a stronger interaction with cell membranes favouring the rapid internalization of dendrimers. It has been recognized that the interaction of dendrimers with lipid bilayers is on the basis of their toxicity (Mecke et al., 2005). Naha et al. (2009) measured EC₅₀ of G4 for *V. fischeri* of 44.2 mg/L (3.11 μM). In this work, however, we found very low toxic effect of G3 for *V. fischeri*, with luminescence inhibition of 21.9 ± 0.1 % for 1000 mg/L (144.7 μM). Our result is closer to the 30 min EC₅₀ reported by

Mortimer et al. (2008) for G2 PAMAM: 632 mg/L (194 μ M). Better agreement can be observed for *D. magna*, whose EC_{50} immobilization by G4 was reported at 9.7 mg/L (0.68 mM) as indicated by Naha et al. (2009). This result favourably compares with the EC_{50} of 1.45 mg/L (0.21 μ M) obtained here for G3. The toxicity of G3 PAMAM-(NH₂)₃₂ for seed germination was low, with EC_{10} in the order of 100 mg/L (14.5 μ M). It is interesting to note that seeds exposed at a low concentration of dendrimer resulted in GI above control. The data are plotted in Fig. 6.8 together with their fitting to Brain-Cousens' model. In all cases the hormetic effect was significant, being particularly intense for *L. sativa*.

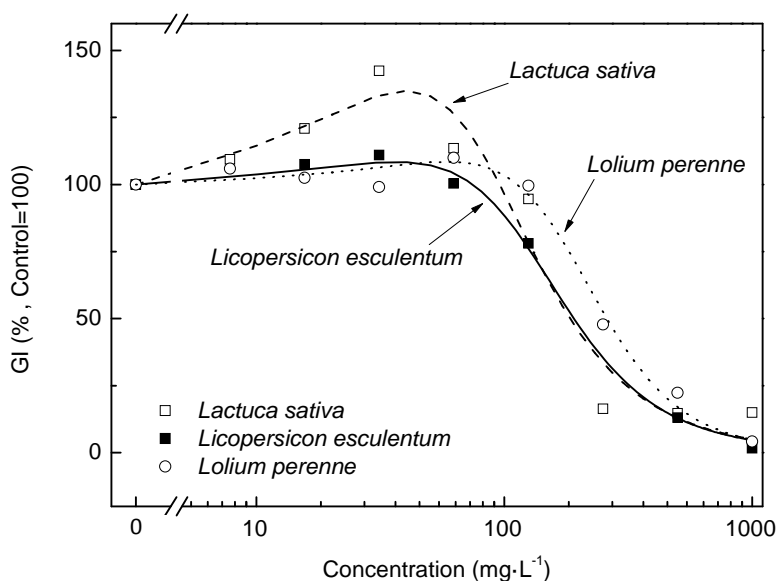


Figure 6.8. Hormesis effect on seeds of *Lactuca sativa*, *Lolium perenne* and *Lycopersicon esculentum* (GI = Germination Index).

Petit et al. (2012) showed that G4 PAMAM-(NH₂)₆₄ was toxic to the green microalga *Chlamydomonas reinhardtii*, in which the stimulation of the photosynthetic process led to the production of ROS. In a previous work, Petit et al. (2010) encountered stimulation of the photosynthetic metabolism of the same green alga in cultures exposed to G2-G4 amine-

terminated PAMAM dendrimers: the amount of active photosystem II reaction centers, the primary charge separation and the electron transport between Q_A and Q_B increased upon exposure. The relationship with ROS production is a consequence of the photosystem being very sensitive to physiological and environmental changes. In fact, ROS are constantly generated as by-products of normal metabolic pathways and their overproduction in response to stress and as a consequence of photo-synthesis impairment has been proved in algae (Darehshouri and Lütz-Meindl, 2010). Fig. 6.9 shows micrographs of *P. subcapitata* cells exposed to 0.5 mg/L G3 PAMAM-(NH₂)₃₂ during 72 h. An intense DCF signal appeared in certain cells and in areas of cell aggregates. In general ROS distribute throughout damaged cells, which coexisted with others with no DCF signal and normal levels of chlorophyll fluorescence. Fig. 6.10 displays chlorophyll and C4-Bodipy micrographs obtained for the same culture. Bodipy reveals lipid peroxidation in endomembranous organelles. The signal of Bodipy appeared linked to the accumulation of aggregates of cells and cell debris

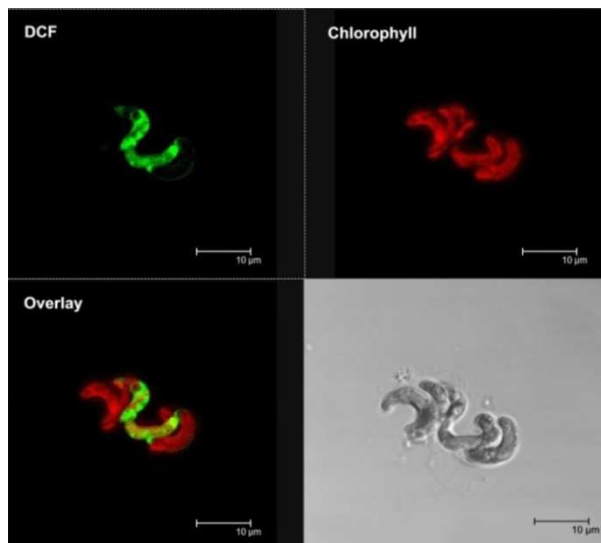


Figure 6.9. Confocal micrographs of *P. subcapitata* exposed for 72 h to 0.5 mg/L G3 PAMAM-(NH₂)₃₂ showing intracellular green DCF fluorescence and red chlorophyll autofluorescence

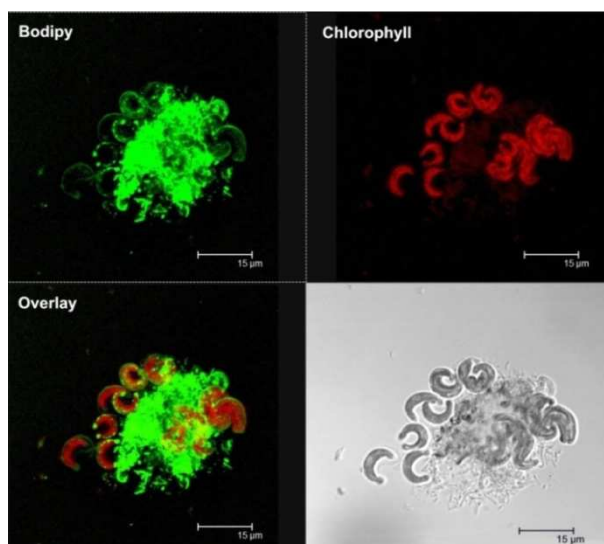


Figure 6.10. Confocal micrographs of *P. subcapitata* exposed for 72 h to 0.5 mg/L G3 PAMAM-(NH₂)₃₂ showing intracellular green C4-Bodipy fluorescence and red chlorophyll autofluorescence.

in which toxic effects are apparent. Lipid peroxidation appeared at certain specific places within green algae, which seemed unrelated with chloroplasts.

Ozonated mixtures presented a toxicity increase that was particularly severe for *D. magna* (Fig. 6.5). Part of this toxicity enhancement could be attributed to the formation of formic acid, whose concentration rose up to 65 mg/L after 130 min of ozonation. This represents about half of the EC₅₀ mobility inhibition for *D. magna*, which is 120 mg/L according to Vershueren (1983). Other acids did not represent a significant contribution to the total toxicity and, for example, oxalic acid was measured in concentrations as high as one tenth its EC₅₀ (Randall and Knopp, 1980). As indicated before, a number of TP were obtained from the decomposition of the polymeric structure originated from C-N bond scission of the amide groups. As ozonation proceeds, the structures obtained were more oxidized and, as indicated before, carboxylic acids and

other oxygenated compounds appear during UV irradiation as well. The positive charge of amino terminated dendrimers has been associated with its higher toxicity compared with their hydroxyl terminated counterparts (Suárez et al., 2011). We obtained, however, high toxicity in mixtures in which the ζ -potential was negative as a consequence of the oxidation of amine terminal groups. This is the case of ozonation after 10 min on stream as indicated in Fig. 6.5, the most probable cause being the formation of low molecular weight carboxylic acids (other than formic), which has been recognized as particularly toxic to *D. magna* (Pintar et al., 2004).

A common explanation for nanoparticle cytotoxicity starts with their internalization according to any endocytosis pathway. Subsequent encapsulation confines nanoparticles in endosomes and lysosomes. The reduced lysosomal activity encountered by Mukherjee et al. (2010) after exposition of several cell lines to G3-G6 PAMAM dendrimers suggests that after early endosomal transport, the dendrimers are released into the cytosol where they interact with intracellular membrane structures. The internalization of polycationic dendrimers into cells may proceed through the formation of transient nano-holes in the cell membrane (Hong et al., 2006). Damage of intracellular membranes could be the consequence of the localization of dendrimers in the mitochondria, which would lead to an increased ROS production and the disruption of the mitochondrial electron transduction chain with an additional ROS production (Lee et al., 2009). The toxicity of TP would be associated with the formation of low molecular weight carboxylic acids.

6.6. Conclusions

Amine terminated G3 PAMAM dendrimer becomes completely depleted by ozone in less than 1 min and by UV germicidal irradiation; although for the latter the most probable mechanism is a hydroxyl-

mediated oxidation rather than direct photolysis. The effect of visible light (> 290 nm) irradiation is much more limited (< 10% depletion after 2 hours).

The extent of mineralization was limited in any case and a number of TP appeared, some of which could be identified by LC/ESI-QTOF-MS. The suggested fragmentation pathway was retro-Michael reaction, which would be the source of most of the observed product ions. The structures proposed consider hydrogen migration and α -cleavage reaction at the less hindered tertiary amines with sequential losses of amino amide branches. The oxidation of this structure gave rise to the formation of carboxylic acids, while the oxidation of secondary amines and tertiary amines would result in the formation of amine oxide, with the presence of some highly oxidized TP.

Both ozonation and irradiation produce transformation products more toxic than the parent dendrimer for certain species. The toxicity increase was particularly apparent for *D. magna* in ozonated mixtures and could be attributed to the formation of low molecular weight oxidized species such as carboxylic acids, including formic acid, which was detected in concentration as high as half of its medium effect value for that organism.

The toxicity of G3 PAMAM-(NH₂)₃₂ was linked to a strong increase of intracellular ROS measured by DCF and Bodipy fluorescence. While DCF signal indicated that ROS-damaged cells coexisted with apparently normal ones, intense lipid peroxidation was localized in certain intracellular bodies of algal cells.

6.7. References

- Allen, J.M., Allen, S.K., Baertschi, S.W., 2000. 2-Nitrobenzaldehyde: a convenient UV-A and UV-B chemical actinometer for drug photostability testing. *Journal of Pharmaceutical and Biomedical Analysis* 24, 167-178.

- Baker, J.R., Majoros, I., 2008. Dendrimer-based nanomedicine. Pan Stanford Publishing, Singapore.
- Darehshouri, A., Lütz-Meindl, U., 2010. H₂O₂ localization in the green alga *Micrasterias* after salt and osmotic stress by TEM-coupled electron energy loss spectroscopy. *Protoplasma* 239, 49-56.
- EPA, 1996. Ecological Effects Test Guidelines. OPPTS 850.4200; Seed Germination/Root Elongation toxicity Test, US Environmental Protection Agency, Washington, DC EPA712-C-96-154.
- Forsström, D., Terselius, B., 2000. Thermo oxidative stability of polyamide 6 films. I. Mechanical and chemical characterization. *Polymer Degradation and Stability* 67, 69-78.
- Hernando, M., Rosenkranz, P., Ulaszewska, M., Fernández-Cruz, M., Fernández-Alba, A., Navas, J., 2012. In vitro dose–response effects of poly (amidoamine) dendrimers [amine-terminated and surface-modified with N-(2-hydroxydodecyl) groups] and quantitative determination by a liquid chromatography–hybrid quadrupole/time-of-flight mass spectrometry based method. *Analytical and Bioanalytical Chemistry* 404, 2749-2763.
- Hong, S., Leroueil, P.R., Janus, E.K., Peters, J.L., Kober, M.M., Islam, M.T., Orr, B.G., Baker, J.R., Holl, M.M.B., 2006. Interaction of polycationic polymers with supported lipid bilayers and cells: nanoscale hole formation and enhanced membrane permeability. *Bioconjugate Chemistry* 17, 728–734.
- Joyner, J.C., Keuper, K.D., Cowan, J.A., 2013. Analysis of RNA cleavage by MALDI-TOF mass spectrometry. *Nucleic Acids Research* 41, e2.
- Kitchens, K.M., Foraker, A.B., Kolhatkar, R.B., Swaan, P.W., Ghandehari, H., 2007. Endocytosis and interaction of poly (amidoamine) dendrimers with Caco-2 cells. *Pharmaceutical Research* 24, 2138-2145.
- Komilis, D.P., Karatzas, E., Halvadakis, C., 2005. The effect of olive mill wastewater on seed germination after various pretreatment techniques. *Journal of Environmental Management*. 74, 339-348.
- Lacorte, S., Fernández-Alba, A.R., 2006. Time-of-flight mass spectrometry applied to the liquid chromatographic analysis of pesticides in water and Food. *Mass Spectrometry Reviews* 25, 866– 880.
- Lánská B., 1991. Degradation and stabilization, in: R. Puffr and V. Kubanek Eds. Lactam based poly-amides, vol. I: Polymerization, structure and properties. Boca Raton: CRC Press, p. 262.
- Lee, J.H., Cha, K.E., Kim, M.S., Hong, H.W., Chung, D.J., Ryu, G., Myung, H., 2009. Nanosized polyamidoamine (PAMAM) dendrimer-induced apoptosis mediated by mitochondrial dysfunction. *Toxicology Letters* 190, 202–207.

- Mecke, A., Lee, D., Ramamoorthy, A., Orr, B., Banaszak Holl, M., 2005. Synthetic and natural polycationic polymer nanoparticles interact selectively with fluid-phase domains of DMPC lipid bilayers. *Langmuir* 21, 8588–8590.
- Mortimer, M., Kasemets, K., Heinlaan, M., Kurvet, I., Kahru, A., 2008. High throughput kinetic *Vibrio fischeri* bioluminescence inhibition assay for study of toxic effects of nanoparticles. *Toxicology in Vitro* 22, 1412-1417.
- Mukherjee, S.P., Lyng, F.M., Garcia, A., Davoren, M., Byrne, H.J., 2010. Mechanistic studies of in vitro cytotoxicity of poly(amidoamine) dendrimers in mammalian cells. *Toxicology and Applied Pharmacology* 248, 259–268.
- Naha, P.C., Davoren, M., Casey, A., Byrne, H.J., 2009. An ecotoxicological study of poly (amidoamine) dendrimers-toward quantitative structure activity relationships. *Environmental Science & Technology* 43, 6864-6869.
- Nicole, I., Delaat, J., Dore, M., Duguet, J.P., Bonnel, C., 1990. Use of Uv-Radiation in Water-Treatment - Measurement of Photonic Flux by Hydrogen-Peroxide Actinometry. *Water Research* 24, 157-168.
- OECD, 2010. List of Manufactured Nanomaterials and List of Endpoints for Phase One of the Sponsorship programme for the testing of manufactured nanomaterials: revision. OECD Paris.
- Petit, A.N., Debenest, T., Eullaffroy, P., Gagné, F., 2010. Toxicity of PAMAM dendrimers to *Chlamydomonas reinhardtii*, *Aquatic Toxicology* 100, 187–193.
- Petit, A.N., Debenest, T., Eullaffroy, P., Gagné, F., 2012. Effects of a cationic PAMAM dendrimer on photosynthesis and ROS production of *Chlamydomonas reinhardtii*. *Nanotoxicology* 6, 315–326.
- Pintar, A., Besson, M., Gallezot, P., Gibert, J., Martin, D., 2004. Toxicity to *Daphnia magna* and *Vibrio fischeri* of Kraft bleach plant effluents treated by catalytic wet-air oxidation. *Water Research* 38, 289–300.
- Randall, T.L., Knopp, P.V., 1980. Detoxification of specific organic substances by wet oxidation, *Journal of the Water Pollution Control Federation* 52, 2117-2130.
- Roberts, J.C., Bhalgat, M.K., Zera, R.T., 1996. Preliminary biological evaluation of polyamidoamine (PAMAM) Starburst™ dendrimers. *Journal of Biomedical Materials Research* 30, 53-65.
- Rosal, R., Rodríguez, A., Gonzalo, M.S., García-Calvo, E., 2008a. Catalytic ozonation of naproxen and carbamazepine on titanium dioxide. *Applied Catalysis B: Environmental* 84, 48-57.
- Rosal, R., Rodríguez, A., Perdigón-Melón, J.A., Mezcua, M., Agüera, A., Hernando, M.D., Letón, P., García-Calvo, E., Fernández-Alba, A.R., 2008b. Removal of pharmaceuticals and kinetics of mineralization by O₃/H₂O₂ in a biotreated municipal wastewater. *Water Research* 42, 3719-3728.

- Santiago-Morales, J., Gómez M.J., Herrera, S., Fernández-Alba, A.R., García-Calvo, E., Rosal, R., 2012. Oxidative and photochemical processes for the removal of galaxolide and tonalide from wastewater. *Water Research* 46, 4435-4447.
- Schmitt-Jansen, M., Bartels, P., Adler, N., Altenburger, R., 2007. Phytotoxicity assessment of diclofenac and its phototransformation products. *Analytical and Bioanalytical Chemistry* 387, 1389-1396.
- Solorzano, L., 1969. Determination of ammonia in natural waters by the phenol hypochlorite method. *Limnology and Oceanography* 14, 799-801.
- Strupat K. 2005. Molecular weight determination of peptides and proteins by ESI and MALDI. *Methods Enzymol.* 405:1-36.
- Suárez, I., Rosal, R., Rodríguez, A., Uclés, A., Fernández-Alba, A., Hernando, M., García-Calvo, E., 2011. Chemical and ecotoxicological assessment of poly(amidoamine) dendrimers in the aquatic environment. *TrAC Trends in Analytical Chemistry* 30, 492-506.
- Svenson, S., Tomalia, D.A., 2005. Dendrimers in biomedical applications—reflections on the field. *Advanced Drug Delivery Reviews* 57, 2106-2129.
- Thomson, J., Roddick, F., Drikas, M., 2002. Natural organic matter removal by enhanced photo-oxidation using low-pressure mercury vapour lamps. *Water Science and Technology* 2, 435-443.
- Ulaszewska, M.M., Hernando, M.D., Uclés, A., Valverde, A., García, E., Fernández-Alba, A.R. 2013. Identification and quantification of poly(amidoamine) PAMAM dendrimers of generations 0 to 3 by liquid chromatography-hybrid quadrupole time-of-flight mass spectrometry (LC-ESI-QTOF-MS/MS) in aqueous medium. *Rapid Communications in Mass Spectrometry* 27, 747-762.
- Ulaszewska, M.M., Hernando, M.D., Uclés, A., Rosal, R., Rodríguez, A., García-Calvo, E., Fernández-Alba, A.R., 2012. Chemical and ecotoxicological assessment of dendrimers in the aquatic environment. In: Farré M and Barceló D eds. *Analysis and Risk of Nanomaterials in Environmental and Food Samples*, Comprehensive Analytical Chemistry V59, Elsevier, Amsterdam, 197-233.
- Vershueren, K., 1983. *Handbook of Environmental Data on Organic Chemicals*, Van Nostrand Reinhold, New York, pp. 146-346.

Chapter 7

Conclusions and Future Challenges

Conclusions and future challenges

7.1. Conclusions

This chapter deals with the general conclusions of this PhD work and summarizes those already explained in detail in previous chapters.

1. Photodegradation treatments, namely ultraviolet and visible light irradiation, led to a lower hydroxyl radical production compared with ozonation processes. The combination of ozone with hydrogen peroxide (O_3/H_2O_2) or radiation (O_3/UV) enhanced the generation of hydroxyl radical per mol of ozone consumed by three orders of magnitude. The efficiency of hydroxyl radical production per fluence rate received increased with ozone usage in photo-assisted ozonation processes. The use of a dual source of hydroxyl radicals involves synergistic effects regarding hydroxyl radical production efficiency.
2. Emerging pollutants were efficiently removed by oxidation and radiative processes. Concerning semipolar and non-polar pollutants, ozone was able to generally achieve higher removal efficiency than that found for Ce-TiO₂ photocatalysis and UV irradiation. During Ce-TiO₂ photocatalysis, there was a clear positive relationship between photocatalytic removal efficiency and octanol-water partition coefficient for a significant group of semipolar and non-polar compounds. Ozonation was by far the most efficient treatment, one order of magnitude ahead of Ce-TiO₂ photocatalysis, which was the

irradiation process requiring the least energy to remove the same amount of micropollutants.

3. The absence of complete mineralization resulted in the accumulation of oxidation by-products identified using liquid chromatography coupled to quadrupole-time-of-flight mass spectrometry (LC-ESI-QTOF-MS) or stir bar sorptive extraction (SBSE) followed by comprehensive two dimensional gas chromatography (SBSE-GCxGC-TOF-MS). Exact mass measurements allowed proposing molecular structures for them and reaction pathways for the removal of fenofibric acid and propranolol. We identified a number of transformation products, most of them due to the addition of hydroxyl groups to the aromatic nuclei or to ring-opening attack by hydroxyl radicals.
4. The toxicity generally decreased during ozone treatments while irradiation processes generally led to a certain toxicity increase due to the accumulation of toxic transformation products. However, a certain toxicity enhancement was observed in almost all cases for some of the partially oxidized and irradiated mixtures. Prolonged irradiation or ozonation treatments offer no advantages in terms of toxicity reduction. Combined processes such as UV/H₂O₂ improved the removal of transformation products and allowed higher toxicity reductions in comparison with processes with lower or no generation of hydroxyl radicals.

7.2. Future challenges

In the present work, extensive research has been conducted in order to obtain a better understanding of oxidative and irradiative processes applied to the removal of emerging pollutants. However, further investigations are needed with this aim in light of the importance of water

pollution issues for sustainable development and the protection of aqueous ecosystems. The identified challenges would be as follows:

1. To develop ecotoxicological methods that allow reliable on-site and real-time monitoring of the toxic effects of water pollutants. The output should be useful for water authorities in order to make decisions to protect human health and aquatic ecosystems.
2. Regarding toxicity endpoints, further work is needed to develop and implement more sensitive and specific endpoints, such as those involving biochemical measurements of toxic or genotoxic responses. The research on the proteomic analysis of stress factors, closely related to the presence of toxicophores and the pollutant uptakes by cells, would be a possible target. Further research is needed on the biochemical background required for the elucidation of the mode of action of pollutants on genome and proteome.
3. In addition to the high resolution analytical techniques used in this work to detect emerging pollutants, further analytical developments would be required to identify and quantify toxicophore occurrence in aqueous media. This would give rise to closer measurements of potential ecotoxicity and a more accurate risk assessment of anthropogenic or natural pollutants.
4. To build a database on the Internet including risk assessment not only of pollutants but also of their potential transformation products obtained under different treatments. This would be useful for decision making in wastewater treatment and for the information of the public in general.

Annexes

Figure index

Chapter 1 Introduction

- Figure 1.1 Overall mechanism of semiconductor photocatalysis. CB = conduction band; VB = valence band; A = electron acceptor; D = electron donor. 42

Chapter 2 Oxidation by-products and ecotoxicity assessment during the photodegradation of fenofibric acid in aqueous solution with UV and UV/H₂O₂

- Figure 2.1. Photolytic decomposition of fenofibric acid at 35°C and pH 6.5. The inset represents the period for which the reaction followed zero order kinetics. 68
- Figure 2.2. $R_{ROH,UV}$ for different initial concentrations of hydrogen peroxide and (inset) evolution of the concentration of pCBA for runs without H₂O₂ (□) and using 10 mg/L H₂O₂ (◆), 50 mg/L H₂O₂ (▲) and 100 mg/L H₂O₂ (■). 70
- Figure 2.3. Plot of the competitive method of kinetic analysis during UV/H₂O₂ oxidation of mixtures of FA and ATZ using 50 mg/L H₂O₂ (●), 100 mg/L H₂O₂ (■) and 200 mg/L H₂O₂ (▲). (95% confidence intervals are shown for reference.) 71
- Figure 2.4. Evolution of TOC during UV/H₂O₂ using 50 mg/L H₂O₂ (■, left) and organic carbon in acetate, formiate and oxalate during the same run (●, left). Increase of chloride in solution during UV/H₂O₂ (50 mg/L, ○, right) and UV (□, right). 73

Figure 2.5.	LC-ESI-QTOF-MS/MS spectra of UV/H ₂ O ₂ and UV transformation products of fenofibric acid.	74
Figure 2.6a.	Proposed reaction pathway for fenofibric acid under UV irradiation.	81
Figure 2.6b.	Proposed reaction pathway for fenofibric acid under UV/H ₂ O ₂	83
Figure 2.7.	Growth inhibition of <i>Pseudokirchneriella subcapitata</i> and chromatographic area of transformation products (A = P291a + P291b + P291c, B = P233 + P249a + P249b, C = P307 + P291a + P291b + P291c).	85
Chapter 3	Transformation products and reaction kinetics in simulated solar light photocatalytic degradation of propranolol using Ce-doped TiO₂	
Figure 3.1.	Catalyst absorbance for different cerium content: (1) 1.0 %, (2) 0.5 %, (3) 0 % (TiO ₂), Xe lamp emission spectrum and propranolol absorption spectrum (5 mg/L).	99
Figure 3.2.	Evolution of propranolol (□, ■) and TOC (○, ●) during irradiation (empty symbols) and photocatalytic oxidation (0.14 g/L, Ce-TiO ₂ 0.5 % wt. Cerium, filled symbols).	106
Figure 3.3.	First-order rate constant as a function of bulk catalyst concentration for different cerium loadings: 1.0 % wt. (●), 0.5 % wt. (■) and TiO ₂ without cerium (▲). Inset: fitting of the logarithmic concentration decay for pure irradiation (without catalyst, Δ) and for 75 mg/L Ce-TiO ₂ , 0.5 % wt. Ce (□).	109
Figure 3.4.	Fitting of competitive kinetics (Eq. 12) for the simultaneous treatment of propranolol and pCBA with 0.14 mg/L Ce-TiO ₂ , 0.5 % wt. Ce.	112

Figure 3.5.	Propranolol depletion for irradiation (\square) and photocatalytic (\blacksquare , 0.14 g/L, Ce-TiO ₂ 0.5 % wt. Ce) runs in spiked wastewater. For comparison similar runs in pure water are included (\circ , \bullet), filled symbols representing photocatalytic experiments.	113
Figure 3.6.	Proposed degradation pathway for propranolol	124
Figure 3.7.	Chromatographic areas of the main transformation product from photocatalytic (a, b) and solar irradiation runs (c, d).	126
Figure 3.8.	Growth inhibition of <i>P. subcapitata</i> during irradiation (\circ) and photocatalytic treatment of propranolol (\bullet , 0.14 g/L, Ce-TiO ₂ 0.5 % wt. cerium) in (a) pure water and (b) spiked wastewater. (Δ): toxicity of non-spiked wastewater during irradiation.	130
Figure 3.9.	Bioluminescence inhibition (30 min) of <i>V. fischeri</i> during irradiation (\circ , \square) and photocatalytic treatment of propranolol (\bullet , \blacksquare , 0.14 g/L, Ce-TiO ₂ 0.5 % wt. cerium) in pure water (circles) and spiked wastewater (squares). (Δ): toxicity of non-spiked wastewater during irradiation.	131
Chapter 4	Oxidative and photochemical processes for the removal of galaxolide and tonalide from wastewater	
Figure 4.1.	Experimental equipment: 1, ozone generator; 2, flow control; 3, cooling device; 4, thermostat; 5, bath; 6, magnetic stirrer; 7, reactor; 8, diffuser; 9, pH electrode; 10, ozone sensor; 11, cooling tube; 12, lamp; 13, sampling device; 14, power supply; 15, ozone analyzer; 16, pH control unit; 17, data acquisition unit; 18, PC.	148
Figure 4.2.	Radical exposure parameters R_{ct} and $R_{OH,UV}$ for ozone and radiation-based processes in pure water and wastewater. (Note that higher values of $-\log(R_{ct})$ or $-\log(R_{OH,UV})$ represent lower generation of hydroxyl radicals.)	156

- Figure 4.3. Concentration profiles for HHCB (a), AHTN (b) and HHCB-lactone (c) during the different treatments assayed: O₃ (●), O₃/H₂O₂ (○), O₃/UV (■), O₃/Xe (□), O₃/Ce-TiO₂ (▲), O₃/Xe/Ce-TiO₂ (Δ), Xe/Ce-TiO₂ (◆), UV (◇), Xe (+) 159
- Figure 4.4. (a) GC×GC-TOFMS contour plot of spiked wastewater before treatment, showing the peaks and the spectra library searches for HHCB, AHTN and HHCB lactone. (b) GC×GC-TOFMS bubble plot showing temporal variation of target compounds. 161
- Figure 4.5. Toxicity of treated samples: relative growth rate of *P. subcapitata* (higher values correspond to lower toxicity; 1 = control). Time on stream: (●) 2 min, (■) 5 min, (○) 10 min, (□) 15 min. Dotted line: untreated pre-ozonated wastewater. (The bars represent confidence intervals.) 163
- Figure 4.6. Toxicity assessed by immobilization of *D. magna*. RWW: Raw waste-water, O₃WW: pre-ozonated wastewater before treatment. 165
- Figure 4.7. Toxicity of treated samples: relative luminescence of *V. fischeri* (higher values correspond to lower toxicities; 1 = control). Time on stream: (●) 2 min, (■) 5 min, (○) 10 min, (□) 15 min. Dotted line: untreated pre-ozonated wastewater. (The bars represent confidence intervals.) 166
- Chapter 5 Energy efficiency for the removal of non-polar pollutants during ultraviolet irradiation, visible light photocatalysis and ozonation of a wastewater effluent**
- Figure 5.1. First-order constant rate for micropollutant removal during UV irradiation as a function of their theoretical rate of photolysis (Eq. 4). For compound identification see Table 5.2. 189

Figure 5.2.	Photocatalytic removal of micropollutants as a function of the apparent octanol-water partition coefficient, K_{ow} . Insert: pollutant adsorption on catalyst surface for photocatalytic runs. The numbers refer to compounds as listed in Table 5.2.	191
Figure 5.3.	Concentration profile for the photodegradation of HHCB (a), AHTN (b), and musk ketone (c), shown by empty symbols, and its main transformation products, HHCB-Lactone (a), AHTN-COOH (b) and 2-amino musk ketone (c) displayed with filled symbols. (ADS: adsorption, IR: irradiation.) The left part of the figure shows the mass spectra identification of HHCB-Lactone (a), AHTN-COOH (b) and 2-amino musk ketone (c).	194
Figure 5.4.	Toxicity of irradiated and ozonated wastewater samples. Ozonation (◆), UV (■), Xe (○), Xe/Ce-TiO ₂ (▲).	196
Figure 5.5.	Removal of the total concentration of micropollutants as a function of the energy transferred to water during Xe, Xe/Ce-TiO ₂ , UV and O ₃ treatments. Transferred energy efficiency (TEE, nmol kJ ⁻¹) is shown in labels.	198
Chapter 6	Fate and toxicity of amine-terminated PAMAM dendrimers under ozonation and irradiation	
Figure 6.1.	G3 PAMAM-(NH ₂) ₃₂ removal during ozone (O ₃), ultra-violet (UV) and visible light irradiation (Xe).	223
Figure 6.2.	Nitrogen release, TOC evolution and carboxylic acids produced during the ozonation of G3 PAMAM-(NH ₂) ₃₂ .	224
Figure 6.3.	(a) LC-ESI-QTOF-MS full scan spectrum of PAMAM dendrimer of third-generation G3. (b) Resolution of isotopic cluster [M+9H] ⁹⁺ . 13C/12C isotopic distribution and isotopic peak spacing.	226

Figure 6.4 (a)	Total ion chromatograms (TIC) of samples collected at different times of treatment (up to 130 min) showing depletion of G3-PAMAM-(NH ₂) ₃₂ and formation of two TP.	227
Figure 6.4(b)	LC-ESI-QTOF-MS full scan spectrum of TP1 (130 min ozonation) and TP2 (15 min ozonation).	228
Figure 6.5.	Toxicity assessment of ozonated and irradiated mixtures	231
Figure 6.6.	G3 PAMAM-(NH ₂) ₃₂ absorption spectrum and Xe and UV lamp emission spectra.	233
Figure 6.7.	Logarithmic decay of TOC as a function of the integral exposure to dissolved ozone. R _i represent the second order rate constants for the mineralization process.	234
Figure 6.8	Hormesis effect on seeds of <i>Lactuca sativa</i> , <i>Lolium perenne</i> and <i>Licopersion esculentum</i> (GI = Germination Index).	241
Figure 6.9.	Confocal micrographs of <i>P. subcapitata</i> exposed for 72 h to 0.5 mg/L G3 PAMAM-(NH ₂) ₃₂ showing intracellular green DCF fluorescence and red chlorophyll autofluorescence	242
Figure 6.10	Confocal micrographs of <i>P. subcapitata</i> exposed for 72 h to 0.5 mg/L G3 PAMAM-(NH ₂) ₃₂ showing intracellular green C4-Bodipy fluorescence and red chlorophyll autofluorescence.	243

Table index

Chapter 1 Introduction

Table 1.1	Classification of advanced oxidation processes.	39
-----------	---	----

Chapter 2 Oxidation by-products and ecotoxicity assessment during the photodegradation of fenofibric acid in aqueous solution with UV and UV/H₂O₂

Table 2.1.	Accurate mass measurements of fenofibric acid and its UV photolysis products by LC-ESI-QTOF-MS and structures proposed for the identified transformation products	75
Table 2.2.	Accurate mass measurements of fenofibric acid and its UV/H ₂ O ₂ products by LC-ESI-QTOF-MS and structures proposed for the identified transformation products	77

Chapter 3 Transformation products and reaction kinetics in simulated solar light photocatalytic degradation of propranolol using Ce-doped TiO₂

Table 3.1.	Main wastewater parameters	98
Table 3.2.	LC-ESI-QTOF-MS/MS mass measurements of propranolol and its transformation products and structures proposed for them (p = parent compound; c = photocatalytic process; s = solar irradiation).	116

Chapter 4	Oxidative and photochemical processes for the removal of galaxolide and tonalide from wastewater	
Table 4.1.	Wastewater characterization parameters for raw and pre ozonated effluent	147
Table 4.2.	Summary of experimental conditions used in this work.	150
Chapter 5	Energy efficiency for the removal of non-polar pollutants during ultraviolet irradiation, visible light photocatalysis and ozonation of a wastewater effluent	
Table 5.1.	Analysis of wastewater	180
Table 5.2.	Removal of pollutants for irradiation, photocatalytic and ozonation treatments (expressed as $c(t)/c_0$). Reaction conditions: UV used a 15W low pressure mercury lamp with fluence rate $6.01 \times 10^{-6} \text{ E L}^{-1} \text{ s}^{-1}$ (254 nm); Xe and Xe-TiO ₂ used a Heraeus TQ Xe 150 Xe-arc lamp with fluence rate $1.05 \times 10^{-6} \text{ E L}^{-1} \text{ s}^{-1}$ (290-400 nm); the catalyst concentration was 200 mg/L; ozone gas flow and concentration were $0.19 \text{ N m}^3 \text{ h}^{-1}$ and 22 g Nm^{-3} .	185
Table 5.3.	Properties of micropollutants	187
Table 5.4.	Properties of micropollutants (continued)	188
Table 5.5.	Water-transferred power (WTP), electrical energy per order (EEO) and collector area per order (ACO) for the different treatments	201
Table 5.6.	Electrical energy per order per order, E_{EO} (kWh m^{-3} order) and and collector area per order, A_{CO} ($\text{m}^2 \text{ m}^{-3}$ order ⁻¹) in the literature.	202

Chapter 6 Fate and toxicity of amine-terminated PAMAM dendrimers under ozonation and irradiation

- Table 6.1. Dose-Effect Relationship Parameters for the bioassays used in this work. In parenthesis 95% confidence intervals. EC₅₀, EC₂₀ and EC₁₀ are expressed in milligrams per liter. GI: Germination Index. ^a Clear microplate (upper and lower irradiation), ^b Black bottom microplate (upper irradiation) 230
- Table 6.2. Identification of transformation products (TP) of PAMAM dendrimer of third generation by LC-ESI-QTOF-MS analysis. Mass measured of major diagnostic ions detected under ozonation and UV irradiation, mass error (ppm), elemental composition and proposed structures. TP1: ozonation, 15 min of treatment; TP2: ozonation 130 min of treatment; TP3: UV irradiation, 15 min of treatment. 236

Curriculum Vitae

Javier Santiago Morales was born on 1st July 1984 in Madrid, Spain. He studied a degree in Agriculture Engineering at Technical University of Madrid (UPM). During the university period, he worked as a junior research awarded with different scholarships in the departments of Physics and Applied Mechanics Fundamentals and Agroforestry Engineering, and Construction and Rural Roads of UPM, and the group of Geochemistry and Environmental Mineralogy in Spanish National Research Centre (CSIC). He graduated in 2008 obtaining third prize for Best Academic Results. Afterward, he decided to study MSc in Hydrology and Water Resources Management at the University of Alcalá (Spain). His master project awarded with the maximum honors was emphasized on reclamation of wastewater by advanced oxidation processes. After his master graduation, he joined to the department of Analytical Chemistry and Chemical Engineering of the University of Alcalá and started his PhD training supervised by Professor Roberto Rosal thanks to a four year PhD scholarship from the Spanish Ministry of Education. His investigation is based on the study of advanced oxidation processes applied for emerging pollutant removal, combining chemical engineering, analytical methods and ecotoxicity. During his PhD, Javier has also worked in the group of Prof. Santiago Esplugas at the University of Barcelona (Spain), the group of Prof. Paul. A. Christensen at Newcastle University (United Kingdom) and under the supervision of Dr. Davide A.L. Vignati and Prof. Jean-François Féraud at the Laboratoire des Interactions Ecotoxicologie, Biodiversité, Ecosystèmes (LIEBE)-CNRS URM 7146 at University of Metz (France).

Publication list

- Santiago, J., Agüera, A., del Mar Gómez-Ramos, M., Fernández Alba, A. R., García-Calvo, E., Rosal, R., 2011. Oxidation by-products and ecotoxicity assessment during the photodegradation of fenofibric acid in aqueous solution with UV and UV/H₂O₂. *Journal of Hazardous Materials* 194, 30-41.
- Rosal, R., Gonzalo, S., Santiago, J., Rodríguez, A., Perdigón-Melón, J. A., García-Calvo, E., 2011. Kinetics and Mechanism of Catalytic Ozonation of Aqueous Pollutants on Metal Oxide Catalysts. *Ozone: Science & Engineering* 33, 434-440. (*Free access*)
- Rodea-Palomares, I., Boltes, K., Fernández-Piñas, F., Leganés, F., García-Calvo, E., Santiago, J., Rosal, R., 2011. Physicochemical characterization and ecotoxicological assessment of CeO₂ nanoparticles using two aquatic microorganisms. *Toxicological Sciences* 119, 135-145. (*Highlighted article*)
- Santiago-Morales, J., Agüera, A., Gómez, M. M., Fernández-Alba, A. R., Giménez, J., Esplugas, S., Rosal, R., 2012. Transformation products and reaction kinetics in simulated solar light photocatalytic degradation of propranolol using Ce-doped TiO₂. *Applied Catalysis B: Environmental* 129, 13-29. (Ranked 14th in Top 25 Hottest Articles from October to December 2012)
- Santiago-Morales, J., Gómez, M. J., Herrera, S., Fernández-Alba, A. R., García-Calvo, E., Rosal, R., 2012. Oxidative and photochemical processes for the removal of galaxolide and tonalide from wastewater. *Water Research* 46, 4435-4447.
- Rodea-Palomares, I., Gonzalo, S., Santiago-Morales, J., Leganés, F., García-Calvo, E., Rosal, R., Fernández-Piñas, F., 2012. An insight into the

mechanisms of nanoceria toxicity in aquatic photosynthetic organisms. *Aquatic Toxicology* 122-123, 133-143.

Herrera López, S., Hernando, M. D., Gómez, M. J., Santiago-Morales, J., Rosal, R., Fernández-Alba, A. R., 2013. Investigation of Galaxolide degradation products generated under oxidative and irradiation processes by liquid chromatography/hybrid quadrupole time-of-flight mass spectrometry and comprehensive two-dimensional gas chromatography/time-of-flight mass spectrometry. *Rapid Communications in Mass Spectrometry* 27, 1237–1250.

Santiago-Morales, J., Gómez, M. J., Herrera-López, S., Fernández-Alba, A. R., García-Calvo, E., Rosal, R. Energy efficiency for the removal of non-polar pollutants during ultraviolet irradiation, visible light photocatalysis and ozonation of a wastewater effluent. *Water Research*, DOI 10.1016 /j.watres. 2013.06.030.

